FORMATION, PROPERTIES, AND STABILITY OF POLY(HEXAMETHYLENE BIGUANIDE) STABILISED SILVER NANOPARTICLES FROM THE PERSPECTIVE OF NOVEL ANTIMICROBIAL AGENTS.

JAKUB SACHARCZUK

Doctor of Philosophy

ASTON UNIVERSITY

SEPTEMBER 2021

Abstract

Rising antimicrobial resistance has increased pressure to develop novel antimicrobial agents. Poly(hexamethylene biguanide) stabilised silver nanoparticles have been suggested as a potential candidate exhibiting strong biocidal properties. This study researches the formation, properties, and stability over time of the PHMB-AgNPs complex.

Silver nanoparticles were synthesised from silver nitrate using a chemical reduction procedure with sodium borohydride in the presence of a stabiliser, PHMB. The obtained complex was characterised by a wide range of complementary methods relying on different analytical principles such as scattering, spectroscopy and microscopy. This allowed for a determination of the physical properties of the complex and the monitoring of changes over time. The preliminary antimicrobial efficacy was assessed using a well diffusion technique and flow cytometer.

AgNPs stabilised with PHMB (concentration from 20 µg/mL to 200 µg/mL) were successfully synthesised and characterised. A noticeable shift in the peak position from typically observed 390 nm for Bare-AgNPs to 420 nm evidenced by UV-Vis and the change in the direction of electrophoretic mobility, confirmed that AgNPs were indeed stabilised with PHMB. The size of spherical silver nanoparticle cores was calculated from Small-Angle X-ray Scattering patterns to be around 13 nm for Bare-AgNPs and 4 nm for PHMB-AgNPs. However, the two-population distribution observed with Dynamic Light Scattering exhibited significant number fluctuation indicating flocculation caused by the polymer. Limits of the PHMB concentration available for complexing were observed at around 60 µg/mL, beyond which polymer presence was recorded in the filtrate residue following membrane filtration. The antimicrobial activity indicated that silver nanoparticles did not exhibit any activity against *E. Coli* or *S. Aureus,* in contrast to the PHMB stabiliser and the PHMB-AgNPs. Long term stability has shown that a minimum PHMB concentration at 60 µg/mL must be achieved to prevent the flocculation of AgNPs over time.

PHMB, AgNPs, Antimicrobial, Stability, silver nanoparticles

Dedication

My deepest gratitude goes to my supervisors, Professor Brian J Tighe and Professor Paul Topham – I could not wish for a better team to overlook my efforts. They offered the freedom to pursue scientific avenues, without judgment but with plenty of banter and parables. Their knowledge and experience inspired and stimulated me through the tireless meetings to review and discuss my results. They made this research possible, viable and enjoyable, steering me through the low points with lots of 'high fives' and stories of being lost in a forest.

My thanks go to the Biomedical Research Unit team, for their supportive and open attitude towards me, for sharing their immense knowledge of science and of the meanders of university life. But the simple truth is that without the wonderful Dr Val Franklin, Dr Aisling Mann, Dr Fiona Lydon and Dr Evita Chundoo I would be completely lost. They were there to help me to find my way around the lab, the project, the equipment and the science. To Nick Crosby for dotting the i's and crossing all the t's.

I will fondly remember all my fellow PhD students: Sian, Joe, Helena, Kinana, George, Carmen, Mike and many others, who shared the joy of conducting research, with its highs and lows. Being able to talk, compare notes, teach other new techniques and waste time was an enormous help.

Finally, I owe a world to my wife, Ivana, for encouraging me to start this PhD and supporting me along the way to completing it. To my children, Luka, Noa and Luna for patiently waiting for me to finish my 'book'. Together they make the most constructive and destructive of all forces.

List of Contents

List of Abbreviations

AMR – Antimicrobial resistance

AgNPs – Silver nanoparticles

Bare-AgNPs – Silver nanoparticles without stabiliser

BF – Bright Field

Cps – Counts per second

CNT – Classical nucleation theory

EDL – Electric double layer

EDS – Energy Dispersive X-ray Spectroscopy

EM – Electron Microscope

ETD –Everhart-Thornley Detector

DLS – Dynamic Light Scattering

DF – Dark Field

ESEM – Environmental Scanning Electron Microscope

FTIR – Fourier-transform Infrared Spectroscopy

FWHM – Full Width Half Maximum

HAADF – High-Angle Annular Dark-Field

HV – High Vacuum

KR samples – Kinetics Reaction Samples

NMR – Nuclear Magnetic Resonance

NP – Nanoparticles

PBS – Phosphate-Buffered Saline

PHMB – Poly(hexamethylene biguanide)

PHMB-AgNPs – Poly(hexamethylene biguanide)-stabilised silver nanoparticles

PVP – Poly(vinyl pyrrolidone)

SAXS – Small-Angle X-ray Scattering

SB samples – Sodium Borohydride Reactions

SEM – scanning electron microscopy

SPR – Surface Plasmon Resonance

SR samples – Standard Reactions Samples

STEM – scanning transmission electron microscopy

STEM-in-SEM – scanning transmission electron microscopy mode in scanning electron microscopy

TEM – transmission electron microscopy

UV-Vis – Ultraviolet-Visible Spectroscopy

WetSTEM – Wet mode in scanning transmission electron microscopy

ZOI – Zone of Inhibition

ZP – Zeta Potential

List of Tables

List of Figures

Chapter 1. Introduction

1.1. Background

In 2020, when COVID-19 emerged and a pandemic was declared by authorities all over the world, awareness of the health threats from viruses increased dramatically. A major multifaceted approach was developed to protect the global population from the threats posed by the COVID-19 virus. As measures such as social distancing, mask wearing, testing and tracing were introduced to slow the spread of the virus, the global scientific community developed vaccinations at breakneck speeds. Antimicrobial resistance was identified as a significant risk to global health many years ago. In fact, the pioneer of penicillin, within a few years of his discovery, realised that bacteria develop resistance to this antibiotic produced by mould. Unlike the response to COVID-19, which required an accelerated response, the scientific community and policymakers were given the benefit of time to work out a response strategy to antimicrobial resistance. As with COVID-19, one such response involved repurposing already available medication and agents to assess their effectiveness against the pathogens. These included the silver, and to a lesser extent, the poly(hexamethylene biguanide) used in this research. The benefit of the time given allows for this research to investigate beyond the antimicrobial efficacy of the proposed complex, to explore the interaction between the components, to emphasise and understand the novel nanostructures created, and to probe the stability of the complex.

1.2. Antimicrobial resistance

Antimicrobial resistance is a naturally occurring phenomenon of microbes' developing resistance to antibiotic drugs as a result of exposure to those agents. When microorganisms are exposed to antibiotics, selective pressure is created, promoting the survival of those able to adapt to the environment [1]. Misuse of antibiotics in healthcare and agriculture results in the ever-increasing presence of antimicrobial agents in the environment, further stimulating the presence of antibiotic-resistant bacteria [2]. This is additionally aggravated by the bacteria's ability of horizontal gene transfer, which allows antimicrobial resistance to spread across the

bacteria strain more easily [1]. Treatment of infections caused by antibiotic-resistant bacteria strains requires the use of more expensive second- or third-line drugs, calls for specialised knowledge and equipment, and can extend hospitalisation periods. There is also significant societal cost due to mortality and lost productivity [3].

Around the globe, countries and organisations have developed various action plans to survey, slow and control the rise of antimicrobial resistance [4], these propose a multifaceted approach to tackle various aspects of this problem. The aim is to reduce the overuse of antimicrobials, develop alternative treatments, improve diagnostics and increase awareness among the population. However, considering only one aspect of this approach – developing alternative treatments – meeting this target is in itself a challenging proposal. Regulation makes developing new antibiotics expensive and slow. Safety concerns raised during clinical trials mean that many preselected candidates do not make the pipeline [4]. In addition, new antibiotics are saved for last-resort use when all others fail, reducing possible market demand and pharmaceutical company profits [5]. Considering the level of investment required, the commercial case for such ventures is limited. Repurposing already approved medical products offers a much shorter time-to-market turnaround [5].

It is estimated that antimicrobial resistance will be responsible for more deaths than all cancers combined by 2050. The urgency of tackling this complex issue cannot be overestimated, but awareness is increasing and plans are being drawn [4] and implemented to combat the problem. One of the avenues involves repurposing already approved medicinal products, and both poly(hexamethylene biguanide) and silver nanoparticles are known to the

regulators and have been used in medicinal environments for a number of years, thus offering great potential for further exploration.

1.3. Polymer stabilised metal nanoparticles

Metal nanoparticles have already been known for millennia and were explored by ancient Romans for i.e. glass staining [6]. Recent developments in synthetic chemistry allowed for more precise synthesis of nanoparticles between 1 and 100 nm in size [7], which led to the resurgence of interest in the use of metal nanoparticles, such as silver [8]. This enthusiasm for the nanoparticles is reflected by the number of research publications generated on the subject between 2005 and 2020, as shown in Figure 1-1. Metal nanoparticles physicochemical properties are significantly different from the bulk metal, i.e. different shapes of nanoparticles result in changes to the surface plasmon resonance [9] which has important applications in fields such as electro-optical sensors or conversion of solar energy [10]. As a result metal nanoparticles are utilised in a wide range of industries including biomaterials [11], medicine

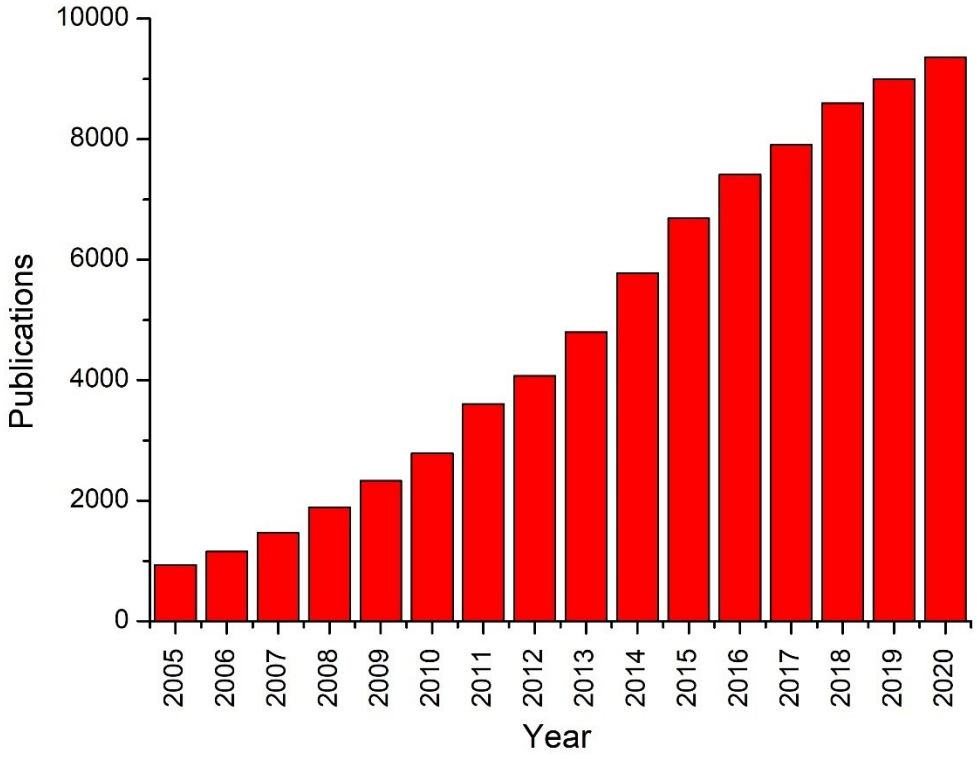

Figure 1-1 Number of articles published each year with keyword 'silver nanoparticles' between 2005 and 2020 as index on the 'ISI Web of Science'

[12] and many others. The applications of the nanoparticles are linked to the exhibited properties, in particular size, shape, stability, and aggregation. In turn, these depend on the synthetic methods chosen, which are categorised as either top-down or bottom-up. The former uses physical methods such as grinding or laser ablation [13-15] which usually produces larger particles with a greater polydispersity, while the latter relies on biological [16] or chemical [13-15] methods which offer better control over the synthesis process allowing for smaller nanoparticles with desired shapes and polydispersity. Chemical methods, and chemical reduction in particular [17], stand out for their high yields, low costs, and ease of production, making this a more suitable candidate to investigate changes in shape and size, as well as stability and aggregation. Different metal nanoparticles can be produced using this method which requires a precursor – usually metal salts, while sodium borohydride is frequently utilised as a reducing agent due to its strong reducing capabilities (but sodium citrate [17] and various others are also exploited [9]). The formation of the nanoparticles is explored in more detail in the introduction to Chapter 5**.** Metal nanoparticles are frequently stabilised with polymers to improve their colloidal stability, polymer forms a steric barrier which prevents the nanoparticles from coming into proximity and aggregating. The use of polymers for nanoparticle stabilization can have several advantages over other stabilization methods [18]. For example, polymers can be easily synthesized and modified to control their size, shape, and surface chemistry, allowing for precise control over the properties of the resulting stabilized nanoparticles. The polymer chains adsorb onto the surface of the nanoparticles, creating a steric hindrance effect that prevents the nanoparticles from interacting with each other [19]. In addition to providing a steric barrier, polymers can also provide electrostatic stabilization by introducing charges on the surface of the nanoparticles. Polymers with charged functional groups, such as carboxylates or biguanides, can interact with ions in the surrounding solution, improving the stabilisation effect [20]. The concept of colloidal stability and the impact various

elements of the nanoparticle system have on it are explored in more detailed in the next section below 1.3.1 – Colloidal stability of nanoparticles.

Adapting those general conditions to different metals, reducing agents and polymers allow for a synthesis of various metal nanoparticles. The examples include using chloroauric acid in the microfluidic reactor with different ratios of gold to poly(vinyl pyrrolidone) (PVP) stabiliser produced small (1nm) stable gold nanoparticles [21]. Modifying conditions allow for comparative studies of how changes to the synthesis process affect the nanoparticles, Luty-Blocho *et al*. [22] compared the rate of nucleation and growth of platinum (from chloroplatinic acid) and gold (from chloroauric acid) nanoparticles. By varying the pH of synthesis, using two different reducing agents, L-ascorbic acid and sodium borohydride, and two different stabilisers, poly(vinyl pyrrolidone) and poly(vinyl alcohol). It was shown how changes to reagents and the synthesis environment affected the properties of obtained particles. Additionally, polymers are often biocompatible and can be used for applications in biomedical imaging, drug delivery, and tissue engineering [23]. Kora et al. [24] applied a biopolymer - gum ghatti – to act as a stabiliser and a reducing agent at a high temperature of 121 °C to form palladium nanoparticles (from palladium chloride). Other metals such as gold (spheres and rods) [18], titanium [25], copper[26], nickel [27], and cobalt [28] nanoparticles can also be synthesised. In these few examples, from many available in the literature, the methods, reagents, conditions and approaches vary greatly because the synthesis of metal nanoparticles is an area of significant progress. It is not yet fully understood how changing reaction parameters such as pH, ionic strength, temperature, reducing agent, and stabiliser manifest in the physicochemical properties of the nanoparticles obtained.

1.3.1. Colloidal stability of nanoparticles

Colloidal stability is the ability of nanoparticles to remain suspended in a medium over time without number fluctuating – sedimentation, aggregation, dissolution. Metal nanoparticles have a large surface-to-volume ratio and unsaturated coordinated sites resulting in highly

reactive surface [19]. This causes adsorption of ions or molecules from the surrounding solution onto the surface. The theoretical background for the behaviour of nanoparticles in solution is provided by the Derjagui-Landau-Verwey-Overbeek (DLVO) theory, it considers colloidal stability as an interplay between attractive Van der Walls and repulsive Coulombic forces [29]. The DLVO theory can be used to calculate the behaviour of the nanoparticles; however, it has several limitations that cannot be omitted, primarily, it assumes a binary system [30]. For two nanoparticles to be stable thermodynamically the energy barrier, the repulsive forces, between them must be greater than the attractive forces, otherwise, an irreversible coagulation takes place (Figure 1-2a).

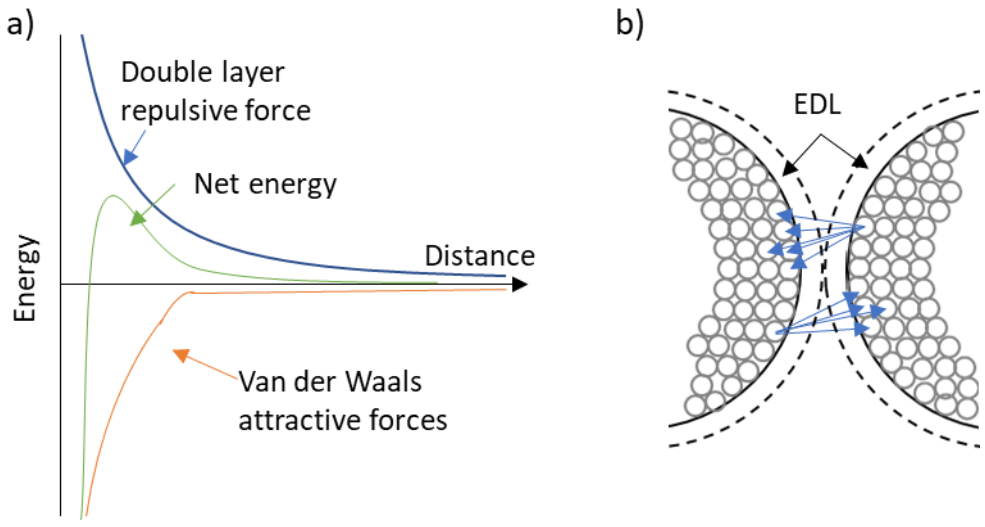

Figure 1-2 a) Energy vs distance plot – the repulsive forces prevent the particles from aggregation unless particles have sufficient energy to overcome the net energy value which will cause attractive forces to adhere them together. b) Consideration of forces between particles - The interacting electric double layer cause repulsive forces equal to osmotic pressure at a midpoint between particles. Van der Walls attractive forces are a sum of all interactions between molecules in one particle multiplied by all molecules in the other particle.

The highly negative surface charge of the nanoparticles attracts counterions to balance it, with the immediate, fixed Stern layer and slipping plane they form an electric double layer (EDL) **(**Figure 1-2b and Figure 1-7**)**. at which the zeta potential of colloidal nanoparticles can be measured using light spectroscopic techniques. Electrostatic repulsion is defined by the properties of the double layer, the hydrodynamic diameter around the nanoparticle, as particles

approach each other the corresponding EDL cannot develop unrestricted. The electrostatic repulsion is therefore equal to the osmotic pressure difference between the mid-plane position of the particles and the bulk of the electrolyte [19]. This can be calculated using a series of approximations but the Gibbs free energy of electric repulsion, potential energy, is a function of charge densities, differential capacities, dimensionless potential, and the valency of the symmetrical electrolyte. For the spherical particles, the situation is further complicated by the fact that the distance between the particles changes with the curvature. Also, the ratio in size between the particle and EDL has repercussions on how the electrostatic repulsions are calculated. The relative distances between the particles mean the repulsion is not negligible for particles that are within a few times the distance of the EDL from each other. All those factors listed above will impact how the repulsive forces will influence the energy vs distance plot (Figure 1-2a), reducing or increasing the net energy required to aggregate the particles.

The attractive van der Waals interactions are a universal attraction between colloidal particles over short distances, a potential energy or work needed to separate particles. The energy needed depends on the material type, geometry, and distance between particles. As the potential energy is a sum of atom interactions between particles multiplied by the sum of equivalent atom interactions in the other particle (Figure 1-2b) [19]. Similarly, to the electrostatic repulsions, the curvature of the particles and the size ratio between them adds complexity to this interaction. As the attraction brings the particles closer, the medium between the particles must be displaced this however increases the repulsive force as the osmotic pressure between the mid point of the particles changes. The van der Waals curve (Figure 1-2a) changes with the factors defined above.

Therefore, the total energy of interaction G_T can be expressed with two forces, electrostatic $-\ G_{elec}$ and van der Waals $-\ G_A$ with the expression

$$G_T = G_{elec} + G_A \qquad \textit{Eq. 1-1}$$

The colloidal stability can be assessed by measuring zeta potential, the potential difference between the nanoparticle and the surrounding solution, it provides insight into the electrostatic interactions between the particles. Based on the result, it is possible to predict the stability of the nanoparticles. It is typically expected that particles with a zeta potential of ±30 mV be stable [31]. Zeta potential is further discussed in section 1.4.3 Dynamic Light Scattering and Zeta Potential. At the same time, the colloidal stability is correlated with the surface charge of the nanoparticle, and several factors can, directly and indirectly, influence it.

The physicochemical properties of the environment (such as pH, ionic strength, electrolyte composition) directly affect the surface charge and the EDL developed around particles. For example, when investigating one component, the ionic strength, the size of the EDL decreases with the increase of the ionic strength impacting the curve for the repulsive forces of the energy vs distance plot (Figure 1-2a). Therefore, the net energy is reduced making the aggregation more likely, this was experimentally confirmed [32]. But when multiple factors are involved including different synthesis pathways (chemical and biological) for the same metal nanoparticles the response in change to the physicochemical properties can have such complexity that it does not fit the theoretical expectations [33]. Nevertheless, electrostatic stabilisation by controlling the repulsive forces is an important avenue for controlling colloidal stability. The alternative is the indirect factors, those that do not change the inherent surface charge of a nanoparticle, but reduce the interactions between them, by forming a physical barrier. Polymers are often exploited for this role, their adsorb on to the surface of the particle creating a steric stabilisation. As the particles approach each other the polymer stabiliser of the particles interpenetrate or compress. The former increases the local concentration of the polymer causing the solvent from the bulk to push into the area, as a result of the osmotic pressure the particles are pushed apart. The latter causes the polymer to lose degree of freedom,

therefore, entropy loss. Li et al. [20] distinguish two such types of stabilisers, steric and electrostatic, with the former providing stability based on the thickness and density of the layer, and the latter providing electrostatic repulsive interactions. Surfactants such as sodium dodecyl sulfate (SDS), which is a small, charged molecule, could be considered members of the electrostatic group. Protection of the nanoparticles is particularly strong in concentrations higher than the critical micelle concentration, as a double layer is then formed over the nanoparticle [20]. On the other hand, a polymer such as poly(vinylpyrrolidone) could be considered in the first – steric – group. Hybrid electrosteric stability is provided by compounds that exhibit properties from both groups discussed above. These are large and charged molecules, such as poly(hexamethylene biguanide).

To achieve lasting stabilisation the polymer must cover the entire particle with sufficient thickness to prevent weak flocculation, at the same time it has to be strongly attached to the surface of the particle [19]. The presence of the stabiliser also affects the aggregation that occurs when the colloidal stability of the particles is not optimal, producing several different types of flocculation mechanisms. A weak (reversible) flocculation depends on the ratio of polymer thickness to the particle. If a minimum is reached the system forms a gel which can be redispersed with shaking. A depletion flocculation occurs in the presence of a free-floating polymer and when a polymer is adsorbed to more than one particle at the same time the system experiences bridging flocculation. While a special case for polyelectrolytes is possible when an insufficient amount of polymer is adsorbed to the particles. The partially covered particle is attracted to the oppositely charged surface of the partially uncovered area of another particle, creating electrostatic patch flocculation. The addition of nonsolvent or change in temperature can also lead to irreversible flocculation [19].

1.3.2. Antimicrobial effect of silver nanoparticles

The antimicrobial properties of metallic silver were recognised by the ancient Greeks [34], and it has been used for this and other purposes for millennia. However, once antibiotics

were developed, the use of silver as an antiseptic decreased. Some applications for silver salts remained in place for special purposes such as the treatment of burn wounds [35]. The wide range of applications that silver nanoparticles can be utilised for contributes towards this steady increase in publications. For the antimicrobial action, the high surface-to-volume ratio displayed by AgNPs is considered a major benefit, even though the exact mode of pathogens killing is not well understood. There are two competing theories; first holds that AgNPs accumulate and aggregate at the bacterial membrane, affecting the membrane's rigidity, stability, and integrity [36]. The second theory assumes that the antimicrobial properties of AgNPs stem from silver ions released from the surface of nanoparticles in the process of dissolution [37]. It is generally accepted that silver ions disrupt bacteria cell walls by interacting with sulphur- and phosphorous-containing groups of proteins [38] to create holes in the cell wall, causing an ionic imbalance in the cell [39, 40], which may eventually lead to cell death. In addition, if Ag^+ enters the cytoplasm, it can cause damage to the DNA and RNA [41], denaturation of the 30S ribosomal subunit, and formation of reactive oxygen species [38]. There are differences observed in the efficacy of the Ag^+ against Gram-negative and Gram-positive bacteria but due to specific multiple mechanisms of antibacterial response, the antimicrobial efficacy remains high for both. However, the mode of action of the silver nanoparticles also poses a challenge of cytotoxicity towards human cells, triggering an inflammatory response [42]. With an ability to cross the blood-brain, testis-blood, and placental barrier [43] any clinical application requires consideration of cytotoxic harmful effects to the benefits offered.

The antimicrobial properties of silver nanoparticles can be exploited to combat rising antimicrobial resistance. There is much uncertainty surrounding AgNPs: the mode of pathogen killing, the kinetics of the reaction and the formation of AgNPs have not been conclusively established. Yet the resulting physical properties, stability and aggregation impact on the

antimicrobial effect offer opportunities to exert control. This can be achieved by changing the reaction process and by introducing additional stabilisers.

1.3.3. PHMB

Physical and chemical properties

Poly(hexamethylene biguanide) hydrochloride, PHMB, is a salt of a polycationic polymer commonly used as a biocide in various applications. Other names found are polyhexanide and the INCI name of polyaminopropyl biguanide. PHMB has biguanide groups separated with a flexible hexamethylene spacer and can be synthesised by various pathways [44, 45]. Commonly, research investigating PHMB or its properties uses stock material supplied by a manufacturer, most often that of Arch Chemicals, currently Lonza, under the brands Cosmocil® and Vantocil® marketed for various industries. Due to intellectual property protection, it is not possible to determine the synthesis path of those products. The most efficient synthetic pathway described in the literature [46], achieving over 99% yield is a melt polymerisation of 1,6-hexamethylenebis(dicyanamide) with hexamethylenediamine (Figure 1-4) in 1:1 stoichiometric proportion and heated to 165 C rising to 180 C. The reaction remains in the polymerisation/depolymerisation equilibrium, and the end groups of the chain can also take one of three possibilities [46, 47]. The formed PHMB has a mer with a mass of 219.72 g/mol, with weight-average molecular weight at around 2400 g/mol [46] and an average degree of polymerisation at 12, with the number of repeating units between 2 and 40. The structure of PHMB is that of alternating hexamethylene and biguanide segments, which are hydrophobic and hydrophilic respectively. This suggests that self-assembly may be expected in aquatic environments: the simplest form possible in such events is small micelles formed by chain segments (Figure 1-3), but other compact and ordered structures were also reported [48]. The critical micelle concentration (CMC) has been established as between 2 and 5 x 10^{-2} mol/dm^3 in water at 273 K or 293 K (this is uncertain, as both temperatures are given) [49]. However, those physical properties of PHMB vary from publication to publication, resulting from

different synthesis routes, a mixture of oligomers and different end groups, all of which create additional challenges in determining the PHMB parameters. Similarly, very few details are available for the chemical and physical properties of commercially available PHMB in data sheets [50] or European Commission consumer safety reports [51].

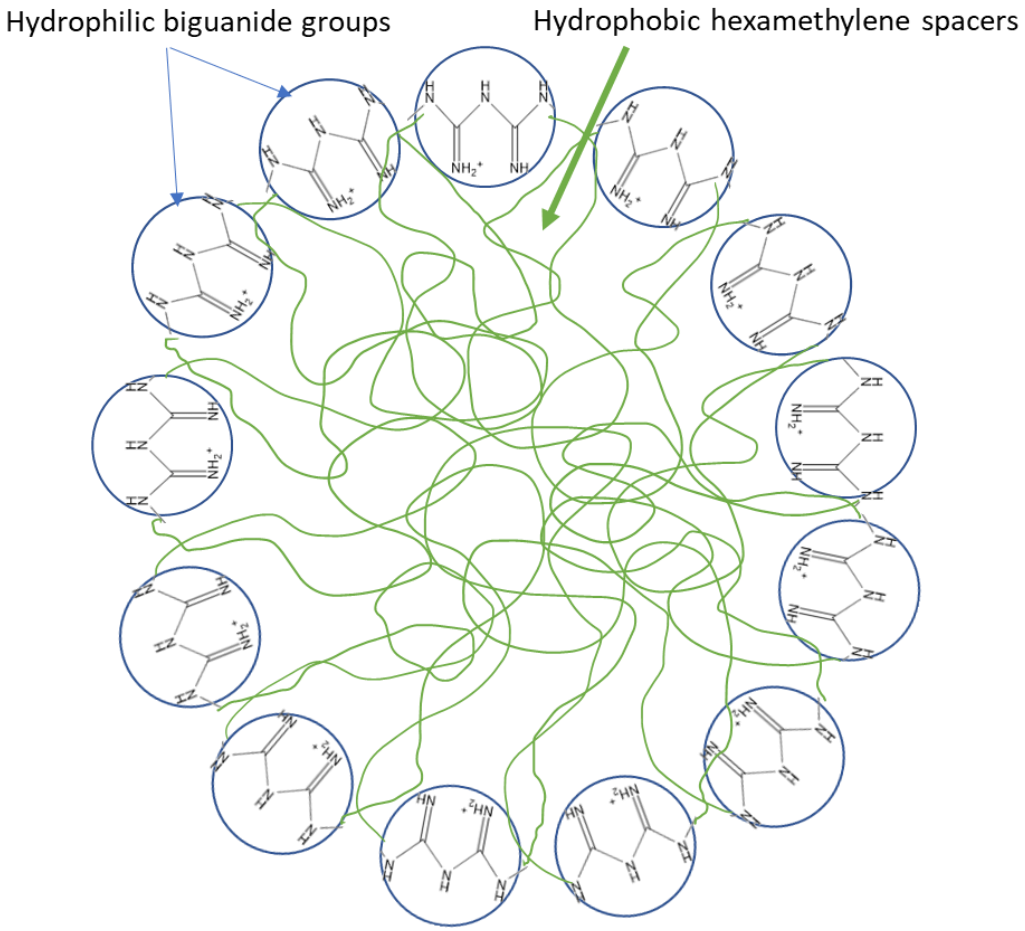

Figure 1-3 PHMB self-assembled micelle in an aqueous environment.

Characterisation techniques used for PHMB analysis vary subject to the application. Typically, UV-Vis can be used as a spectroscopic method for PHMB analysis, as it has a strong absorption at 192.4 nm and 236 nm due to the $\pi - \pi^*$ transition in -C=N [52]. FTIR, NMR [46, 47, 49] and DLS [49] are also employed as characterisation techniques for PHMB solutions. However, as PHMB is used as an additive in various applications, additional techniques such as titrimetric methods [53], capillary electrophoresis with contactless conductivity [54], colourimetric assay [55], and reversed-phase HPLC [56] are used to define

the presence or concentration of the polymer in the final products when a high degree of sensitivity is required. The ability of a compound to donate proton is described by the acidity constant, K_a value, which is calculated from the concentrations of hydrogens ions [H^+], concentration of the conjugate base of the acid [A^-], and [HA] is the concentration of the acid using the equation 1.2

$$K_a = \frac{[H^+][A^-]}{[HA]} \qquad \textit{Eq. 1-2}$$

For convenience the K_a is reported as a common logarithm. The pK_a value of a molecule indicates the pH at which half of the molecules are in the acid form and half are in the conjugate base form. Although, typically K_a values are reported, the corresponding K_b – the basicity constant indicates the ability of a molecule to accept the proton ($pK_a + pK_b = 14$) [57]. The biguanide group with five conjugated amines has two pK_a, one at around 13.5 and second one at around 3 [58], Additionally, computational analysis showed that at pH 7, PHMB is most likely to be in +1 ionised form, with the charge being delocalised over the whole of the biguanide segment. In the presence of a counterion, the form taken was of a globular spherical shape with a radius of gyration (Rg) of 22 Å [58]. It is also likely that PHMB hydrogen bonds with itself in the biguanide group and potentially between other oligomers to form networks [58].

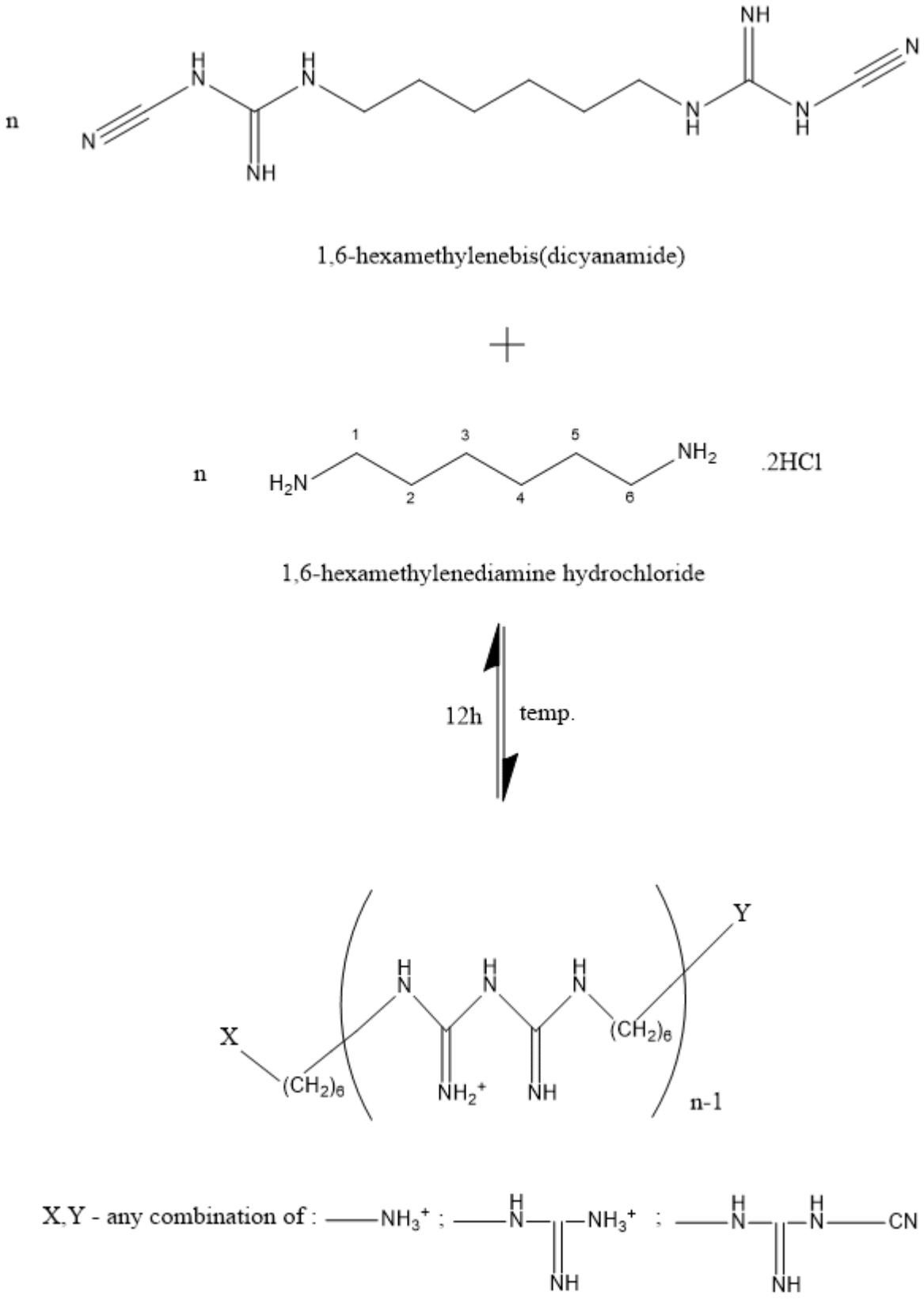

Figure 1-4 Synthesis path for melt polymerisation of PHMB following the methods described by East *et al.*[46].

Applications and antimicrobial properties

PHMB is used in a variety of applications as a disinfectant or preservative, due to its antimicrobial properties. It has been used for a number of years, initially as a swimming pool sanitiser (under the tradename Baqacil®) and hospital disinfectant, and later in wound care, burn treatment and other local anti-infective treatment [59-64]. More recently, it entered customer-applied products such as contact lens disinfectant [61], fibre preservative [65] and oral mouthwash [66]. PHMB has been also used for the treatment of *Acanthamoeba keratitis* infections [67]. Yet regardless of the wide application spectrum, no bacteria are known to have developed resistance to PHMB [68]. The overall consensus on the antimicrobial mode of action is that PHMB disrupts the functioning of the bacterial membrane by displacing Mg^{2+} and Ca^{2+} ions [69], causing increasing permeability and leading to bacterial death [70]. However, it has also been shown that PHMB enters the cell and selectively condenses bacterial chromosomes [71]. At the same time, PHMB has low toxicity towards mammalian cells [47, 72]. PHMB is effective against a variety of pathogens, gram-positive and gram-negative bacteria [73, 74], viruses [75, 76], and fungi [77]. The structure of PHMB, with five conjugated amines, similar to other biguanides, makes it a good candidate for other purposes, such as a metal chelator [78] or for supramolecular chemistry [79, 80].

Poly(hexamethylene biguanide) is a polycationic polymer found in various applications for a number of decades, though uncertainty remains over some aspects of its physical and chemical properties, and the antimicrobial mode of action has not been fully explained. But PHMB has proven effective against a broad spectrum of pathogens without any reported rise in bacterial resistance, coupled with low toxicity towards mammalian cells. This makes it an ideal candidate to further explore the possibility of forming complexes with other antimicrobial agents to increase effectiveness against microorganisms.

1.3.4. PHMB stabilised silver nanoparticles

The PHMB as a cationic polymer used for stabilisation of the silver nanoparticles has been explored before [81-84]. The synthetic pathway chosen uses the wet chemical reduction of silver nitrate using sodium borohydride with PHMB added as a capping agent. Some differences can be noted between the reaction processes taken between them. In one approach the reducing agent is added dropwise to the mixture of silver nitrate and PHMB as opposed to the other which adds it quickly. This can have an impact on the nucleation and growth of the nanoparticles as the concentration of atomic silver is suppressed. A significant difference is also noted in terms of applications, Gusev *et al*. [83] and Krutyakov *et al*.[84], explore the complex as a plant protection product. Unfortunately, the experimental section of both papers is limited in detail, therefore, the reproduction of the methods is challenging. The work of Yi *et al.* and Ashraf *et al*. [82] is focused on the antimicrobial activity of the complex formed. This work directly builds on the synthetic method developed by Ashraf *et al*. [82]

Silver nanoparticles were synthesised in the presence of the PHMB with the use of sodium borohydride as a reducing agent. The necessity for this complex is justified by the need for a 'hybrid' product with enhanced antimicrobial properties [82]. The approach is translated from work combining silver nanoparticles with other non-bacterial active agents to improve the biocidal response from AgNPs. The assumption formed early in the work is that the PHMB-AgNPs complex is a stronger antimicrobial agent than the individual components. The authors aim to achieve smaller particles due to the improved antimicrobial response expected for smaller size particles, which is a fact well supported in the research literature. Although a range of concentrations of PHMB is used during the synthesis process, only UV-Vis plots for 3 concentrations are presented with a claim that the narrower SPR peak presented a more uniform size, however, this is not reinforced with any supporting characterisation techniques or literature. The PHMB at higher concentration present in synthesis formed a milky suspension, the exact concentration, however, is not specified. The sizing using DLS appears to be out of

the ordinary, the more detailed results are not provided. FT-IR and zeta potential measurements are effectively used to prove the interaction between the PHMB and AgNPs. There is some uncertainty concerning the concentration used in antimicrobial studies. The true concentration of the PHMB-AgNPs in the final product has not been determined, neither the final concentration of the PHMB following centrifugation. Therefore, comparing the aliquots used to the PHMB alone or the AgNPs concentrations found in literature is not alike. However, relative values for the antimicrobial activity clearly show an increasing trend in bacterial growth inhibition with increasing polymer concentration in the PHMB-AgNPs complex.

The study [82] clearly showed the formation of the PHMB-AgNPs complex with a possible application as an antimicrobial agent. This opened new avenues to explore, further investigation of the complexation process between the polymer and silver nanoparticles, and the more detailed antimicrobial studies to prove the efficacy of the complex. Yi *et al.* [81] carried out a detailed study to investigate the impact of the PHMB-AgNPs synthesised using the method described by Ashraf *et al*. [82] on the *s. aureus*. The complex caused bacterial membrane damage resulting in leakage of the intracellular content. However, the method uses the PHMB in concentrations of mg/mL rather than µg/mL as it was described initially indicating 1000 fold increase in polymer concentration.

1.4. Characterisation

1.4.1. Ultraviolet-visible light spectroscopy (UV-Vis)

Ultraviolet-visible light spectroscopy (UV-Vis) is a technique that measures the difference between orbitals when electrons are excited from the ground state and transition from the highest occupied to the lowest unoccupied molecular orbitals, the HOMO-LUMO gap. This occurs as a result of the energy being absorbed from the ultraviolet or visible light directed at the sample, and the wavelength of the absorptions indicates the energy difference between the orbitals concerned [85]. The intensity of the absorption has been shown to be

independent of the intensity of the light but proportionate to the concentration of the absorbing molecules [86]. This relationship can be expressed with Beer-Lambert's equation:

$$log_{10}\frac{I_0}{I} = \varepsilon.l.c \qquad \textit{Eq. 1-3}$$

Where I = intensity of transmitted light, I_0 = intensity of incident light, ε = molar extinction coefficient, c = concentration, l = path length of the absorbing solution (mm). The spectrometer measures the difference in the intensity of transmitted beams between the reference sample – pure solvent – and the (usually highly diluted) sample of the compound under investigation.

Poly(hexamethylene biguanide) (PHMB) can be characterised using UV-Vis, as it has strong absorptions at 192.4 nm and 236 nm [49]. However, the vacuum ultraviolet range for absorptions between 120 and 200 nm that result from σ-bonds is challenging to measure because of the necessity to remove the air from the instrument [85]. Absorption at 236 nm resulting from $\pi - \pi^*$ transition in the -C=N [52] conjugated system is readily available and gives rise to strong peaks.

Nanoparticles have been studied extensively using UV-Vis due to the Surface Plasmon Resonance (SPR) phenomenon, which is based on the fact that free electrons in the metal can be considered as plasma (high-density liquid), and that as such they oscillate. These oscillations are represented by plasmons, occurring in bulk media or in localised areas such as the surface. In the latter case, the electrons behave in a modified way due to the boundary between a metallic and a dielectric surface, and interact strongly with light [87]. The absorption and scattering of the incident light, often expressed as efficiencies (or efficiency factors), are dependent on the cross-section of a particle [88]. Therefore, the size distribution of the particles enables prediction of the extinction spectrum, and in reverse, particle distribution can be modelled using the obtained extinction spectrum. There has been some work to apply this

theory to characterising metal nanoparticles, in particular research carried out by L.B. Scaffardi and related researchers [89-94]. However, it is important to stress that the modelling assumes that polymer and silver nanoparticles are in a core-shell arrangement.

For coated silver nanoparticles, a model can be developed for the radius of the core and the radius of the core with the coating. By making these calculations, it is possible to draw the extinction spectra for various size nanoparticles, but importantly, also to determine the core size and shell thickness.

Overall the UV-Vis peak depends on [94]:

- Metallic core radius
- Thickness of dielectric coating
- Refractive index of surrounding media
- Refractive index of the coating

Schinca *et al*. [94] make a case that the wavelength (λ_{max}) value for the extinction shifts towards lower wavelengths with a decrease in the size of nanoparticles, but not for those smaller than 10 nm. Beyond 10 nm, the intensity of the peak reduces with size reduction. Additionally, UV-Vis spectroscopy, both theoretical and experimental, provides information on full width at half maximum 'FWHM'. It can be used to determine the size of nanoparticles, as it depends mainly on the core size rather than coating thickness, whereas plasmon resonance wavelength depends mostly on shell thickness and not the core [90, 94].

UV-Vis is a spectroscopic technique capable of fast and efficient characterisation of various compounds; samples are in liquid form and require minimal preparation before analysis. Both PHMB and AgNPs are suitable for characterisation using UV-Vis due to strong absorptions resulting from the biguanide conjugated system and SPR respectively. Additional quantitative analysis can be performed to further understand how the PHMB-AgNPs complex

interacts, and the impact that polymer coating of silver nanoparticles has on the extinction spectra. Using further modelling, the physical parameters of the particles, such as coating thickness, core diameter or size distribution, can be estimated. However, complicated theoretical calculations must be carried out first to ensure all physical parameters are defined to minimise the possibility of error. More importantly, the interaction between silver nanoparticles and polymer has to be well defined; it is not possible to achieve this using UV-Vis alone, and other complementary techniques such as Dynamic Light Scattering (DLS) and Electron Microscopy should be used. This is because the results obtained from UV-Vis are not unambiguous and might be misinterpreted without additional information [95]. Once those conditions are met, UV-Vis might offer an efficient way to fine-tune silver nanoparticles to create materials having the desired properties without extensive and time-consuming characterisation.

1.4.2. Small-Angle X-ray Scattering

X-rays are high-frequency electromagnetic waves that have been widely employed to investigate material properties due to their characteristic scattering interactions. This gave rise to materials characterisation techniques such as Small-Angle X-ray Scattering (SAXS), Ultra Small-Angle X-ray Scattering (USAXS) and Wide-Angle X-ray Scattering (WAXS). SAXS measures the angular deviation of incident X-rays generating a characteristic scattering pattern, which carries information about the shape and size of particles, typically between 1 and 100 nm [96]. The scattering patterns are produced as a function of the magnitude of the scattering vector, q, and is defined by the equation:

$$I(q) \sim V^2(\Delta\rho)^2 \int_0^\infty [F(qr)]^2 n(r) S(qr) dr \qquad \textit{Eq. 1-4}$$

Where I = intensity of scattering, V = total volume of illuminated particles, $(\Delta\rho)$ = electron density contrast and the integral performed over all radii. The integrated term is a function of the form factor, $F(qr)$, the size distribution of the illuminated particles, $n(r)$ and

the structure factor, $S(qr)$. Each of these terms contains important information about the particles: $F(qr)$ represents their shape and is reflected in the shape of the radially integrated scattering patterns; $n(r)$ can be represented as Gaussian, log normal or Schulz; and $S(qr)$ describes particle-particle interactions in concentrated samples (typically > 1.0% w/w). The form factor and size distribution can be extracted from the intensity vs. q plot, but to do so, various assumptions are required due to the interrelation between the two parameters. Information from other complementary techniques provides important guidance in making those assumptions such as an indication of size and shape necessary to predetermine the form factor. Different structure factor models have been developed to account for particle-particle interactions, and the 'hard spheres' that define distances between particles' centres are frequently used [97].

From an operational perspective for x-ray scattering experiments, the x-ray beam is collimated using a series of slits and thus becomes monochromatic. In SAXS, the beam is then transmitted through the sample with the detector positioned behind it. The beam stop is placed in the direct line of the high flux x-ray beam to increase sensitivity to the scattered X-rays and to avoid damaging the detector. (Figure 1-5).

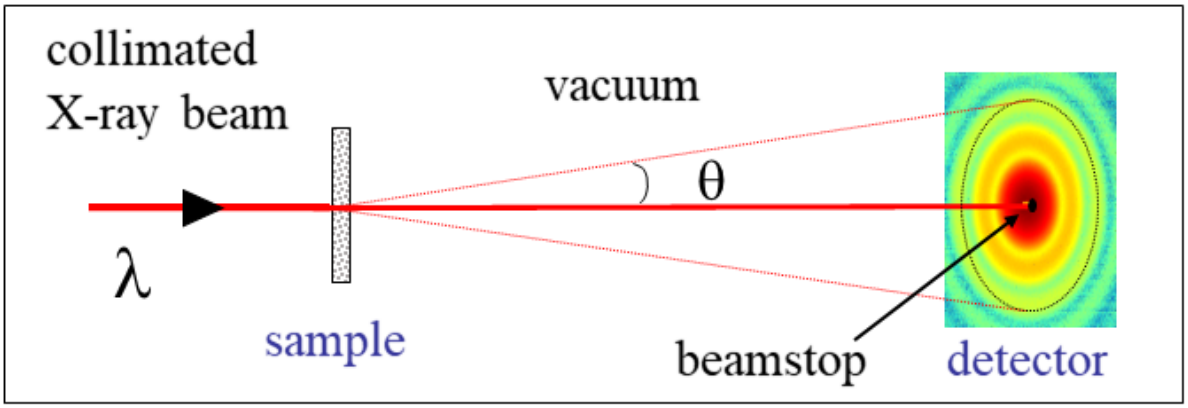

Figure 1-5 Schematic overview of a Small-Angle X-ray Scattering setup for measurements. (Reproduced under Creative Commons Attribution (CC BY) license from [98])

The beam is in a vacuum to avoid scattering by air. The scattering vector (q) and its magnitude are defined by:

$$q = \frac{4\pi}{\lambda} \sin\left(\frac{\theta}{2}\right) \qquad \textit{Eq. 1-5}$$

Where λ = X-ray wavelength and θ = scattering angle [98].

As the scattering angle is measured by the detector, the scattering vector (q) is calculated with Eq. 1-5. As a result, the form factor, the structure factor and the size distribution can be modelled to fit the pattern. The use of dedicated software with the ability to integrate multiple levels of analysis simultaneously allows for more accurate and comprehensive estimates - the unified level model fitting [99].

SAXS is widely seen as a powerful method to characterise nanoparticles [100]. The high-influx beam obtained from a synchrotron source is often employed for *in situ* experiments, for example, to investigate the nucleation and growth of nanoparticles [101]. Results obtained from SAXS are typically combined with other methodologies to provide detailed properties of nanoparticles [102] and to better understand interactions between different elements of the systems such as alloys or stabilisers [103].

1.4.3. Dynamic Light Scattering and Zeta Potential

Dynamic Light Scattering

Dynamic Light Scattering (DLS) and Zeta Potential (ZP) emerged as colloidal techniques used to measure diffusion coefficients [104, 105] and originate from physical colloidal chemistry. The way a particle scatters light can be determined by the dimensionless size parameter α, defined by:

$$\alpha = \frac{\pi D_p}{\lambda} \qquad \textit{Eq. 1-6}$$

Where πD_p = circumference of the particle with D_p being a diameter of a particle and λ = the wavelength of the incident radiation. As a result, the dimensionless size parameter α depends on the type of scattering resulting from different particle sizes (Figure 1-6). Increasing the particle size has a major impact on how the light is scattered [106].

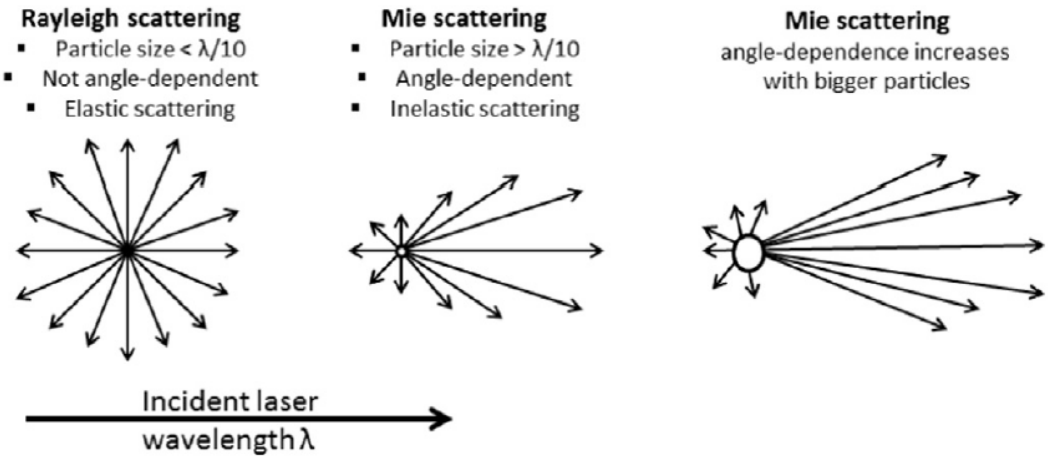

Figure 1-6 Difference in the light scattering of particles with different size parameter α (Reprinted with permission from Elsevier from [31], p. 339)

Particles in suspension are in continuous interaction with the surrounding liquid and are in random motion. This Brownian motion can be defined using the Stokes-Einstein theory, which describes particle motion. It can be rearranged to obtain the hydrodynamic diameter from the diffusion coefficients using the equation (*Eq. 1-7*) [107-109]:

$$d_H = \frac{kT}{3\pi\eta D} \qquad \textit{Eq. 1-7}$$

Where d_H = hydrodynamic diameter, k = Boltzmann's constant, T = absolute temperature, η = viscosity, and D = diffusion coefficient

When the light of a given wavelength is directed at the particles in continuous motion in dispersion, the scattered light fluctuates over time. The fluctuation is recorded by a detector

mounted in the DLS equipment, and a correlogram is generated from the raw correlation function plotted against time delay, which itself is based on the autocorrelation and field correlation functions. For small particles when Rayleigh scattering applies, the autocorrelation function is calculated by data fitting using the exponential expression [31]:

$$G(\tau) = 1 + b.e^{-2Dq^2\tau} \qquad \textit{Eq. 1-8}$$

Where b = constant depending on the optics and geometry of the instruments, D = translations diffusion coefficient, τ = time delay and the scattering vector (q) is given by:

$$|q| = \frac{4\pi n_o}{\lambda_o \, sin\frac{\theta}{2}} \qquad \textit{Eq. 1-9}$$

Where n_o = refractive index of the medium, λ_o= wavelength in a vacuum and θ = scattering angle. It is important to note that the above can only be used for samples with a monomodal distribution of particles (single population) [110]. For samples with multimodal particles (more than one population), a more complex analysis must be carried out, which uses a multi-exponential model to produce the distribution. The algorithm applies a regulariser to estimate the noise within the correlogram [111]; however, the value depends on the sample and the method is, therefore, less precise than that for monomodal distributions.

As a result, the diffusion coefficient necessary for the Stoke-Einstein equation (*Eq. 1-7*) is obtained. It is then possible to calculate the hydrodynamic diameter, the hypothetical hard sphere which diffuses at the same rate as the particle characterised using DLS. This is an important assumption to consider: hypothetical hard spheres seldom exist, in particular when considering charged nanoparticles. It is more likely that particles will be solvated/hydrated with a corona of counterions formed around them [112]. This is known as the electric double layer (EDL) and is discussed in more detail in the Zeta Potential section below. Because the EDL is taken into account for sizing, factors that affect it impact the results obtained, in particular the

ionic strength. In addition, as the size is a result of the autocorrelation of decay vs. time, a surface structure that slows the particle down will produce an increased diameter. Finally, the shape of the particles can affect the results if the vertical vs. horizontal movement is distorted.

The technique has been significantly improved over time. Modern DLS machines such as the Malvern Nano series use non-invasive back scattering (NIBS). This improves area illumination and reception of signal from smaller molecules. A major benefit of DLS is minimal sample preparation required for characterisation; however, the concentration of the sample has to be selected appropriately to ensure that the possibility of multi-scattering is reduced. When this occurs, the recorded result may be smaller than the actual size. In addition, high concentrations can increase the possibility of agglomeration [113]. On the other hand, the concentration of the sample must be sufficiently high to provide enough signal-to-noise ratio for the detector to record. These drawbacks can be mitigated with the use of equipment that auto-optimises the attenuator and measurement positions to achieve best results.

Reporting results from DLS can take the form of intensity, volume or number: these can provide different results for size and distribution. However, the principal DLS measuring technique reports intensity, with the number and volume being generated by applying mathematical calculations to the primary intensity results to present volume or number distributions. These calculations are extremely prone to error, as any discrepancy in the intensity size distribution is exacerbated by significantly for the volume and even more so for the number [31].

A major disadvantage of DLS is that larger particles have greater scattering potential, so cumulative analysis, which requires very little input from the investigator, is not suitable for polydisperse samples. A more complex distribution analysis must be conducted, but even then, scattering by larger particles can overpower the signal and the presence of smaller particles. Investigation into the detection limits of DLS and AgNPs showed that the presence of a few

percent of larger particles may completely conceal presence of smaller ones [95]. Due to the challenges already discussed in obtaining volume and number distributions, these should only be used for reporting the relative amounts of each peak in the distribution.

Zeta Potential

Zeta potential, otherwise known as electrokinetic potential, represents the difference in potential between the electric double layer (EDL) and the electrolyte around it at the slipping/shear plane. The colloidal particles are electrophoretically mobile, i.e. they move when an electric field is applied [114]. This physical property reflects the colloidal stability of the nanoparticles and is underpinned by the DLVO theory discussed in Chapter 5 below.

Charged nanoparticles dispersed in a solvent develop an EDL on the surface. The first, known as the Stern layer, consists of ions or molecules with the opposite charge to the surface of the particle. The second, diffuse layer is formed by counterions due to electrostatic effects [115] and theoretically stretches to infinity, but can experimentally be established to only a few nanometres from the Stern layer. Within this distance, molecules and ions of both charges are present, and the diffuse layer is highly dynamic. However, this is dependent on local conditions such as pH, ionic strength and concentration (Figure 1-7).

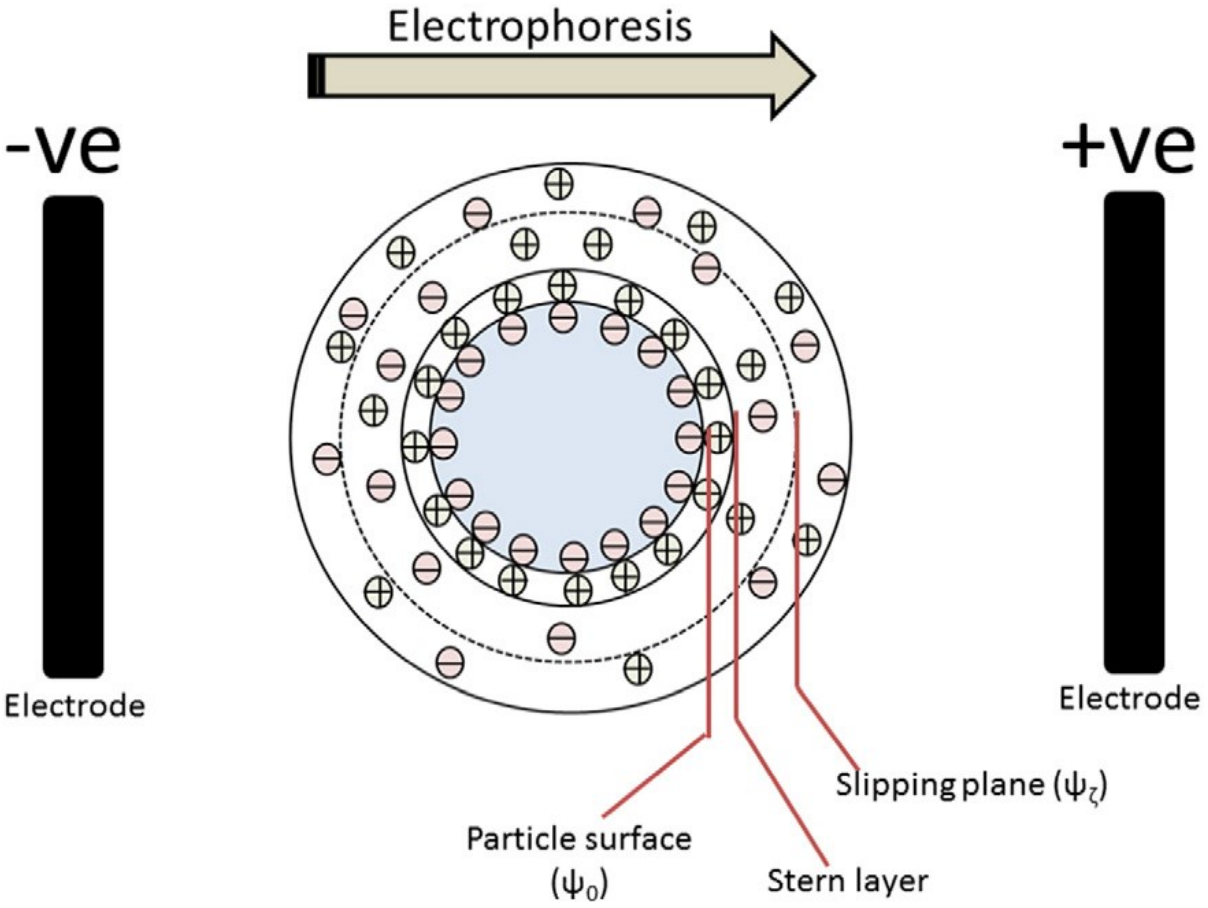

Figure 1-7 Graphic representation of a negatively charged particle with the Stern layer found immediately on the particle surface, and beyond, the diffuse layer of positive and negative charges. Together the layers form the electric double layer (EDL). If an electrical field is applied the particle will move toward the electrode (direction of travel subject to charge), forming an interface between the diffuse layer and dispersant, known as the slipping plane. The zeta potential is the electrokinetic potential measured at this interface. (Reprinted with permission from Elsevier from [31], page 346)

If an electric field is applied to such a system, charged particles will flow toward the electrode with the opposite charge, which is widely known as electrophoresis. Electrophoretic mobility (μ_e) can be calculated using equation [116]:

$$\mu_e = \frac{V}{E} \qquad \textit{Eq. 1-10}$$

Where V = particle velocity (μm/s), E = electric field strength (volt/cm).

When applying a laser to the particles in electrophoretic movement, the scattered light has a different frequency from the original laser beam, with the recordable shift proportional to the speed of the particles. This phenomenon, known as the Doppler effect, allows the

instrument to calculate the particle velocity [31]. As a result of movement, a hypothetical shear/slipping plane forms between the diffuse layer and the dispersant around it. It is at this plane where the zeta potential is measured. However, the potential cannot be measured directly, but is calculated based on the electrophoretic mobility of the particle in a known electric field using Henry's equation [117]:

$$\mu_e = \frac{2\varepsilon_r \varepsilon_0 \xi f(Ka)}{3\eta} \qquad \textit{Eq. 1-11}$$

Where ε_r = relative permittivity/ dielectric constant, ε_0 = permittivity of vacuum, ξ = zeta potential, $f(Ka)$ = Henry's function and η = viscosity

The parameters required for the calculations will depend on the size of the nanoparticle, in particular, how the EDL compares to the whole of the particle. For large particles, where the EDL is much smaller in comparison, $f(Ka)$ is taken as 1.5 and Henry's equation (Eq. 1-11) is modified to the Helmholtz-Smoluchowski equation [118]:

$$\mu_e = \frac{\varepsilon_r \varepsilon_0 \xi}{\eta} \qquad \textit{Eq. 1-12}$$

For small particles, where the EDL is much greater, $f(Ka)$ is taken as 1 and Henry's equation (Eq. 1-11) is modified to the Hückel equation [118]:

$$\mu_e = \frac{2\varepsilon_r \varepsilon_0 \xi}{3\eta} \qquad \textit{Eq. 1-13}$$

However, it has been shown that nanoparticles synthesised using wet chemical pathways are more likely to be in the intermediate region between those two formulas [118].

Zeta potential is an important indication of the colloidal stability of the nanoparticles and provides an insight into factors that affect this property, which is relevant to controlling aggregation. The particle itself can be influenced to modify the charge as well as the EDL

formed around it, creating a local environment that differs from the bulk of the dispersant. Both the surface and the local environment have a significant impact on the interactions with other particles.

The surface of the nanoparticles is sensitive to changes in the pH if the colloidal stability is provided by ions or electrostatic stabilisers. The charge of Bare-AgNPs is reported in the literature as negative [119], and although the actual pH for the measurement is not given, it is stated that it was measured in ultrapure water. When the pH of the dispersant is adjusted, the zeta potential changes, as the screening of the nanoparticles may become either more or less effective. The minimum of the screening effectiveness is reached at the isoelectric point (pI) when $pH = pI$ [120]. At this point the colloidal stability of the nanoparticles is also at a minimum. If the pH is further adjusted the charge of the recorded zeta potential changes sign. Sadowki *et al*. [121] found that for biologically synthesised AgNPs, the highest stability is recorded for pH over 8, with a gradual decrease of zeta potential with decreasing pH; however, the isoelectric point has not been reached. The behaviour of the nanoparticles in the presence of the ions is therefore a state of equilibrium of protonation/deprotonation at/of the surface of the particle. When a stabiliser is introduced, this equilibrium is disrupted, and another factor is added to the equation. This means a new equilibrium is required between the ions and both the surface and ligand. In certain cases when the nanoparticle is stabilised by, for example, steric ligands, the measured charge no longer responds to the changes in pH, i.e. is pH independent.

Ionic strength is another important factor affecting the electrophoretic mobility of the nanoparticles. If the diffuse layer screens the charge well, mobility is reduced as the attraction towards electrodes in the electric field is lowered. It also means that the van der Waal's attraction becomes dominant and the nanoparticles are much more likely to aggregate. Not all ions have the same effect on the zeta potential; it has been reported that chaotropic anions (i.e. SO_4^-) have a stabilising effect while kosmotropic (i.e. SCN^-) anions do not [122]. The NO_3^-

anions relevant to this study have also been reported to provide additional stability to AgNPs [123].

Measuring zeta potential is a simple and efficient technique used to gain an understanding of the expected colloidal stability of the nanoparticles, with pH and ionic strength as means of controlling nanoparticle behaviour and promoting (in)stability, subject to requirements. However, it is important to note that both factors are dependent on each other and on the local environment formed around the nanoparticles, therefore, theoretical or experimental fine-tuning of the nanoparticle behaviour is limited due to the number of factors involved.

1.4.4. Environmental Scanning Electron Microscope and Energy Dispersive X-ray Spectroscopy

Environmental Scanning Electron Microscope (ESEM)

Electron microscopy (EM) uses electrons instead of light to obtain an image of the sample under observation. This allows for high magnification as a result of the very short wavelength that the electrons exhibit, permitting imaging samples in the order of 0.1 nm. There are two main types of EM, transmission electron microscopy (TEM) and scanning electron microscopy (SEM). TEM, which is more akin to transmitted light microscopy, acquires images as a result of electrons passing through the sample, with illumination taking place before the sample and magnification after the sample with detectors. SEM, rather than illuminating the whole sample at once, uses a focused electron beam that scans the area of the specimen. The beam source is an electron gun controlled by the electromagnetic optics column. The beam scans across the sample, with electrons interacting with the sample in a number of ways. Backscattered Electrons (BSE) are electrons from the beam that were elastically scattered by the nucleus. BSEs have low-depth penetration and a strong correlation to the atomic number. Secondary Electrons (SE) are electrons knocked out by the beam electrons, creating an empty space in the shell; when detected, the SEs provide topographic information. In addition, as the

electron from the outer shell drops down to fill the empty vacancy, the energy difference associated with the change of shell is emitted as x-rays, this can be captured and forms a basis for Energy Dispersive Spectroscopy (see section below). The penetration depth depends on the Z number of the element and the accelerating voltage. This interaction volume varies but for 5kV acceleration on carbon, it can be estimated as 0.4 μm deep and 1 μm wide with a teardrop shape. Both SEM and TEM require a high vacuum in a chamber to be able to operate. To mitigate this, environmental scanning electron microscopy (ESEM) has been developed. The column in ESEM is divided into separate pressure zones with apertures allowing an electron gun to maintain a high vacuum while the chamber can operate at a few hundred Pascals. The additional important benefit is that the interaction of the electrons from the beam with the gas molecules present in the chamber produces positive ions. This prevents a build-up of charge on non-conductive samples, and as a result, it is not necessary to apply a conductive surface coating. However, ESEM cannot achieve the same levels of resolution as when imaging samples under a vacuum. This led to the application of this method primarily for aggregation investigation and the impact of sample drying and artefact formation [124].

Based on the principles of the two main types of electron microscopes, SEM and TEM, another method has been developed: Scanning Transmission Electron Microscopy (STEM). The beam scans across the sample, with the detector located directly underneath the sample. It is important to distinguish a difference between different STEM types: SuperSTEM uses purpose-built equipment operating at high keV, more akin to those in TEM, and STEM-in-SEM, or as Stokes [124] puts it, ‘poor man’s’ STEM, which uses standard SEM equipment but has additional detectors that can be placed under the sample. STEM-in-SEM can also be used in ESEM machines, allowing for samples to be imaged in water using STEM, giving rise to WetSTEM [125]. The STEM detector produces different images subject to the diffraction of electrons by the sample. The undiffracted electrons are collected by the bright-field (BF) zone, while the diffracted electrons are detected by various dark-field (DF) zones and the High Angle

Annular Dark Field (HAADF). Together, the different detection modes provide information on the elemental contrast and grain boundaries of the sample [126].

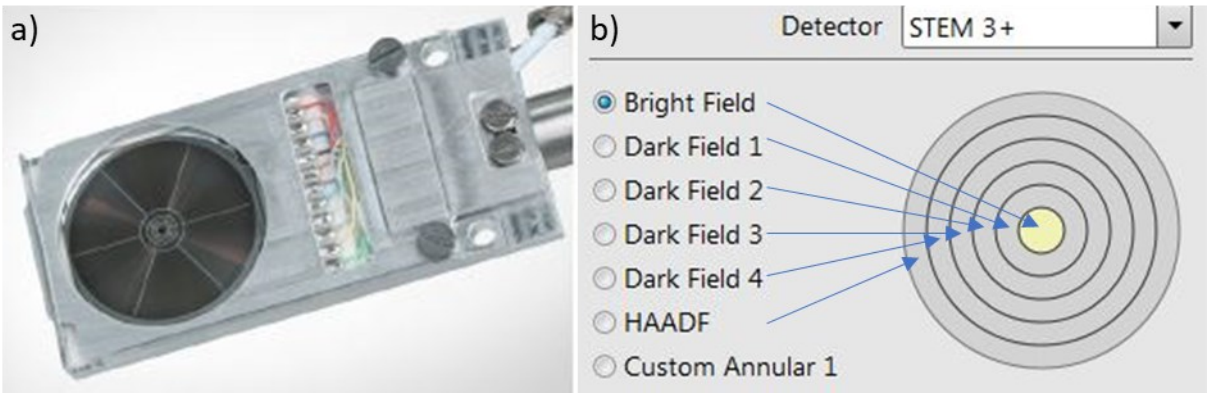

Figure 1-8 An example of a STEM 3+ detector on an image giving a choice and various angular and circular detection segments.

Modern SEM instruments, with their selection of available detectors and a choice of imaging modes, allow for acceptable contrast to be attained between NPs and the surrounding medium [127]. With its lower voltages, SEM does not suffer from lens aberrations and allows high-angle detections, increasing the signal level and improving contrast between materials [125].

Energy Dispersive X-ray Spectroscopy (EDX)

Energy Dispersive X-ray Scattering (EDX) is a technique that provides a chemical analysis of a material. It requires an electron source, and for that reason is commonly coupled with electron microscopes. The electrons from the beam interact with the material under observation; one such interaction is an inelastic scattering that occurs when an orbital electron in an element is dislodged by the beam. The resultant unfavourable electronic configuration prompts an electron from the higher energy shell to fill the vacancy. As this occurs, the energy is emitted as a characteristic x-ray [128]. It is defined by the energy level in which the vacancy occurs K, L, M, and the energy level from which the electron originates (α), (β), (γ) [129]. The interaction is dependent on the z number of the sample [130], and each transition has a defined energy potential, but they all occur if enough energy is supplied. As a result, each element will

have a particular signature of peaks, with defined intensity and positioning. However, it can also happen that the x-ray emitted hits another element, and if carrying sufficient energy, dislodges another electron, giving rise to secondary fluorescence upon relaxing [130].

X-rays produced during this process travel to the detector located at an angle to the sample within the chamber. The detector contains a collimator and an electron trap to protect the window from incoming electrons and X-rays emitted by the sample stage [130]. The x-ray hitting the silicon drift detector is converted to a current, amplified and processed. A limited number of X-rays are available for analysis, as some are discarded to protect the pulse height analyser. The ratio of processed to discarded pulses is defined by the dead time (%)[130].

The spectrum produced contains counts vs energy, the number of incident x-rays carrying a particular energy. Each K, L, M and (α), (β), (γ) transition for each element will have a specific location on the spectrum where they can be found. However, they often overlap, requiring careful peak decoupling and equipment setup to ensure the reliability of results for complex samples [130]. Modern advances in electron microscopy allow for sets of spectra to be collected from sample points. Once collated, they provide spectral imaging or mapping [128]. This method of data presentation does suffer from some artefact formation – the relationship between peaks remains constant even if the intensity of one element increases; the ratio between peaks remains the same regardless of whether the other elements' intensity has changed. The mapping relies on the peak and background intensity; the latter varies with the local atomic number of the sample, causing intensity variations even for elements that are not detected in the sample [128].

The data obtained from EDX can be analysed in both a quantitative and qualitative manner. The former establishes whether a particular element can be detected or not based on the K, L and M line peaks and their location. The latter offers calculations on the elemental concentration; however, it requires the sample to be thick enough for the beam not to excite

the substrate underneath. If this condition is not met, a relative concentration can be calculated by using an internal standard specimen as a benchmark [131].

The method can also produce false results under certain conditions related to various collection and analytical stages. The sample and the depth of penetration by the electron beam are crucial. The EDX requires the sample's geometry to be flat. If it is not, artefacts relating to secondary fluorescence are more likely to occur, and some X-rays will not reach the detector due to the angle [128, 132]. In addition, if the interaction volume is not homogeneous, unexpected results can be generated [130]. Artefacts can also form when x-rays hit the detector, such as a sum peak – two x-rays hitting the crystal in the detector at the same time, giving rise to an unexpected peak [132] – or escape peak – when energy equal to the silicon is lost as a result of hitting the silicon detector, giving rise to a peak different from that expected.

These artefacts and uncertainties require the user to ensure that each spectrum considered is quantified in the same way for the process of peak deconvolution and when removing background to measure peak intensities [132]. However, if applied systematically and responsibly, EDX provides information about the type of elements present and their concentration in the sample under the area of observation [128].

The application of EDX to the analysis of silver nanoparticles has been widely explored due to the availability of the method, frequently coupled with electron microscopes. The detail of information obtained depends on the acquisition of spectra and the analysis. In qualitative evaluation, it provides a reliable way to confirm successful synthesis [133] or embedding of AgNPs into other materials [134]. Spectral mapping can be used to distinguish the arrangement of elements in, for example, gold-silver alloys [135]. Quantitative analysis is more complex but can provide information that is difficult to obtain from other sources, such as the change in relative sample composition due to oxidation of the AgNPs over time [136].

EDX as a method for chemical analysis provides a unique insight into the elemental composition of the sample. The technique is widely established and available, though the spectra obtained can be challenging to decouple, due to the stringent requirements in relation to sample preparation and data acquisition. Qualitative analysis is less complex and can be used to obtain valuable information about the chemical composition, so this method is frequently applied to nanoparticle characterisation.

1.4.5. Antimicrobial assessment

Assessing the response of bacteria to an antimicrobial agent requires careful prior consideration. The foremost concern is the purpose of the work carried out. It frequently occurs in the literature that the preliminary investigation into the antimicrobial efficacy of agents is carried out to complement the physico-chemical study [137]. But if the investigators are not skilled biologists, the data produced, although indicative of the agent's efficacy, is not comparable between various publications. Antimicrobial testing is carried out using several different methods mainly relaying on two key concepts – diffusion and dilution – each with their advantages and limitations.

Methods based on diffusion assess the antimicrobial response by measuring the zone of inhibition (ZOI) around the active agent, which can be applied as a disk. The agent applied diffuses through the agar plate with bacteria cultures present, and the efficacy of growth inhibition is visible on the plate. The disk diffusion method, in particular, is well recognised, with a standardised approach developed and published by international organisations (i.e. Eucast) [138]. This permits additional quality control checks to verify the reproducibility of results and ensures comparability to various other known antimicrobial agents. Diffusion methods are often used due to their ease of application, speed, low costs, and the wide range of materials suitable for testing. However, substances (e.g. some hydrogels) not compatible with agar plates are not suitable for this method, due to the impact they might have on bacterial growth as a result of the material's properties rather than the agent itself [139]. With this

method, it is also not possible to fully assess the mechanism of antimicrobial effect (i.e. bacteriostatic vs bactericidal) because growth inhibition is not equivalent to death. A variation of this method uses wells punched into the agar plate into which the agent is placed, with the zone of inhibition measured around it [137].

The dilution method using broth (liquid media) involves using identical volumes (macro or micro volumes) of broth with known numbers of bacteria and added antimicrobial solution to assess the minimum inhibitory concentration (MIC) [137]. It allows investigation of the minimum amount of the agent required to prevent the appearance of visible growth of a microorganism. As with the agar-disk diffusion method, international standards for broth dilution for various antimicrobial agents and bacteria strains were developed to improve quality control and comparability [140]. Because it is possible to cultivate test bacteria in the broth, it is possible to determine the minimum bactericidal concentration (MBC) of the agent to inform on the mechanism of antimicrobial action [141]. Although broth dilution increases accuracy, it is less versatile than the diffusion methods, being more suitable for solutions but not necessarily for biomaterials. Broth dilution also entails increased technical difficulty and is more time-consuming to perform. A variation of this method called agar dilution uses an antimicrobial agent diluted in the agar and poured into plates, allowing multiple microbial strains to be tested simultaneously against a concentration of the agent [137].

A number of other methods have been developed, such as ATP bioluminescence assay or time-kill test – the latter was also standardised by the Clinical Laboratory Standards Institute [142]. An interesting opportunity is presented with the use of the flow cytometer, a high-through-output device capable of individually analysing thousands of bacteria at great speeds [137]. Various dyes (e.g. propidium iodine [PI]) are applied to the microorganism solution and fluoresce when exposed to particular biological markers, allowing for the detection of different microorganism subpopulations (dead, live, damaged) [143]. It, therefore, allows detailed

analysis of the mechanism of antimicrobial action at greater speeds but requires dedicated equipment.

The choice of antimicrobial testing method is subject to the requirements of the study being conducted and the availability of the materials and equipment. Methods with standard developed protocols should allow for direct comparison against a wide choice of other agents, but in exchange, require greater dedication to apply them methodically. Others, without the standard protocols, such as agar well diffusion or flow cytometer, can be used as a screening method to select areas that offer the greatest opportunity for future detailed investigation.

1.5. Conclusions

The challenge of antimicrobial resistance has prompted an increased interest in alternative biocidal agents. The well-known antimicrobial activity of silver has led to increased research focused on silver nanoparticles. The somewhat unpredictable behaviour of AgNPs can be controlled by introducing a stabiliser, with a potential additional synergistic antimicrobial effect resulting from complexing both agents. This research addresses some important aspects of the PHMB-AgNPs complex when considering antimicrobial applications. Firstly, the interaction between AgNPs and PHMB has not been explored to date. An understanding of how components interact is often required for a better understanding of the mode of bacteria killing and the expected environmental faith following the use of the agent. Secondly, the physiochemical properties of the formed PHMB-AgNPs, although already explored in previous research will benefit from the additional weight of evidence. In addition, new characterisation methods were added (SAXS, WetSTEM) to complement those already used (SEM, DLS, UV-Vis) which increases confidence in the results. Finally, the stability over time of silver nanoparticles has been explored by a number of researchers; however, not when complexed with PHMB. Understanding how the unique type of electrosteric stabilisation brought by this polymer affects the nanoparticles is important for any future applications or commercialisation. It can also further inform how stability is affected by the properties of the complex.

In the next Chapter (2), the methods and materials used during this study are presented. In Chapter 3, these methods are discussed in detail because the analysis can yield different results depending on the process used to conduct it. Data is only reliable if there is trust in the analysis conducted. Literature focused on colloidal stability often sidelines quality analysis of the data with only a brief overview of the process in the methods and materials section, or this is relegated to supporting material. This Chapter (3) aims to remove some of the mist surrounding data collection, quality control and analysis to produce results. Once the reliability of the data is established, overall results are presented and discussed for the observed characteristics of the PHMB-AgNPs complex in Chapter 4. To gain a better understanding of PHMB-AgNPs, in Chapter 5, the formation of the complex is investigated as the reaction progresses. Interaction between the silver nanoparticles and the stabilising polymer together with the resulting properties are then tested for stability over time, with details presented in Chapter 6. Finally, in Chapter 7, overall conclusions and the possible future outlook on applications for PHMB-AgNPs are discussed.

Chapter 2. Methodology and Materials

2.1. Synthesis

2.1.1. Standard reaction

Following the previously described synthesis methodology [82], at room temperature, an aqueous (fresh deionised water from a "Purite Select" purification system) solution of PHMB (Cosmocil® CQ 20%, Lonza – 20% aqueous solution) (15 ml, various concentrations, between 10 and 200 µg/ml) was added to an aqueous solution of silver nitrate (Sigma-Aldrich, >99%) (25 ml, 1 mM) and left for two hours under vigorous stirring in a polypropylene beaker using a magnetic plate. A freshly prepared aqueous solution of sodium borohydride (Merck-Millipore) (5 ml, 0.8 mg/ml) was then added to the reaction. The reaction was left stirring for five hours and then kept for 24 hours in a dark cupboard before placing the suspension in the centrifuge filters (Amicon Ultra 15 filters) and spinning for 10 minutes at 6000 rpm. The silver nanoparticles were then pipetted out to a sample vial and stored in the cupboard at room temperature. An overview of the reaction scheme is presented in Figure 2-1

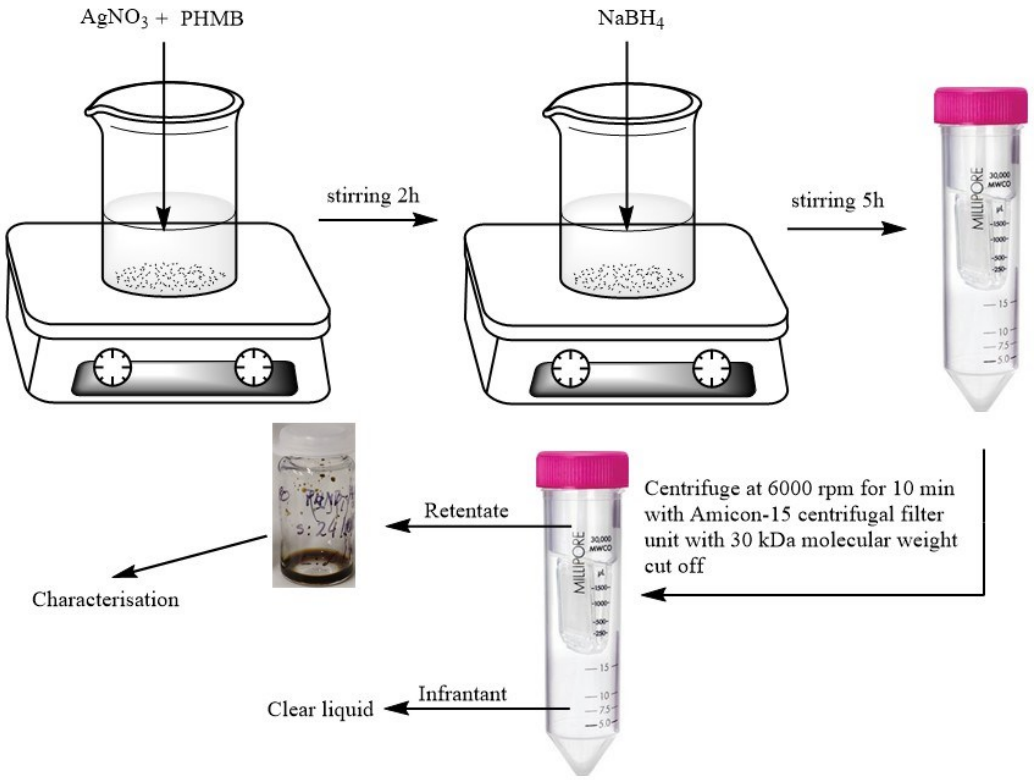

Figure 2-1 Schematic overview of the reaction process.

2.2. Characterisation

2.2.1. Ultraviolet-visible light spectroscopy (UV-Vis)

Samples were prepared by adding 2 µl (10 µl for Nov18 samples) of PHMB-AgNPs to 2 ml of deionised water and analysed using a SpectraMax M2 by Molecular Devices using SoftMax Pro 5 software and 10 mm quartz cuvettes.

2.2.2. Small-Angle X-ray Scattering (SAXS)

Small-Angle X-ray Scattering measurements were carried out on a Beamline B21 at Diamond Light Source, UK, which uses a bending magnet source to deliver ca. $3\,x\,10^{12}$ photons per second. The wavelength used for measurements was λ=0.9464 Å with a beam cross-section of 0.8 mm x 2 mm. Measurements were recorded at room temperature (ca. 20 °C). Samples, approximately 20 µl of undiluted aliquots (as obtained following description 2.1.1 Standard reaction above), were loaded into glass capillaries (mark-tubes made of Quartzglass, supplied by Capillary Tube Supplies, with an outside diameter of 1.5 mm and wall thickness of 0.01 mm). During loading, capillaries were repeatedly flicked to remove any air bubbles. The capillary was then manually placed into the stainless-steel holder on the beamline. The x-ray exposure time was 5 seconds for centrifuged samples, and a total of about 100 measurements were taken. The detector was configured to measure a scattering vector in the range of 0.0032 to 0.38 $Å^{-1}$. Scattering patterns for the deionised water used during synthesis were also acquired to serve as a background.

The scattering patterns obtained were analysed using Igor Pro software with IRENA macro add-on [144]. The scattering patterns obtained for AgNPs had the background (deionised water) subtracted. Contrast for the elemental silver used for the modelling was calculated using the same software to be 4643 [$x10^{20}$ cm^{-2}] with Gaussian distribution type, form factor set as spheroid and structure factor where appropriate. In addition, a unified level representing aggregates was required to achieve a good fit (all modelling data can be found in Appendix 1).

2.2.3. Dynamic Light Scattering (DLS) and Zeta Potential (ZP)

DLS and ZP measurements were carried out using a Malvern Zetasizer Nano ZSP fitted with a 10 mW, 632.8 nm laser and analysed using the accompanying software (v. 7.13) with algorithms extracting decay rates for 70 size classes. The measurements were taken with the detector located at 173° - the backscattering method. The refractive index (RI) was set at 0.135 and absorption at 3.990 [145]. The measurements were taken in repeats of 6, unless stipulated otherwise, with PHMB-AgNPs (or Bare-AgNPs) concentration of 40 µl in 1 mL of DI water. More details on the method development can be found in 3.2.3 Dynamic light scattering (DLS) and zeta potential.

2.2.4. Electron Microscopy (SEM, WetSTEM, STEM-in-SEM)

Samples were imaged using a Thermo Fisher Scientific Quattro S equipped with a field emission filament (FEG). The WetSTEM (Scanning Transmission Electron Microscopy) method was adapted from Teulon *et al*. [146]: a 2 µl aliquot sample was dissolved in 1 ml of deionised water and stirred to achieve a homogenous colour. The Peltier stage was mounted in the ESEM and cooling was used to reduce the temperature of the stage to 2 °C. The 200-mesh copper grid with holey carbon film was placed in the holder and inserted into the precooled Peltier stage. A drop of water was placed in every corner of the stage and a drop of diluted (2 µL/mL) sample was placed on the mesh. The ESEM was then pumped with 2 purges between 800 and 1200 Pa with desired pressure of 700 Pa. The STEM detector was inserted. The pressure in the chamber was reduced to 650 Pa, to encourage water vaporisation until the mesh started to appear, at which point the pressure was increased to between 710 and 720 Pa to stop water evaporation and to maintain a water phase on the copper grid thin enough to permit imaging of the samples, effectively finding an equilibrium between liquid and gaseous phases. The chamber conditions had to be adapted to the process of imaging, and although the equipment was able to maintain fairly consistent conditions, some drifting from the desired conditions was noted in both temperature and pressure. Upon completing the imaging, the

ESEM was vented; the copper grid was removed from the holder, placed on the horizontal holder on the stand covered within the enclosure and allowed to air dry. After a few days of drying, the horizontal holder was added to the multipurpose stage, and the sample was imaged again in High Vacuum (HV) mode. In this mode, as well as STEM-in-SEM, some images were taken using a conventional ETD detector.

The STEM detector has a number of detection modes, Bright Field (BF), Dark Field 2 to 4 (DF) and HAADF. ESEM permits the viewing of 4 modes simultaneously, and when taking a photo, it is possible to take 1 or all 4 quadrants at the same time. A resolution of 1536x1094 pixels was chosen for the photos at 45 µs dwell time, to strike a balance between time acquisition and image clarity.

The images were processed using ImageJ software. It was not possible to use the automatic particle analysis embedded into the software; it was, therefore, necessary to analyse the particles manually. The aim was to analyse around 150 particles per image (although this target was not always met) and to include larger and smaller particles when present. The measurements taken were analysed using Original Lab software.

2.2.5. Energy Dispersive X-ray Spectroscopy (EDX)

ESEM was coupled with EDX which allows for the automatic acquisition of images and X-ray dispersive analysis of the material under the beam.

Pathfinder software was used to acquire and analyse the data. The image was taken at a resolution of 512x384 pixels, and x-ray spectral mapping was conducted. The accelerating voltage was set at 30 kV with spot size 5 and the number of frames set to ‘infinite’. For samples in WetSTEM, the drift correction option was turned on to compensate for particles drifting. The collection time varied, but the aim was to collect data for at least 40 minutes or longer, with dead time at around 10% with 3-5 kcps (thousand counts per second). For STEM-in-SEM, the collection was conducted within 10 minutes with dead time at around 40% and 11-13 kcps.

2.2.6. Antimicrobial assessment

Antimicrobial studies for bacteria were selected to represent the two most common groups, gram-positive and gram-negative, with *Escherichia Coli* (10535) and *Staphylococcus Aureus* (6538) respectively. Bacteria were kept on the agar plate in the fridge at 5 °C and were replated every three months. Experiments conducted using the flow cytometer were carried out using fresh strains of bacteria to minimise storage effects on the results. The agar plates were prepared by dissolving 5.6 grams of agar nutrients in 200 ml of deionised water in an autoclavable bottle, stirring vigorously to ensure all powder had dissolved and autoclaved (25 min at 125 °C). The solution was then poured onto 10 ± 1 plates in the sterile fume cupboard, left to cool, and then kept in the sealed bag in the fridge.

The nutrient broth was prepared by dissolving 5.6 grams of agar nutrients in 200 ml of deionised water in an autoclavable bottle, stirring vigorously to ensure all powder had dissolved and autoclaved.

Zone of Inhibition

Using sterile pipettes, 10 ml of nutrient broth was placed in a universal tube, and a sweep across the bacteria plate was taken using a plastic loop and transferred to the universal tube. The tube was then placed in the shaker/incubator (Biosan ES-20/60 set to 150 rpm and 37 °C) and left for 18-24 hours.

Next, a cotton swab was used to transfer bacteria from the universal tube to the agar plate, with swipes across the entire plate with two repeats. Seven wells were then made in the agar plate using a glass pipette. 40 µl of undiluted samples were loaded into the wells, then the plates were left in the fume cupboard for approximately 1 hour and then transferred into the incubator (set at 37 °C) and left for 18 hours.

Images of the zone of inhibition (ZOI) were taken using a mobile phone camera with a ruler present for scale, and the ZOI was then measured using ImageJ software.

Flow Cytometry

Fluorescent labels were used to stain cells for detection with a filter 533/30 BP (FL1-A) for bis (1.3-dibutylbarbituric acid) trimethine oxonol (abbreviated here to BOX) and 670 LP filter (FL3-A) for propidium iodide (abbreviated here to PI). BOX (Fisher Scientific) a stock concentration of 10 mg/ml was diluted with DMSO to a working concentration of 100 ng/ml. The PI (Fisher Scientific) stock solution, 200 µg/ml, was diluted with deionised water to 100 ng/ml.

Flow cytometer analysis was carried out on the *E. Coli* bacteria only; two controls were prepared to assess the 'live' and 'dead' counts. The measurements for bacteria-containing samples were carried out with a limit of 25000 events of the total counts. During the collection stage of the measurements, the flow cytometer was set to a slow rate of 12 µl/min. All chemicals used – phosphate-buffered saline (PBS), ethanol and water – were filtered using a 0.2 µm filter.

Having incubated the *E. Coli* for 18-24 hours in the shaker/incubator, 10-40 µl of the solution was added to PBS to make up a volume of 1 ml. The sample was then analysed using a flow cytometer (BD Accuri C6 plus) with an aim of between 1000 and 4000 counts per second (cps), and the volume of bacteria was adjusted to meet the target cps and set the standard for 'live' *E. Coli* bacteria.

The negative control was carried out by taking 1 ml of *E. Coli* solution that was incubated for 18-24 hours and centrifuged in the Eppendorf tube for 1 minute at 13000 rpm. The liquid in the tube was pipetted out and the sediment was dissolved in 1 ml of 70% ethanol. A volume of between 10-40 µl of the solution was added to PBS to make up 1 ml volume. The sample was then analysed using a flow cytometer with an aim of between 1000 and 4000 counts per second (cps), and the volume of bacteria was adjusted to meet the target cps and set the standard for 'dead' *E. Coli* bacteria.

Both ‘dead’ and ’live’ controls were dyed with working solutions PI (5 µl) and BOX (10 µl) and incubated for 2 minutes before being analysed again using a flow cytometer.

Bare-AgNPs and PHMB-AgNPs were analysed using a flow cytometer by diluting 2 µl of AgNPs in 998 µl of PBS and measured for up to 1000 events, then 5 µl of PI and 10 µl of BOX were added, and the solutions were incubated for 2 minutes before being analysed again.

The antimicrobial effectiveness of the AgNPs was measured by adding an aliquot of bacteria to the PBS and then adding an aliquot of AgNPs. The volumes were determined by the counts recorded in the standards (‘dead’/’live’ standards described above) and the design of the experiment. The total sample volume was made up to 1 ml (i.e. 985 µl of PBS, 10 µl of bacteria, 5 µl of AgNPs). The sample was then incubated for a number of minutes (time subject to the design of experiment), then 5 µl of PI and 10 µl of BOX were added and the solutions were incubated for 2 minutes before being analysed.

Between measurements, the flow cytometer was flushed at a fast rate (66 µl/min) with distilled water, 70% ethanol and distilled water for 45 seconds at each stage to ensure that the events/second count was in the range 0-10. The results were analysed using BD Accuri C6 Plus software (version 1.0.27.1).

Chapter 3. Poly(hexamethylene biguanide) stabilised silver nanoparticles: characterisation.

3.1. Introduction

Understanding the system created by the polymer and silver nanoparticles requires sophisticated characterisation techniques at the nanoscale. Observations of a dynamic environment at the 10^{-9} metre magnitude can seldom be performed using a single method. Developments in advancing already available techniques, such as in the field of microscopy and improvements in the availability of equipment present a plethora of choices. However, the scale and detail necessary for informed analysis come at an increasing financial cost. In addition, time- and resource-intensive setups requiring highly skilled staff are needed. Even then, the data obtained provides only a narrow insight into the system and gives a multiplicity of choices when interpreting the results. Within a modern research environment, access to obtain data and carry out analysis can be achieved through interdisciplinary means within a university's various research groups and networks of external stakeholders. This decentralisation of equipment and knowledge access creates a challenge to 'own' the analytical methods. In this chapter, the objective is to collate the characterisation methods with corresponding protocols for data collection, quality control and analysis, to establish the reliability of the results obtained.

Silver nanoparticles have physical properties such as shape, morphology, size distribution, surface area and dispersivity in solution, that determine their behaviour (such as aggregation) and performance (in this case, antimicrobial activity). Although this interrelation is usually complex, it is often possible to derive information from behaviour or physical property performance, especially if other complementary data is available. The methods selected for this research have been chosen to obtain results using techniques based on different principles, to improve the reliability of the results.

The initial section of this chapter presents the naming conventions used, together with a discussion on the synthesis process and mass balance of the samples obtained. In the

following section, characterisation techniques are discussed in detail to provide an understanding of the method development and optimisation of the conditions. In addition, an example data analysis is carried out to introduce the presentation of results replicated in other parts of the thesis. Finally, the benefits and drawbacks of the methods applied are assessed so that the limitations can be fully appreciated when discussing the results. Understanding this section is important to all other chapters in this thesis in relation to the results presented.

3.2. Development of the results and their limitations

3.2.1. Synthesis process and mass balance

The following naming convention was adopted throughout this thesis. When synthesising the PHMB-AgNPs, 15 ml of various concentrations of PHMB were added. The concentration varied between 0 and 200 µg/ml, and it is this concentration level that is denoted in the sample names, e.g. '20 µg/ml PHMB-AgNPs'. Silver nanoparticles formed without any PHMB were named Bare-AgNPs. It is important to note that the actual concentration of the PHMB in the sample is not the same, due to the centrifugation process and removal of excess solvent. The individual batches synthesised have the following naming convention: a number representing the concentration of PHMB used in the synthesis process, 3 letters denoting the month of synthesis, and a two-digit number representing a year of synthesis, i.e. 0Feb19 denotes Bare-AgNPs synthesised in February 2019; 20Mar20 denotes 20 µg/ml PHMB-AgNPs synthesised in March 2020. For clarity, when the individual batches are not relevant to the discussion, the standard convention is used.

During the synthesis of batch Jul20, the reaction vessel and storage vials were weighed to determine the mass of the samples obtained. The mass balance was important for estimating the concentration of the PHMB in the final samples. The PHMB concentration to which this research refers in names relates to the 15 ml of polymer added to the beaker at the start of the reaction and varies between 0 and 200 µg/ml. The actual concentration of the polymer in the solution is diluted by 25 ml of $AgNO_3$ solution and later by an additional 5 ml of 10 mM

$NaBH_4$, at which point it drops to between 0 and 66.67 µg/ml. Upon completion of the reaction, the solution is centrifuged. The volume and mass of the retentate varies from sample to sample. The concentration of polymer in the collected sample is unknown and had to be calculated. Table 3-1 presents the mass of the samples obtained from the reaction using the methodology described previously for the Jul20 batch.

Table 3-1 Table presenting mass balance analysis and the final concentration of PHMB in the sample carried out on the AgNPs batch Jul20. *Two important assumptions were made to arrive at the result – the density of water was used when converting mass to volume; the concentration was valid if no PHMB is removed during the centrifugation process.

Sample ref. (µg/mL)	Weight of reaction solution (g)	Retentate weight (g)	Infranatant weight (g)	Weight loss (g)	Total mass of PHMB in solution (µg)	PHMB concentration in sample (*)
Bare	44.2580	1.0436	42.2181	0.9963	0	0.0000%
20	44.3618	0.6536	41.5384	2.1698	300	0.0459%
40	44.5399	1.0569	41.6302	1.8528	600	0.0568%
60	44.5636	0.8603	40.1868	3.5165	900	0.1046%
80	44.4974	0.6855	40.9746	2.8373	1200	0.1751%
100	44.5491	0.7535	41.4552	2.3404	1500	0.1991%
120	44.4628	0.9189	41.5977	1.9462	1800	0.1959%
140	44.4944	0.9928	40.9675	2.5341	2100	0.2115%
160	44.2788	0.7313	39.6270	3.9205	2400	0.3282%
200	44.3009	0.8205	42.2509	1.2295	3000	0.3656%

The mass loss took place in three stages: first – during synthesis, some splashing occurred causing the liquid to sit on the side walls and the lid; second – it was not possible to collect all the liquid when transferring the solution from the reaction beaker to centrifuge filter; third – it was not possible to collect the entire sample from the filter after centrifugation.

An attempt to calculate yield was made by conducting an experiment using 20 µg/ml and 80 µg/ml PHMB-AgNPs for which the volume was scaled up by a factor of 5, otherwise, a standard procedure (described in 2.1.1 Standard reaction) was followed. The centrifuged

samples were kept in a freezer for 24 hours and freeze-dried overnight to remove the water content. The dry weight of the dark powder obtained was 0.0102 g and 0.0080 g respectively. This would correspond to the yields of 68% and 58%, but it was noted that some of the grey powder had been observed on the lid of the freeze dryer. Most likely, this resulted from uneven penetration of the ice phase, causing the removal of some silver particles during the process.

Mass balance and the actual concentration of the polymer in the sample were important when comparing the efficiency of individual agents such as PHMB against performance – the antimicrobial activity. PHMB is used as an antimicrobial agent for various applications: it can typically be found in concentrations of 0.0005% in multipurpose contact lens solutions but is reportedly used in concentrations as high as 0.02% for treatment against *Acanthamoeba Keratitis* [147]. For the purpose of antimicrobial efficacy, two additional PHMB solutions were prepared with concentrations of 0.04% and 0.18%, which would be equivalent to the respective concentrations of around 20 μg/ml and 80 μg/ml of the PHMB-AgNPs samples.

3.2.2. Ultra-violet and visible light spectroscopy (UV-Vis)

Silver nanoparticles have a strong surface plasmon resonance which can be recorded using UV-Vis. Similarly, the PHMB exhibits a peak at 236 nm due to the $\pi - \pi^*$ transition in -C=N [52], even at a low concentration of 10 μg/mL (Figure 3-1)

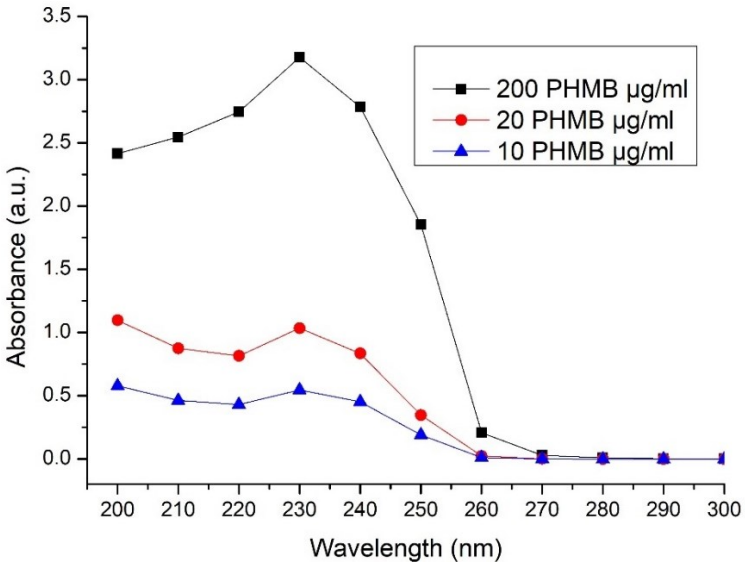

Figure 3-1 UV-Vis absorbance of PHMB polymer solution in deionised water.

By scanning the spectrum between 200 and 800 nm, a peak is recorded. A noticeable initial decrease from PHMB with silver nanoparticle peak sensitive to the size, shape, and concentration.

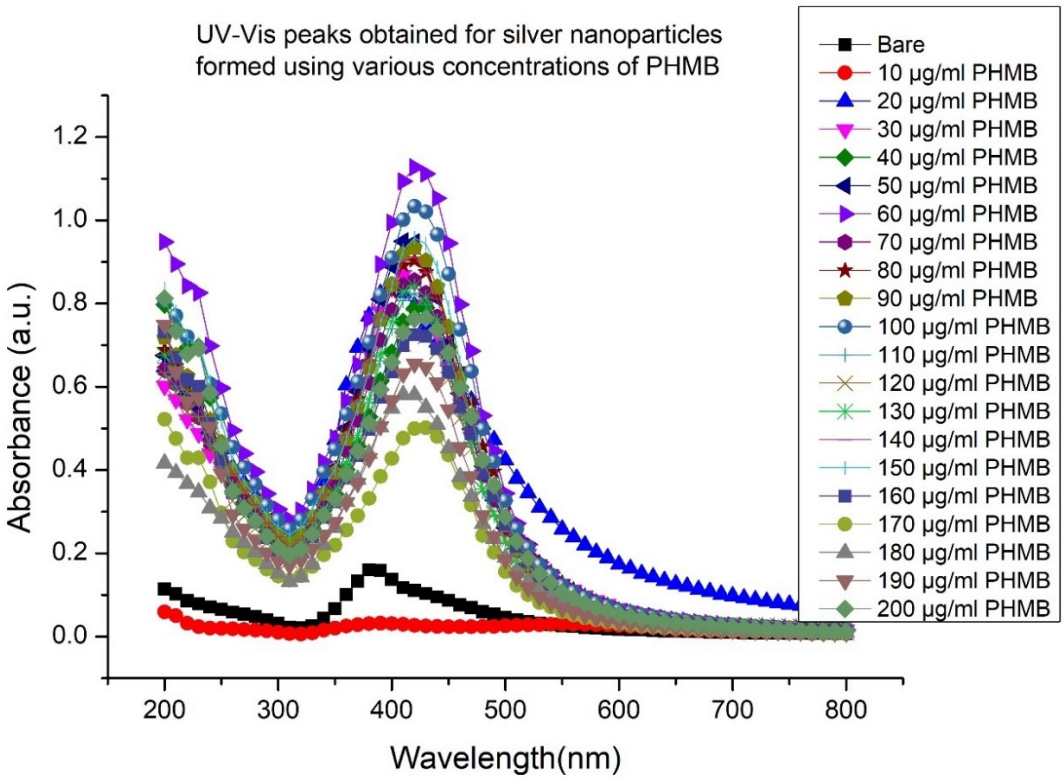

Figure 3-2 UV-Vis spectra obtained for a batch Nov18 showing a strong peak between 300 and 550 nm.

Comparing the peaks itself presented a challenge in maintaining the readability of the results. To track changes, compare between different batches synthesised, and better understand the features presented, the UV-Vis results have been reduced to three variables. The lambda maximum – the wavelength at which the maximum absorbance (λ_{max}) was recorded (Figure 3-3a – red circles); the full width half maximum (FWHM) – the width of the peak in nanometres at λ_{max} at half-height of the maximum absorbance (Figure 3-3a – black squares); and the maximum absorbance itself (Figure 3-3b). Similarly, peak λ_{max} and FWHM were very sensitive to the size and shape of the nanoparticles, but were independent of the concentration of the particles. Both proved to be particularly helpful in gaining a better understanding of the PHMB-AgNPs complex formed.

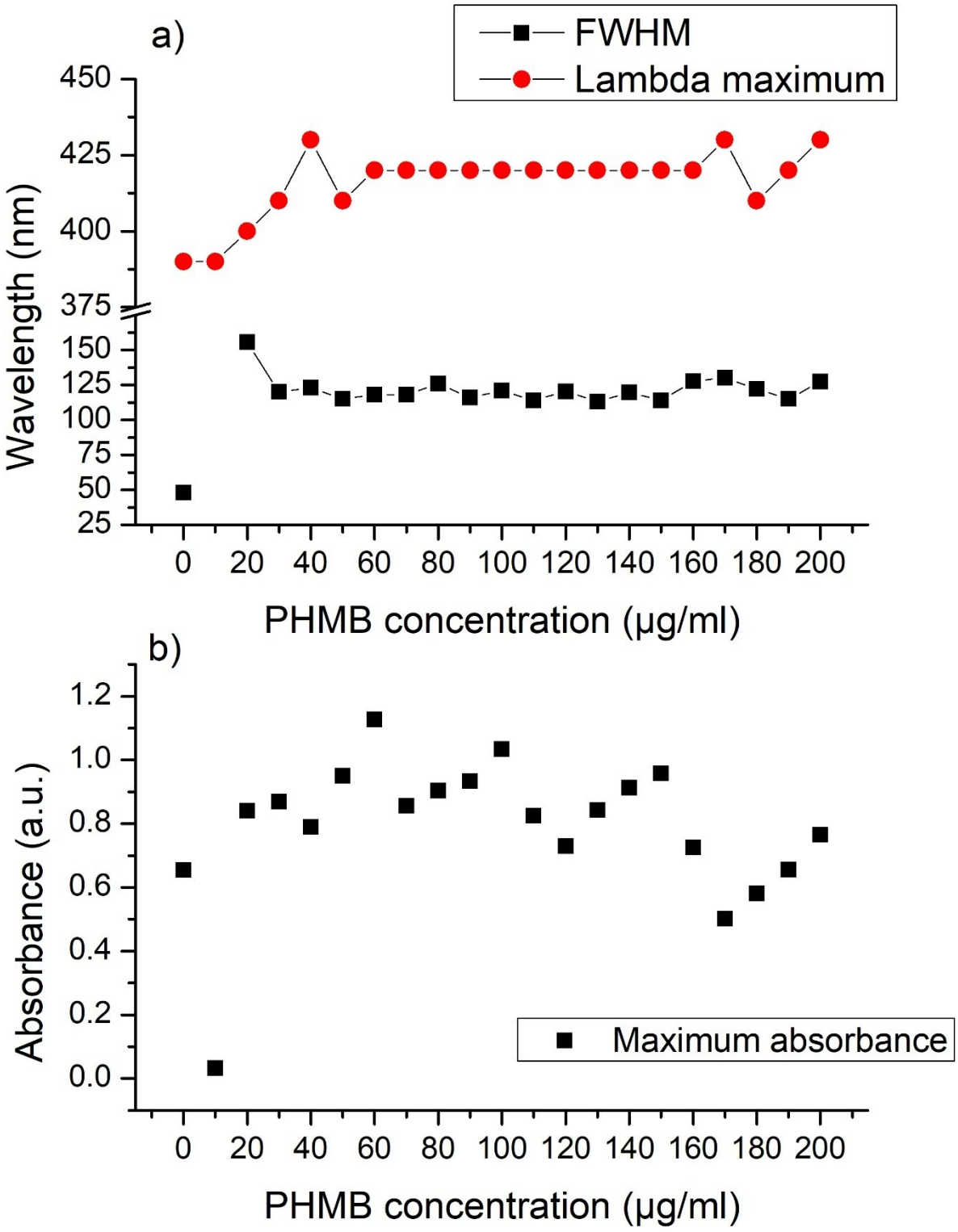

Figure 3-3 UV-Vis spectra obtained in the course of batch Jul20 reduced to variables of a) lambda max (red circles) and full width half maximum (FWHM) (black squares), and b) maximum absorbance. FWHM of the 10 µg/ml PHMB-AgNPs was excluded due to the double peak.

Maximum absorbance was, however, much more difficult to assess, due to the variability and fluctuations recorded. To measure the impact of concentration on absorbance, additional experiments were carried out to test whether the concentration of the sample was directly proportional to it. The Beer-Lambert law indicates that the absorbance of solute per fixed volume of the same sample should be constant. Therefore, the absorbance plotted against changing concentration of solute should produce a linear relationship. However, when this relation was tested it was found that at higher concentrations, the absorbance fluctuates (Figure 3-4), and this brought a change in the UV-Vis method: the 10 µl of AgNPs aliquot initially used was reduced to 2 µl per 2 ml of deionised water. This fluctuation was accounted for by the increased scattering between particles in the sample giving skewed readings [148].

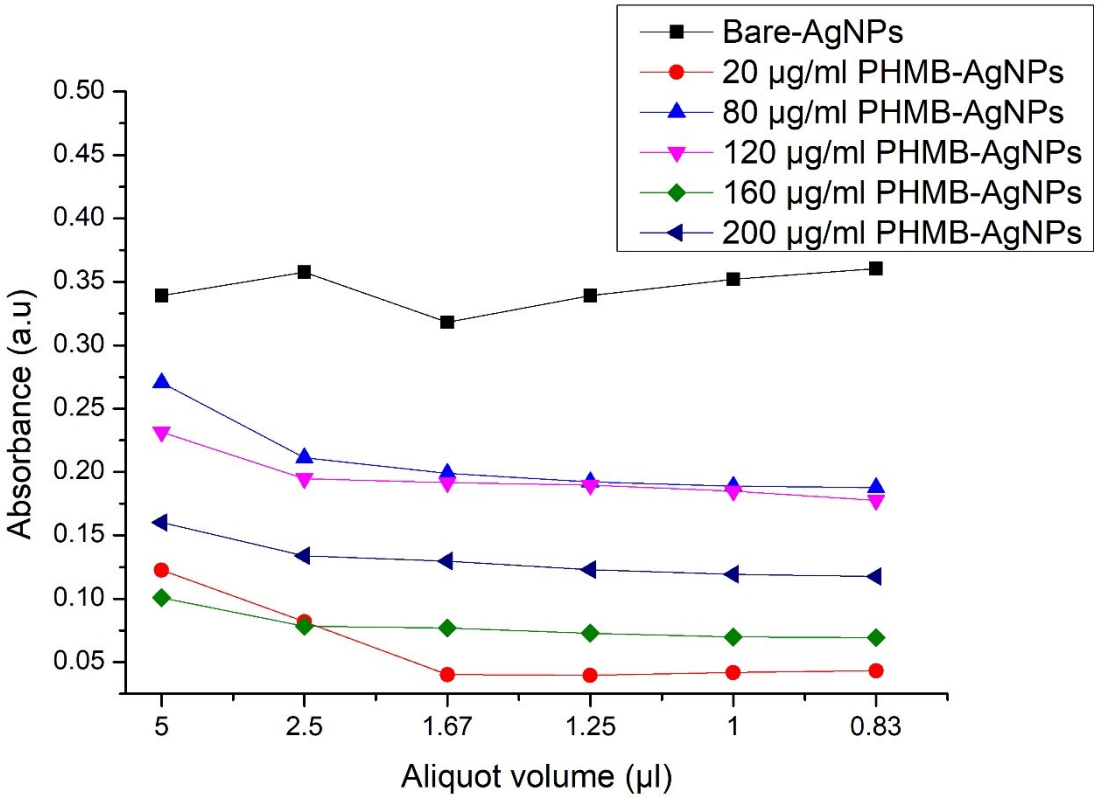

Figure 3-4 Analysis of maximum absorbance per 1 ml of aliquot used to establish the impact of concentration on absorbance fluctuation

After synthesising PHMB-AgNPs using various concentrations of polymer (between 0 and 200 µg/ml in 10 µg/ml increments), it was noted that above 20 µg/ml, the peaks obtained

using UV-Vis had a number of similarities. To better differentiate changes between peaks, the resolution of the UV-Vis spectra was increased to 1 nm from the initial 10 nm. This provided a better understanding of how the key UV-Vis variables – λ_{max}, FWHM and maximum absorbance – were changing with increasing concentration of the PHMB used during synthesis.

UV-Vis has proven a very effective and fast technique for characterising silver nanoparticles. The SPR peak can readily be recorded, and subtle changes in the position and width of the peak provide additional evidence. The technique is easy to use, requires minimal sample preparation, is non-destructive, and is highly sensitive to any changes within the system, making UV-Vis very efficient when comparing individual synthesis batches to identify trends. However, some important limitations must be noted. There is a very limited possibility to relate changes in physical structure, or interaction between the polymer and silver nanoparticles, to the changes in the peak recorded using UV-Vis. Mathematical models were developed [149] to make projections of how UV-Vis peaks change with various stabilisers, as well as to measure the impact of the ratio of silver core and polymeric shell. These, however, are complex to perform and are derived mainly from feeding the model with accurate data to make further predictions [94]. A number of assumptions were made: for example, the structure of stabilised silver nanoparticles was defined as core and shell, and the amount of polymer interacting with the silver core was assumed to grow without limitations. For those and other reasons, which are discussed in this thesis, this modelling after initial assessment for applicability was not explored further. UV-Vis results obtained are used in a relative way and provide substantial complementary data in this thesis.

3.2.3. Dynamic light scattering (DLS) and zeta potential

Dynamic Light Scattering is a technique commonly used to determine the size of nanoparticles. Equipment from two different manufacturers was used, initially the Brookhaven Nanobrook and later the Malvern Zetasizer ZSP. When a laser beam of fixed wavelength is directed at the sample, particles interfere with and scatter the beam, and this is captured by the

detector. This scattering is related to the Brownian movement of the particles, and fluctuation in the scattering is recorded. Because it is of a very low magnitude, the signal at the time has to be compared with its delayed version, with the auto-correlation drawn as a result. Effectively, the primary information from DLS is the diffusion coefficient of the particles, and then the distribution of the diffusion coefficients. To transform this data into the size and size distribution by intensity, the inversion technique must be applied, and various algorithms can be used for this purpose. DLS always produces a result, but its reliability depends on the method and requires quality analysis to ensure its appropriate use. Subject to quality assurance, different ways of reporting results can be used. In addition, DLS is often coupled with zeta potential, which measures electrophoretic potential from the light scattering of particles subjected to an electrical field.

Method development

During method development, the concentration of the sample and how this might affect the measurements taken were considered. The assessment was carried out using the Zetasizer DLS. The volume of the sample required for DLS is about 1 ml and the volume of silver nanoparticles synthesised in one batch is just short of this volume. It was possible to use the whole of the sample to perform measurement; the backscattering angle (173°) of the measurement allows the characterisation of samples with very high turbidity. The measurement position in relation to the edge of the cuvette is adaptable to fit the requirements. A sample of 20 µg/ml PHMB-AgNPs (20Jan19) was selected to investigate what sample concentration could be used. A number of concentrations were tested, with 3 measurements taken for each sample before diluting with deionised water. The concentration of the PHMB-AgNPs was reduced from 100% for undiluted samples to 0.5% of PHMB-AgNPs. There is a certain degree of variability in the measurements taken (the full table of results can be found in Appendix 2). The ‘in range’ figure – one of the quality indicators – fluctuates at around 93.7 with a standard deviation of ± 2.89. With the aim of using the smallest possible volume of the sample while

achieving measurements of reasonable quality, it was decided that such balance was achieved using 40 µl per 1 ml of deionised water. This was also close to the concentration used for the Nanobrook DLS: the suggested concentration when using this equipment was 100 µl of silver nanoparticles in 1.9 ml of deionised water. The optical clarity is important for this equipment, as it uses the 90° detection angle. On the rare occasions when there was not enough sample to achieve this concentration the maximum available was used.

The initial number of measurements was set at 3 per sample; this approach was adopted when using the Nanobrook and also initially with the Zetasizer. After completing the samples Jan19 and Feb19, it was noted that for the purposes of data quality and analysis, conducting 6 measurements per sample provided more reliable results. This approach was adopted for all cases where time was not of the essence in situations where there were time constraints, such as during the investigation into the impact of sodium borohydride ageing on synthesis (Chapter 5 below), only 3 measurements per sample were made.

Data quality analysis

Using the Nanobrook DLS, quality analysis was limited to the inspection of the correlograms, and it was not possible to inspect multiple plots simultaneously, which hindered appreciation of how different measurements in each set fitted together. The Zetasizer DLS software allowed far more flexibility with data analysis. Both DLS used in this study provide a mean or 'z-average' – a singly reported average for the whole of the distribution. The calculations made to arrive at this number, the cumulants analysis, are performed by plotting a gaussian distribution over the whole range of sizes expected for a monomodal sample. However, almost all the AgNPs synthesised for this study showed a multimodal sample distribution, with more than one peak observed in the results obtained using DLS. Therefore, a more complex multimodal analysis should be carried out to confirm the size reported by DLS. Nevertheless, the z-average can be a helpful tool in tracking changes in overall size distribution.

Before data analysis was carried out, the results obtained had to be assessed for quality, as the DLS always produces a result, even in cases of poor quality.

Investigating the correlogram for consecutive measurements carried out for 200 µg/ml PHMB-AgNPs (Figure 3-5), it was apparent that they did not superimpose as they should; instead, the spread was significant. Such discrepancies were a result of the number fluctuations; in other words, the samples were aggregating or dissolving. The fact that there are no clear patterns in the discrepancies suggests that both processes were happening concurrently. The same issues were observed for all samples synthesised with PHMB concentration higher than 40-60 µg/ml. The increase in discrepancy was progressive as concentration increased.

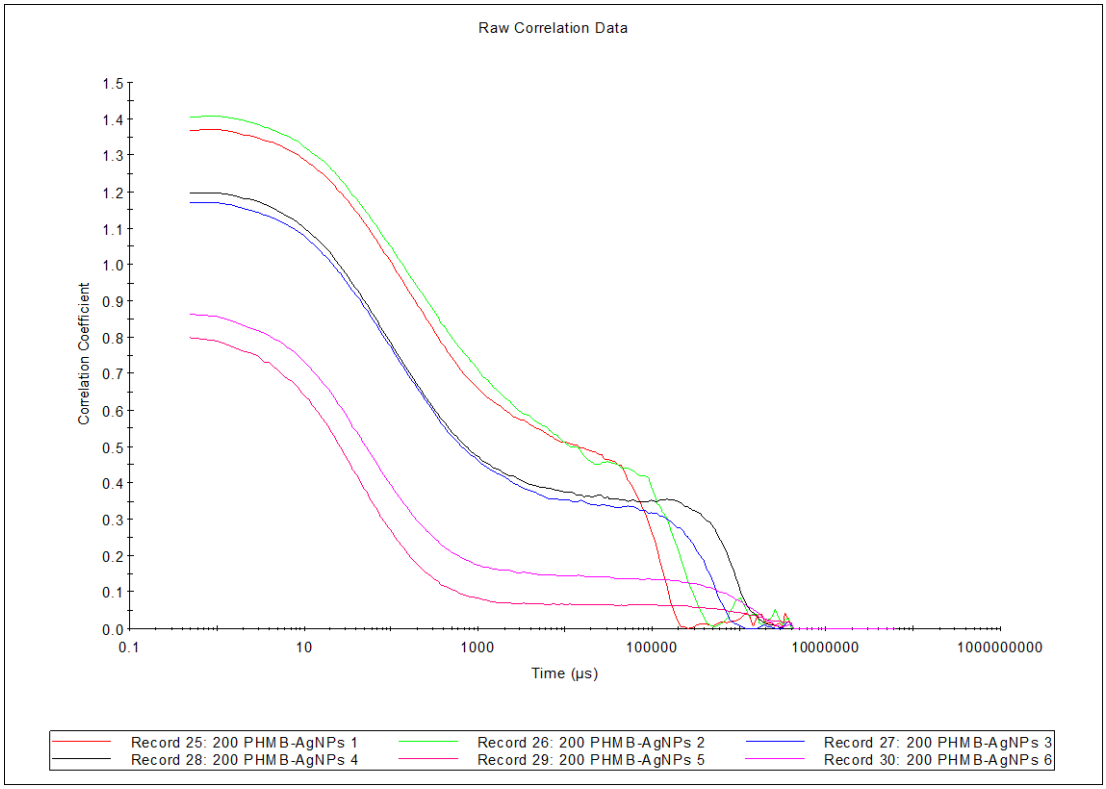

Figure 3-5 Correlograms for the same sample showing the issue of number fluctuations for 200 µg/ml PHMB-AgNPs synthesised in higher concentrations of the polymer.

The data in Table 3-2 presents the average of measurements made for the Jun19 samples. It can be argued that the measurements taken for the PHMB concentrations of 0 (bare), 20, 40 and 60 µg/ml are of good quality. The 'in range' figure is above the 90% recommended by the manufacturer, and the fit errors are below 0.005, indicating the size fitting to the

correlation function is of good quality, if not in cumulants then at least in multimodal analysis. The measured intercept for all the samples recorded is below the expected approximate 0.9, but this drop could be associated with the light absorbance that silver nanoparticles have at 622 nm, the light source of the DLS equipment. Beyond an 80 µg/ml concentration of PHMB-AgNPs, there is a noticeable drop in all the key indicators, raising doubt about the quality standard.

Table 3-2 Average results obtained from the Zetasizer DLS for the batch Jun19, presenting dropping quality of the measurements taken with increased concentration of the PHMB present in the synthesis process.

Sample Name	Z-Ave (d.nm)	In Range	Cumulants Fit Error	Multimodal Fit Error	PDI
Bare-AgNPs average	30.12	98.3	0.00605	0.0000473	0.9358
20 PHMB-AgNPs average	85.98	97.2	0.00355	0.00103	0.3033
40 PHMB-AgNPs average	26.31	98.1	0.00946	0.00174	0.5925
60 PHMB-AgNPs average	43.56	97.3	0.00682	0.00281	0.4525
80 PHMB-AgNPs average	63.47	85.1	0.0654	0.00574	0.4008
100 PHMB-AgNPs average	190.2	84.4	0.0361	0.0213	0.4325
120 PHMB-AgNPs average	162.5	83	0.0841	0.0496	0.4483
140 PHMB-AgNPs average	106	80.1	0.0941	0.021	0.1958
160 PHMB-AgNPs average	260	71.7	0.0901	0.0444	0.2872
200 PHMB-AgNPs average	346.7	76.9	0.0616	0.0872	0.6123

It also becomes important to conduct quality analysis before using the software's 'average' feature, which creates an average plot from the measurements taken. Compiling averages for measurements that do not meet quality standards leads to erroneous results (Figure 3-6).

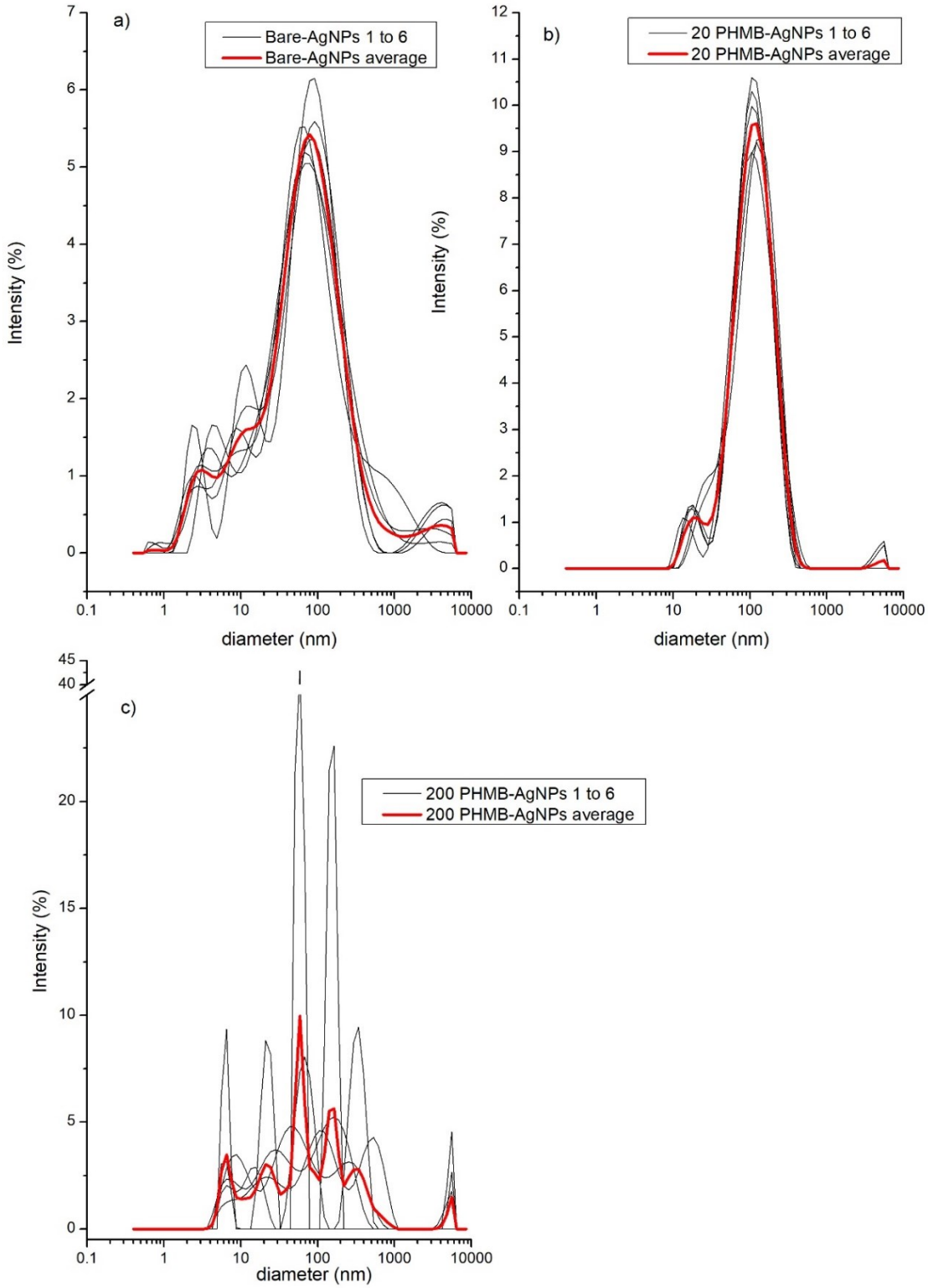

Figure 3-6 DLS data presenting the challenge of obtaining the average result for data of poor quality (200 µg/ml PHMB-AgNPs Jun19), if the sample did not produce reproducible measurements (thin black lines) the average (thick red) generated gave false result.

Data analysis

Initially, the Brookhaven Nanobrook DLS was used to characterise the silver nanoparticles, and the whole spectrum prepared as part of the Nov18 series was measured using this

equipment. Analysing and presenting data for discussion proved to be extremely challenging. The difficulty stems from the key feature of the sample being analysed – multimodal distribution. Usually, two or three peaks were observed when measurements were taken, which for quality assurance reasons was done several times (3 or 6 times). The multimodality in itself made use of the mean average figure unreliable for reporting the nanoparticle sizes – in certain circumstances, it provided sizes that did not exist in the sample. The multimodal analysis takes this into account and assesses the individual peaks in each set of measurements taken.

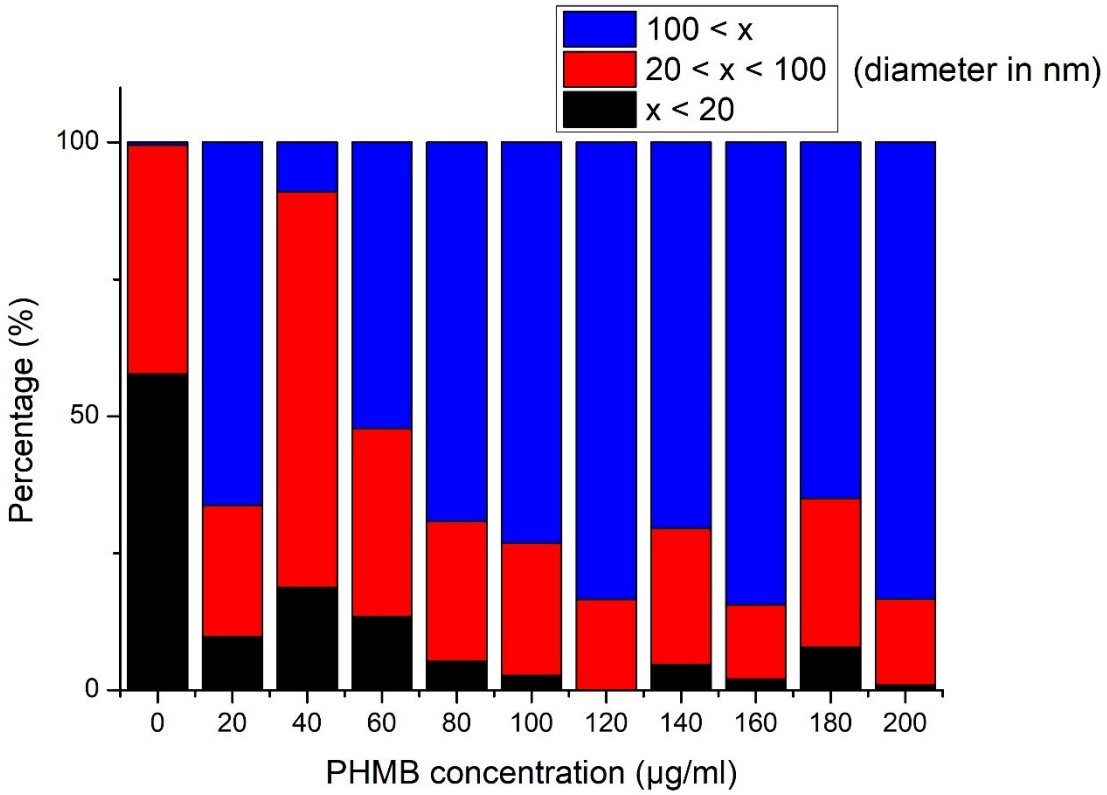

Figure 3-7 Data analysis of measurements obtained from Nanobrook DLS, with particles categorised into three groups by size, due to challenging multimodal distribution of the samples.

However, the peaks observed were rarely superimposed on one another, and peaks were sometimes observed in one measurement but not the next. The shifting of the peak and its occasional disappearance made tracking individual peaks almost impossible. In addition, the inherent limitation of DLS is that larger particles scatter far more light; when this is taken into account, reporting size and distribution becomes very challenging. A partial solution to these

problems was to prepare a percentage distribution of the nanoparticles (Figure 3-7). The peak positions were no longer relevant, as a percentage of the total would fall into one of three categories, smaller than 20 nm, between 20 and 100 nm, and larger than 100 nm. A similar approach was tested with the data obtained from the Zetasizer DLS; however, once the quality analysis had shown that the data was unreliable for PHMB concentrations over 60-80 µg/ml PHMB-AgNPs, the number of data points was greatly reduced, and individual averages were created for each sample. The aggregated results are presented in Chapter 4.2.1-Results - Dynamic Light Scattering (DLS) on page 119.

Volume and Number analysis

The primary result of the DLS measurements is intensity size distributions, which only require dispersant viscosity and refractive index, both easily accessible reference values. However, [95] large particles can overpower the intensity distribution plots. Using the Mie theory, it was possible to determine the volume and number size distribution (Figure 3-8). These transformations require that the refractive index and adsorption, the optical properties of particles, be known. This information was available for silver, but it was not possible to assess how the PHMB might affect those properties. The transformations and the assumptions required make sizing reporting using those distributions inaccurate, as any error in the intensity size distribution is significantly magnified when the calculations are carried out. However, the relative amount in each peak in those distributions can be used with some degree of confidence. The transformation into volume and number distributions carries increasing error; their use must be carefully considered, and their limitations understood before figures are taken as real values. But the volume and number distributions offer opportunities to link the results from DLS with other techniques used in the scope of this research, UV-Vis and Small Angle X-ray Scattering (SAXS). Both are volume-based characterisation techniques and microscopy is a number-based technique. Using Figure 3-8 (table insert in particular) as an example the results

from the intensity distribution point to multimodal distribution with two/three populations. Minor - very small particles of about 14 nm and major – larger group at around 106 nm

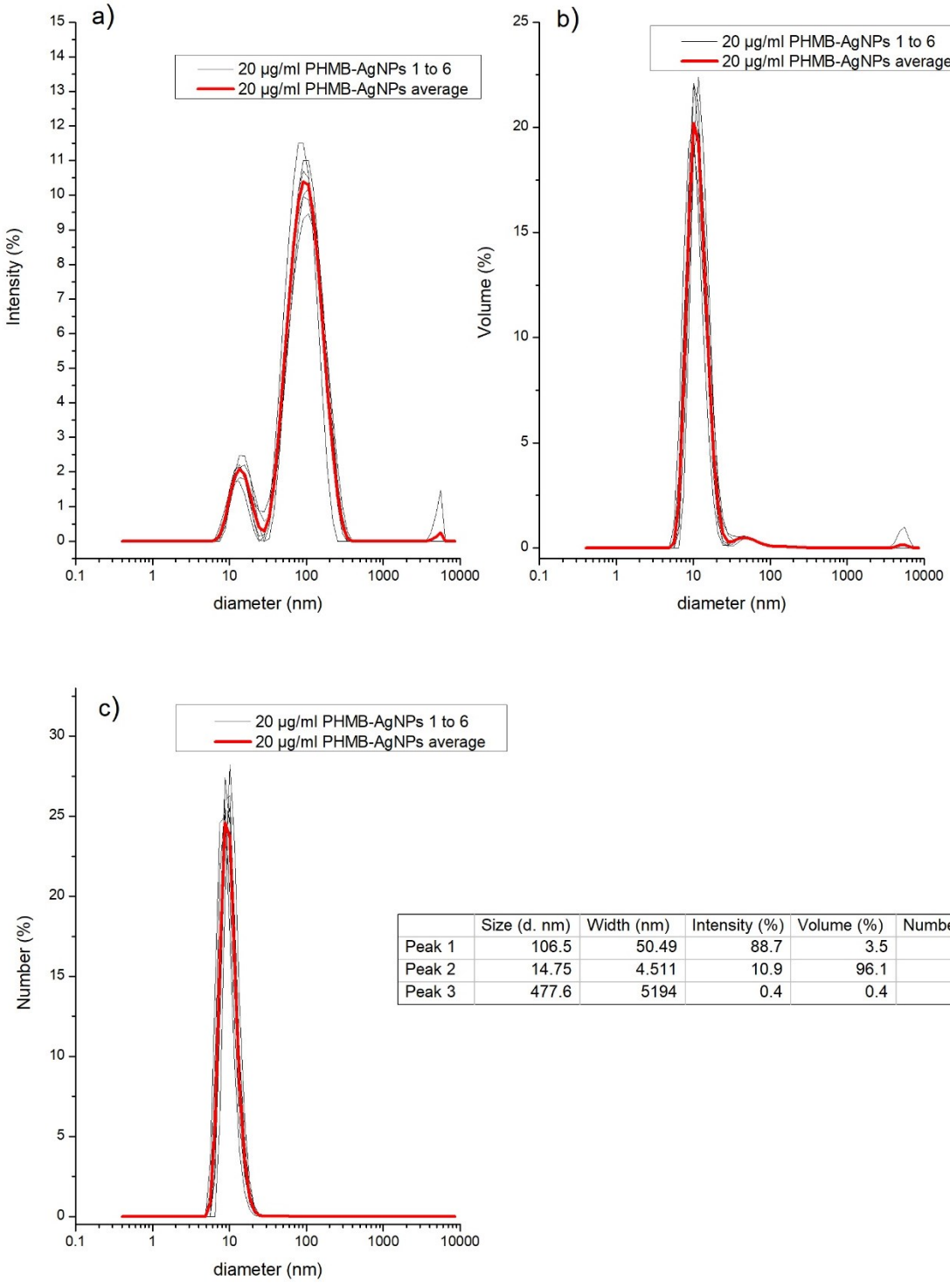

	Size (d. nm)	Width (nm)	Intensity (%)	Volume (%)	Number (%)
Peak 1	106.5	50.49	88.7	3.5	0
Peak 2	14.75	4.511	10.9	96.1	100
Peak 3	477.6	5194	0.4	0.4	0

Figure 3-8 a) Intensity distribution recorded by DLS and transformation to, b) Volume and c) Number distributions, the table insert present joined analysis of peaks in each distribution. For correct reporting, the size after transformation to volume or number is not reported; peak percentage was cited, as the size given by the intensity distribution was the most reliable.

When transforming into the volume (Figure 3-8b) the percentage of the particles present in those groups is recalculated indicating that particles at 14 nm are a dominating population by volume. While the larger particles are a minor group, the larger particles scatter more light and, hence dominate the intensity distribution. The information obtained from converting into the volume distribution was tested during the modelling of SAXS data. Because SAXS is a volume-based technique attempts were made if the populations determined by DLS can be used as a starting point in developing models to fit obtained scattering patterns. Further discussion on this aspect can be found in the section below 3.2.6 Small-Angle X-ray Scattering. While converting to number size distribution (Figure 3-8c) renders the 106 nm population negligible and, therefore, in SEM imagining it was expected to mainly observe small particles. Detailed analysis of the results from DLS, SAXS and SEM can be found in section 4.3.1 Size and shape

Zeta potential

Zeta potential measures the charge at the shear plane of the particle, deduced from the electrophoretic mobility of the particle. The samples measured were the same as those used for the DLS measurements. As with the DLS results, three repeats of the measurements were taken, due to some variation in the results. The Zetasizer software would not compute average results, so instead zeta potential results for a particular sample were averaged together and presented with standard deviation (Figure 3-9).

Measurements of the zeta potential were also taken against a variety of different pH values. However, this was carried out manually – synthesised particles were added to 1 ml of deionised water with its pH adjusted to a range between 4 and 10 using HNO_3 or NaOH. As AgNPs were dissolved in the pH-adjusted solution and measurements were taken subsequently, it is possible that the particles readjusted to the environment by aggregating/dissolving to find a new equilibrium. Due to previously explained difficulties, sizing was not possible except for two samples: Bare-AgNPs and 50 µg/ml PHMB-AgNPs. This, therefore, provided insufficient data points to draw conclusions.

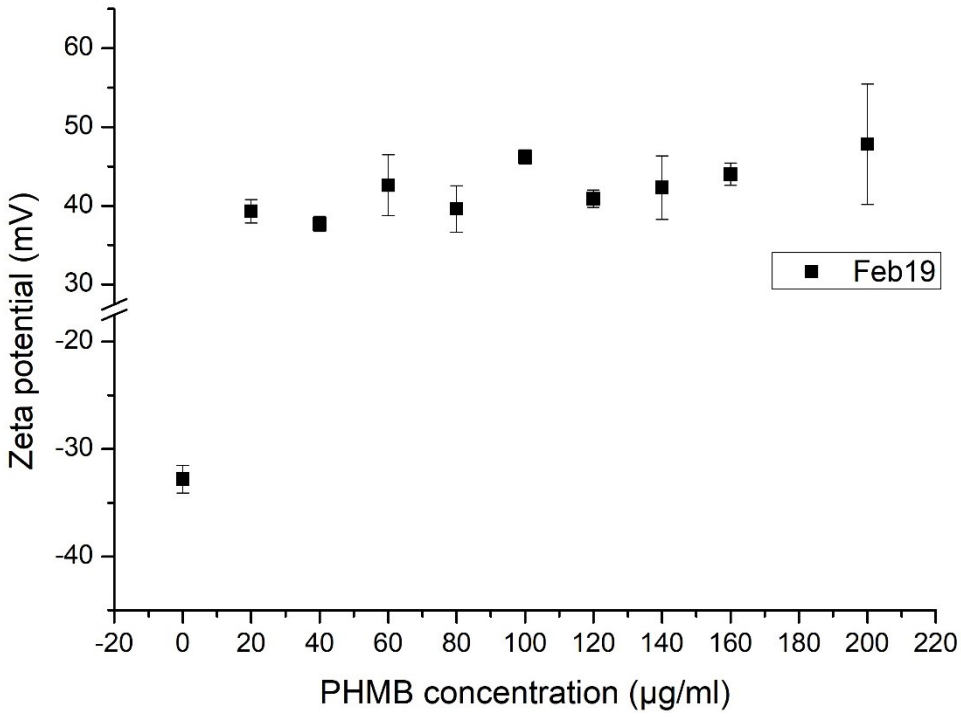

Figure 3-9 Results obtained for AgNPs showing the impact the PHMB has on the zeta potential. Measurements taken in DI water recorded a pH of 7 ±0.1

Summary

DLS is a fast and non-invasive technique, commonly used to determine the size of nanoparticles. Two different pieces of equipment, with different detection angles, were used in this research, with similar results. The data obtained showed a multimodal distribution of AgNPs in all samples, creating difficulties in relying on the singly reported size average and requiring more complex multimodal analysis. Further data quality analysis showed deterioration of quality as the concentration of the polymer present in the sample increased, preventing the use of results obtained for those samples. Due to these limitations, not all the results can be relied upon, and the analysis carried out has to be applied with caution. Volume and number distributions can only be partially relied on, as DLS is extremely sensitive to larger particles, and the smaller particles have to be in great excess to be recorded by the DLS [95]. Understanding this limitation offers an opportunity to conduct analysis of more than the particle sizes measured, since the changes in quality signify certain aspects of particle behaviour, hence giving a better insight into the system under investigation. The zeta potential showed a reliable result of electrophoretic mobility of the particles, with and without the polymer present.

3.2.4. Environmental Scanning Electron Microscope (ESEM)

The electron microscope offers the opportunity to conduct direct observation of the samples under investigation. Typically, SEM operates under high vacuum; this provides the best imaging results but requires sample preparation, such as coating, to ensure sample conductivity. In addition, samples might form artefacts under high vacuum. The ESEM can operate under variable pressure, by the addition of the water phase into the chamber. It is therefore possible to image non-conductive samples without additional preparation. The water particles in the chamber are sufficient to prevent charge building up, which normally occurs on the non-conductive sample under the electron beam. With the introduction of a Peltier stage capable of sample cooling, the use of an appropriate detector and further pressure increase, it becomes possible to maintain a sample within the water phase. Method development was required to image samples in the wet and high vacuum modes and generate quality images suitable for analysis. Comparing the two modes offered an opportunity to understand the differences in artefact formation.

Method development

The choice of the detector plays an important role in imaging, as they detect different types of electrons, secondary or backscattered. The detectors are either mounted within the chamber or on the standard insert of the beam column and serve as pressure-limiting apertures to support variable chamber pressure. The cone mounted on the detector will also affect the distance to the sample (working distance). The Gaseous Secondary Electron Detector (GSED) was selected for most of the imaging, due to its ease of mounting and use compared with the alternative High Pressure Gaseous Analytical Detector (ESEM-GAD).

It was determined during method development that imaging using either of the detectors is not very efficient in producing high quality images. For the most part, this detector was used only in the initial stages of imaging for finding the sample. The alternative detector available was the Scanning Transmission Electron Microscope Detector (STEM) mounted under the

sample, and provided transmission electron microscope capabilities at lower acceleration voltages, resulting in higher contrasts.

The chamber pressure has an impact on the skirting of the beam and therefore on image quality. This skirting effect depends on three variables: the accelerating voltage (in kV); the pressure in the chamber; and the distance from the sample to the pressure-limiting aperture mounted on the detector. It is more favourable to reduce the skirting effect to achieve better imaging quality and, therefore, promoting higher kV, a smaller distance from the detector and the lowest possible pressure in the chamber. However, to maintain the sample in the liquid state, the temperature/pressure phase diagram of water was used to determine that if the temperature is reduced to 2 °C, which can be achieved with the use of the Peltier stage, the pressure of water vapour (at 100% humidity) required was 705 Pa. Deionised water (1 ml) was used to dilute 2 µl of the test sample; for best results, the water was precooled to achieve better control over the evaporation/condensation equilibrium. Once the drop of the silver nanoparticle solution was placed on the copper grid and the chamber pumped to the required pressure, it had to be repeatedly adjusted to respond to the behaviour of the liquid on the grid. The pressure was varied between 650 and 1800 Pa, and by monitoring using GSED, the evaporation/condensation of the liquid was stabilised over time to minimise fluctuations. The acceleration voltage used was 30 kV, and the spot varied between 1 and 3; high resolution imaging was achieved under those conditions, example of the WetSTEM image is presented in Figure 3-10.

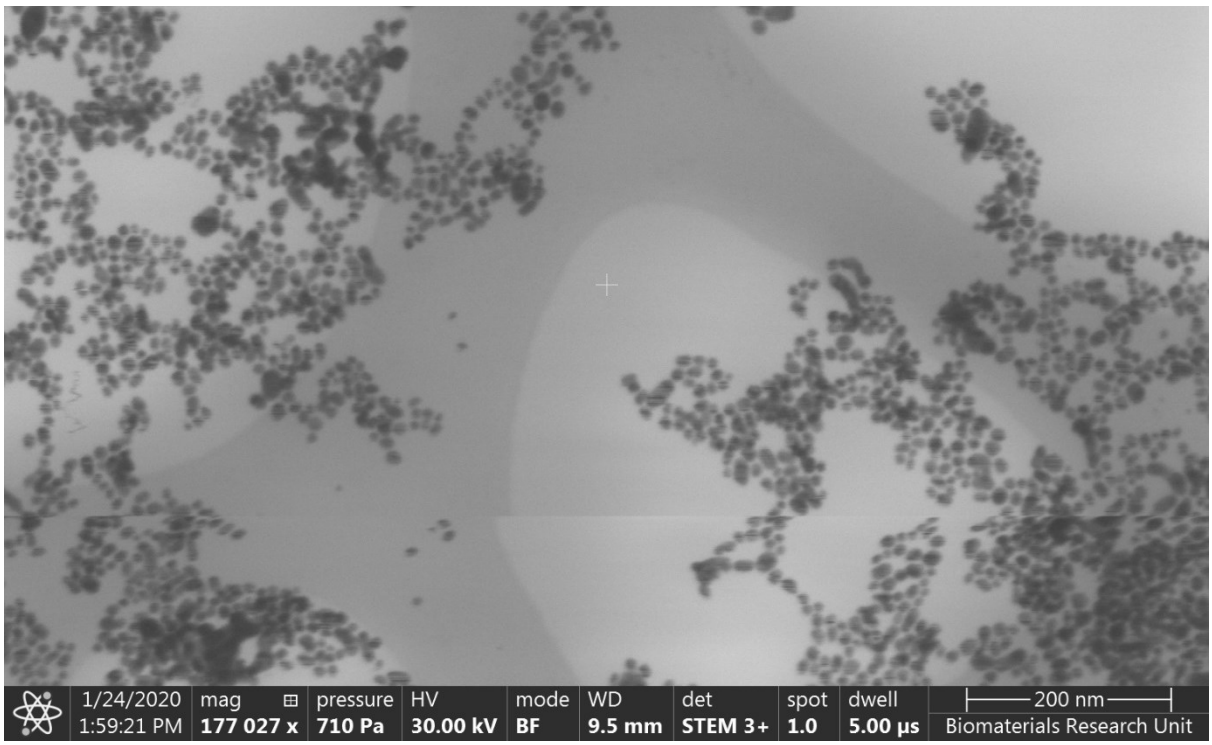

Figure 3-10 WetSTEM image of 20 µg/ml PHMB-AgNPs (Jan20)

The beam damage was observable and therefore focus was often carried out in another part of the grid and moved to the area of interest for image-taking to minimise this effect. Time under observation would differ from sample to sample, and maintaining the precise pressure and temperature for long periods was challenging for the equipment: after a time, the sample would either be flooded causing a loss of image, or the water would evaporate, leaving the silver nanoparticles deposited on the holey carbon film of the copper grid. One of the greatest challenges in using wet mode was the drifting of the sample. AgNPs are mobile in the liquid phase, and the settings for image acquisition were established at a long dwell time (45 µs) to produce clear high-resolution imaging. If particles move or the sample shifts during image-taking, the picture becomes distorted. The recurrence of these events coupled with loss of contrast resulted in a progressive reduction of image quality as the sample was scanned. The higher the observation magnification, the greater the challenge of minimising drifting became.

After imaging, the sample was removed and placed on the horizontal holder outside the chamber under a cover to air dry for a few days. The dried grids would be then imaged in a

high vacuum. Using this mode was much less challenging and much faster to complete, as it was easier to focus on the areas of interest. Multiple grids were loaded into the chamber at once, reducing the need to pump and vent the chamber repeatedly. Working in a high vacuum completely removes the sample drifting problem common to the WetSTEM, making it possible to achieve higher magnification without a loss of image quality. As with the GSED detector in wet mode, when using the secondary electrons detector (Everhart-Thornley Detector - ETD), it was not possible to image nanoparticles to the desired resolution, and the high acceleration voltage produced poorly visible images of the artefacts formed as a result of drying (Figure 3-11a). Better SEM imaging was possible with ETD at greatly reduced voltage, but then the particles present inside the structure were not visible. Using STEM-in-SEM operated best in the same electron beam conditions as WetSTEM, i.e. 30 kV acceleration voltage and spot size between 1 and 3, and resulted in a large number of good-quality images (Figure 3-11b).

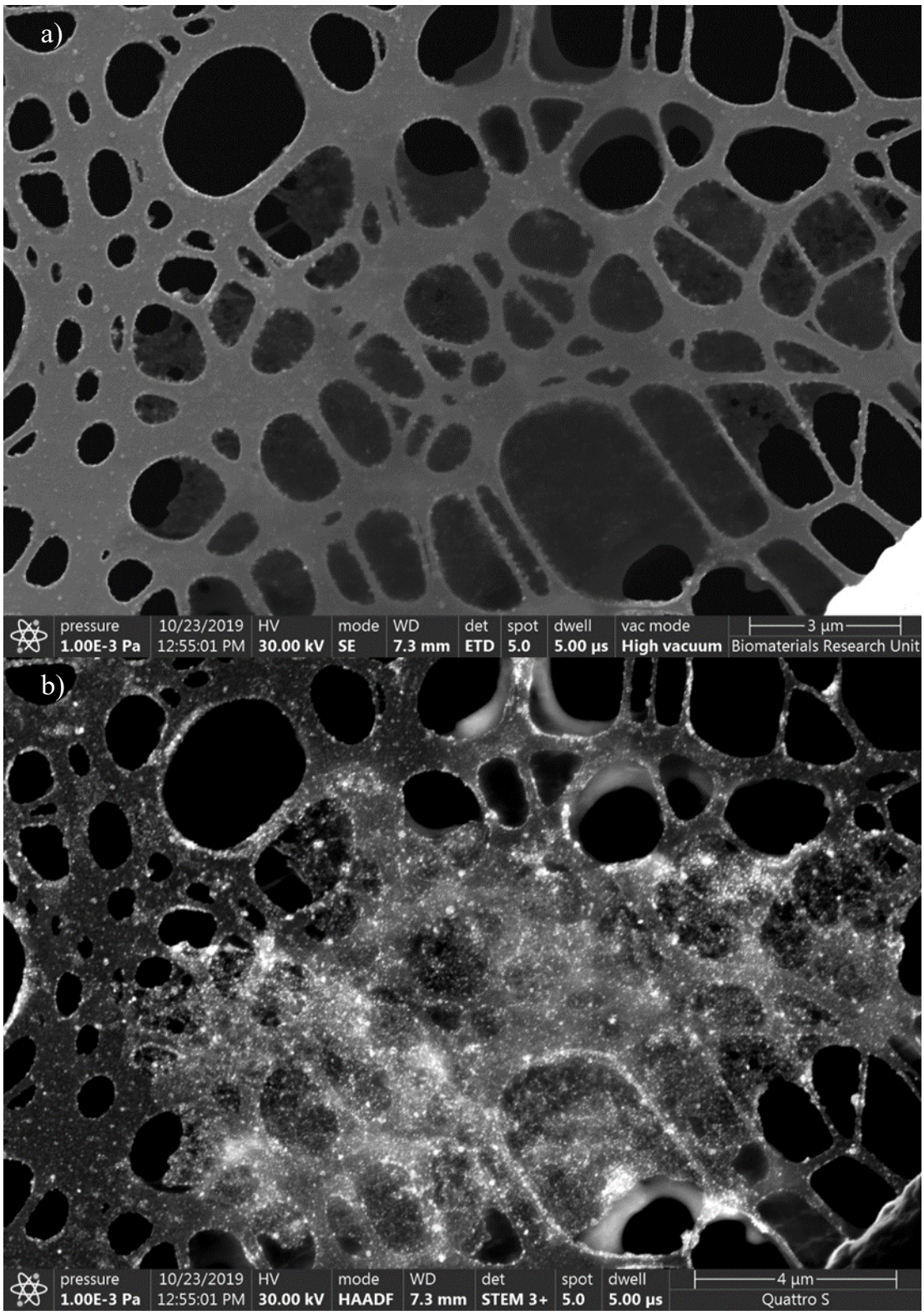

Figure 3-11 Images obtained for a sample of 20 µg/ml PHMB-AgNPs using: a) ETD detector, b) STEM-in-SEM for the same area, showing poorly visible amorphous mass present in the centre of the image, and for comparison HAADF detection mode with bright white spots representing AgNPs.

Results analysis

The images obtained were analysed using ImageJ software, and manual measurement of the particles was carried out. Although the aim was to perform at least 150 measurements on each image to use for analysis, this was not always possible. Because a limited number of images was produced using WetSTEM compared with STEM-in-SEM, it became important to understand how the sizes reported using high vacuum compare to those obtained in wet mode.

It is important to remember that the manual measurement of individual nanoparticles suffers from a number of limitations. Much of the process of imaging and analysis is arbitrary and depends on the user. The area of interest selected for imaging might not best represent the bulk of the sample, and the measurements themselves are not carried out on all particles in the image, but on a limited number, and are therefore subject to bias. Larger particles are easier to see and may be more likely to be included in the analysis Figure 3-12. A lack of sufficient contrast between the background and particles made it impossible to conduct automatic measurements of all the particles present in the image.

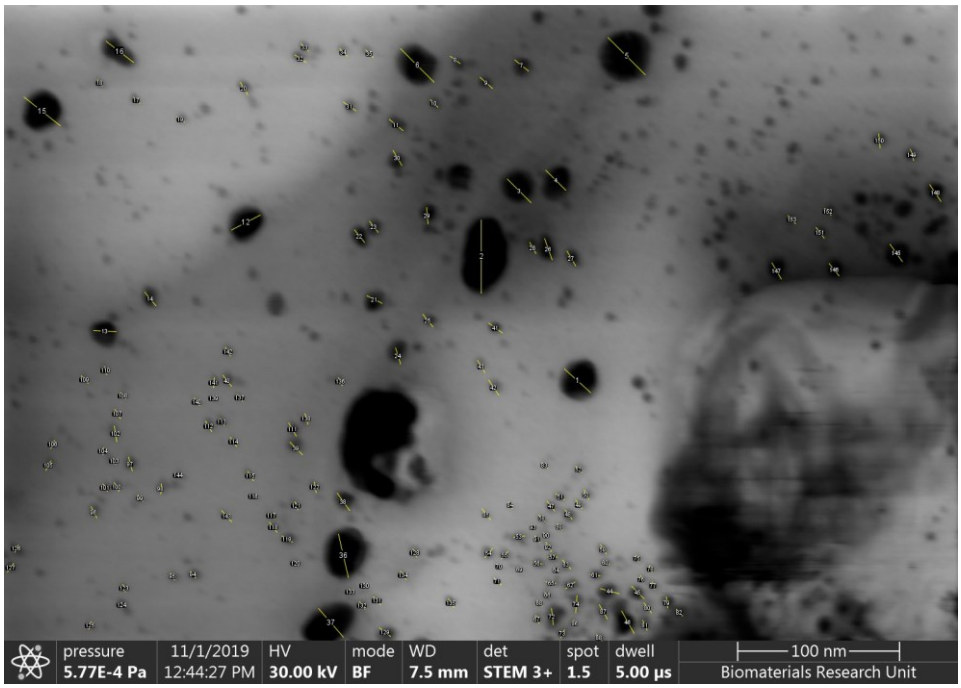

Figure 3-12 WetSTEM image of 80 µg/ml PHMB-AgNPs with measurements overlaid and used for the analysis of size distribution.

The best imaging results were achieved on the 6 samples produced as part of the Jan20 synthesis (Figure 3-13). Size analysis of the particles showed a distribution of particles. However, a notable increase in the particle size of the 140 and 200 µg/ml PHMB-AgNPs should be assigned to the decreased image quality, rather than to an increase in size associated with higher concentrations of the polymer present. This was a common issue in the wet mode imaging for particles with higher concentrations of PHMB. The particles were more prone to drifting from the image, causing notable distortions in the image and rendering it unusable. Countering this effect by decreasing the dwell time so that the image is acquired faster reduces the resolution, making the sizing more prone to error. When the same samples were later analysed in high vacuum mode, it was possible to achieve higher-resolution imaging for a more detailed sizing analysis. The results for the dry samples of Bare-AgNPs, 20 and 80 µg/ml PHMB-AgNPs corresponded very well to the results obtained in wet mode (Figure 3-13). Furthermore, it would not be expected for the particles to decrease in size as a result of drying; it was, therefore, safe to assume that the size of the nanoparticles obtained in a high vacuum was a good representation of the silver nanoparticles present in wet mode.

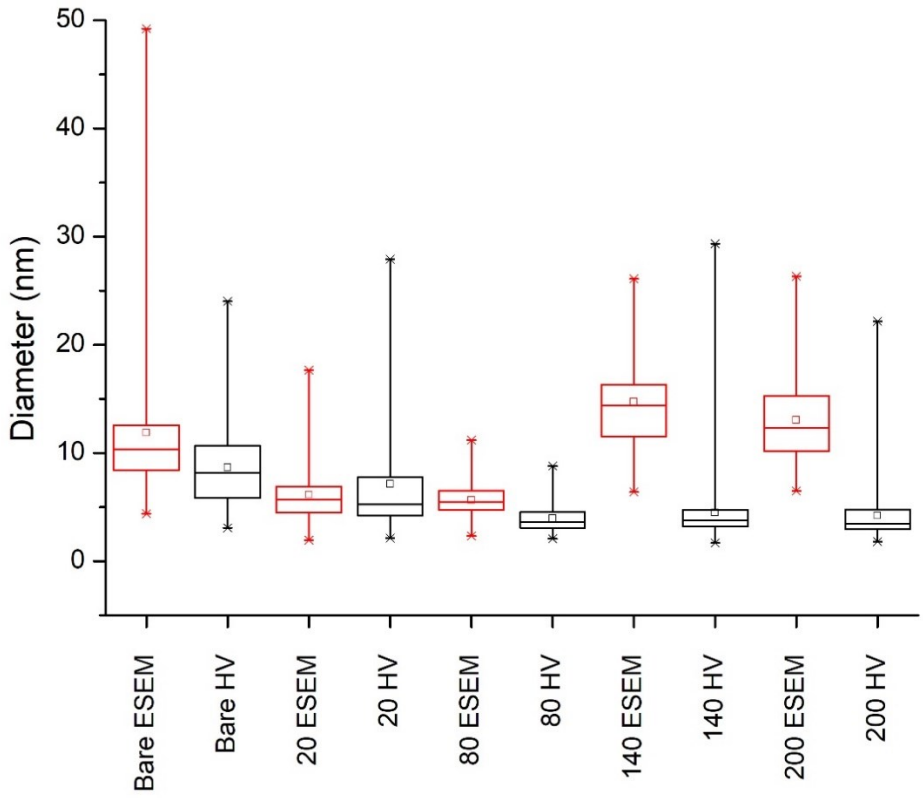

Figure 3-13 Comparisons of measurements taken for images obtained from the sample Jan20 in wet mode (marked ESEM) and in STEM-in-SEM (marked HV) showing how the two modes correspond to each other. The number before the sample name denotes the polymer concentration (in µg/ml) used in synthesis. The following marking was used: the lower edge of the box marks 25% of results, the middle 50%, and the upper line 75%. The whiskers are in the range of 1% to 99%. The square in the box represents a mean value.

Following a similar methodology, analysis was carried out on the images obtained for the samples from the Oct19 series (Figure 3-14). The images obtained as part of this series were some of the early attempts, and suffer from reduced image quality and resolution. However, analyzing selected images, in particular in a high vacuum, does allow size determination. Due to the limited images and the resolution issues, wet mode produced highly variable results, and any size analysis may be prone to errors. Discussion of individual images and features observed follows in Section 4.2, together with the Reproducibility of results.

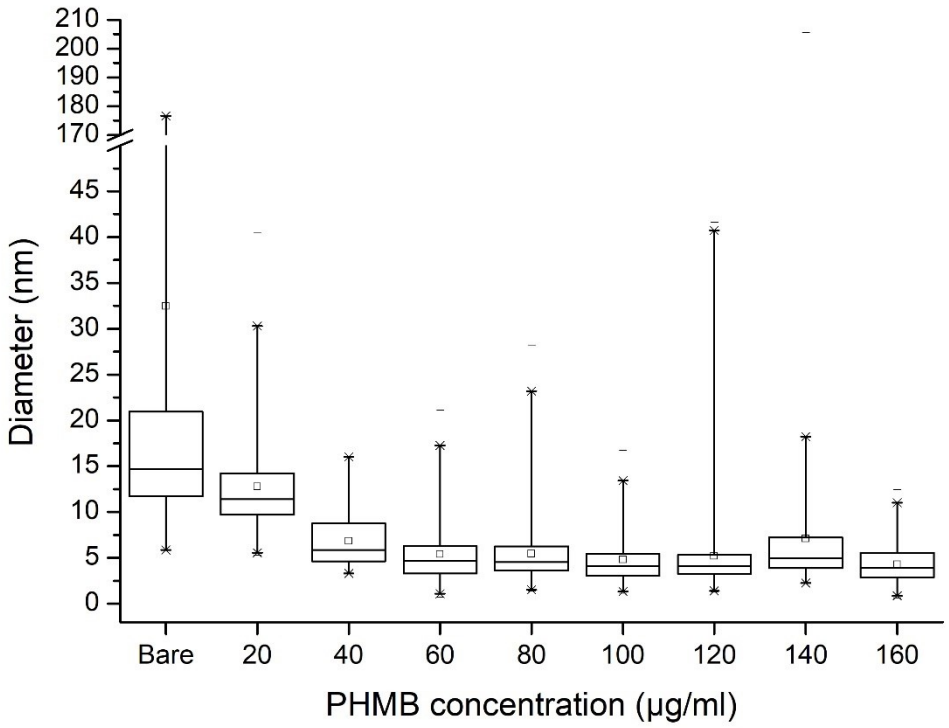

Figure 3-14 Size measurements obtained from image analysis of the Oct19 batch samples imaged in STEM-in-SEM. The figure has the following marking: the lower edge of the box marks 25% of results, the middle 50%, and the upper line 75%. The whiskers are in the range of 5% to 95%. The square in the middle of the box represents a mean value, with cross marking 99% and 1% and a dash for maximum and minimum measurements.

Summary

Imaging in wet mode and in high vacuum present opportunities to observe actual nanoparticles and describe their shape and size. These properties are very important when other methodologies are considered, such as DLS, which assumes a perfect sphere to conduct diameter calculations. One of the major limitations of this method is that it may not be representative of the whole sample. Only a relatively small number of particles are observed, and an even smaller proportion is measured. In addition, WetSTEM mode requires significant effort to maintain the water phase with sufficient thinness to allow imaging. This creates opportunities for artefacts to form and for them to differ between the same samples as a result of different conditions of drying.

3.2.5. Energy Dispersive X-ray Spectroscopy

Introduction

Energy Dispersive X-ray Spectroscopy (EDX), also known as Energy Dispersive X-ray Analysis, offers an opportunity to identify the elemental composition of materials present in the sample. EDX is coupled with Scanning Electron Microscope (SEM) and the x-ray analysis is associated with an image obtained from EM.

The electrons in the beam emitted by the source of a microscope interact with atoms in the sample in a number of ways, one of which is dislodging electrons, creating a hole in the atomic shell. The unstable configurations cause electrons from outer shells to fill the vacancy. As this occurs, energy is released specific to the transition that occurs. The wavelength of the energy emitted is recorded by the detector placed in the chamber and analysed to produce an atomic composition spectrum of the material under observation.

Method development

This section introduces the method development undertaken to obtain x-ray analyses and the principles used to analyse the data to produce results. The limitations of the techniques used are presented in the summary part of this section.

Image acquisition and conditions

EDX can use images obtained with the various detectors or modes described previously in Section 3.2.4. Environmental Scanning Electron Microscope. Each of these image acquisition methods has its benefits and drawbacks, which are mirrored in the use of these techniques, with some key differences and similarities. Image resolution was an important factor in the speed and detail of the analysis carried out. An image measuring 256x192 pixels contains around 50,000 pixels, whereas an image measuring 512x384 pixels contains 4 times more. Because the x-ray counts are assigned to each pixel image, the number of pixels directly influences the time needed for data acquisition. The quality of the image itself was irrelevant

for the purposes of the EDX, and the method can be used without visually observing the sample, but it was important to understand a spectral map of what was being analysed. However, the conditions set to obtain the image, the acceleration voltage and the spot size, had significant effects on the x-ray counts recorded. Obtaining images in WetSTEM mode presents various challenges such as sample drifting, reduced quality and maintaining the water phase (see Section 3.2.4. Environmental Scanning Electron Microscope). Significant effort was required to optimise the imaging conditions and offset those drawbacks.

Mapping and conditions

The association of x-ray counts per pixel of SEM image is a feature of 'spectral mapping' data acquisition. Other three modes were available: 'spectrum', 'point ID', and 'linescan', but obtaining a complete x-ray spectral image linked to the SEM image makes it possible to perform all other modes of analysis offline at a later date. An example of the spectrum obtained in post analysis from the spectral map is presented in Figure 3-15. Conducting spectral mapping was time-consuming and depended on the number of pixels in the image and the stored rate of counts per second (cps). These varied according to the microscopy parameters; the higher the accelerating voltage and spot size, the greater the cps; however, excessively high cps cause overloading of the detector. The resulting dead time has to be controlled by an operator and must be tailored to the type of analysis being carried out, but is generally between 20% and 60% [130].

Optimisation and troubleshooting

The recommended acceleration voltage should be 1.5 times the expected energy peaks of the elements of interest. For silver, those transitions occur between 2.984 and 3.519 keV for the L-line, and between 22.166 and 24.916 keV for the K-line [130]. However, the 5 kV (which was sufficient for the L-line), when coupled with spot size 5 to improve the storage rate, results in very poor image quality. The acceleration voltage was therefore set at 30 kV, but this, in

turn, resulted in the acquisition of far more background data and required manual selection of elements of interest during the analysis.

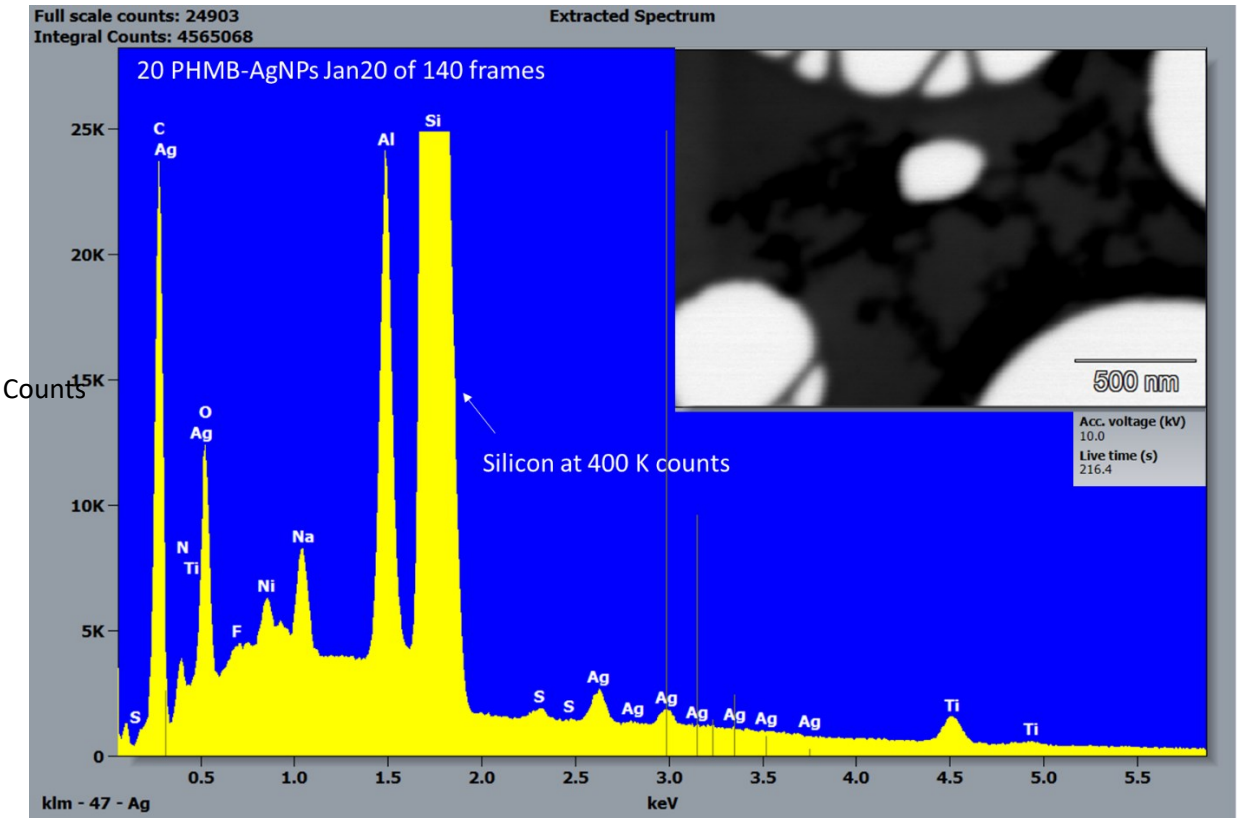

Figure 3-15 EDX spectrum obtained on the elemental analysis of 20µg/ml PHMB-AgNPs (Jan20) with autodetection of elements. The spectrum was recorded against the image in the insert at an acceleration voltage of 10 kV for 216 seconds. The spectrum is zoomed to about 6 kV to improve the resolution, no further peaks were detected in the range 6-10 kV.

The choice was made to rely on the L-line transitions for the silver because the K-lines required energy that was at the limit of the SEM settings producing insufficient K-line transitions for analysis. At the same time, the L-line transitions for other elements autoidentified in the spectrum were located in the very noisy low-keV part of the spectrum. The second highest atomic number after silver (46), was copper (29): the L-lines transition for this element can be found around 1 keV. A number of other elements were also located in the area, which together with the background Bremsstrahlung made peak decoupling very challenging. As a result, the K-lines, which are found at higher energy values, were more favourable.

When using WetSTEM, the major problem was sample drift. The software's capacity to compensate for drift was not always sufficient, forcing data collection stoppages. EDX analysis in WetSTEM may be improved by using the ESEM-Gaseous Analytical Detector (ESEM-GAD), which is fitted with cone-minimising beam skirting, hence reducing background data. Other strategies might include finding the spot size that provides the optimal balance between SEM image quality and storage rate (acquisition time).

Carrying out the spectral mapping in STEM-in-SEM was far more successful. The acceleration voltage of 30 kV achieved image quality that permitted individual particles to be distinguished. Using a spot size of 5 gives about 30 kcps and a dead time of 40%, which remains within the recommended limits of the equipment. Although these parameters result in significant background data being collected, the spectral image acquisition in 512x384 pixels took around 10 minutes before enough frames were collected to allow analysis.

Data analysis

The acquired image counts map was processed using Full Shift Kernel size to produce a quant map (size used: 3x3 or 5x5 or 7x7), which increased the quantity of data points at the cost of resolution. Instead of looking at individual pixels, the software considers squares of the pixels and moves along one pixel to carry out the same action, the effect it has on the number of counts can be observed in Figure 3-15 where the original 'Full scale count' increase by a factor of about 183 improving the resolution of peaks detected. Quant maps available are net count, atomic (Figure 3-16) or weight percent. Then a manual selection of elements was carried out, using Figure 3-16 as an example, according to the imaging parameters selected. Otherwise, autoidentification of the spectrum peaks can suggest the presence of elements that were not present in the sample, but were present in the chamber, or a misidentification of elements due to sum or escape peaks (for example, titanium or aluminium, which can be commonly found in various elements of the ESEM). Continuing with the analysis, there were immediate candidates to be discarded from the analysis, such as sodium, phosphorus, iron, titanium, and

nickel. The quant maps showed a wide and even spread for those elements over the entirety of the image, suggesting that they were erroneous suggestions produced by flooding the chamber with X-rays. Two further elements, carbon and silicon, show some features of the SEM image. The AgNPs were placed on the copper grid with holey carbon and it was therefore expected to see carbon in high intensity over the grid, with visible holes. The presence of the elemental carbon over the hole was a strong indication of the imperfections of this method, but a clear contrast was visible. The opposite was found with silicon: again the outline of the features found on the image was noted, but the increased intensity at the carbon hole suggests that the signal is coming from underneath the sample, perhaps from the STEM3+ detector itself or another part of the ESEM. Interestingly, where the large particles were found in the middle of the image, the intensity reduced further, as the thickening of the sample in that area meant that fewer electrons were able to penetrate the sample, producing a weaker signal from underneath. The remaining elements of copper, aluminium and sulphur remained to be resolved. Except for the latter, these elements may have been present as impurities or together as an alloy. This could have therefore been a piece of copper form the grid, aluminium from tweezers or a sum peak formed by multiple X-rays hitting the detector at the same time. Other possibilities were stray X-rays from other materials present in the chamber, or by fluorescent effect, where an x-ray emitted from one element has sufficient energy to interact with another atom to eject another electron from it. Resolving the remaining three elements would require a more detailed qualitative analysis of the sample. For this, further data acquisition would be needed under different conditions. For the purpose of this research, assumptions are made regarding the irregularities, they are acknowledged but unexpected results from EDX were treated as artefacts.

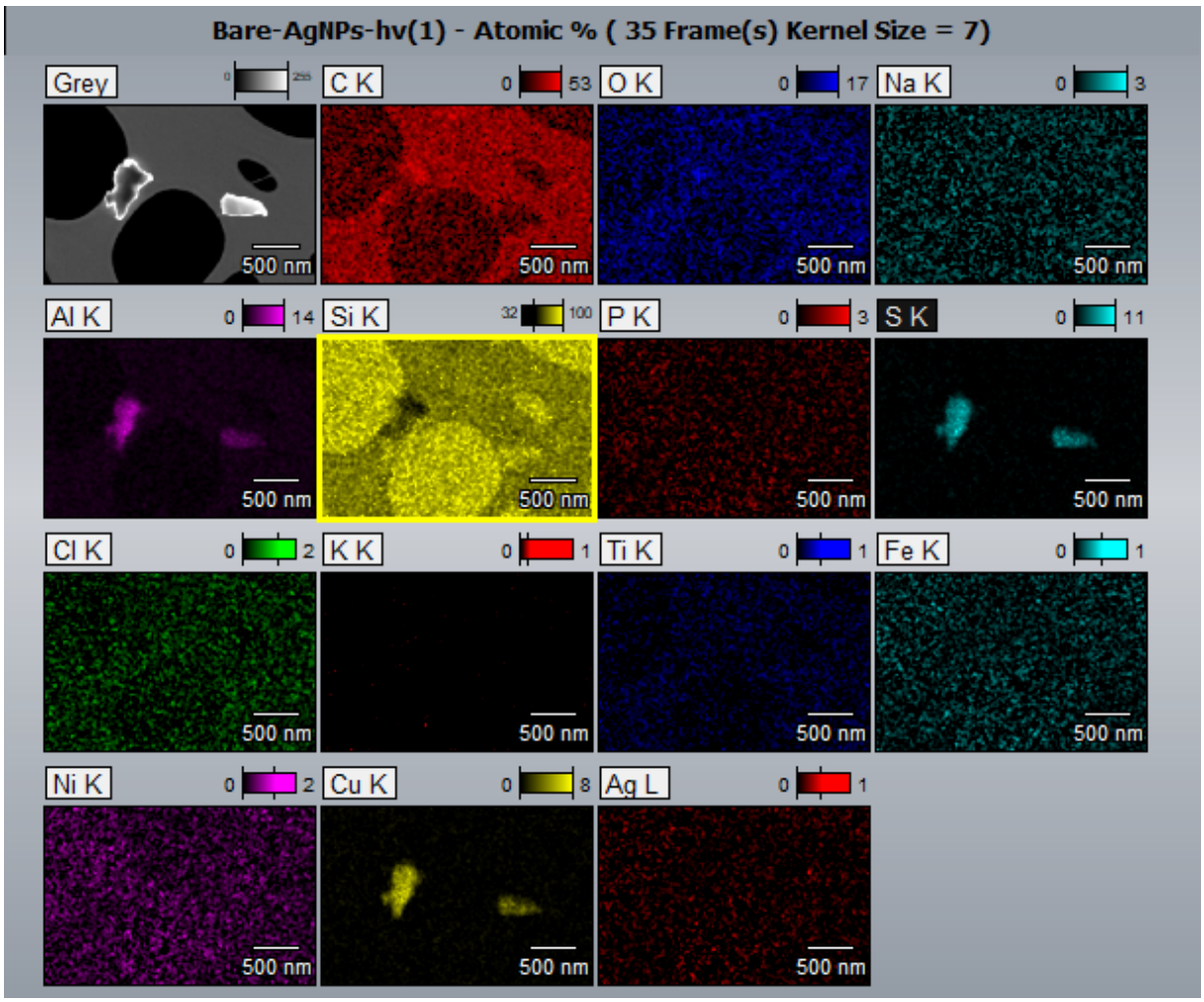

Figure 3-16 Full spectral imaging acquired for a feature found in the Bare-AgNPs sample during the imaging in STEM-in-SEM.

Summary

There were a number of limitations in using EDX, related to the conditions required for imaging the sample. Obtaining a sufficient number of counts was necessary for reliable readings, but this was time-consuming. The sample under observation was very thin and the acceleration voltage selected was high; most of the electrons travelled through it and interacted with other elements of the chamber. As a result, elements which were not expected to be found were marked as present, and manual selection then had to be carried out. The results obtained from EDX require significant analysis and manual element selection. To improve the accuracy and detection of the method, a time-consuming and labour-intensive process would be required. Consideration must be given to the level of detail desired, and if a commitment to improvement

provided the anticipated gains, one such would be the quantification of the elements present to arrive at the total mass of analysed volume.

3.2.6. Small-Angle X-ray Scattering

The transmission-mode SAXS used as a part of this research is an analytical method that detects scattering caused by interaction between the x-rays and the sample. The nature of this interaction is such that each particle in the path of the beam will give a characteristic signal based on the distribution of electrons. The scattering is presented as a scattering pattern which depends on the internal structure of the material under observation. Average particle structures can therefore be deduced from the pattern with assistance from complementary techniques such as microscopy. In the following sections, the challenges associated with data collection and analysis are discussed in detail. Developing models requires assumptions that have an effect on the final results. but defining the pathway of how modelling was performed is an important validation process to ensure the future reproducibility of results.

The use of SAXS with synchrotron radiation was granted on a proposal basis for automated sample loading using a mail-in system available on the beamline B21 at the Diamond Light Source facility in the UK. The available unallocated capacity of the research centre offered an opportunity to test the suitability of the samples for SAXS analysis. However, the automatic loading failed due to the formation of air bubbles made the sample incompatible. A further proposal was made on a rapid access basis so that manual loading could be carried out. The full description of the method and equipment settings can be found in Section 2.2 Characterisation – Small-Angle X-ray Scattering (SAXS).

A systematic approach was taken to analyse the experimental scattering patterns. The analytical method chosen was that of modelling, computing theoretical models to fit the patterns obtained. To avoid a scenario where a good fit to the pattern is achieved based on erroneous assumptions, information available from other techniques was collected and used to

ensure the quality of the models developed. The use of IgorPRO software with the Irena add-on macro to handle collected data permitted complex manipulations of the patterns and models developed. In the first instance, the background (deionised water) was subtracted from the patterns obtained with examples of the patterns in Figure 3-17.

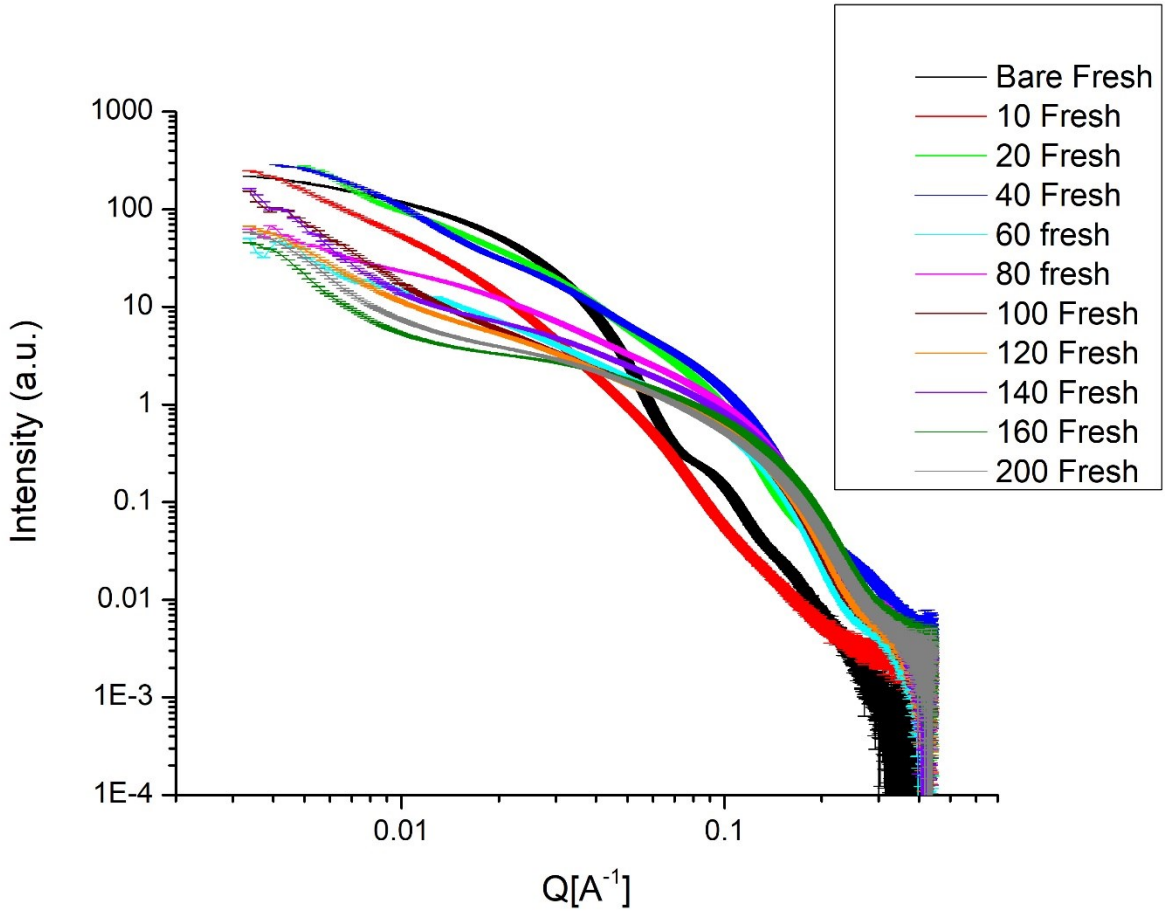

Figure 3-17 SAXS patterns obtained for a batch (Oct19) of PHMB-AgNPs. The number in the legend relates to the concentration of the polymer used during the synthesis process in µg/ml.

The second stage involved deciding which parameters were kept constant throughout the modelling and which were fitted to data (details can be found in Table 3-3). Decisions about them were made either based on knowledge and experience or by investigating the impact that they had on the data. Maintaining a uniform approach to parameters ensured that they were not selected in a way that might produce contradictory results.

Table 3-3 Table presenting parameters defined in the modelling software, indicating whether they were fitted to the data or kept fixed for all modelling attempts. R_g – radius of gyration

<table>
<tr><th colspan="2">Parameters fitted</th></tr>
<tr><td colspan="2">Mean size [A]; Standard deviation [A]; Scale; B (scale factor); P (pattern gradient); Background.</td></tr>
<tr><td colspan="2">Parameters kept constant</td></tr>
<tr><td></td><td>
<table>
<tr><th>Parameter</th><th>Value</th></tr>
<tr><td>Rg cut off</td><td>Bare-AgNPs – 169
20 µg/ml and 40 µg/ml PHMB-AgNPs – 50
Rest of the samples - 33</td></tr>
<tr><td>G</td><td>10 000</td></tr>
<tr><td>Rg [A]</td><td>10 000</td></tr>
<tr><td>Contrast</td><td>4643 x 10^{20}</td></tr>
</table>
</td></tr>
</table>

One of the key factors affecting the SAXS patterns is the shape of the particles. From the ESEM imaging Figure 3-10, it was concluded that they are spherical in shape. DLS data available has repeatedly shown a multimodal distribution of two or three populations of the particles Figure 3-6. Therefore, testing was performed to establish whether the two population models could be replicated to fit scattering patterns. This was not achieved due to the significant overlap between the populations: the mean size and standard deviations for each population were so close together that they significantly overlapped. This two-population approach was employed in an attempt to fit several SAXS patterns but with limited success. For some patterns, a good fit was achieved, while for others it was not possible to fit without producing contradictory results (i.e. structure factor smaller than the modelled particle diameter). An example of two population fits and the challenges associated are presented in Appendix 1c and 1d. In the spirit of maintaining a uniform approach, the method was then reassessed to focus on the mid-to-high q range and to achieve a one population fitting for this part of the pattern only. This was achieved for all of the PHMB-AgNPs samples. A summary table with results obtained from modelling is presented in Appendix 1 with a model for 40 µg/ml PHMB-AgNPs (Oct19) against the collected data in Figure 3-18 with the reminder of this batch presented in Appendix 1b. The intensity of scattering data in the low q for the PHMB-AgNPs samples is an indication of aggregation, which was modelled using a scale

factor B and the pattern gradient $-P$, where $I(q) \sim q^{-P}$, with limited trends being observed (Figure 3-19). Fitting also benefited from changing the aspect ratio of the particles. Once the suitable model had been developed and tested across various sample patterns, it was extended to all samples measured.

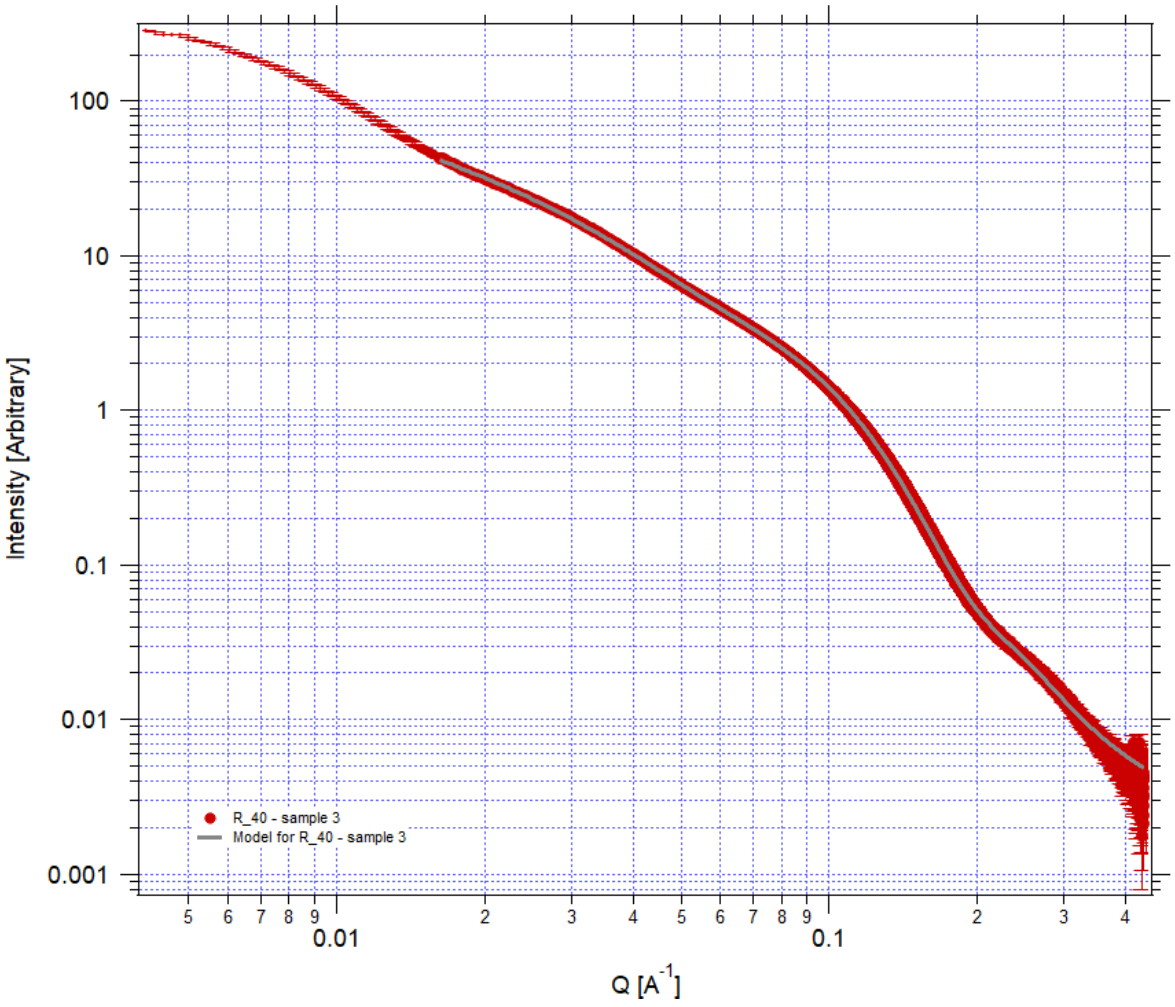

Figure 3-18 An example of a model fit (grey line) against the collected SAXS data for 40 µg/ml PHMB-AgNPs.

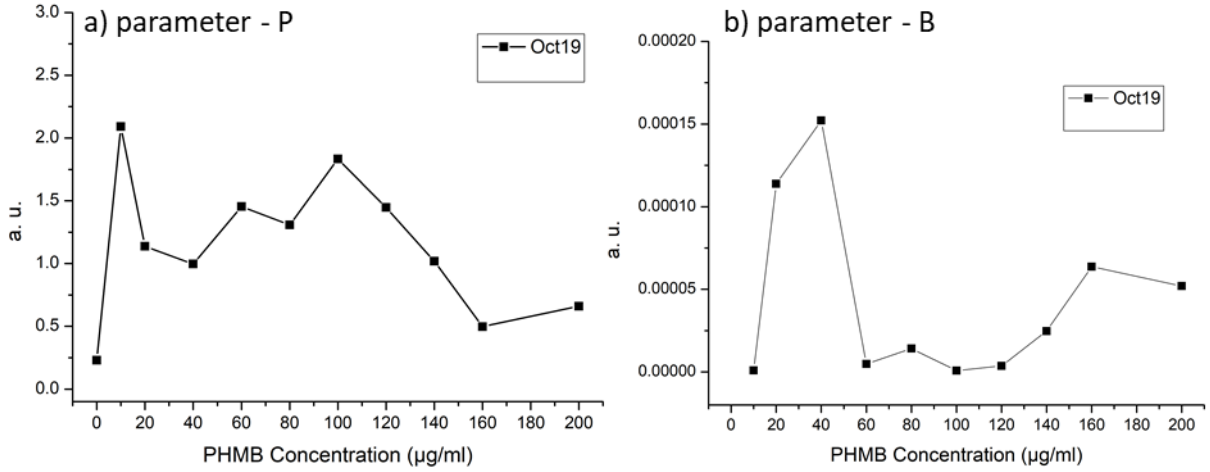

Figure 3-19 Results for the parameters a) *P* – pattern gradient, and b) *B* – scale factor obtained as a result of modelling for the samples of Oct19 showing a lack of noticeable trends.

The silver nanoparticles have a very high electron density compared to the PHMB, and as a result, the intensity of scattered x-rays is much greater from the AgNPs than it is from the polymer. SAXS experiments conducted on the 200 µg/ml PHMB solution showed very limited scattering (Figure 3-20). Other concentrations of the PHMB should be tested to confirm if the polymer in higher doses affects the SAXS pattern. Due to the centrifugation process, the solvent was removed, resulting in higher polymer concentrations in the sample. As silver has a high electron density compared to polymer, it was assumed that the scattering pattern was sensitive to the silver core only. This assumption may explain some imperfections in the model fitting.

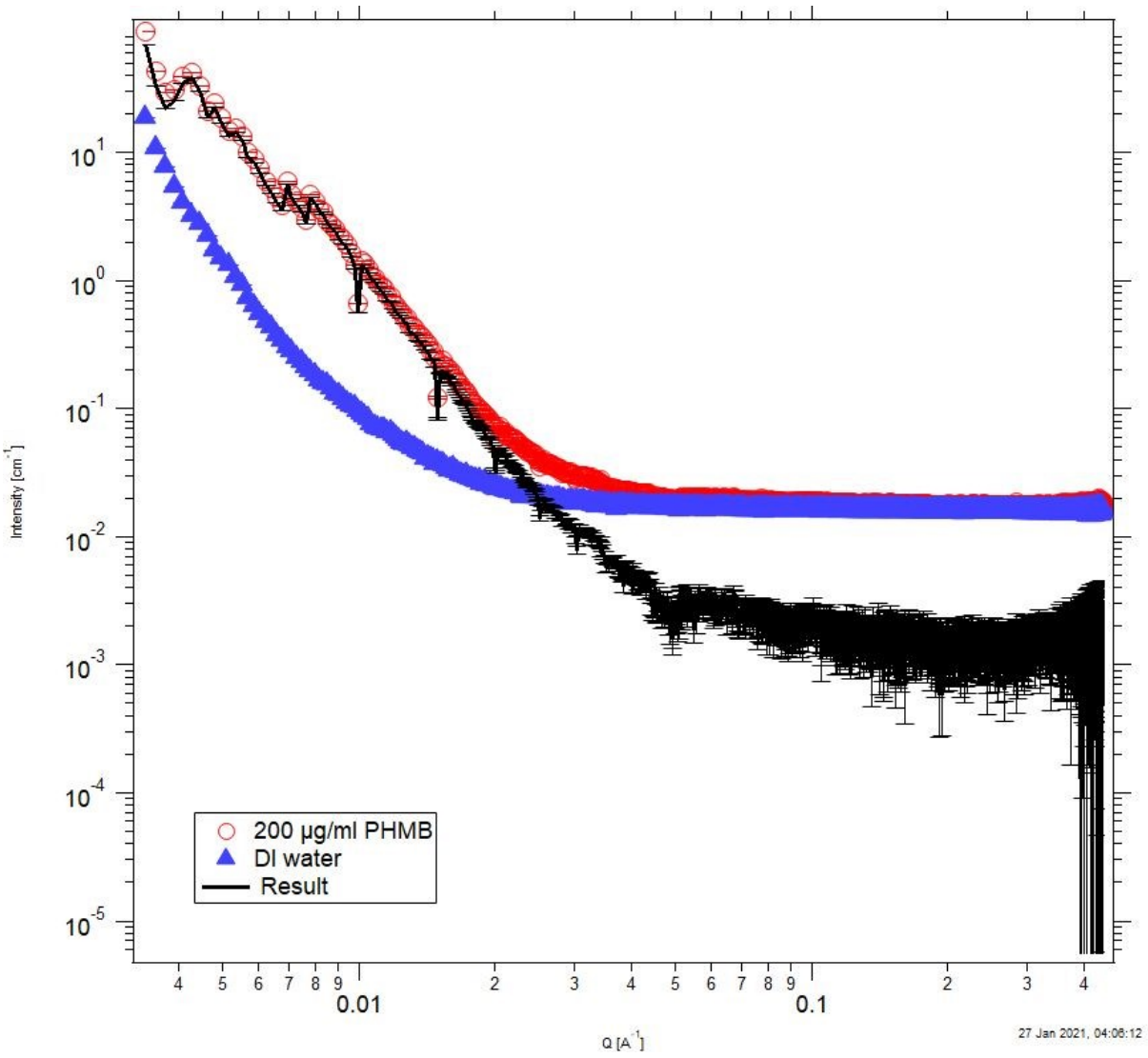

Figure 3-20 Scattering pattern for 200 µg/ml PHMB (red circle) in deionised water (blue triangle), the background subtracted data (black line).

SAXS as an analytical technique has provided important evidence in understanding the PHMB-AgNPs system, thanks to the ability to analyse undiluted liquid samples. Although fitting models to patterns is complex, the process was informed by available evidence from other complementary techniques available, such as microscopy and DLS, thus producing highly reliable results. It is important to note that all SAXS measurements were performed on the same day. Therefore, data obtained is limited to the particular samples at a particular time after the synthesis. Any SAXS data collected was not repeated and relied on one measurement only.

3.2.7. Discussion of characterisation results.

The characterisation techniques confirmed the formation of the PHMB-AgNPs complex with a significant change to zeta potential and a presence of characteristic to silver nanoparticles peak in the UV-Vis. However, there were some challenges in applying some of the methods. The results from DLS have decreasing quality because of the number fluctuations. This issue appears in concentrations above 60-80 µg/ml of PHMB used in synthesis. This coincides with results from size analysis of the particles visible on the SEM imagining. There is a clear reduction in size observed from the Bare-AgNPs but the gradient of the decrease levels at around 60 µg/ml. The increasing concentration of the polymer also negatively affects the ability to conduct imagining in WetSTEM mode. The B parameter of the SAXS patterns shows a sharp initial increase followed by a drop to close to 0 for 60 µg/ml indicating a possible instability around those concentrations. It is expected that the PHMB will act as a stabiliser to the AgNPs. Zeta potential confirms that complexation already occurs at 20 µg/ml, but the DLS results show a significant increase in hydrodynamic diameter of particle sizes on this initial addition of PHMB. If the stabiliser is not thick enough to shield the particle charge the EDL will be developed and detected by DLS. Alternatively, the PHMB might be only partially covering particle. As it was not possible to model using structure factor to measure distance between the particles it is possible that some kind of flocculation occurs which is interrupted once the concentration of polymer is increased from 20 to 40 µg/ml. A similar phenomenon, although it is likely to be of a different mechanism, can be observed for PHMB-AgNPs synthesised in high concentrations of polymer, which results in number fluctuations in DLS results.

3.2.8. Antimicrobial assessment

Introduction

Silver nanoparticles and the polymer used to stabilise them are both known antimicrobial agents, and complexing them together affects their behaviour. It is therefore

important to assess the antimicrobial potency of the PHMB-AgNPs in relation to each agent to establish if any synergistic effects can be noted. In any case, understanding how physical properties impact the efficiency of the complex would aid in explaining changes caused by the interaction between polymer and silver nanoparticles.

Testing of the samples was conducted with the use of two different methodologies: zone of inhibition and flow cytometry. Each of these techniques required the development of methodology and data analysis, and each had limitations and advantages.

Zone of Inhibition

Zone of Inhibition (ZOI) was used as an initial technique for its simplicity of use and efficient data analysis. Each plate had reference measurements taken with deionised water, 1 mM $AgNO_3$ and 200 µg/ml PHMB. The results showed very limited antimicrobial properties of the Bare-AgNPs (the well marked 8 in Figure 3-21) and significant improvements in antimicrobial activity for the PHMB-AgNPs (wells marked 9-11 in Figure 3-21). These results encouraged further research into the complex and the experiment was repeated. In addition, the infranatant was assessed for antimicrobial properties: some antimicrobial activity was noted for the infranatant obtained during centrifugation of AgNPs obtained in higher concentrations of PHMB.

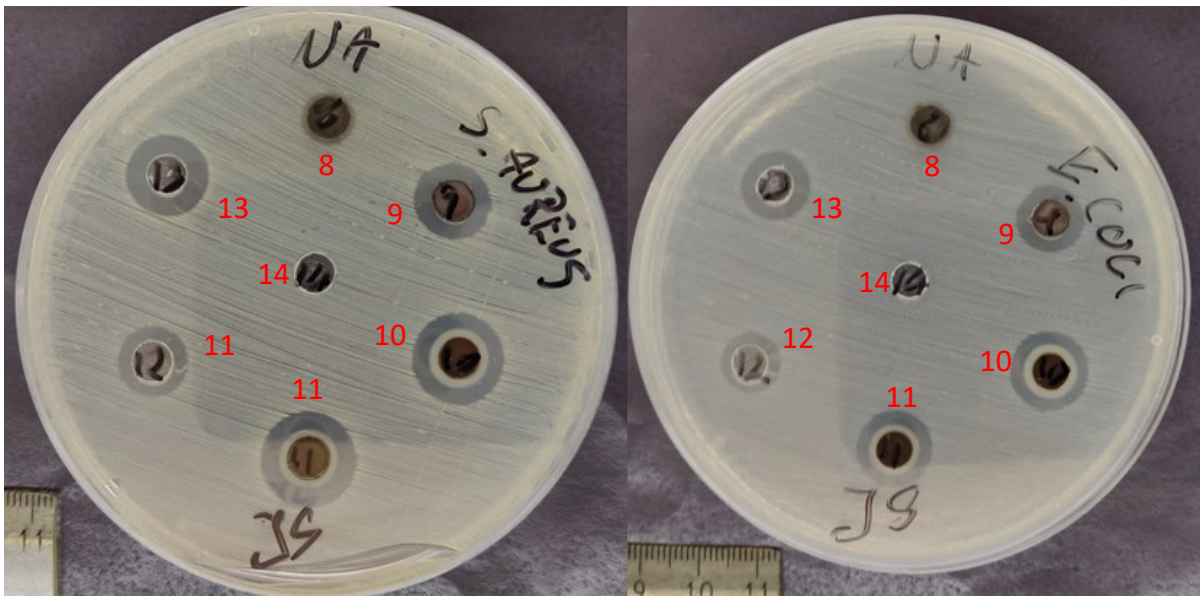

Figure 3-21 The zone of inhibition recorded against *S. Aureus* and *E. Coli* using various samples of PHMB-AgNPs (wells 9-11), deionised water (well 14); 200 µg/ml PHMB (well 12) and 1 mM $AgNO_3$ (well 13).

There are some important limitations to this technique in the form applied during this study. Firstly, a lack of standards on bacteria health and culture count during the study. The growth of bacteria during the incubation period is uncontrolled and therefore the concentration of the cultures could have been assessed before the measurements were taken. Secondly, the technique only produces an absolute result and does not provide any insight into the mode of action of the antimicrobial activity of the agent. Thirdly, the method uses an aliquot of 40 µl of concentrated AgNPs. Finally, while the bacteria are spread on top of the agar gel only, no assessment was carried out to understand how PHMB-AgNPs or their individual components diffuse through this medium. There is evidence in publications [150, 151] of this diffusion. Improvements can therefore be made to reduce these limitations in the future. In any event, the results have shown promising improvements in antimicrobial activity.

Flow Cytometer

Flow cytometry was chosen as a secondary technique to eliminate some of the limitations of the Zone of Inhibition. The two dyes selected for the experiments were bis-(1,3-dibutylbarbituric acid) trimethine (BOX) and propidium iodide (PI) have different modes of

action and therefore provide the possibility to determine if the bacteria are damaged (BOX) or dead (PI) following incubation with the silver nanoparticles.

At the start of the experiment, a series of bacteria counts are carried out. Aliquots (between 10 and 40 µl) of healthy bacteria are dispersed in PBS, and a measurement is taken to establish the volume required to produce a bacteria count within selected limits (1000 and 4000 events per second). A positive control is carried out by centrifuging 1 ml for 30 seconds at 17000 rpm. The retentate is collected with a pipette and replaced with 70% ethanol, which is effective in killing the microbes, and the bacteria is resuspended using a shaker. Measurement is taken before (Figure 3-22a) and after (Figure 3-22b) the addition of the 10 µl of PI and 5 µl of BOX. Negative controls are carried out by measuring a bacteria sample before (Figure 3-22c) and after (Figure 3-22d) adding dyes. Control groups are generated for bacteria for a number of purposes: to ensure that dye concentration is suitable for the experiments; to determine the health of the bacteria population before analysis using antimicrobial agents; and to determine the location of the quadrants for the analysis of the antimicrobial activity of the agent.

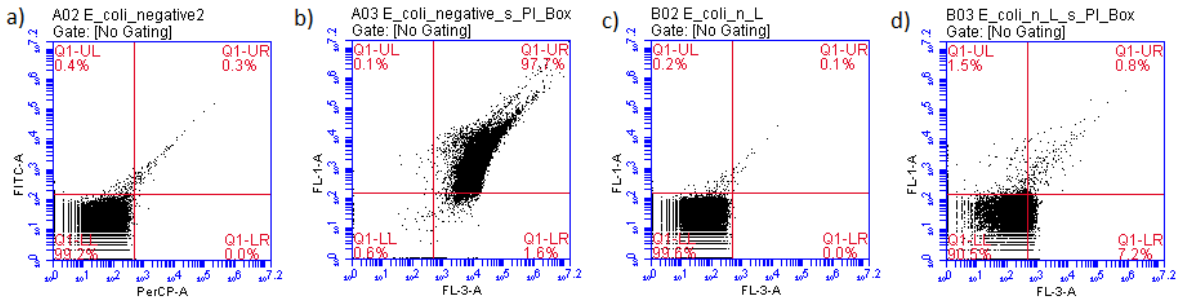

Figure 3-22 The series of control measurements carried out at the start of each experiment using a flow cytometer to assess the bacteria health and dye efficiency. a) bacteria resuspended in 70% ethanol, b) bacteria resuspended in 70% ethanol following incubation with PI and BOX dyes, c) healthy bacteria, d) healthy bacteria following incubation with PI and BOX dyes.

To determine the time of incubation with the agent and the concentration required for measurements, design of experiment was developed for Bare-AgNPs and PHMB-AgNPs

(concentrations: 20, 80, 140 and 200 µg/ml). The limits of the experiment were set between 2 and 10 µl for the sample volumes and between 12 and 60 minutes for incubation time. The analysis showed that the model is significant, however, amending the results to exclude the Bare-AgNPs changes this to not significant. The reason for the change was that there was a significant improvement in antimicrobial activity between Bare-AgNPs and PHMB-AgNPs, but there was no statistical significance between sample volume and incubation time of the different concentrations of PHMB in PHMB-AgNPs used within the selected limits (table with results can be found in Appendix 3). As a result, the volume of samples was set at 2 µl and the incubation time at 10 minutes plus additional 2 minutes following dye addition to allow for development.

Due to the SPR peak observable in the UV-Vis and the operational application of the flow cytometer, which uses a laser for bacterial analysis, it was expected that the AgNPs would be recorded using this method. For this purpose, additional controls were carried out for AgNPs only, and also in the presence of the dyes to ensure that the AgNPs could be removed from the final bacteria count (Figure 3-23a-h). AgNPs appear in the plot with partial overlap over the bacteria; they interact with the dyes and are visible in the damaged and dead quadrants. To prevent adverse effects on the results, gating has been used, whereby the signature of particles was marked in the measurements of AgNPs +PI + BOX and then removed from the bacteria-containing measurements. This approach produced more reliable results; however, exclusion can be very high in relation to the total number of events analysed and varied from 18% up to 95% of a total count, in some cases reducing the total number of events analysed to around 300 from 25000.

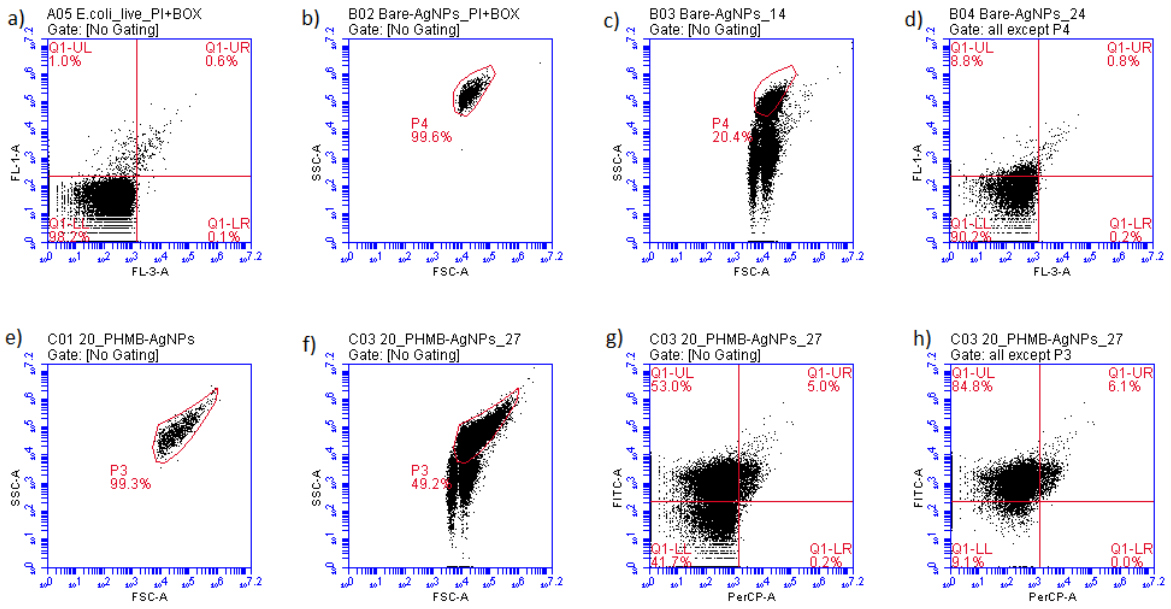

Figure 3-23 Result obtained from the flow cytometer had to be adjusted ('gated') from the AgNPs that would interfere with bacteria measurements, a) healthy bacteria with the PI and BOX dyes were used to establish the quadrants, b) 1000 events were recorded for Bare-AgNPs with PI and BOX dyes; an area to encompass the majority was drawn, d) Bacteria with Bare-AgNPs, PI and BOX was analysed; the marked area was the same as in b; d) results showing the distribution of Q1 – Live, Q2 – Damaged, Q3 – Dead is obtained with results marked within the area excluded. The 20 µg/ml PHMB-AgNPs are also presented in e) and f), g) showing results without gating and h) results with the exclusion of the area marked P3 on f).

In addition to the AgNPs that were assessed for antimicrobial efficiency, the infranatant, collected following centrifugation, was also analysed using both methods. Data collected from the flow cytometer did not require gating, as it was found that there is no interaction between the infranatant and the dyes. As a result, the data collected relies on 25,000 events that were envisaged as a part of the experiments. These measurements were repeated three times for each sample.

The FC method provides a relative result. Determination of the quadrants is carried out by eye, and to minimise error, a number of repeats are required. In addition, the method was only applied to the *E. Coli* bacteria, as attempts to replicate the same method with *S. Aureus* cultures failed (Figure 3-24). The choice of dyes and concentration would require further work.

It was not possible to generate negative control groups for these bacteria: heat may be required instead of 70% ethanol.

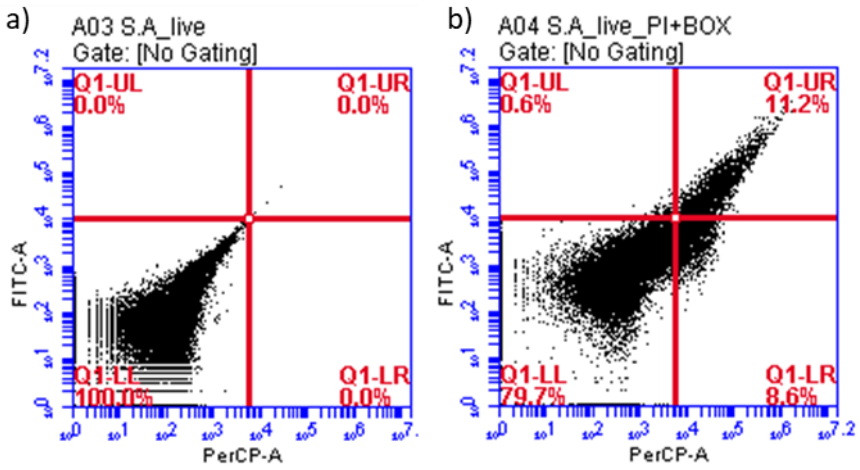

Figure 3-24 The results from the flow cytometer for *Staphylococcus Aureus* a) live cultures and b) live cultures with PI and BOX dyes. To carry out the analysis the live bacteria has to be benchmarked in the Q1 which was not possible to achieve.

Combining the results from the two techniques provided an opportunity to reduce the limitations of the antimicrobial assessment carried out and allowed for a better understanding of the antimicrobial activity of the complex and that of the infranatant. Finally, it is important to recognise that ZOI assesses inhibition of the bacteria in the presence of the agent, which prevents it from colonising an area, whereas with the FC, the ability to damage/kill already grown bacteria is being assessed.

3.3. Conclusions

The methods used in this study were chosen on the basis of the information they can provide to further the understanding of the system under investigation, their availability and the opportunity for analysis. However, in the process of acquiring the experimental data number of issues were noticed requiring optimisation of the protocols and adjustments in the data analysis. These details are often omitted in the research papers yet can have a significant impact on the reproducibility of the data between different research centres. The key issue noted was in relation to the Dynamic Light Scattering, it is important to interrogate the results

in fine detail. To inspect the correlograms to assess the quality of the data to ensure that the size distributions generated can be relied upon. Other techniques described in this chapter also have their limitations with artefact formation and limited sample representability (SEM), complex modelling (SAXS), low resolution (UV-Vis), and strict biological protocols required for assessment of the antimicrobial efficacy. However, each of those methods brings in a fragment of information and, while awareness of the limitations guides the process, they can be pieced together to give an understanding of the behaviour of the PHMB-AgNPs. The physical properties, behaviour and performance that can be explored using those techniques are presented in Table 3-4 below.

Table 3-4 Summary of the characterisation techniques used as part of this research project.

	UV-Vis	DLS	ZP	ESEM	EDX	SAXS	AM
Size	✓	✓		✓		✓	
Shape	✓			✓		✓	
Polydispersity		✓		✓		✓	
Material analysis					✓		
Aggregation		✓	✓				
Antimicrobial efficacy							✓

Chapter 4. Poly(hexamethylene biguanide) stabilised silver nanoparticles: novel antimicrobial agent.

4.1. Introduction

In this chapter, the different methodologies used to characterise silver nanoparticles are brought together and presented as an informative discussion of the PHMB-AgNPs system. In the previous chapter (Chapter 3), the focus was placed on the development of the methodology and how the data from different characterisations available were analysed to arrive at reliable, reproducible results. In the following sections, those results are compiled to define the information gathered and to determine the overlap between characterisations linking the variables together. Drawing attention to the irregularities found in the results serves as a reminder of the limitations of the methodologies from which they were derived. Then, the two sections are used to form a discussion of how PHMB and AgNPs interact to produce PHMB-AgNPs and how those particles interact with each other and the complex's characteristics.

4.2. Reproducibility of results

The results presented below are derived using the methodology described in Chapter 2 and Chapter 3 above. The results from each individual characterisation are brought together and discussed for reproducibility over different batches synthesised with analysis over discrepancies. In addition, unexpected and irregular results have been separated for discussion on their origin and the impact the irregularities have on the data analysis.

4.2.1. Results

UV-Vis

The simplest and most available method of characterisation was UV-Vis spectroscopy. The results obtained using this methodology have been reduced to three trackable variables: lambda maximum - λ_{max}, Full Width Half Maximum -(FWHM) and maximum absorbance. This offered a direct comparison between samples obtained during different synthesis batches and provided a helpful indication of whether any changes were taking place when synthetic variables were introduced, such as ageing of the reducing agent ($NaBH_4$) – (Chapter 5 –

'Formation of PHMB-AgNPs – interaction between silver nanoparticles and poly(hexamethylene biguanide)').

There was a clear shift in the Surface Plasmon Resonance (SPR) of the peak recorded when the polymer was added to the synthesis. Typically, SPR observed for Bare-AgNPs was around 390 nm; upon addition of the PHMB to the reaction process, a steep initial impact was observed and λ_{max} increased to around 420 for 60 μg/ml PHMB-AgNPs. Then a much weaker upward trend was recorded associated with the increasing concentration of PHMB used in the synthesis (Figure 4-1c). The shift in the peak is typically associated with the formation of a complex between the silver nanoparticle and stabiliser [152].

The maximum absorbance recorded was initially seen as random. However, once the average number of runs is created, some trends can be noted (Figure 4-1b). In concentrations up to 80 μg/ml PHMB, the maximum absorbance has some degree of variation, making it difficult to determine a particular trend. However, from that concentration onward there was a noticeable trend of reduction in the absorbance recorded. Considering the Beer-Lambert law, the incident light and path length remain constant for all measurements. This indicates that either the concentration of the particles was reduced or the molar extinction coefficient changed with increasing concentration of PHMB. The SPR peak is a function of size and shape: if the introduction of PHMB causes a change in the size of the particle then the concentration will also change, as the amount of silver in the reaction was constant. The particles may have reduced/increased in size to the extent that they no longer exhibit SPR. Other available methodologies will make it possible to verify if the change in size and therefore particle concentration was a cause of the drop in maximum absorbance unless the increasing concentration of the PHMB in the medium affects absorbance [153].

The FWHM recorded, as with lambda max, shows good reproducibility between different synthesis batches. However, some variances can be noted in the low concentration of

the PHMB (Figure 4-1a). Bare-AgNPs and 20 µg/ml PHMB-AgNPs have shown greater variability in those results.

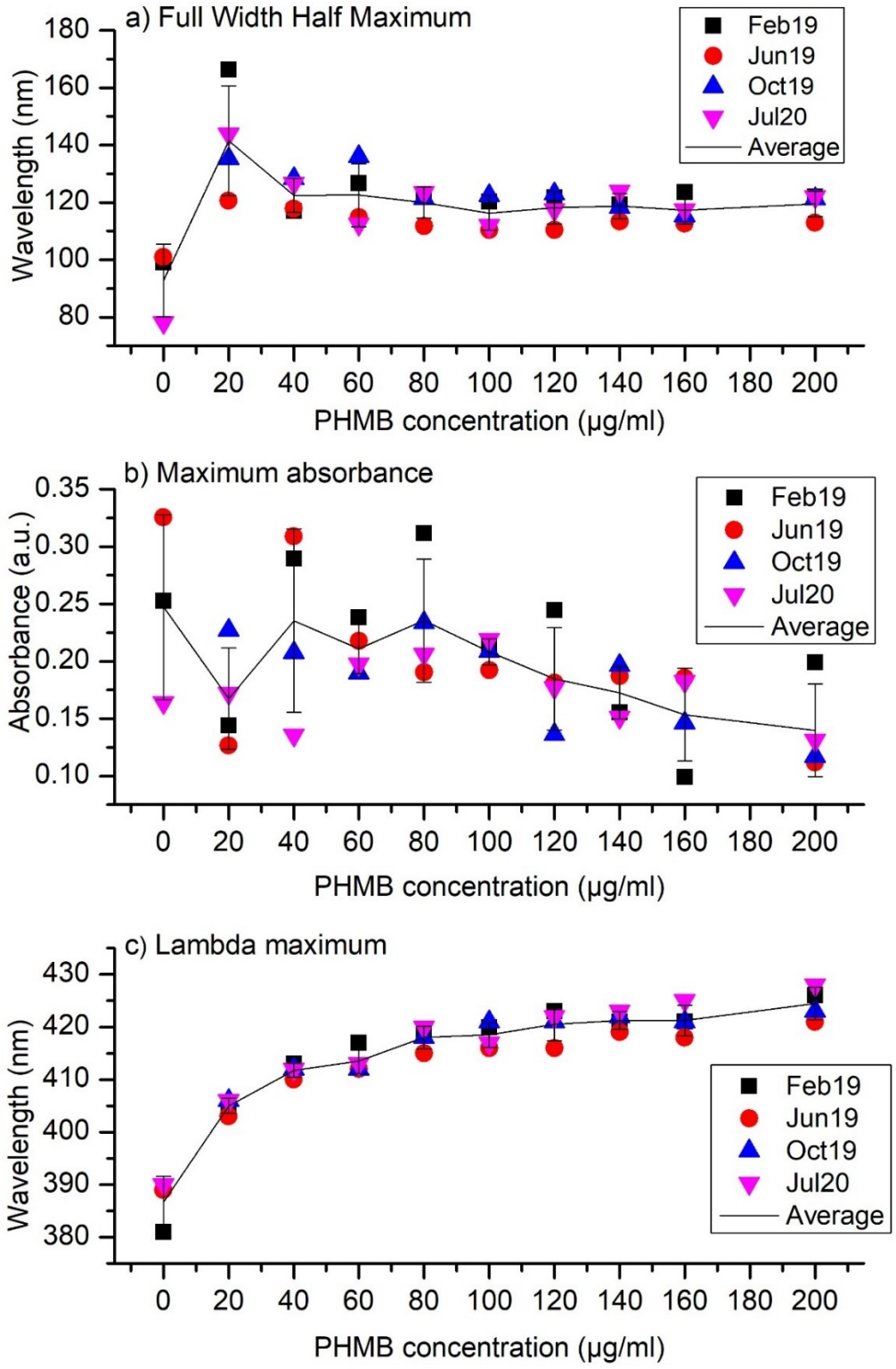

Figure 4-1 UV-Vis results for various concentration of PHMB-AgNPs; peaks recorded were simplified to a) Full Width Half Maximum, b) Maximum absorbance, c) Lambda maximum. Bare-AgNPs are marked as 0 concentration on the X-axis.

Results obtained using the UV-Vis provide confidence that the synthesis process has achieved good reproducibility. The addition of the PHMB to the reaction has a clear impact on the formation of the AgNPs. The initial change in the UV-Vis was significant and continues with increasing concentrations of PHMB; however, the pace of impact levels out, with only minimal trends noticeable for higher polymer concentrations.

Dynamic Light Scattering (DLS)

The DLS which was widely employed during this research was shown to produce unreliable results once the concentration of PHMB used during synthesis was increased. Data obtained for a sample of Bare-AgNPs and 20 µg/ml PHMB-AgNPs always met quality standards described in Chapter 3 (3.2.3 3.2.3Dynamic light scattering (DLS) and zeta potential), and some results for 40, 60 and 80 µg/ml PHMB-AgNPs were suitable for analysis.

The analysis of the data meeting quality criteria standards was conducted for a number of parameters: z-average, intensity distribution and volume distribution. The multimodal style of the results and the high polydispersity index (ranging from 0.19 to 0.93 – details in Table 3-2) make the analysis challenging, but it was apparent that Bare-AgNPs generate more broadly distributed particles, as both the width of the peaks and the reproducibility between the synthesis showed greater variation. Without the presence of an additional stabiliser, control over the synthesis was reduced to produce more divergence between different samples and measurements (Figure 4-2a). The introduction of 20 µg/ml PHMB as a stabiliser produced a very positive effect on the reproducibility between different batches (Figure 4-2b). There was a noticeable increase in the hydrodynamic diameter of the particle of both peaks and the z-average (Figure 4-2d). This trend is reversed with a further increase of the polymer presence, the results stabilise to give a z-average at around 50 nm but the contribution from the two peaks in terms of intensity and volume distribution fluctuates (Figure 4-2c). In addition, the

reproducibility of results is also reduced due to the falling quality of the measurements taken and the increase in the number fluctuations in the sample.

The greatly increased size of the 20 µg/ml PHMB-AgNPs compared to other AgNPs obtained in this study could be caused by either – flocculation of the particles to form larger particles – bridging or patch flocculation; or due to charge neutralisation of the counterions in the shear plane. In the former the polymer acts as a bridge between different particles, spanning and bringing them to proximity creating agglomerates – weakly bound particles; or if the polymer was unable to fully shield the particle, parts of the particle may have been exposed, leading to patch flocculation. Alternatively, if the polymer forms a steric protection between the particles to prevent aggregation – fused particles – but the charge of the nanoparticles is not fully shielded and extends beyond this protective layer, forcing counterions into the shear plane. This causes the DLS to detect larger particles than they may be in reality.

The DLS results were important in two areas during the quality analysis. First, it was discovered that increasing the concentration of the PHMB causes deterioration of the data quality, suggesting an interaction between particles making data unreliable. Second, when size analysis was carried out on the sample meeting quality criteria, it showed that the size of nanoparticles increased upon the addition of stabiliser. The size of samples of 20 µg/ml PHMB-AgNPs increases more than the others.

a) Bare-AgNPs

	Size (d. nm)	Width (nm)	Intensity (%)	Volume (%)
Peak 1	98.38	142.70	78.10	0.00
Peak 2	3.04	1.90	18.80	100.00
Peak 3	1324.00	3224.00	0.00	0.00

b) 20 µg/ml PHMB- AgNPs

	Size (d. nm)	Width (nm	Intensity (%)	Volume (%)
Peak 1	125.70	74.19	86.70	1.10
Peak 2	18.33	5.74	12.20	97.20
Peak 3	863.30	4636.00	1.10	1.70

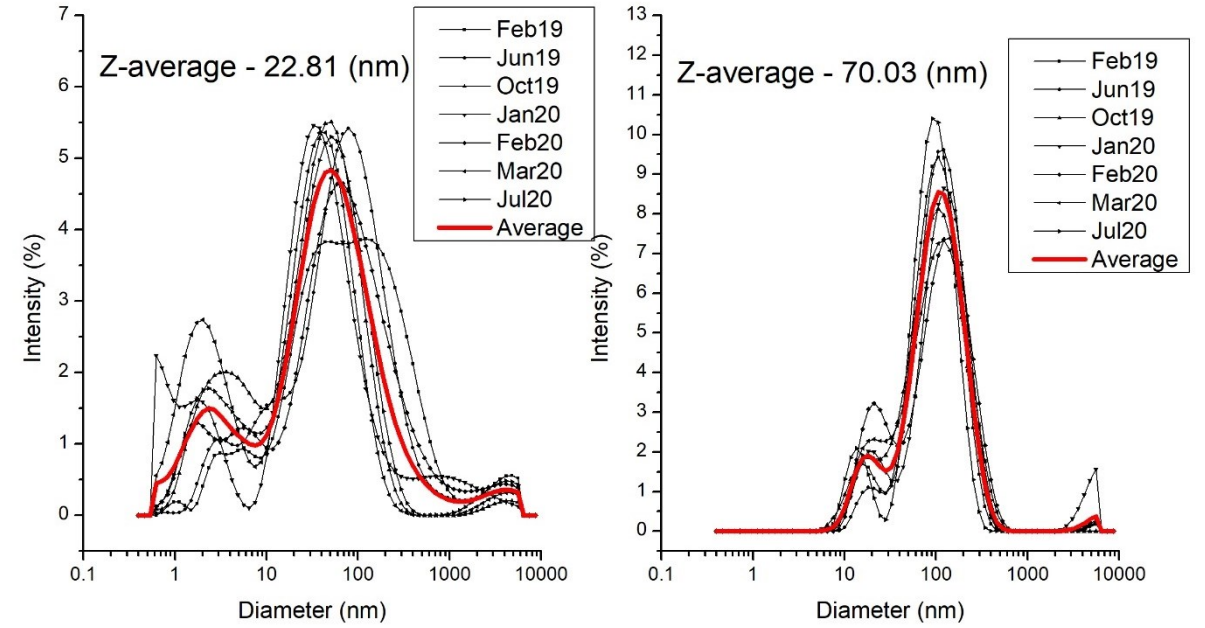

c) 40 µg/ml PHMB- AgNPs

	Size (d. nm	Width (nm	Intensity (%)	Volume (%)
Peak 1	98.52	73.33	88.00	0.10
Peak 2	6.55	2.95	10.50	99.50
Peak 3	970.00	4393.00	1.50	0.40

d) Z-average and peaks

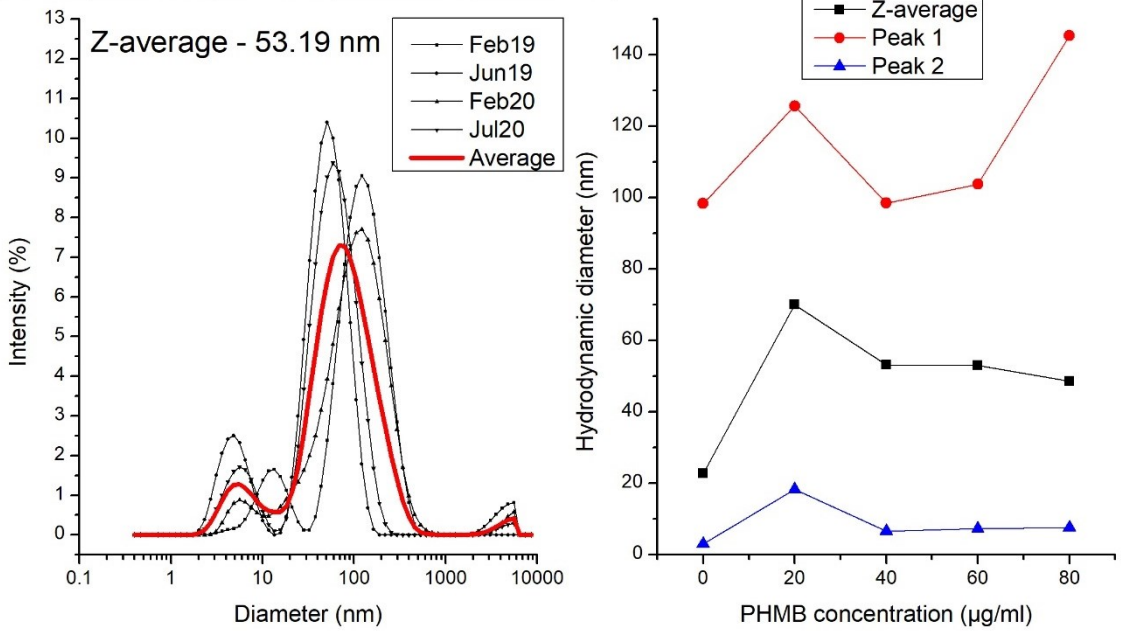

Figure 4-2 Intensity distribution of particle hydrodynamic diameter obtained from DLS for a) Bare-AgNPs, b) 20 µg/ml PHMB-AgNPs, c) 40 µg/ml PHMB-AgNPs, d) tracking for 2 major peaks displayed by the AgNPs and Z-average. The table inserted above the graph contains a modal report, i.e. transformation of the intensity to volume distribution.

Zeta potential

The results from zeta potential showed good reproducibility across the different samples synthesised, showing figures above/below the ±30 mV indicating good colloidal stability (Figure 4-3). The change in the sign of the zeta potential noted from Bare-AgNPs to PHMB-AgNPs results from the fact that upon the addition of the PHMB, a polycationic polymer, the direction of travel of the sample was reversed. This was an important indication that the AgNPs preferred behaviour in the electrical field was completely masked by the presence of the polymer, suggesting a strong interaction between the two agents.

They also indicated that the zeta potential was almost unaffected by the increasing concentration of the polymer; the shear plane at which the measurement was taken remains broadly the same for all the samples present (with a minor upward trend). This was a sign that the AgNPs were not influenced by other materials than the PHMB.

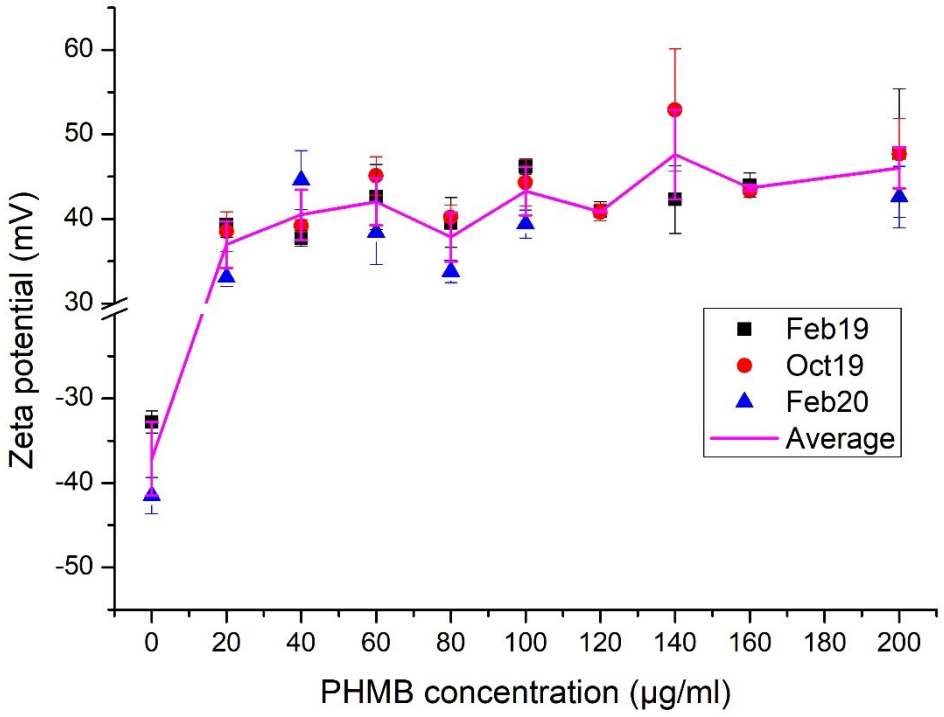

Figure 4-3 Zeta potential results obtained for silver nanoparticles showing a strong interaction between the PHMB and AgNPs. The line on the graph represents average results and has been added for the benefit of clarity; it did not signify the presence of the isoelectric point. pH measured in DI water of pH 7 ± 0.1

Zeta potential was also measured against changing pH in the range between 4 and 10 (Figure 4-4).

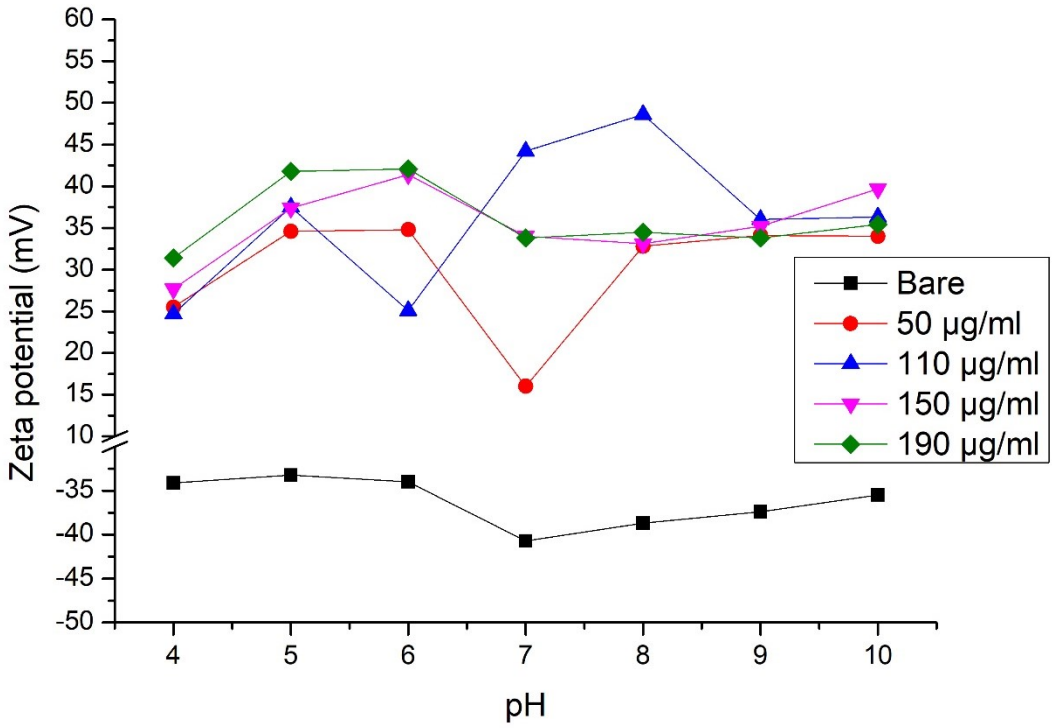

Figure 4-4 Zeta potential results obtained for AgNPs obtained in varying pH.

The results show good stability over the measured range, and the isoelectric point has not been found. PHMB has two pK_a points around 2 and around 13; it would be interesting to extend the measurements to establish if the isoelectric can be found at one of those points, in the lower value in particular, where the PHMB would be expected to be fully protonated and might no longer be complexed with AgNPs, and the silver nanoparticles might coagulate or be measured with negative zeta potential akin to Bare-AgNPs.

ESEM

Imaging using a scanning electron microscope (SEM) allowed for direct observation of the morphology of the particles synthesised. Moreover, the use of the WetSTEM method allowed the observations to be carried out with minimal sample preparation and in the aqueous environment, thus reducing the possibility of artefact formation.

Bare-AgNPs (Figure 4-5a) synthesised were present as singular spherical nanoparticles. They were observed forming agglomerates and aggregates, but individual particles were visible. For some, it was possible to note longer particles with fluctuating density (Figure 4-5b), indicating the formation of aggregates by the coalescing of individual particles. This may have occurred as a result of the increasing concentration of the Bare-AgNPs due to the removal of water to permit imaging, which would make it an artefact of sample treatment. It has been noted that the stability over time of Bare-AgNPs was much lower than that of PHMB-AgNPs. There was a strong tendency for Bare-AgNPs to precipitate from the solution as particles. The changes observed may indicate a degradation of the sample over time.

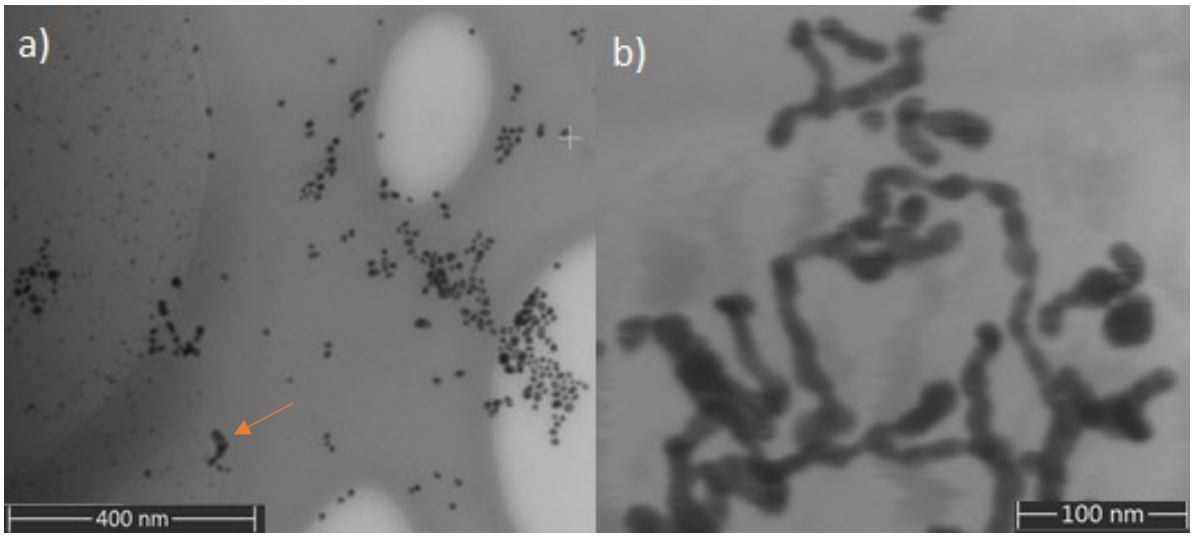

Figure 4-5 WetSTEM images obtained for Bare-AgNPs showing two noticeable populations of a) spherical and b) connected beads. A similar coagulated particle as presented in image b) can also be observed in image a) (marked with an arrow).

However, samples of Bare-AgNPs when imaged under the conditions described tend to form undefined networks of connected particles (Figure 4-6a). PHMB-AgNPs formed in lower concentrations of stabiliser tend to display similar structures, but the presence of individual AgNPs becomes more difficult to observe (Figure 4-6b). There was also a general operational difficulty in imaging particles formed in increased concentration of the PHMB, with the clarity of the particle boundary and sharpness of the image reduced.

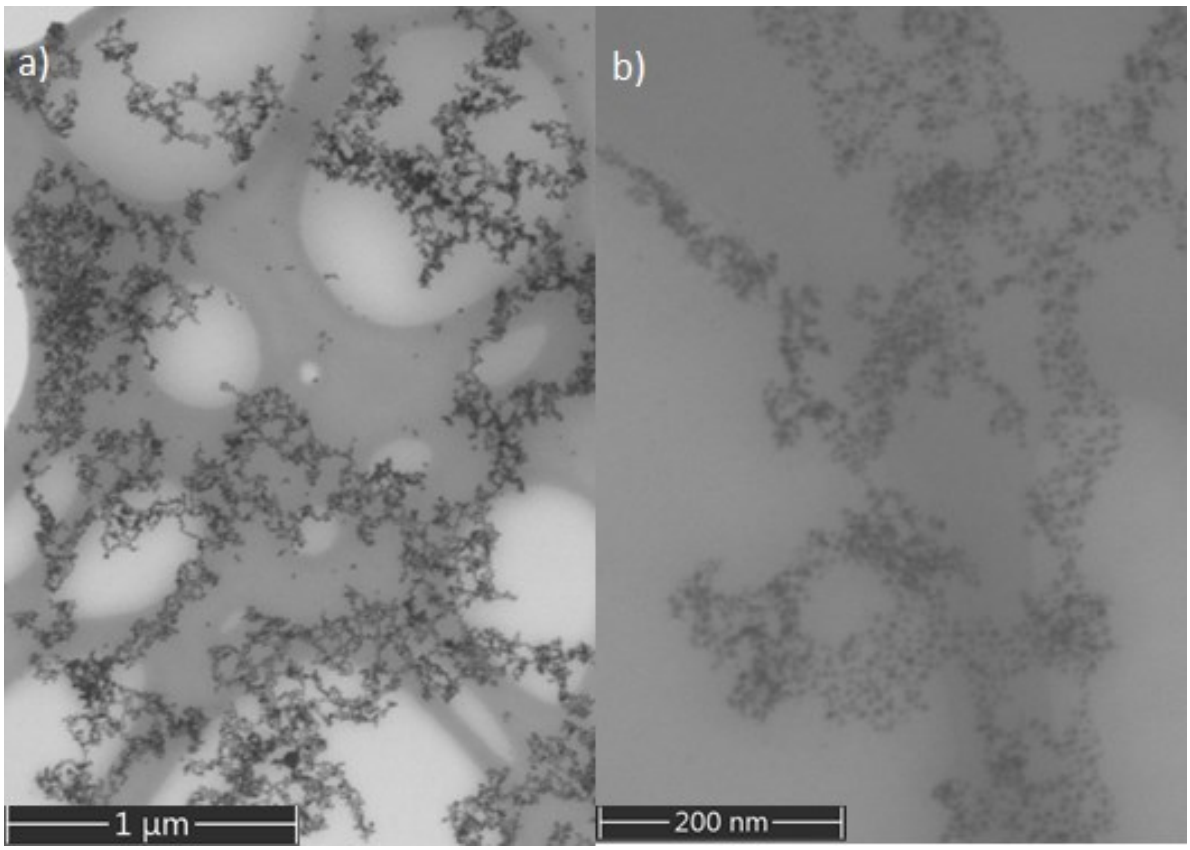

Figure 4-6 WetSTEM image a) Bare-AgNPs and b) 20 µg/ml PHMB-AgNPs and the undefined networks formed by the AgNPs without the presence of the PHMB and in low concentration of the polymer. There was a gradual decrease in the quality of imaging associated with increasing the stabiliser concentration.

The increased presence of polymer changes the formation of these structures, which appear much more interconnected, with larger clusters of high-density particles formed instead of networks. Using the example of 80 µg/ml PHMB-AgNPs (Figure 4-7a), small particle clusters were observed in addition to large, densely packed clusters of AgNPs. Further increase to 140 µg/ml PHMB-AgNPs makes those clusters thicker and harder to penetrate (Figure 4-7b). Different detection modes available in the STEM3+ detector improved analytical possibility and showed that the thickness of the layer present on the grid varies between different areas of the image. In addition, the silver particles were present in a higher concentration in those areas, suggesting that it was an amorphous polymer mass with particles present within it. Clusters of various sizes become dominant in the PHMB-AgNPs formed in the high concentrations of PHMB (Figure 4-8a-d). In addition, the uneven thickness of the layer becomes more evident and covers larger areas of the grid (Figure 4-8d).

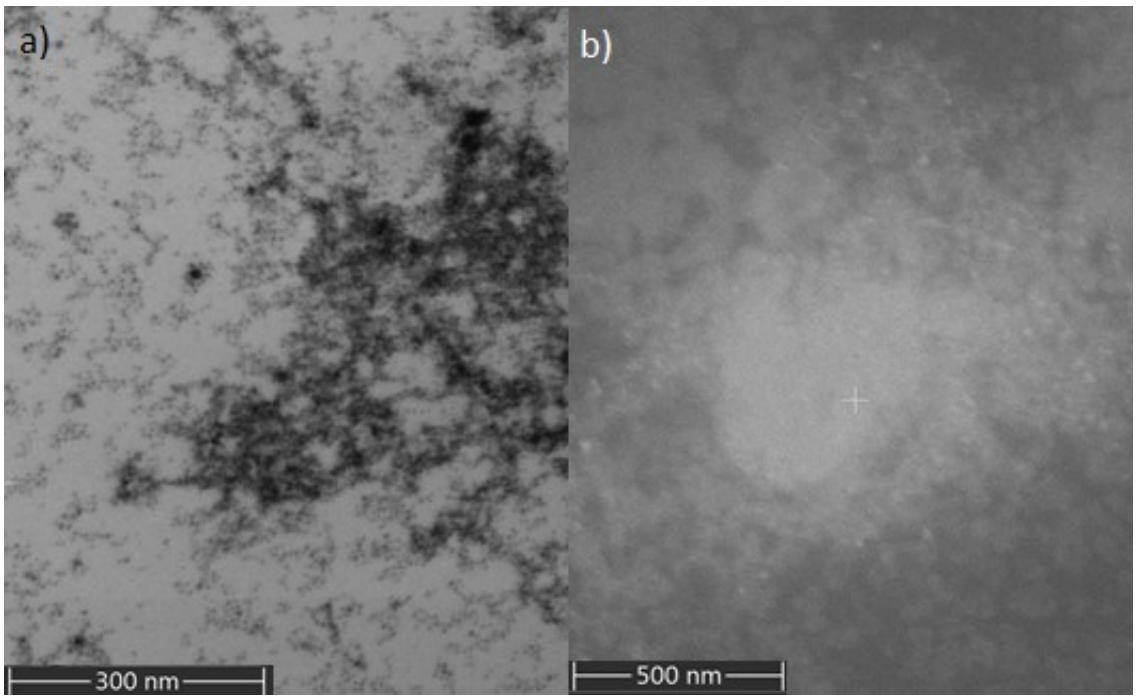

Figure 4-7 WetSTEM image of cluster formation for PHMB-AgNPs formed in higher concentrations of polymer a) 80 µg/ml and b) 140 µg/ml. The thick layer formed in 140 µg/ml required different STEM3+ detection modes to penetrate the area under observation.

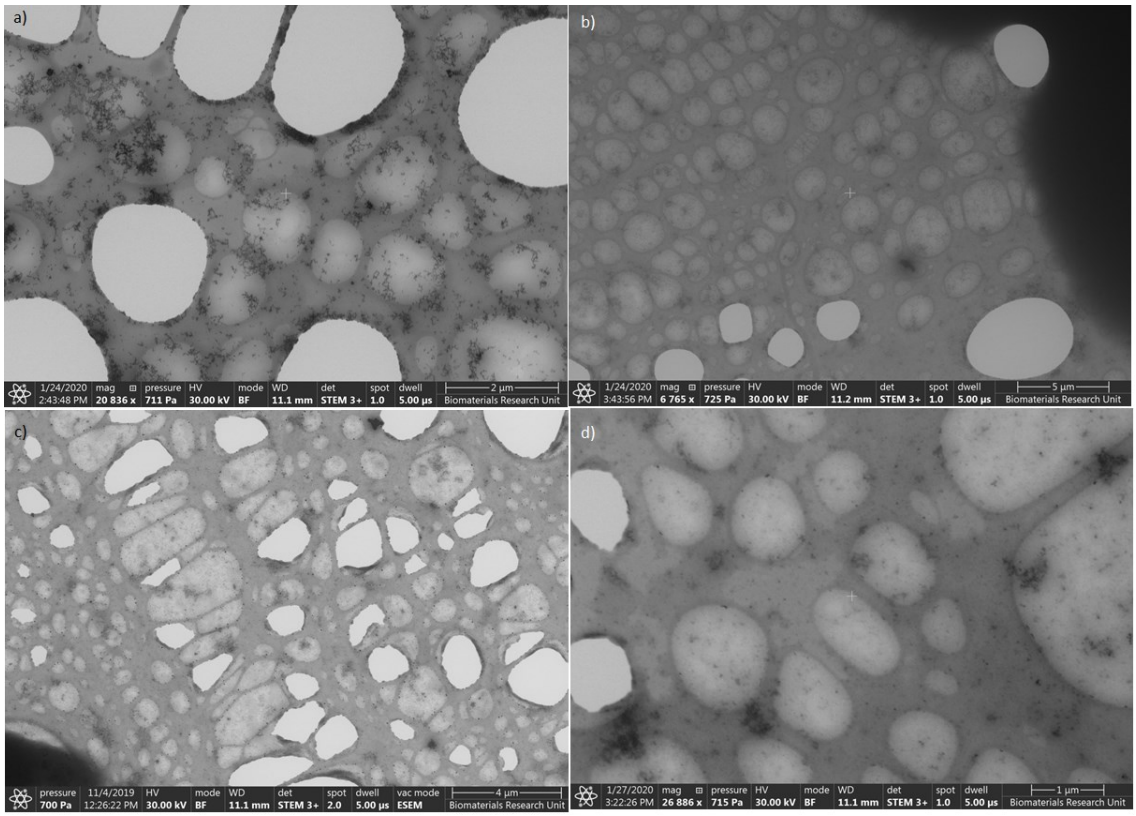

Figure 4-8 WetSTEM images showing changing cluster formation with increasing PHMB presence with a) 20 µg/ml PHMB-AgNPs, b) 80 µg/ml PHMB-AgNPs, c) 120 µg/ml PHMB-AgNPs, d) 200 µg/ml PHMB-AgNPs. The highest polymer concentration has also visible differences in the thickness of the liquid on the holey carbon.

Artefact formation

The samples were dried to allow better imaging using STEM-in-SEM. Removal of water from the sample imaged in the WetSTEM was controlled by the ESEM operator but occurred spontaneously if the temperature or pressure destabilised or were not in equilibrium. When this was carried out slowly, with pressure reduced from 700 Pa to 500 Pa, the drying left some identifiable features.

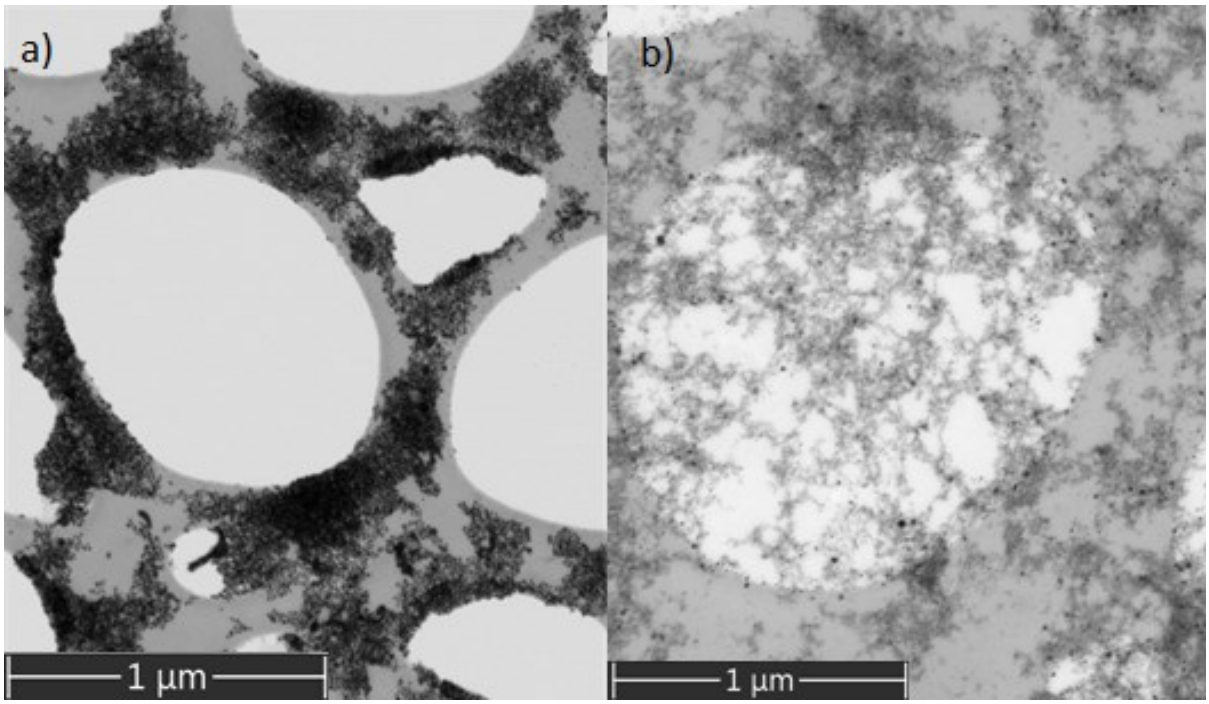

Figure 4-9 STEM-in-SEM images for a) Bare-AgNPs in high vacuum, highly compacted, and b) 80 µg/ml PHMB-AgNPs in high vacuum showing aggregation but not as compact as the particles without polymer.

The undefined networks formed by the Bare-AgNPs compressed to form more closely packed structures (Figure 4-9a). A similar effect was observed in the 20 µg/ml PHMB-AgNPs and the 80 µg/ml PHMB-AgNPs (Figure 4-9b). Little evidence of polymer presence can be found in those structures, but the PHMB-AgNPs clusters had less-dense structures for the higher PHMB content and were also able to span the holes in the carbon film used as a support.

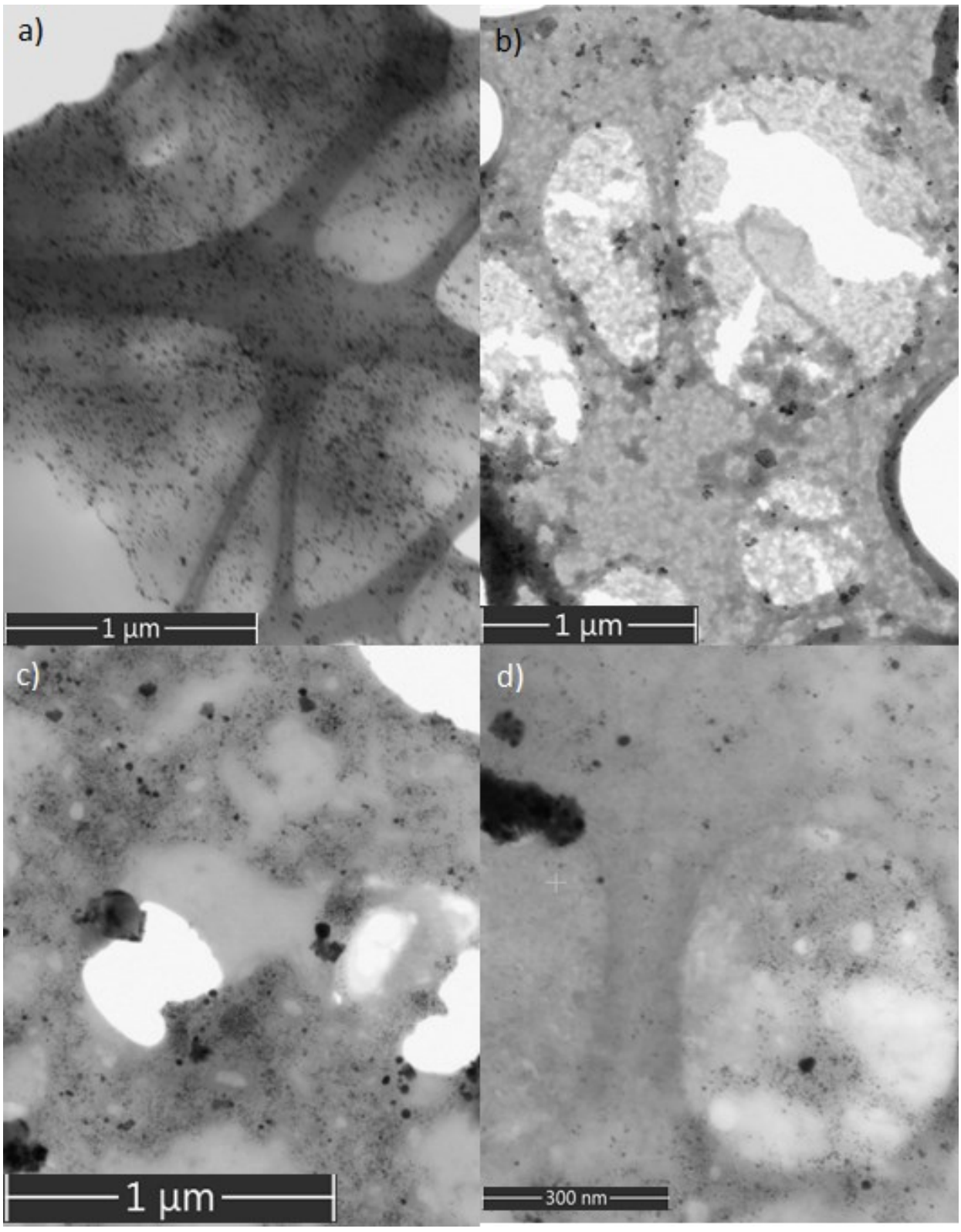

Figure 4-10 STEM-in-SEM images of the semi-transparent film with particles imbedded, observed in a) 20 µg/ml PHMB-AgNPs, b) 80 µg/ml PHMB-AgNPs, c) 140 µg/ml PHMB-AgNPs and d) 200 µg/ml PHMB-AgNPs.

In addition to those features presented, another type of feature was observed in the PHMB-AgNPs. These were areas covered, under SEM observation, with semi-transparent film

with nanoparticles imbedded within them it (Figure 4-10a-d). The number of areas covered with film increased with the concentration of the PHMB used in synthesis, suggesting that the polymer gelled in those conditions. These areas were also sensitive to beam damage: the film formed over the holes in the carbon broke during observation or image acquisition. Some areas were observed covered with gel but with low silver nanoparticle content present. This occurred most frequently at the high end of polymer concentration measured in this study (140, 160, 200 µg/ml) (Figure 4-11).

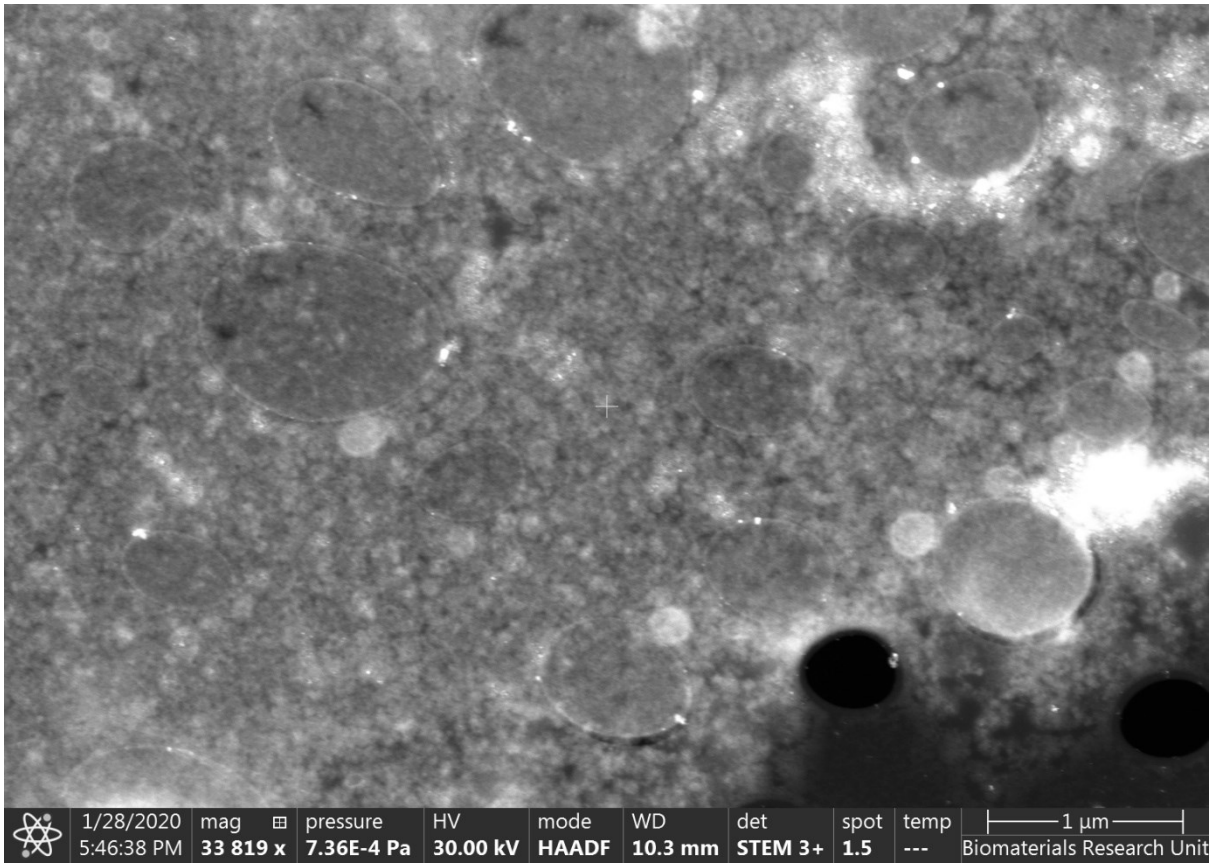

Figure 4-11 Image for 140 µg/ml PHMB-AgNPs taken in STEM-in-SEM mode showing the area of holey carbon covered with polymer gel with low AgNPs presence.

The drying features chosen above were a product of slow drying from a flooded sample. In the case of fast drying resulting from sudden pressure drop, pattern formation can again be linked to the increase of the concentration causing a tendency to form highly dense areas of polymer and particles. As the water meniscus receded, it produced a separation barrier between the unaffected copper grid and the amorphous gel with nanoparticles within it (Figure 4-12 a-

d). Such stark separation did not form in lower PHMB concentrations, instead producing intermittent results. Features formed during both fast and slow drying were consistent with the fact that with increased concentration of polymer added to the reaction, the final sample produced had increased stabiliser mass present, affecting the behaviour of the particles in nano- and macroscale.

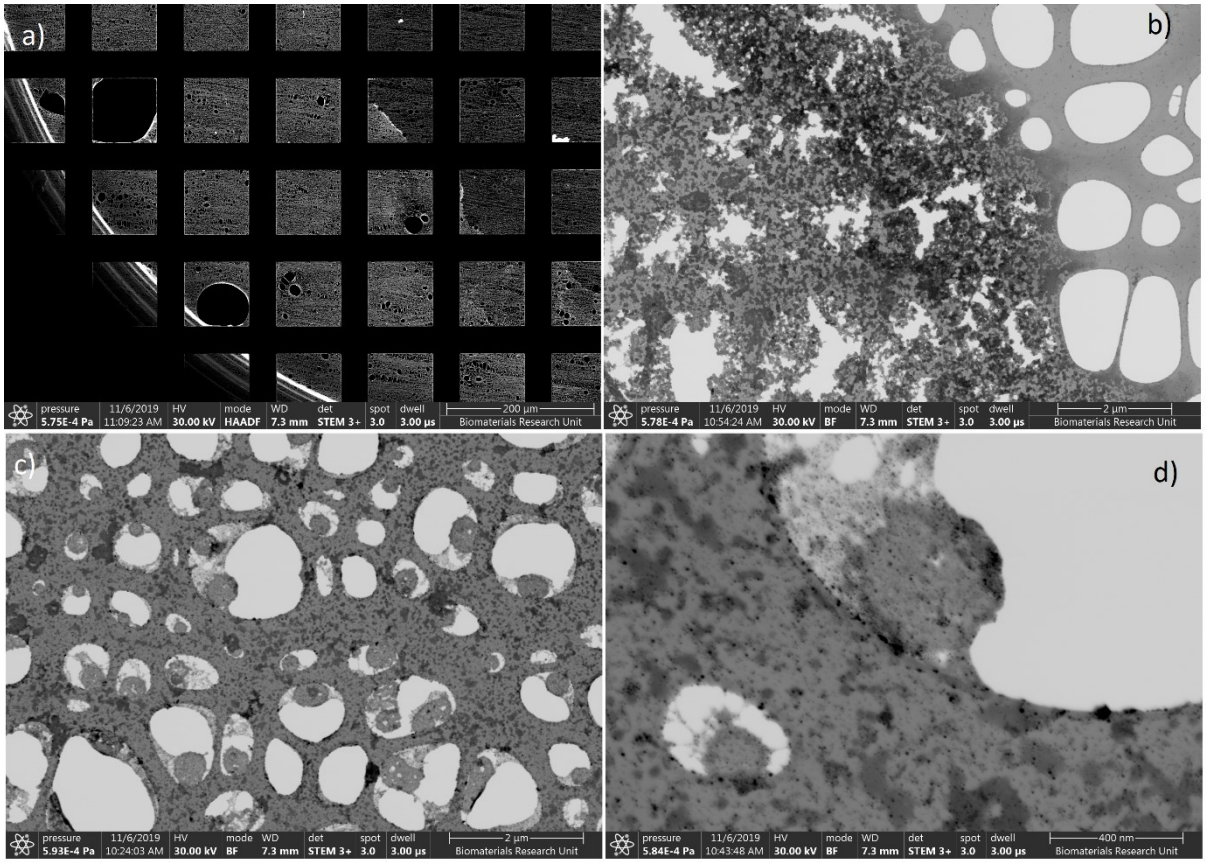

Figure 4-12 STEM-in-SEM showing increasing magnification on the 160 µg/ml PHMB-AgNPs sample a) overview of the grid with a clear separation between holey carbon and the sample, b) magnification of the boundary formed with highly condensed structures, c) overview of structures formed on the side where PHMB-AgNPs deposited, and d) magnification of the features formed.

Sizing analysis

The use of STEM-in-SEM was much more successful in obtaining good-quality imaging of the AgNPs than WetSTEM. As has been previously established (Chapter 3, section 3.2.4 - Environmental Scanning Electron Microscope (ESEM)), the images taken for the STEM-in-SEM provide a good representation of particle size, regardless of the possibility of artefact formation caused by drying.

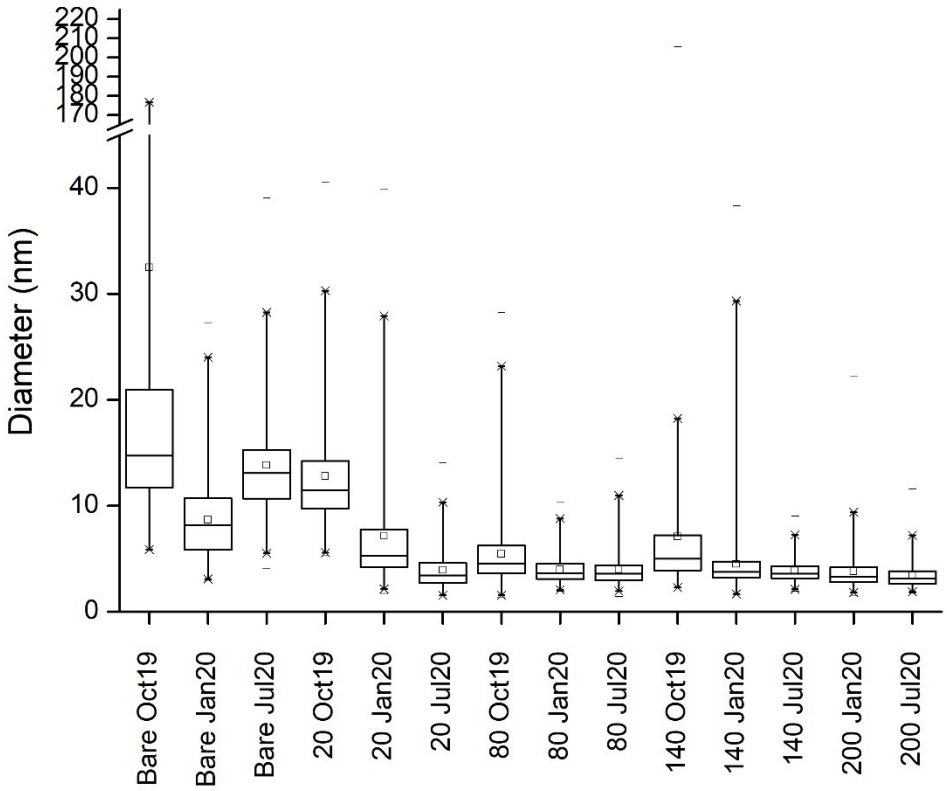

Figure 4-13 Reproducibility of the measurements taken on images from different samples acquired in STEM-in-SEM mode. The following marking was used: the lower edge of the box marks 25% of results, the middle 50%, and the upper line 75%. The whiskers are in the range of 5% to 95%. The small square represents a mean value, with cross marking 99% and 1% and a dash for maximum and minimum measurements.

Comparing results from different synthesis batches provides confidence that the results are consistent between them (Figure 4-13). The results in the lower concentrations of the PHMB (Bare, 20 µg/ml) and the results obtained using samples from Oct19 batch show greater variability. Although the latter might be caused by imperfections in the method development, which was still ongoing at the time, the former is consistent with measurements taken for other batches. Reinforcing the premise that good reproducibility between batches has been achieved and that those particles formed without or in low concentrations of polymer exhibit a greater distribution of particles.

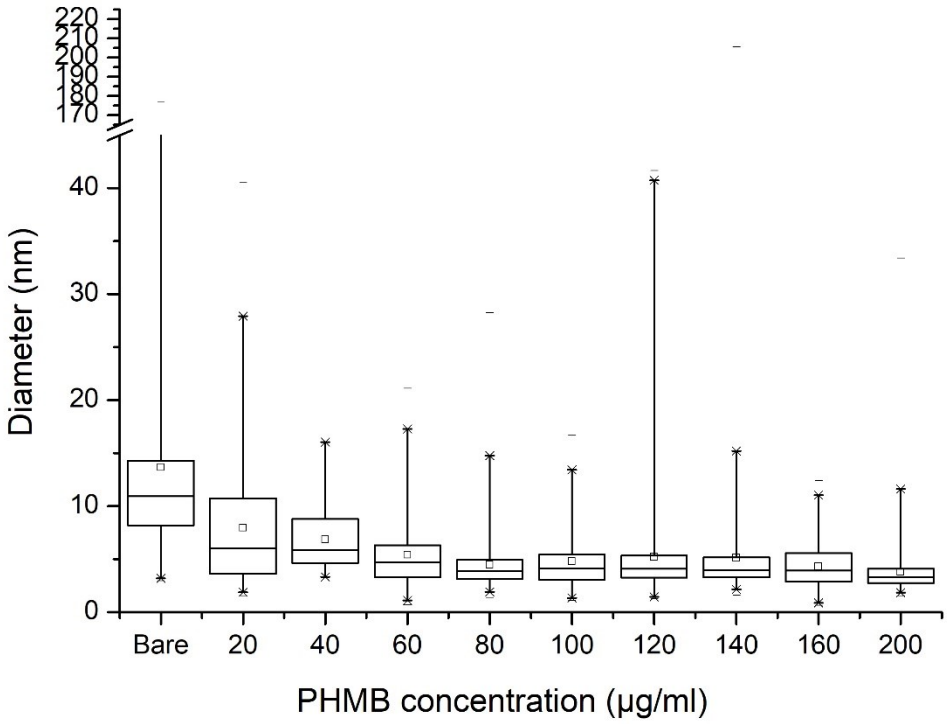

Figure 4-14 Aggregated results representing different batches synthesised and a spectrum of concentrations of PHMB-AgNPs analysed using STEM-in-SEM. The following marking has been used: the lower edge of the box marks 25% of results, the middle 50%, and the upper line 75%. The whiskers are in the range of 5% to 95%, the small square represents a mean value, with cross marking 99% and 1% and a dash for maximum and minimum measurements.

Compiling all available measurements using the images obtained in STEM-in-SEM mode, a size distribution was prepared for all AgNPs (Figure 4-14); a table of measurements used can be found in Appendix 4. There was a clear reduction in the size of the nanoparticles observed using SEM. Bare-AgNPs have noticeably larger polydispersity compared with the PHMB-AgNPs, and there were outliners present in both cases. But the mean value for the particles shows a trend of decreasing diameter once the PHMB is added to the synthesis process and a continuing decrease until the concentration of the polymer reaches 60 – 80 µg/ml. In addition, the distribution of the particles followed the same reducing trend.

Summary

Imaging using SEM provided additional evidence and indication of the behaviour of the nanoparticles in the presence of PHMB. Increasing the concentration of the stabiliser affected the interaction between AgNPs, resulting in increased cluster formation. However,

from the drying process, it became apparent that those clusters were more likely to remain as clusters of nanoparticles rather than highly aggregated structures formed by Bare-AgNPs. Imaging also allowed important observations to be made about the size and shape of particles formed, with detailed analysis of the size of silver nanoparticles present in the samples synthesised.

Energy Dispersive X-ray Spectroscopy (EDX)

EDX provides elemental analysis of the samples under observation using an electron microscope. It contributes important evidence of the chemical composition of the sample. EDX analysis was carried out in ESEM high-vacuum mode because of the improved data acquisition compared with wet mode. However, due to the complexities in the data acquisition detailed previously (Chapter 3), the analysis was more focused on the larger structures observed in the STEM-in-SEM. Moreover, the EDX was a late addition as a characterisation technique, and due to other unforeseen circumstances, it was not systematically and effectively applied until imaging of the samples from batch Jul20 and two months after the synthesis date. Nevertheless, in the process of method development, a number of individual acquisitions were taken with sufficient data quality to allow analysis.

In the following section, the results from EDX are discussed to establish the presence of elemental silver in the data obtained and its relationship to other elements detected.

Presence of silver

Elemental analysis was carried out of a feature located within a Bare-AgNPs sample assumed to be an aggregate of AgNPs (Figure 4-15). The feature on the image can be confirmed by elemental analysis as having strong peaks for silver, and the counts acquired superimpose well on the actual image. Other elements such as copper and aluminium were detected in the same area (see Chapter 3, section 3.2.5 - Energy Dispersive X-ray Spectroscopy for method development and elements identification). However, the two elements were probably detected

as a result of x-ray fluorescence due to the uneven surface of the particles. Some distortion in the intensity of the carbon and silicon observed was also noted, which indicated a relationship between the thickness of the sample and the counts acquired from the material below.

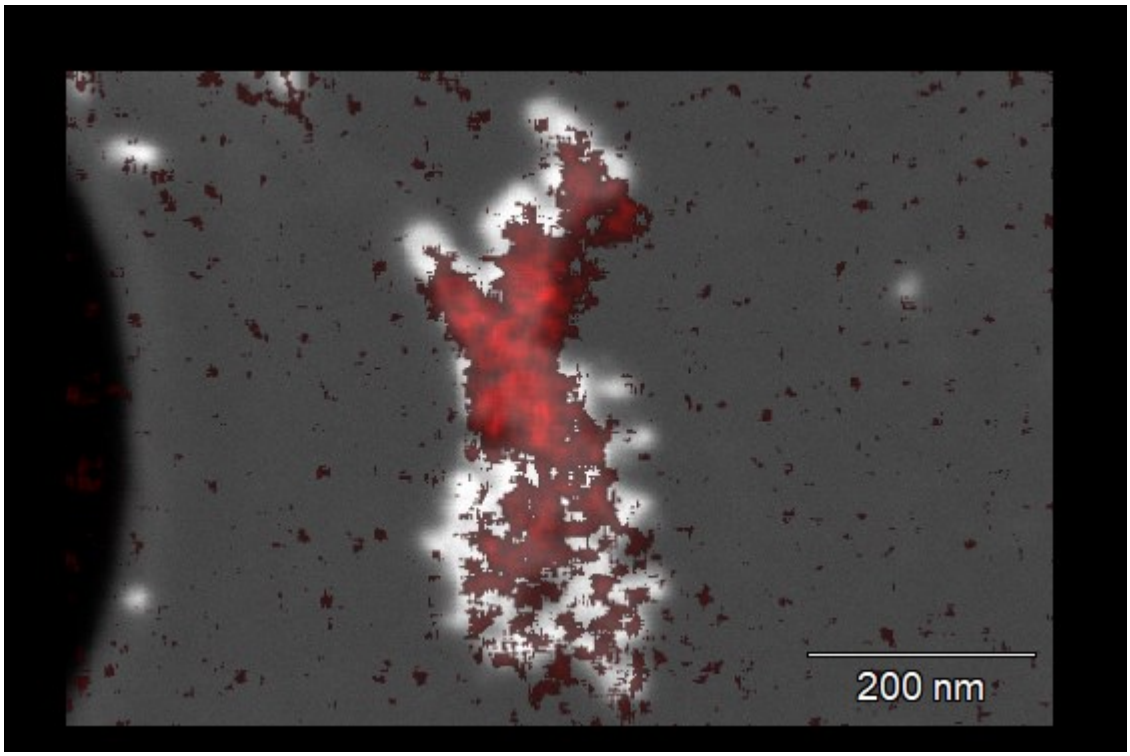

Figure 4-15 Quant map of atomic percent for elemental silver overlaid on the SEM image obtained for Bare-AgNPs

Obtaining the image magnification and resolution required to be able to resolve individual particles was not possible. It was achievable to obtain an overview of the distribution and confirmation that elemental silver is present in the sample (Figure 4-16). Importantly detected silver is located in the same areas as suspected AgNPs; however, autoidentification of the elements showed similar issues to those previously reported. Other elements were identified in the same areas, making qualitative analysis of the composition impractical. In addition, it was not possible to achieve a better resolution to further investigate if the polymer presence may be recoded within the particle aggregates or around the particles themselves. Nor that it was possible to obtain reliable EDX spectra for the PHMB itself. The low atomic number elements dominating the polymer do not lend themselves to this analytical method.

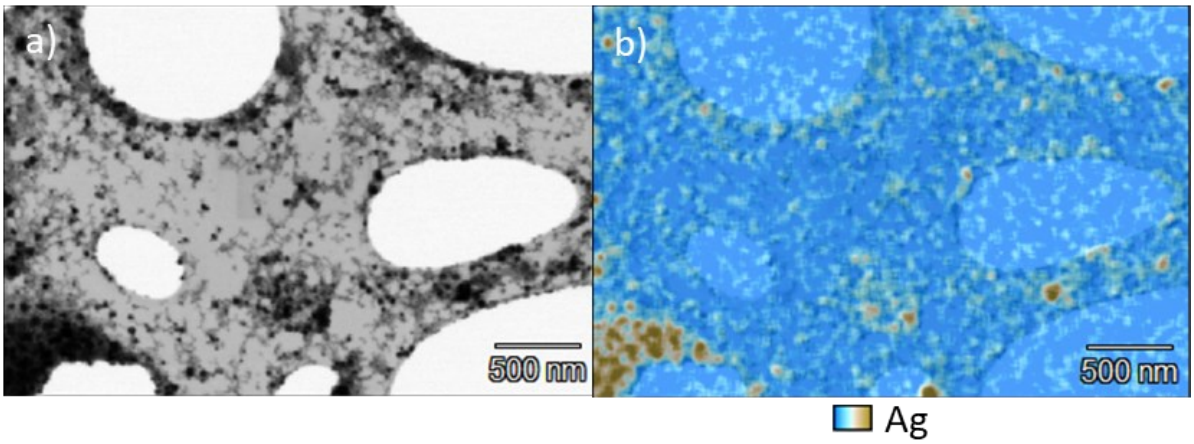

Figure 4-16 Image on which EDX analysis was carried out for the sample of a) 20 µg/ml PHMB-AgNPs and the atomic percent quant map for elemental silver (L-line) with hot pixel suppression overlaid on the image, clearly showing the presence of elemental silver in the areas of dark spots where AgNPs were expected.

Both Bare-AgNPs and 20 PHMB-AgNPs show that particle analysis is limited to larger features. Using the settings applied, it was not possible to carry out a detailed point-by-point analysis of the sample's elemental composition. However, it was possible to determine the presence of silver in larger aggregates/particles.

Interaction with other elements

EDX was also used to investigate one of the features commonly observed in STEM-in-SEM: what appears to be a gel formed with AgNPs within this amorphous mass. An example of this feature is presented in Figure 4-17 below as an image taken separately and before conducting EDX spectral mapping acquisition. All previously discussed elements were identified (see Chapter 3); however, the feature has increased carbon intensity in the atomic percent quant maps, which may correspond to amorphous PHMB (Figure 4-18b). In addition, silicon is very strongly blocked from that area (Figure 4-18c). Previous experience suggests that this is an area of considerable thickness. Silver is detected, however, and superimposes well on the central area showing a large concentration of the particles (Figure 4-18d).

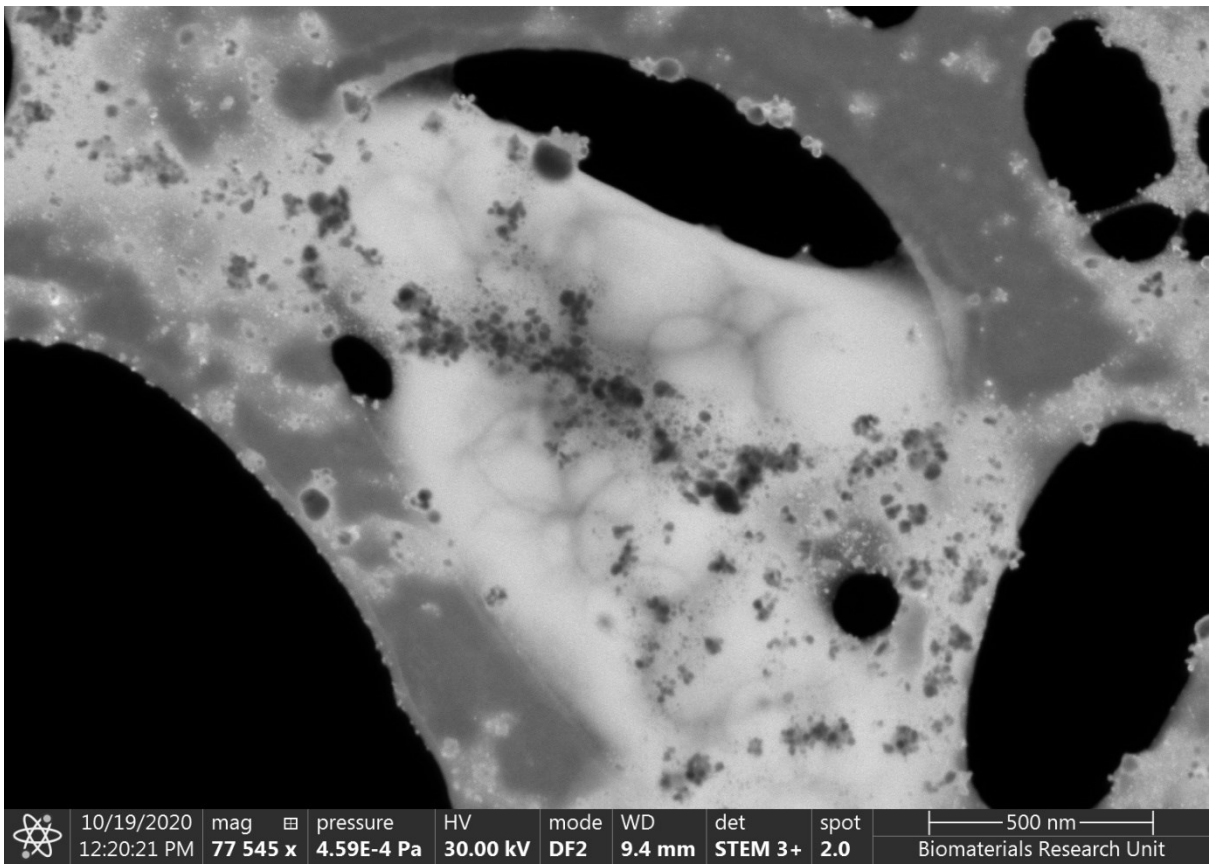

Figure 4-17 STEM-in-SEM image obtained for 200 µg/ml PHMB-AgNPs taken separately from the EDX acquisition but over the same sample part.

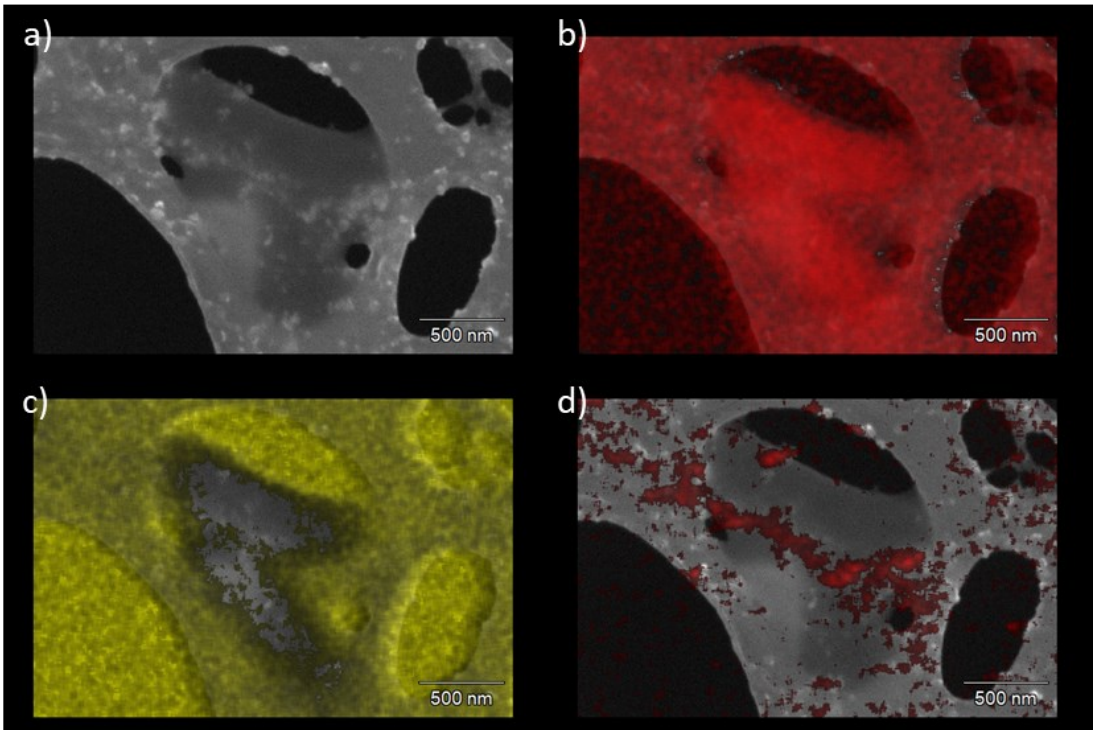

Figure 4-18 EDX data obtained from spectral imaging of the 200 µg/ml PHMB-AgNPs: a) image obtained from ETD SEM; b) carbon atomic percent quant map overlayed over the image; c) silicon atomic percent quant map overlayed over the image; d) silver atomic percent quant map overlayed over the image.

A similar analytical approach is taken to two distinct areas of the 140 µg/ml PHMB-AgNPs. In the first feature (Figure 4-19a), carbon (Figure 4-19b) and silver (Figure 4-19c) have an increased detection intensity on the maps, though impurities were detected (all autoidentified elements attached in Appendix 5a and 5b). Correlation between silver and carbon was particularly apparent when 'linescan' was conducted over a section of the feature. Silver and carbon have very closely related trends, indicating a strong affinity between them (Figure 4-19d).

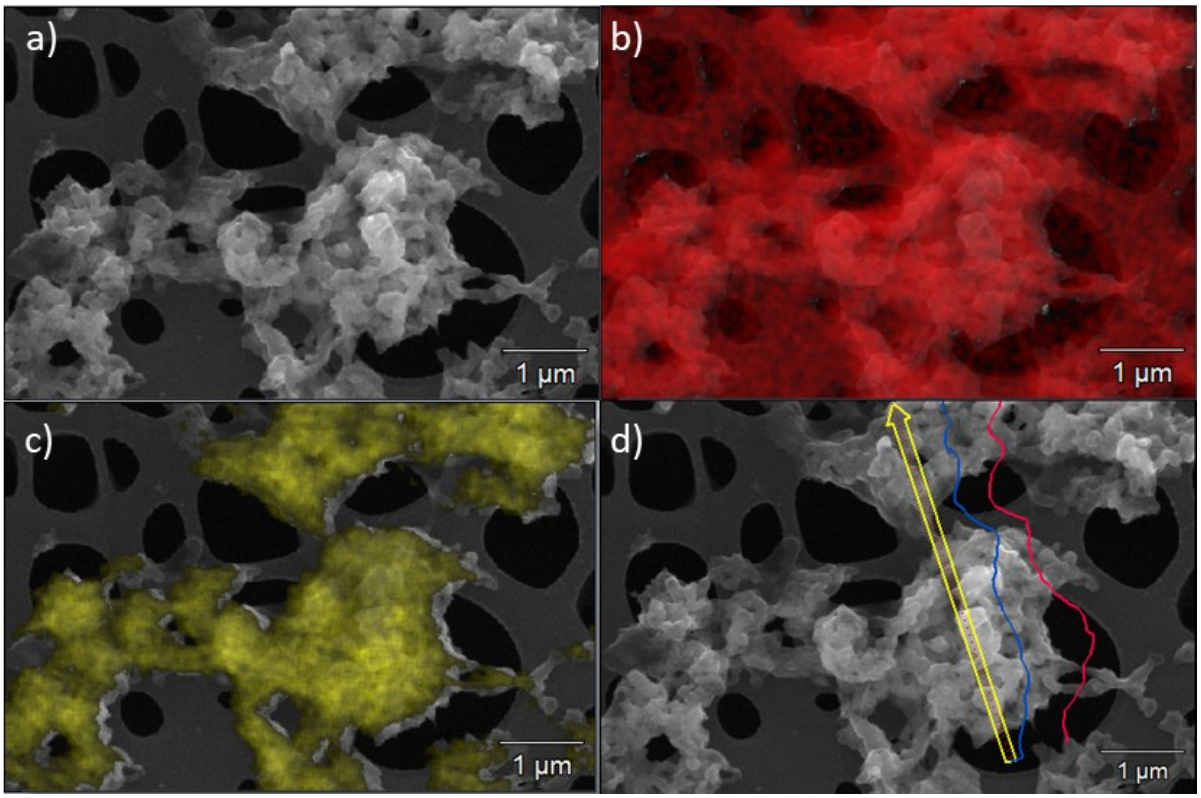

Figure 4-19 a) Feature observed in STEM-in-SEM for 140 µg/ml PHMB-AgNPs with b) carbon c) silver atomic percent spectral map overlaid, d) 'linescan' over the spectral image showing elemental carbon (blue) and elemental silver (red) and the association between them (the ratio percentage between the lines is not to scale)

Reviewing another area in the same sample gave contradictory conclusions (Figure 4-20). The image contains two distinct features (roman numerals I. – green rectangle and II. – orange rectangle). Both can be interpreted as polymer gel containing particles. The large feature (II.) in the lower-right corner has a detectable silver particle concentration within it that overlays with visible particles, but the carbon intensity is much reduced compared with what

would be expected based on previous observations. However, another less visible feature (I.) exists in the upper-right corner, which has increased carbon intensity but no detectable elemental silver. It might be the case that the large feature (II.) in the right bottom of the image has a significantly raised profile, blocking x-rays from the area in the upper-left part (I.) from reaching the detector. However, further investigation is required to determine the cause of these discrepancies in the data collected.

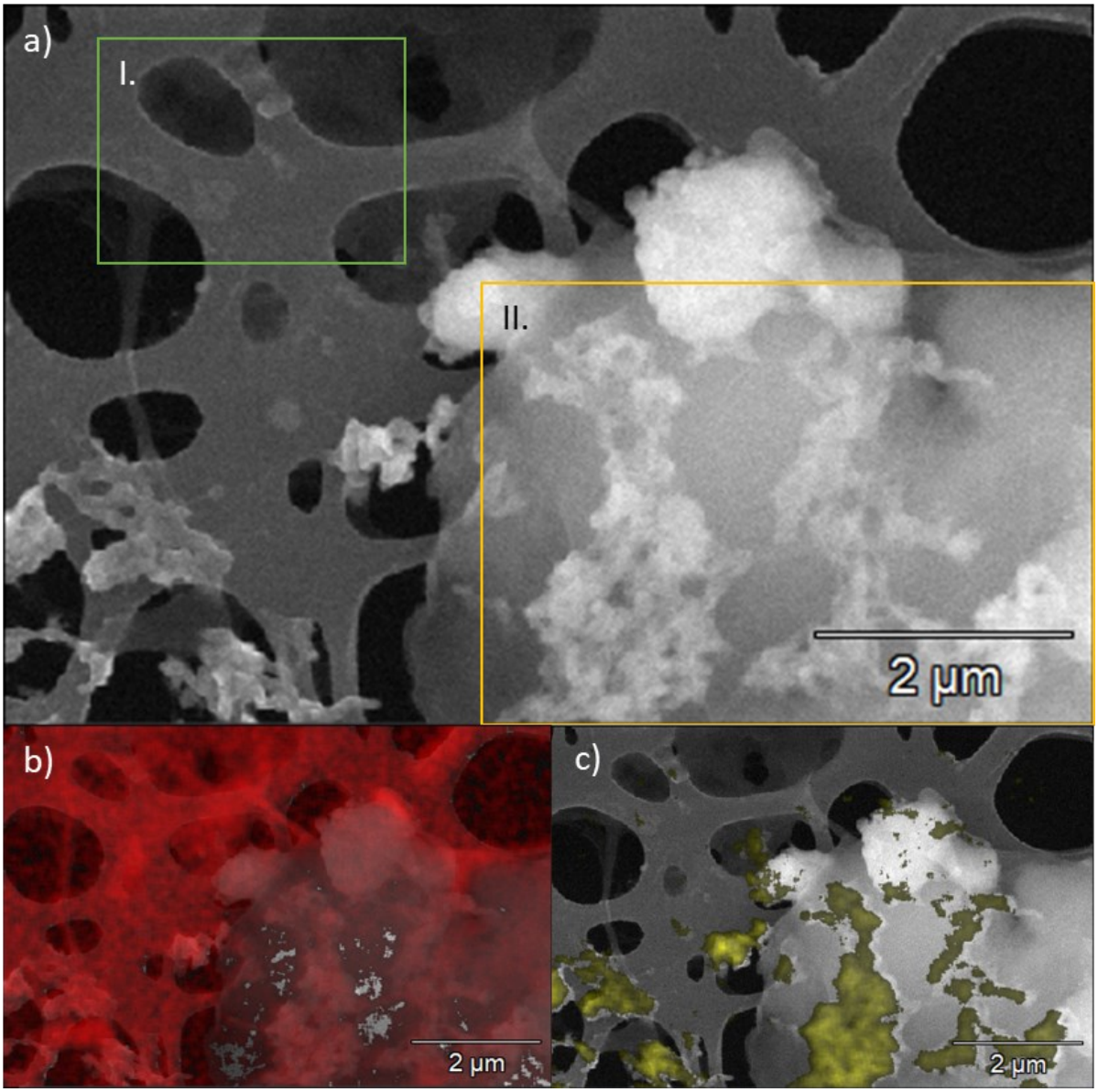

Figure 4-20 a) image obtained for a sample of 140 µg/ml PHMB-AgNPs using ETD detector for EDX purposes showing two distinct features I. (green square) and II. (orange square). With overlaid atomic percent quants map for b) carbon and c) silver.

Summary

Results obtained using EDX provide evidence that elemental silver was present within the samples observed using SEM. It also provides an indication of the relationship between silver and carbon detected within the PHMB-AgNPs samples, implying that the amorphous mass was indeed gelated PHMB with particles present within it. However, there are strong limitations to this technique requiring investigation of the complexities associated with the data collection to establish the reproducibility of the results and analysis. An additional strength of the technique was that it supports the determination of what constitutes the bulk of the sample and provides important evidence on the impurities, artefacts and irregularities observed.

Small-Angle X-ray Spectroscopy (SAXS)

Following modelling of the freshly synthesised samples, results indicate that the size of the nanoparticles synthesised as part of sample batch Oct19 varied between 12.31 ± 1.87 nm (Bare-AgNPs) and 3.03 ± 0.61 nm (200 µg/ml PHMB-AgNPs) (Figure 4-21). It is important to reiterate that the analysis excludes the low q region of the SAXS pattern, which would contain information about aggregation and/or large particles present within. There was a clear downward trend in mean nanoparticle diameter once the polymer was added; the decrease was particularly noticeable in the low concentrations of PHMB and weakened once a concentration of around 80 µg/ml PHMB-AgNPs was reached.

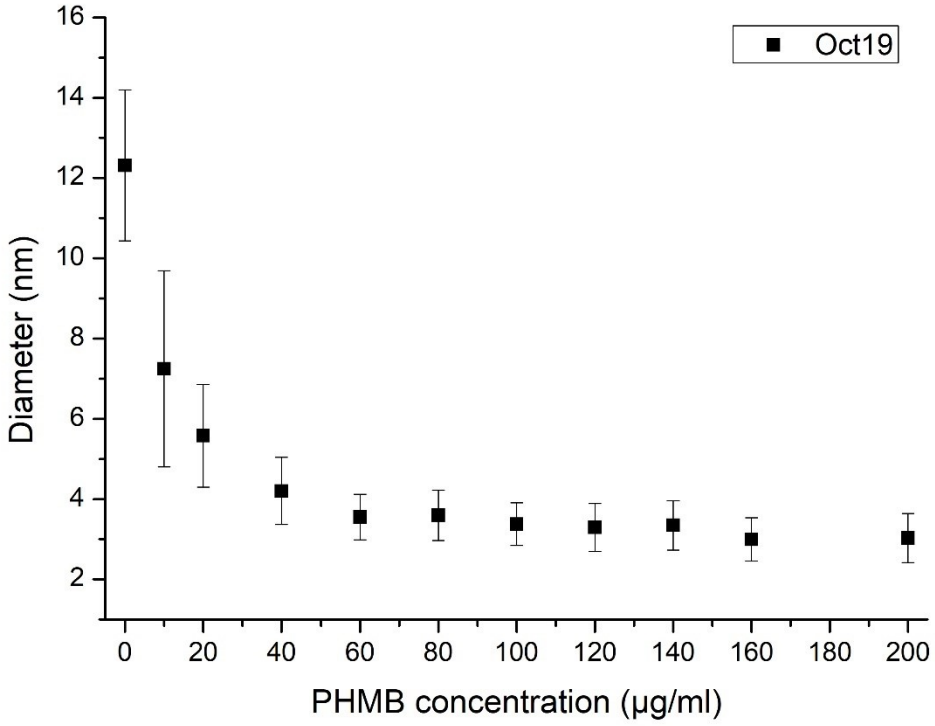

Figure 4-21 Mean sizes with standard deviation obtained as a result of scattering pattern analysis for samples synthesised as a part of a batch Oct19.

Zone of Inhibition

Measuring the antimicrobial efficacy of the agents requires a detailed understanding of the microbiological systems under investigation. A comprehensive investigation into antimicrobial activity requires careful consideration when designing the experiments to include a significant number of variables (such as modes of action, different bacteria and strains, and others). The antimicrobial study designed for this research does not claim such a broad approach; instead, it uses observations of antimicrobial performance to advance understanding of the PHMB-AgNPs system. Measuring the zone of bacteria growth inhibition (ZOI) provides a fast and effective way to assess the antimicrobial performance of the agent.

Assessment of antimicrobial properties using ZOI showed strong and significant improvement to the antimicrobial efficacy of the AgNPs with the addition of PHMB (Figure

4-22). There was a surprising lack of antimicrobial properties for Bare-AgNPs. At the same time, increasing the concentration of PHMB used in the synthesis process had very little impact on efficacy. However, an aliquot of 40 µl of undiluted PHMB-AgNPs was used to conduct measurements. The zone of inhibition was recorded between 12 and 14 mm for all the concentrations. Similar measurements were taken for the 1 mM AgNO3, and the same molarity was used during the synthesis of AgNPs. Therefore, there was a possibility that the distance from the well observed was a natural limit to the diffusion of the agent in the agar gel. It is important to acknowledge the agent's equal efficacy for both of the bacteria strains, gram-negative *E. Coli,* and gram-positive *S. Aureus*. The improvement in antimicrobial efficacy upon complexing the AgNPs with PHMB encouraged further studies.

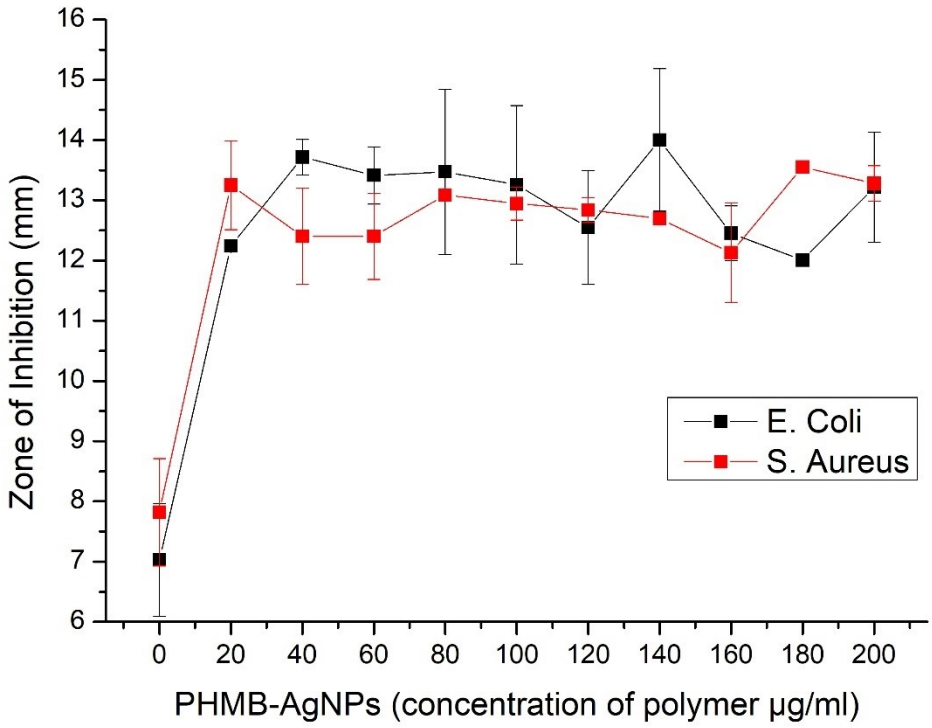

Figure 4-22 Results of the zone of inhibition of bacteria growth for different concentrations of PHMB-AgNPs on the agar plate against *E. Coli* and *S. Aureus*. Bare-AgNPs marked as the concentration of 0. Well diameter of the agent was just over 6 mm across. Data is based on two separate measurements per concentration except for 180 µg/ml PHMB-AgNPs.

The solutions of different concentrations of PHMB used during synthesis were tested using ZOI for antimicrobial efficacy (Figure 4-23). The samples were diluted with 30 ml of DI water to match the concentration found in the reaction vessel. The results showed a lack of antimicrobial properties for the lowest concentrations (20 µg/ml) and increased to about 8.5 nm for 60 µg/ml PHMB, remaining constant for the remaining concentrations. This unexpected lack of gradual increase indicated a possible limit to the diffusion of PHMB through the agar gel. However, the 200 µg/ml PHMB used for positive reference on the plates regularly recorded stronger antimicrobial activity (9.47 ± 1.89 mm – *E. Coli*, 10.32 ± 1.07 mm – *S. Aureus*), suggesting that a correlation between concentration and the antimicrobial effectiveness recorded using ZOI was possible.

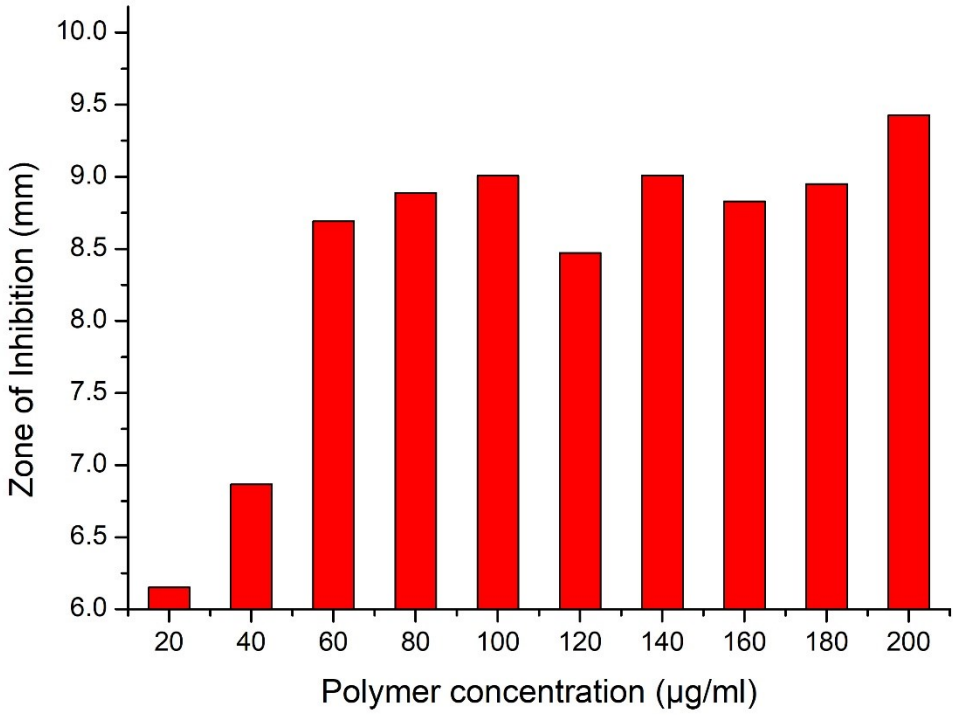

Figure 4-23 Various concentrations of PHMB were assessed for antimicrobial activity against *Escherichia Coli*. Well size is around 6 mm.

Infranatant obtained in the process of centrifugation was assessed for antimicrobial purposes in the process of establishing the efficiency of reaction synthesis. Infranatant from

five reactions (Bare, 20, 80, 140 and 200 µg/ml) was assessed, and the results indicate that the higher the concentration of the polymer used, the stronger the residual antimicrobial efficiency of the infranatant (Figure 4-24). The silver nitrate and PHMB both show antimicrobial activity; however, an additional 5 ml of fresh sodium borohydride was added to the infranatant to confirm that all AgNO3 was used. No change of colour was observed, suggesting clearly that the cause of the antimicrobial activity was PHMB leaching during the centrifugation process. The filtrate was also measured using UV-Vis but was below detection limits.

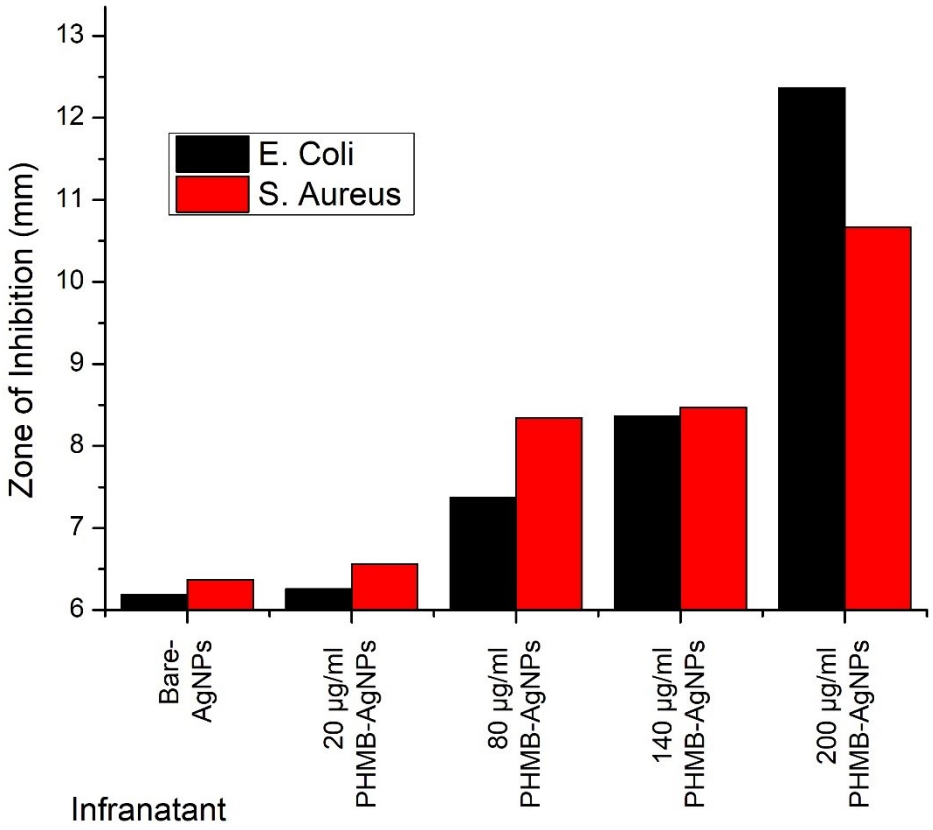

Figure 4-24 Results of the zone of inhibition of bacteria growth for infranatant from selected AgNPs synthesis reactions on the agar plate against *E. Coli* and *S. Aureus*. Well size is just over 6 mm.

Measuring antimicrobial properties using a zone of inhibition is a commonly used method to assess antimicrobial efficacy. It was used in this study to show that there was a significant increase in the efficiency of the complex against the bacteria compared with the individual agents. Bare-AgNPs showed very limited antimicrobial action, but when AgNPs were coupled with the PHMB, there was a noticeable improvement in the measurements

recorded. It has also been shown that the infranatant obtained from the centrifugation process exhibits antimicrobial properties. However, no correlation can be made between those results. The concentration of the active agents was different in each case; the study, therefore, requires redesign to ensure consistency in the approach taken. Nevertheless, important findings were established that served as a starting point when considering the use of flow cytometry – another method for assessing antimicrobial activity.

Flow cytometry

The analysis carried out using zone of inhibition showed that improvements were required to the antimicrobial analysis to achieve comparability between the different systems investigated, such as when trying to compare the antimicrobial activity of various PHMB concentrations with the results obtained for PHMB-AgNPs. Flow cytometry was chosen as a technique with much greater sensitivity toward measurements taken. The different dyes used with different modes of action, provide the possibility to determine if the bacteria are damaged (BOX) or dead (PI). The methodology used was changed from that used with ZOI, which assessed bacteria growth suppression, to instead measure antimicrobial efficacy against viable bacteria. The experiments using flow cytometry were restricted to one strain of bacteria – *E. Coli*.

The results from flow cytometry using the data obtained from the samples synthesised as part of the Jul20 batch showed that there was a progressive increase in the bacteria recorded in Q2 – damaged with the increased polymer concentration present within the sample (Figure 4-25). This indicated that the antimicrobial activity is related to the PHMB, a known bacteriostatic agent causing damage to bacteria rather than killing them [81]. This is observed with the BOX dye (Q2) as it interacts with the intracellular proteins or membrane which is detectable with a flow cytometer, compared to PI which requires DNA material to be detected [154]. There is a strong change in the readings between Bare-AgNPs and 20 µg/ml PHMB-AgNPs, but the trend of increasing percentage of bacteria damaged weakens with

concentrations around 80-100 µg/ml. The fluctuations recorded were most likely the result of insufficient repetition.

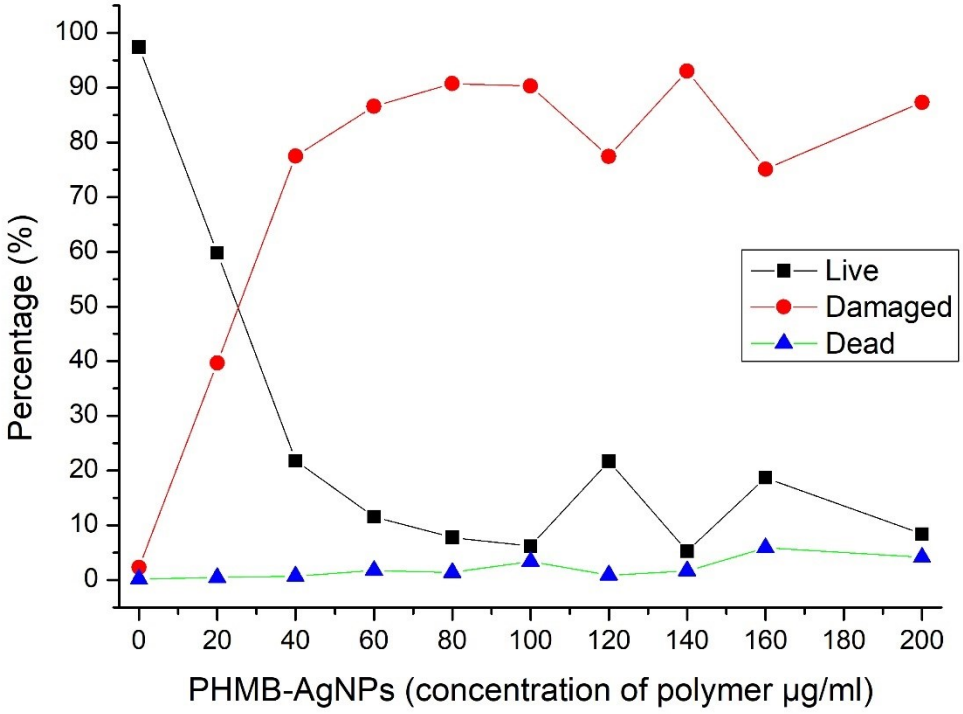

Figure 4-25 Analysis of the flow cytometer results assessing the antimicrobial activity of the Jul20 samples. Bare-AgNPs are marked as 0 µg/ml PHMB-AgNPs.

The antimicrobial efficacy of the PHMB-AgNPs samples assessed was compared with the concentrations of PHMB prepared to correspond to the concentration estimated using a mass balance (Section 3.2.1). Two concentrations (0.04% and 0.18%) of PHMB solution were prepared and assessed against *E. Coli* in the same manner as the PHMB-AgNPs, i.e. 2 µl of sample to make up to 1 ml of bacteria in PBS. The resulting solutions correspond to concentrations of 0.00008% and 0.00036% of PHMB respectively. This was comparable to the concentration of PHMB found in 20 and 80 µg/ml PHMB-AgNPs. However, it is important to remember that the estimates assume that no PHMB leached during the centrifugation process. The 0.04% PHMB concentration showed that the efficacy in damaging the bacteria exceeds

that observed for 20 µg/ml PHMB-AgNPs. The other sample of 0.18% PHMB concentration achieved a result comparable to the sample of 80 µg/ml PHMB-AgNPs (Figure 4-26).

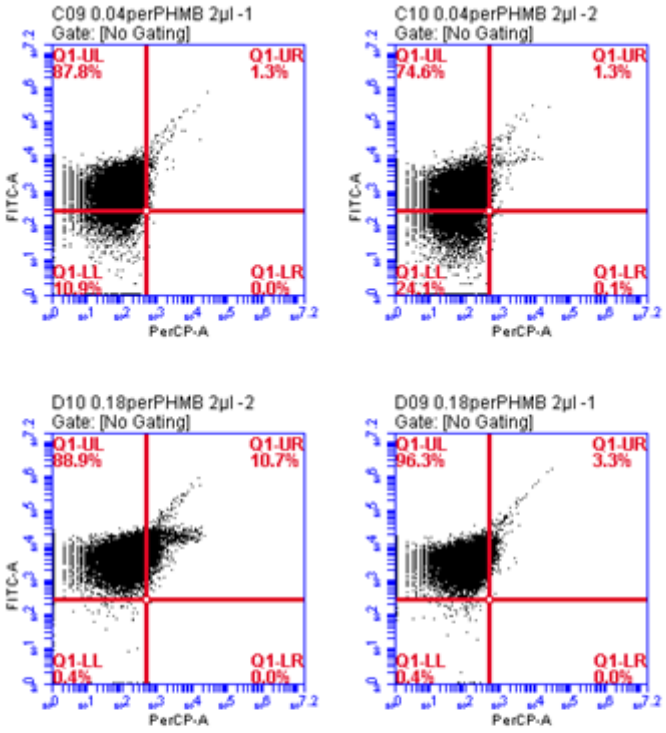

Sample	Live	Damaged	Dead
0.04%	17.5±6.6	81.2±6.6	1.3±0
0.18%	0.4±0	92.6±3.7	7±3.7

Figure 4-26 Results from the flow cytometer assessing the antimicrobial activity of 0.04% and 0.18% PHMB solutions against *E. Coli*. The table insert presents averaged results with standard deviation.

The infranatant obtained following centrifugation of the AgNPs synthesis was collected and assessed for antimicrobial activity. A strong progressive increase in Q2 was recorded for the infranatant, which corresponded to the increase in PHMB concentration used during the reaction (Figure 4-27). The increase in the number of damaged bacteria cells strongly suggests that this was a result of PHMB presence in the infranatant. The PHMB was removed from the

final PHMB-AgNPs obtained during centrifugation; therefore, the actual concentration of the polymer present and involved in stabilising silver nanoparticles is reduced.

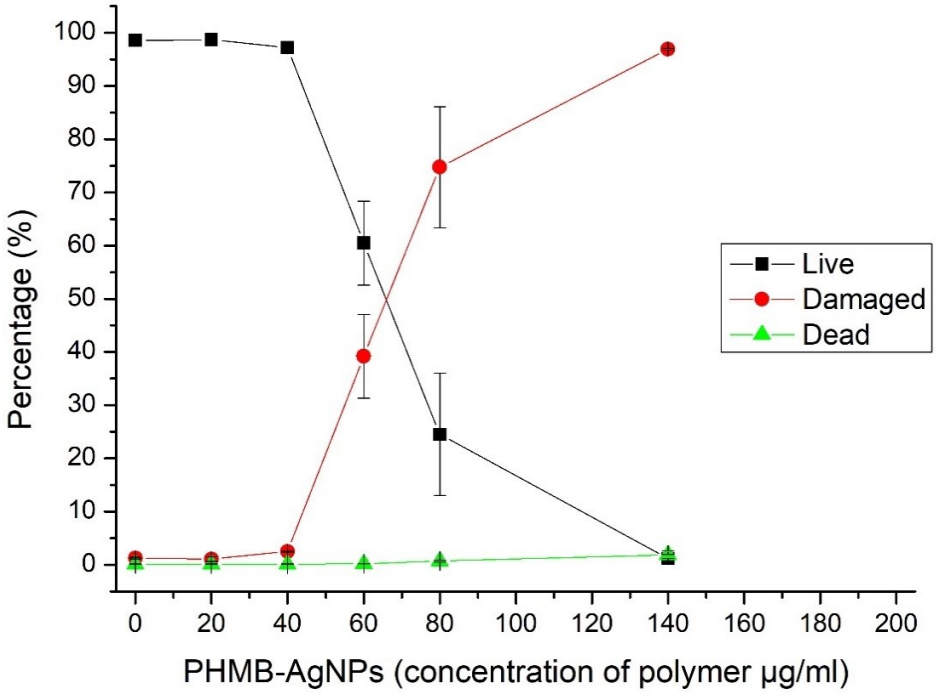

Figure 4-27 Flow cytometer results for infranatant obtained during the centrifugation of the Jul20 PHMB-AgNPs samples with a concentration of polymer corresponding to the concentration of PHMB used during the reaction. Bare-AgNPs are marked as 0 µg/ml PHMB-AgNPs

The results from flow cytometry reinforce the findings following analysis using ZOI. There was a lack of antimicrobial activity from Bare-AgNPs in the conditions tested, and the antimicrobial effects were a result of PHMB presence. In addition, some PHMB was removed during the centrifugation stage of the synthesis process. Further assessments are necessary to gain an understanding of how PHMB-AgNPs interact with bacteria. This relationship is paramount to understanding whether the entire particle engages with bacteria or PHMB detaches from AgNPs to interact with bacteria, removing the stabilising effect it has on the silver nanoparticles.

4.2.2. Irregularities

10 µg/ml PHMB-AgNPs

During the synthesis of batch Nov18, the concentration of polymer was adjusted by 10 µg/ml instead of the usual 20 µg/ml, this was carried out to reduce intervals between data points and to achieve greater data granularity. It was noted that the 10 µg/ml PHMB-AgNPs displayed a different colour compared with the other PHMB-AgNPs obtained. The UV-Vis carried out on this sample showed a double peak instead of the single peak typically observed. To exclude that the irregular spectra were a product of synthesis error, a number of repeats were carried out, each showing strong similarity (Figure 4-28). The obtained samples were also analysed using DLS; the results showed a strong single peak (Figure 4-29).

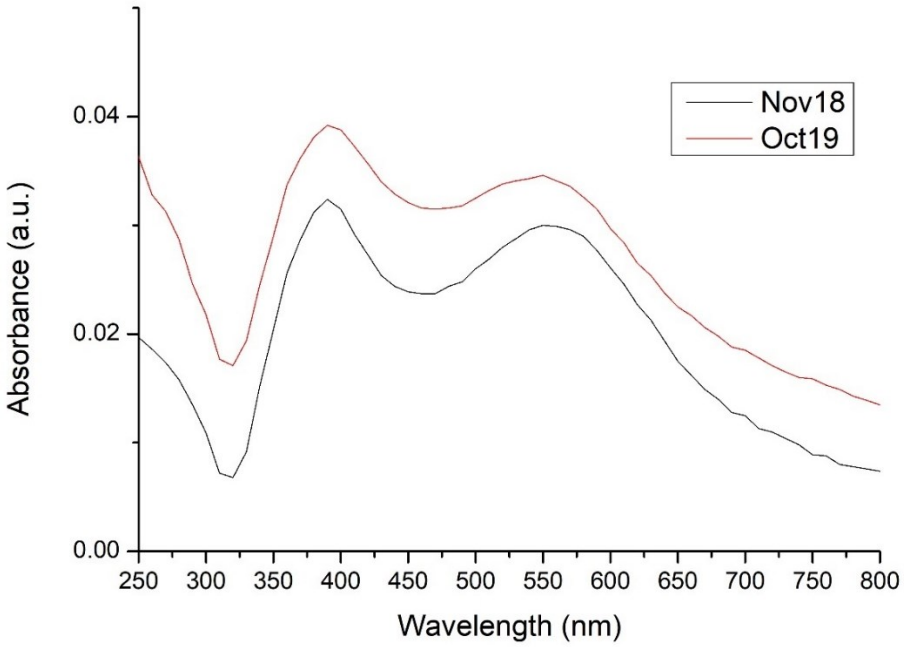

Figure 4-28 UV-Vis spectra obtained for freshly synthesised 10 µg/ml PHMB-AgNPs showing strong plasmon resonance peaks at around 400 nm and 550 nm

Z-Average (d.nm):	93.61	Size (d.nm):	Width (nm)	% Intensity :	Volume :	Number
PdI:	0.407	Peak 1:	143.6	89.89	97.9	12.0	13.0
Intercept:	0.834	Peak 2:	4351	963.2	2.1	50.4	32.2
Result quality :	Good	Peak 3:	0.000	0.000	0.0	10.1	54.8

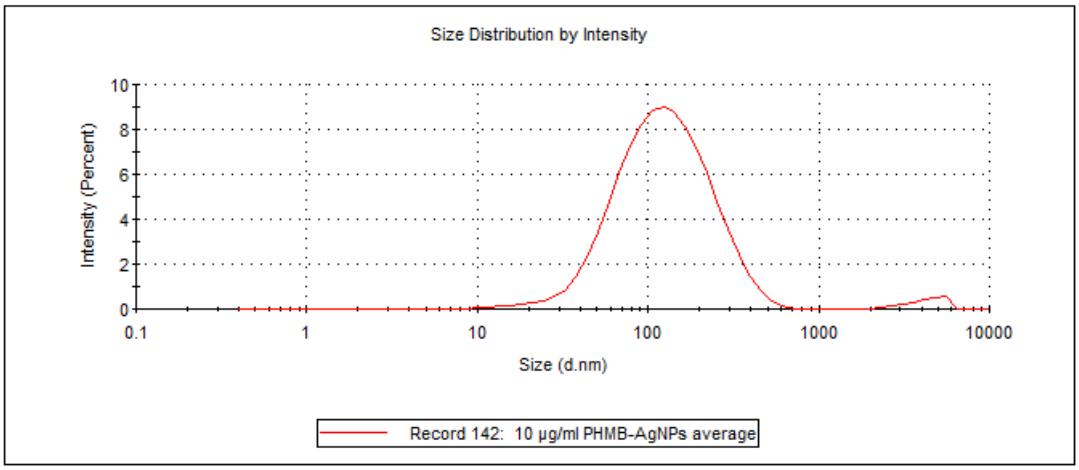

Figure 4-29 Averaged result of size distribution obtained from DLS for 10 µg/ml PHMB-AgNPs.

Imaging was carried out using ESEM, but success was limited to just one sample, showing complex particle size and shape with numerous large particles of variable shapes. EDX analysis was not carried out, limiting confidence as to whether the features under observation were, in fact, AgNPs (Figure 4-30).

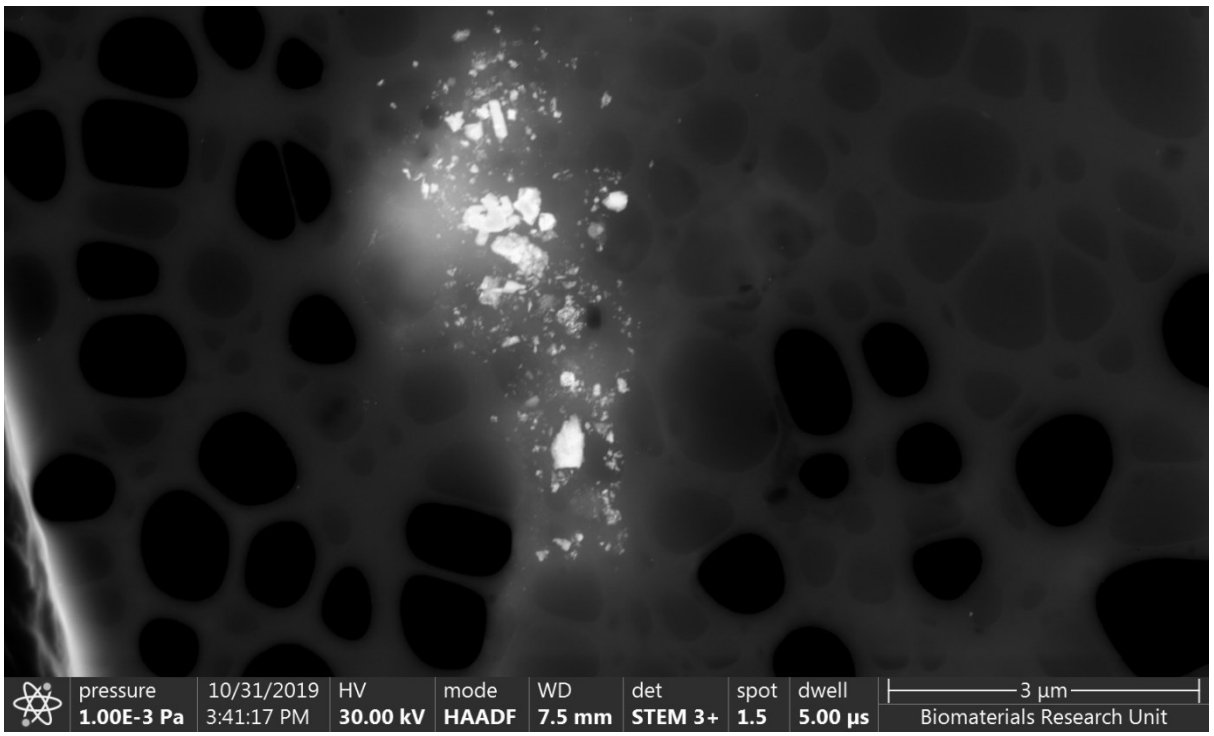

Figure 4-30 STEM-in-SEM HAADF image of 10 µg/ml PHMB-AgNPs showing a collection of particles.

The scattering pattern of 10 µg/ml PHMB-AgNPs was also obtained using SAXS, and the modelling showed the average particle size at 7.24 ± 2.44 nm, placing this distribution within the trend of reducing size with increasing polymer concentration discussed in 4.2.1 - Small-Angle X-ray Spectroscopy (SAXS) above.

The results obtained for 10 µg/ml PHMB-AgNPs showed that the introduction of the polymer did have a dramatic but gradual impact on the particles obtained. The changes to the UV-Vis spectra when compared to other Bare-AgNPs and PHMB-AgNPs clearly showed a double peak indicating a double population of the particles. This double peak also made measuring FWHM very challenging; while the spectra could be split by peak, it would not produce data comparable with other results. DLS strongly indicated that the predominant population of particles is sized around 100 nm. The development of the second peak in the UV-Vis spectra, coupled with the disappearance of the second smaller peak in DLS typically observed for other AgNPs, suggests that the sensitivity of DLS toward large particles was such that it completely overpowered the population of smaller particles. The results obtained for

10 µg/ml PHMB-AgNPs were unexpected but provided valuable insight into the development of the PHMB-AgNPs colloidal stability. Further reference is made to the results presented here in Section 6.3.1 – 'Relationship with 10 µg/ml PHMB-AgNPs', discussing the findings shown in this section compared with observations made of changes to other samples over time.

ESEM/EDX

A number of different irregularities were observed when images were obtained using the electron microscope (EM) and energy dispersive spectroscopy (EDX). When samples are imaged using EM, the operator decides which particles are being observed, which may result in 'observer bias'. It can be the case that unusual and exceptional features more readily catch the operator's attention. This is particularly important when viewing samples in STEM-in-SEM mode, which can contain artefacts from sample drying. It, therefore, becomes important to be able to distinguish between various features.

Aside from the silver nanoparticles observed in the images and discussed in the sections above, other features observed included very large structures. The origin of those structures was not known, but some appeared to be external impurities. This is particularly visible if the ETD detector is used with low acceleration voltage, giving depth and dimension to the image obtained. Features were observed in front of the grid with clearly visible AgNPs located on them (Figure 4-31). The EDX spectral map shows that the feature has a significant carbon presence, suggesting that it may be a polymer formation. Alternatively, it could be an impurity that was present within the liquid sample and attracted PHMB-AgNPs to deposit on top of it.

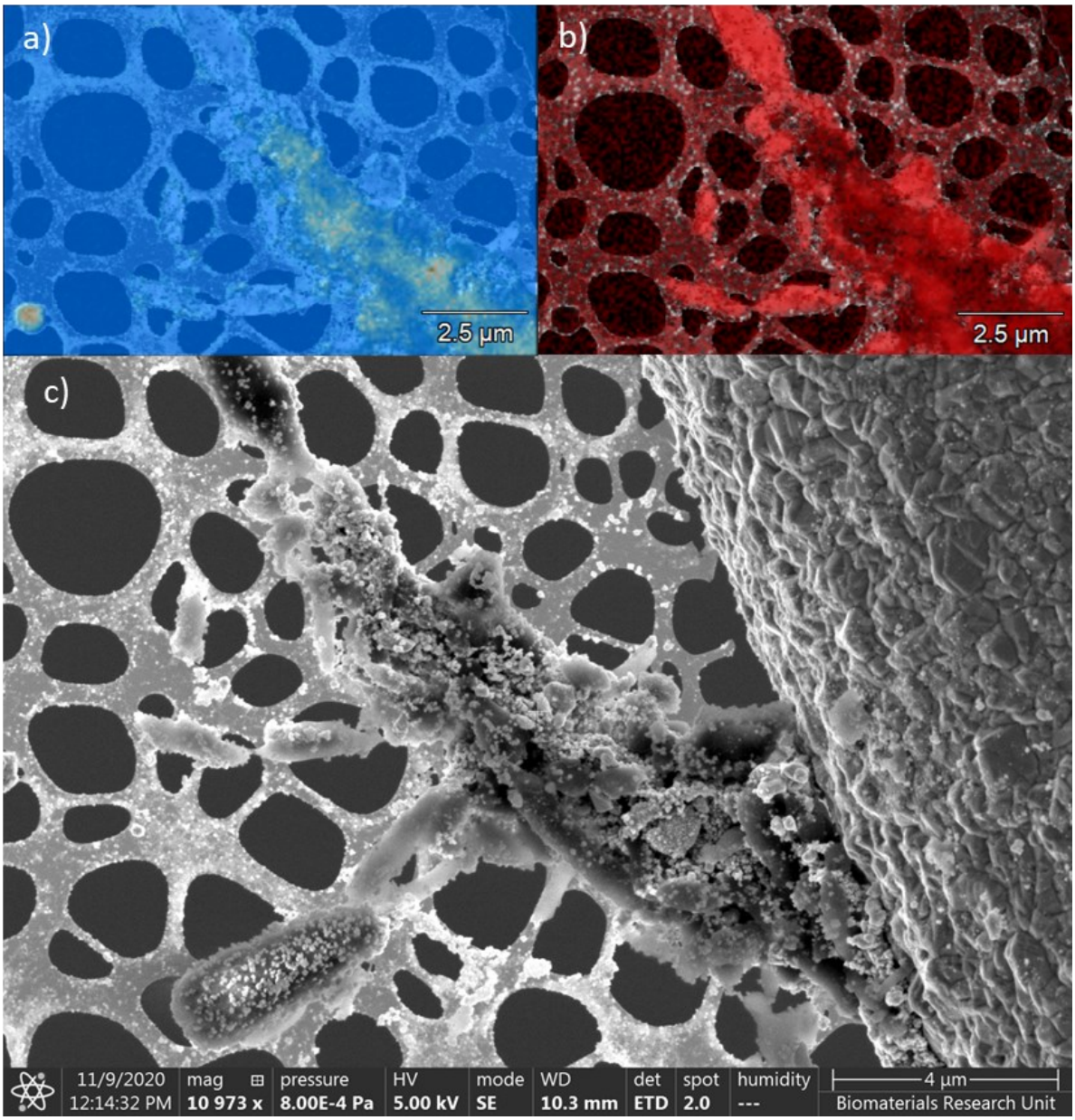

Figure 4-31 Feature observed in high vacuum showing a) AgNPs deposited on the b) carbon-rich structure (in red). The wall-like structure on the left of the image c) is a copper grid.

In addition to the features observed in front of (Figure 4-32a) the grid some were located behind (Figure 4-32b), allowing for determination of whether they were likely to be the result of artefact formation or debris picked up when moving a grid or during transfer between various imaging scenarios.

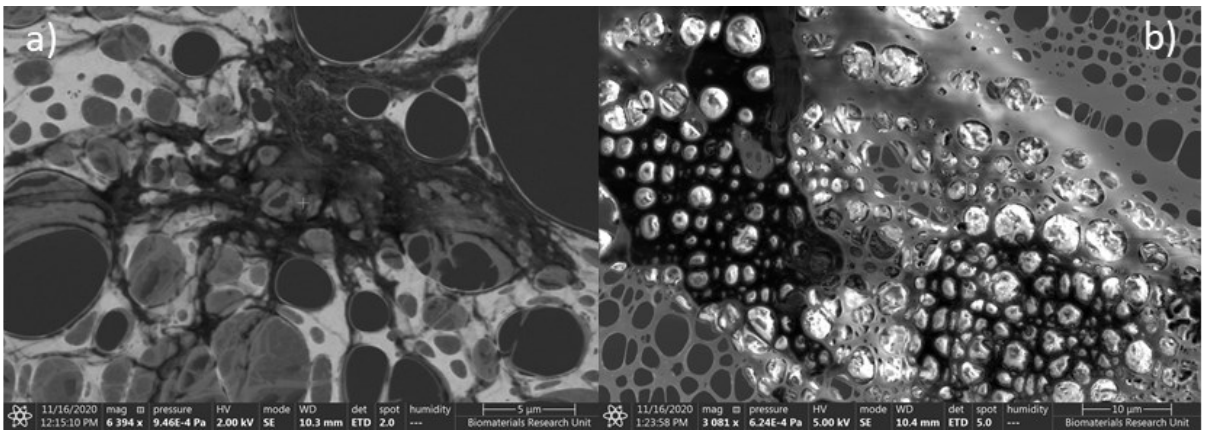

Figure 4-32 Complex large-scale features observed in high-vacuum mode. Using the ETD detector allowed for distinguishing whether the view was a) in front of or b) behind the copper grid.

Finally, for some of the STEM-in-SEM images, areas of high particle agglomeration were observed with 'tentacles' of particles extending out. The vicinity and the arrangement suggest a possible interaction between the cluster and particles.

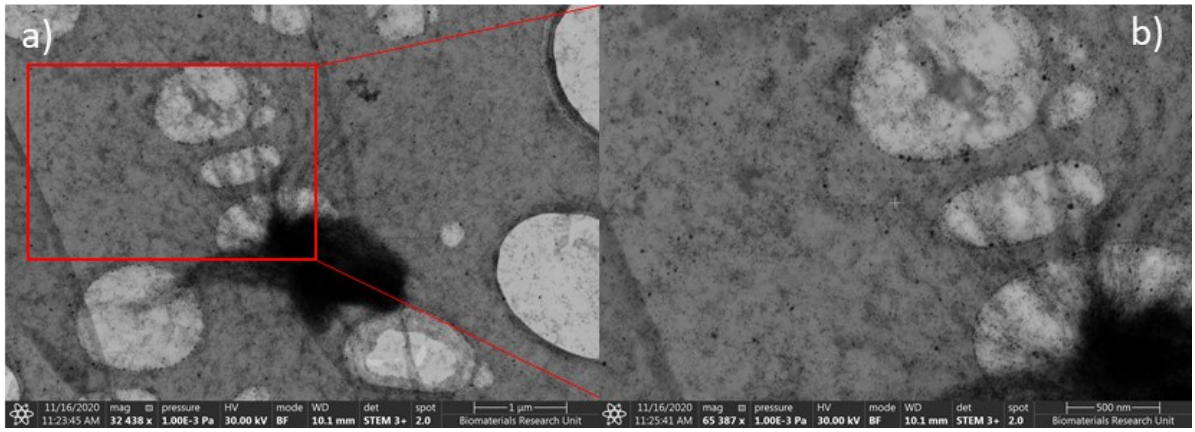

Figure 4-33 Artefact of drying PHMB-AgNPs to form a) large cluster with particles agglomerated, and particles in the vicinity interacting with it. The red square in image a) is shown under larger magnification in image b)

The substrates used during synthesis were poly(hexamethylene) biguanide hydrochloride, silver nitrate and sodium borohydride. It is possible that sodium and chloride ions remained within the sample. During the imaging of the Jul20 samples, round features were observed (Figure 4-34a) and analysed using EDX, and showed a very strong signal for silver (Figure 4-34b), sodium (Figure 4-34c), and chloride (Figure 4-34d) presence in the large particle. This suggests that in the dry state, sodium chloride salt with AgNPs can form,

confirming that the ions remain within the sample. This presence is important from the perspective of EDX analysis of the samples. As previously discussed, both sodium and chloride were detected in the spectral mapping, but without hotspots of concentrations indicating very low concentration. Nevertheless, there may be elements of stability that the counterions provide to both negatively charged silver and positively charged PHMB.

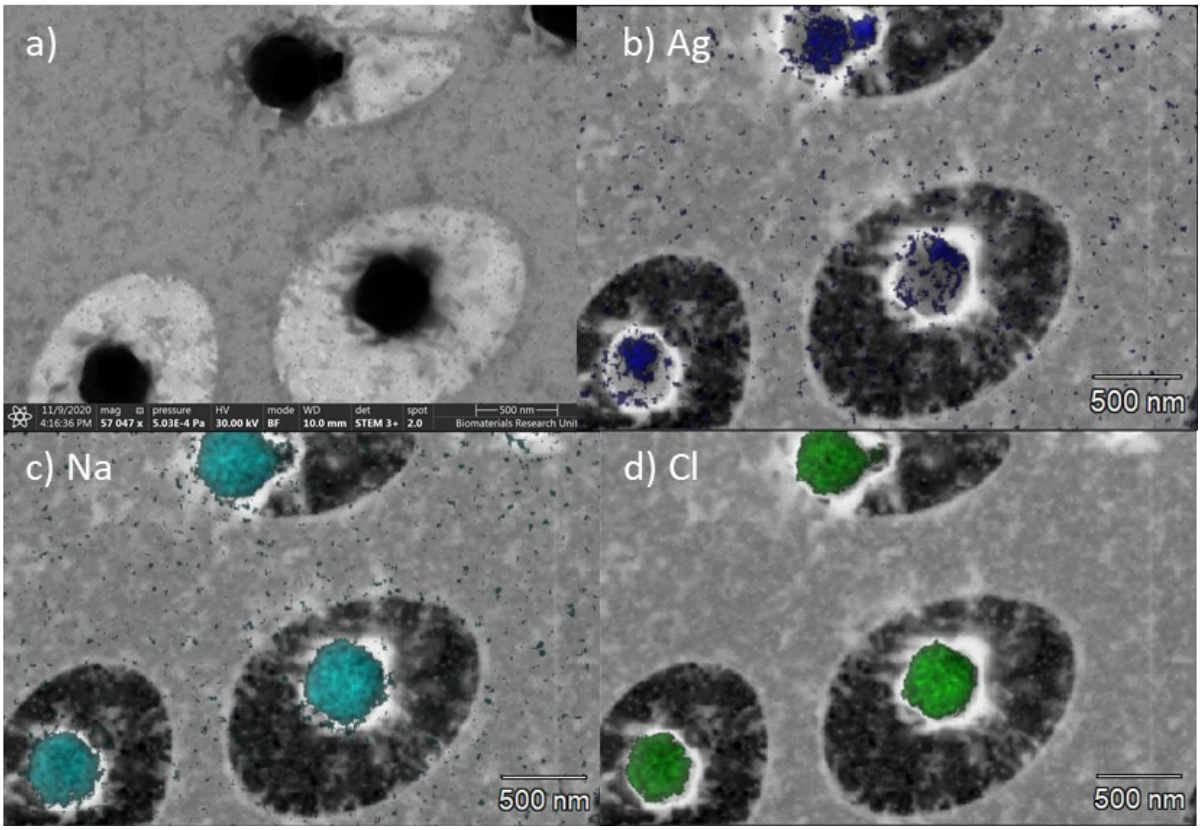

Figure 4-34 a) Large spherical objects were observed for Jul20 200 µg/ml PHMB-AgNPs. The EDX analysis has shown that they were composed of b) Ag, c) sodium and d) chloride.

When using electron microscopy, it was not always possible to be sure what was under observation. Various objects of unclear origin were often noted within the image. An example of such an irregularity collected using EDX shows what appears to be two larger particles of silver (Figure 4-35a) is actually a particle of silver and another of iron (Figure 4-35b). In such cases, DLS would not be able to differentiate between the different materials, this would skew the results for the intensity distribution of the particles due to their larger size.

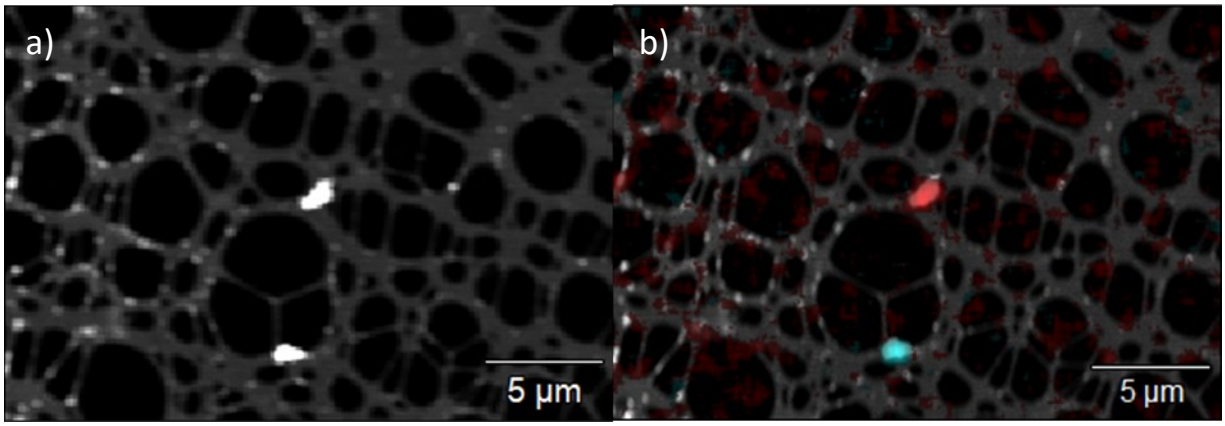

Figure 4-35 a) STEM-in-SEM image obtained as part of EDX analysis, and b) the same image with elemental mapping superimposed showing silver in red and iron in light blue.

Interesting features appeared in some of the images. In the Bare-AgNPs, an amorphous mass with a large number of differently shaped particles was observed in STEM-in-SEM mode. This surprising find was also imaged using the ETD detector, showing that particles were within it. The origin and composition of the features are unknown, but EDX mapping would allow for detailed analysis. Similar features were observed in PHMB-AgNPs, and it was initially thought that the formations were the result of polymer gelation with nanoparticles present. It was, therefore, unexpected to observe such features in Bare-AgNPs without the presence of PHMB.

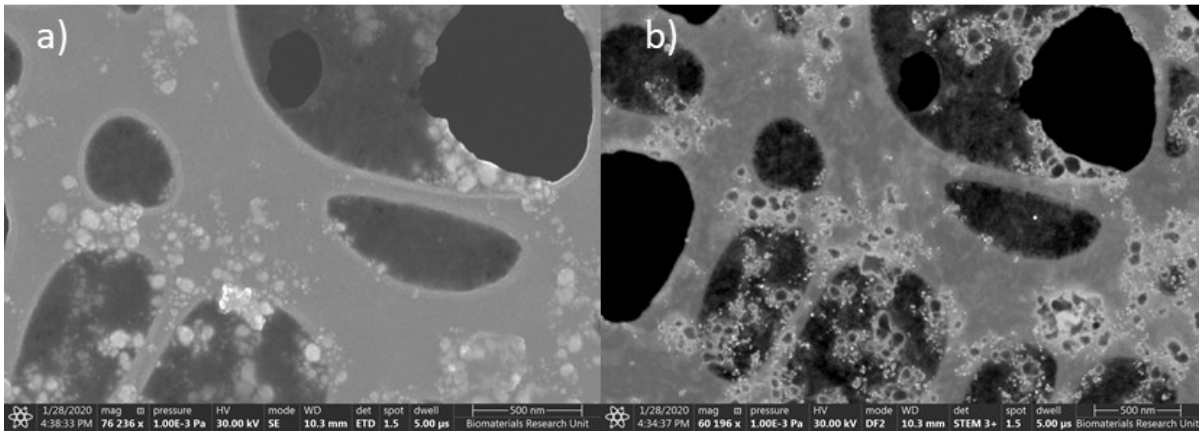

Figure 4-36 Images of Bare-AgNPs taken using a) EDT and b) STEM-in-SEM showing silver nanoparticles present within an amorphous mass. Similar features were observed for various concentrations of PHMB-AgNPs as well.

4.2.3. Summary

The results above brought together data obtained using different methodologies for silver nanoparticles, defining the limits of their applicability and discussing the irregularities noted during collection. The data acquired showed good reproducibility of results between different batches synthesised and marked important differences in samples obtained with increasing concentrations of PHMB resulting from the interaction between the polymer and the silver nanoparticles. The impact of this interaction was reflected in the variables observed for the purpose of investigating size, shape, polydispersity, material analysis and the impact the interaction has on the aggregation and antimicrobial activity of this novel agent.

4.3. Discussion of complex characteristics

The following section discusses the results presented above in a holistic manner to provide an explanation of the physical properties and particle behaviour observed.

4.3.1. Size and shape

Size and shape are important physical properties of the silver nanoparticles, stabilised or not. These features have been widely reported in the literature as having a key impact on the antimicrobial properties of AgNPs [155].

The SPR peak is very sensitive to the shape of the particle. The lambda max between 390 and 430 nm gives a strong indication that the AgNPs were spherical [12]. ESEM imaging in both WetSTEM and STEM-in-SEM modes confirmed this shape. Analysis using SAXS indicated that the aspect ratio for the newly synthesised PHMB-AgNPs varied between 1 and 1.82, suggesting some distortion from a perfect sphere.

Three different methods of sizing have been used in this study: intensity-based– DLS; volume-based – SAXS; and number based – SEM. Very different principles govern these techniques. SAXS and SEM measure the electron-dense silver nanoparticles, but only so many measurements can be taken using image analysis, whereas the use of the synchrotron X-ray

beam obtains a scattering of many more particles at once. As a result, the mean of the particle from SAXS was expected to be greater than that of SEM. Although the results (Figure 4-37) of this study do not follow this expectation, the SAXS modelling did not take into account the low q region of the pattern were larger particles and aggregates would be located, while the SEM included a range of particles visible. However, both SAXS and SEM showed a similar pattern of particle sizes formed in the synthesis of AgNPs. The mean size, initially around 13 nm for Bare-AgNPs, reduces as the PHMB is added to the synthesis process. The colloidal stability of the particles no longer has to be achieved by an increase in the size of the silver nanoparticles, but instead is provided by the presence of polycationic polymer chains. Once the availability of the AgNPs complexation sites was exhausted at a concentration of around 60 - 80 µg/ml PHMB, further addition of polymer has a limited impact on the size of silver nanoparticles.

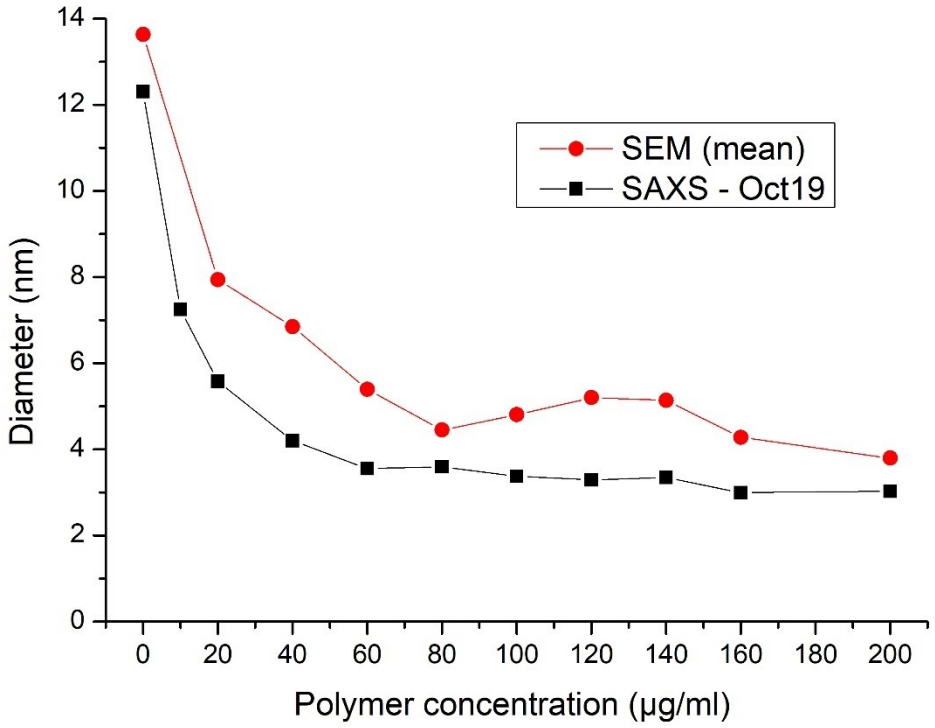

Figure 4-37 Mean sizes of the particles obtained from SAXS and SEM analysis. Bare-AgNPs presented as concentration of 0 µg/ml.

DLS operates by correlating the intensity of scattering against the motion of the particle at the shear plane to determine the hydrodynamic diameter, which would be expected to be larger than with the other methods used. The z-average for Bare-AgNPs at around 23 nm was in line with those expectations, but the trend of change from Bare-AgNPs and 20 µg/ml PHMB-AgNPs is reversed compared with the SEM/SAXS trend for the same measurements (Figure 4-38).

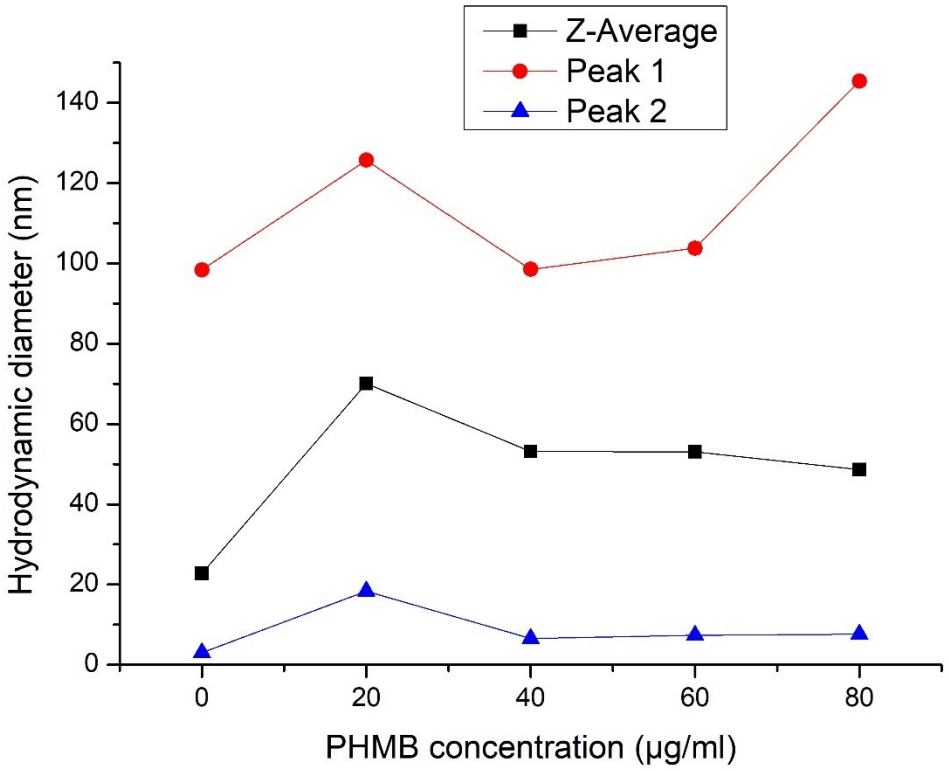

Figure 4-38 Results for hydrodynamic diameter given by DLS showing variation in the size of the particles against the concentration of PHMB used during the synthesis. The multimodality of the sample relied on the z-average problematic and the sizes of the individual peaks are therefore presented. The Bare-AgNPs are marked as 0 µg/ml PHMB concentration.

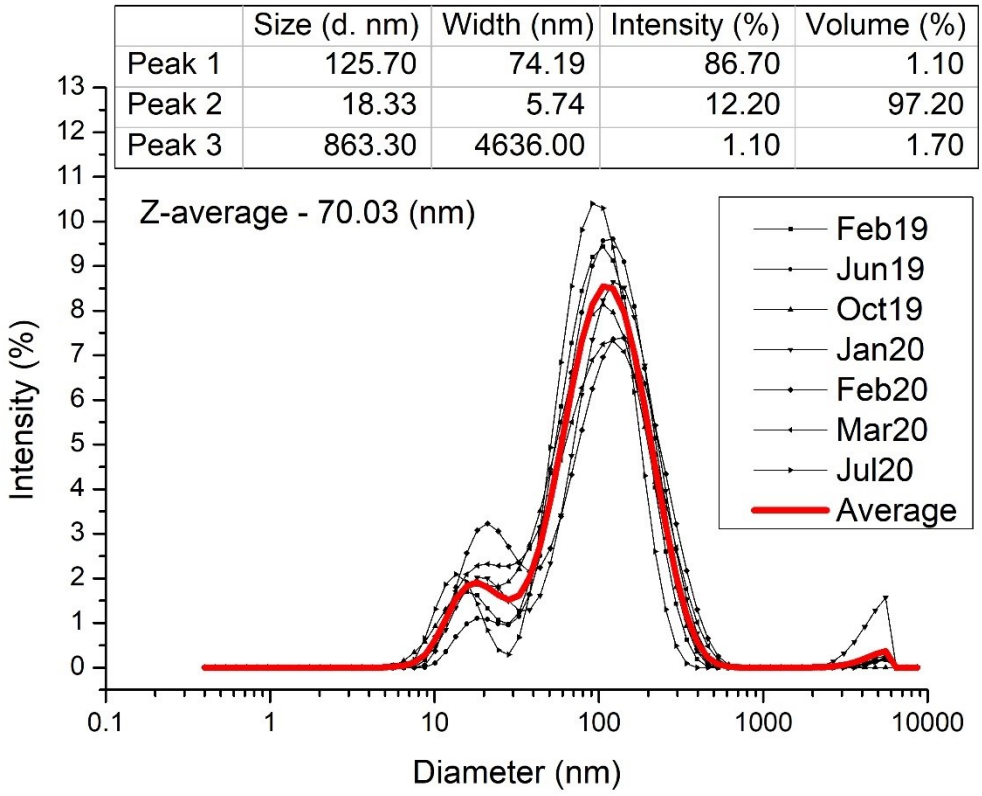

Figure 4-39 DLS results for 20 µg/ml PHMB-AgNPs for all available data. The table insert shows the peak analysis (position and width) with the percentage that the size contributes to intensity and volume distribution.

Careful consideration must be given to the 20 µg/ml PHMB-AgNPs (Figure 4-39) to explain the considerable increase in the hydrodynamic diameter of the nanoparticles recorded using DLS. Investigation of the volume distribution also suggests that the smaller peak at 18 nm was significantly larger than in the results from SAXS and SEM. An immediate conclusion was that the increase in size results from an increase in the shell of the polymer around the nanoparticle, but such an occurrence would result in a greater lambda max recorded using UV-Vis. For 20 µg/ml PHMB-AgNPs, it was observed at around 405 nm and was in line with the gradual increase between Bare-AgNPs and higher concentrations of PHMB-AgNPs. Alternatively, the polymer provides insufficient shielding of the silver core, causing the extension of the shear plane far beyond expectations. However, the difference between DLS and SAXS/SEM measurements was much greater than anticipated, even when compared to those recorded for other concentrations. An important insight into the explanation was provided

by the results obtained for 10 µg/ml PHMB-AgNPs. These can be summarised as in line with the SAXS measurements, showing a continued reduction in the size of silver nanoparticles, yet DLS showed even a greater increase in the hydrodynamic diameter of the particles than for 20 µg/ml PHMB-AgNPs. The UV-Vis for the 10 µg/ml PHMB-AgNPs was highly unusual when compared to the other concentration. It has a double peak and the FWHM was therefore much greater compared with any other sample. The FWHM is sensitive to the silver core; trends similar to those for SAXS and SEM were expected, but instead, it followed the same trend as the DLS measurements. Two distinctions should be made: the Bare-AgNPs and PHMB-AgNPs differ significantly in the spectra obtained using UV-Vis because it was not only the silver core that had an impact on the peak, but also the presence of the polymer and the interaction between the two agents. Therefore, a direct comparison cannot be made between Bare-AgNPs and PHMB-AgNPs. Secondly, the much greater FWHM for 10 and 20 µg/ml PHMB-AgNPs compared with other concentrations as a result of the presence of larger particles must be considered. The double peak in the 10 µg/ml PHMB-AgNPs UV-Vis spectra indicates that two populations of particles were present and that this was directly related to the concentration of polymer used. For 20 µg/ml PHMB-AgNPs, this population of AgNPs was already present within the sample but was masked within the spectra obtained, though it caused a broadening of the peak recorded. This subtle change in the UV-Vis was amplified in the intensity-based DLS measurements, causing an increase in the Z-Average and the three populations recorded. DLS was simply too sensitive to the larger particles so the major population of small particles detected by SAXS and SEM was masked and remained undetected [95]. The analysis of the long-term stability presented in Chapter 6 below further discusses these results.

The remainder of the partial DLS results available for 40, 60, and 80 µg/ml PHMB-AgNPs show a z-average at around 50 nm, which is significantly greater than the results from SAXS/ESEM. However, if the volume-based distribution is considered, the second peak,

representing a population of small particles around 7 nm in diameter, becomes dominant and fits well with the other sizing techniques, albeit slightly larger as it represents a hydrodynamic diameter (Figure 4-40).

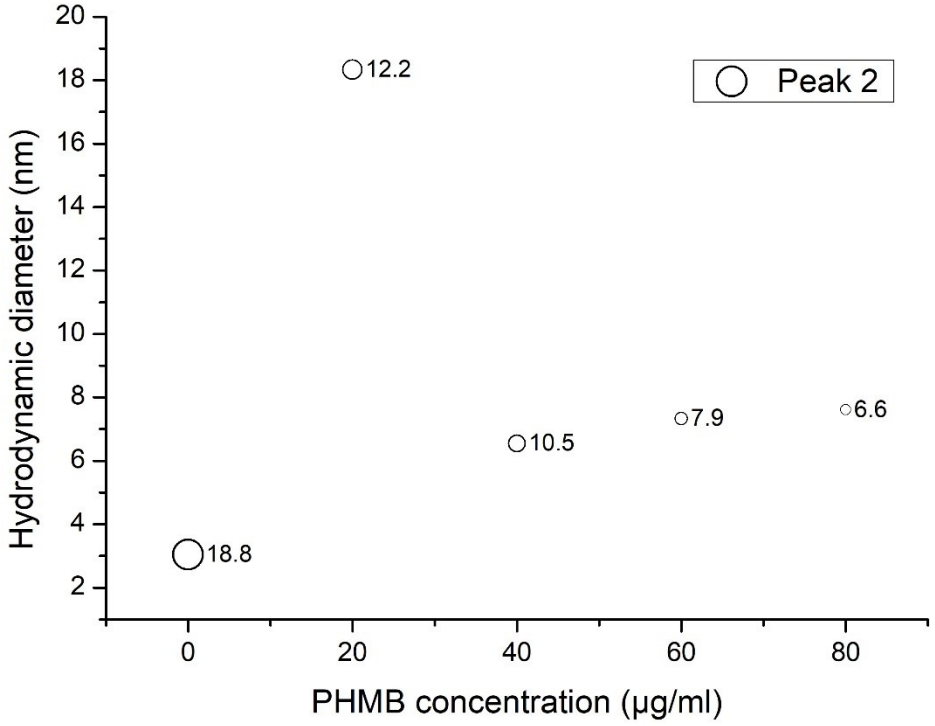

Figure 4-40 DLS results for the hydrodynamic diameter for the minor peak detected in the intensity distribution with the size of the circle (scale: 1) corresponding to the percentage contribution to the overall distribution.

It was not possible to fully explain why the Bare-AgNPs were smaller than PHMB-AgNPs when measured using DLS, also including the smaller population sized at *ca*. 3 nm. One possible explanation involved the greater polydispersity of the Bare-AgNPs. The intensity of the peaks was much lower compared with PHMB-AgNPs suggesting a wider distribution of the particles. Alternatively, the difference may have been that the SAXS and DLS measurements were taken in different dilutions: for SAXS, undiluted samples were used, whereas, for DLS, the samples were diluted in deionised water. The change in concentration might have impacted the results obtained due to the change in the colloidal environment of the nanoparticles.

4.3.2. PHMB presence and interaction

Upon addition of the PHMB to the AgNPs synthesis, the UV-Vis spectra shifted to a higher wavelength, and lambda maximum gradually increased from 390 nm for Bare-AgNPs to around 430 nm for 200 μg/ml PHMB-AgNPs. This was the result of an interaction between the polymer and silver nanoparticles; the zeta potential (ζ) measurements showed a complete change of direction of travel under the applied voltage. Values for ζ remain about the same regardless of the increase in the polymer concentration, suggesting that it was the PHMB that provided stability to AgNPs and not any other material or substance. However, the addition of the polymer to the synthesis process ceased to meaningfully affect the size of the silver nanoparticle in samples around 60 μg/ml PHMB-AgNPs and higher. Moreover, from this concentration onward, there was evidence from flow cytometry that the antimicrobial property of the infranatant had begun to appear. This antimicrobial effect was of the same nature as that noted for the PHMB itself, indicating that the polymer was removed from the PHMB-AgNPs during the centrifugation process. The antimicrobial effect gradually increased, suggesting there was a natural limit to mass, volume or the number of polymer chains available to interact with the silver nanoparticles, and that the excess was partially removed. This was not a fixed amount, however; the lambda max continued the red shift, and the polymer presence increased, but the pace of change was much reduced. The same pace of change was observed in the size reduction determined by SAXS and SEM. Imaging of the particles also showed that in STEM-in-SEM, areas of gel only were observed. Such uncomplex PHMB was prone to separation and removal during the centrifugation process. The precise mode of interaction between PHMB and AgNPs has not been fully assessed. Some indications are discussed in Chapter 5 below, but the assertion is that the biguanide groups interact with the surface of the silver particle. As the polymer concentration increases, the polymeric shell formed between PHMB and AgNPs was less densely packed and gave rise to interactions between polymer chains of neighbouring particles. These short-lived interactions did not have any impact on the

hydrodynamic diameter recorded but did cause the number fluctuations observed in DLS, which gradually decreased the reliability of the data obtained using this technique. Because the interactions were short-lived, the SAXS pattern modelling was unsuccessful in including the structural factor, and the low Q of the patterns, where aggregates and agglomerates are typically found, had to be excluded from the analysis.

4.3.3. Antimicrobial properties

Antimicrobial activity was measured using a zone of inhibition and flow cytometry. ZOI showed a significant increase in biocidal effect for the silver nanoparticles synthesised in the presence of PHMB. However, when further investigation was carried out using flow cytometry, it was noted that the increase in PHMB in the synthesis process had a limited effect on antimicrobial activity. In addition, antimicrobial activity occurred mainly in Q2 of the graphs, indicating that the bacteria were damaged rather than dead. A similar effect was previously found for PHMB alone, as well as for the infranatant obtained from the centrifugation process. Therefore, the antimicrobial activity measured using the methodology described previously can be ascribed to the presence of PHMB rather than the AgNPs. It has been shown in this study that Bare-AgNPs had no or very limited antimicrobial activity on their own. The biocidal effect of the infranatant indicates that PHMB was removed from the reaction solution during the centrifugation process. It was not possible to assess the concentration of the PHMB in the solution, but some estimates were made based on mass balance, showing that the concentration was comparable to that found in the multipurpose solution used for contact lens care [156].

4.4. Conclusions

The results from zeta potential confirmed that the PHMB and AgNPs form a complex. Even in the lowest concentration widely tested, 20 µg/ml, the PHMB-AgNPs became strongly positive. Increasing concentration of the polymer produced an observable decrease in the size of silver nanoparticles as observed with SAXS and SEM. Following the initial change in size,

from concentrations of around 80 µg/ml PHMB-AgNPs, a further decrease was much less pronounced. The same trend was observed in the positioning of the UV-Vis peak. The initial shift of the peak from around 390 nm to around 415 nm for 60 µg/ml PHMB-AgNPs was followed by a slow increase to 430 nm for 200 µg/ml. In opposition to SAXS, SEM, UV-Vis, which are methods based on the silver nanoparticles only, DLS measure hydrodynamic diameter which takes polymer into account. Those results showed an initial increase in size (for 20 µg/ml PHMB-AgNPs), which can be assigned to the detection limits of the methodology, which resulted in larger particles overpowering the resolving capacity of the equipment. However, they can also be indicating patch flocculation of the particles due to insufficient coverage of the particle with the polymer. The increase in the polymer involved in stabilising was limited, as there was evidence that it was removed in the centrifugation process. It was not, however, limited to a specific concentration, data from SAXS, SEM, UV-Vis continue to show changes to the size of silver nanoparticles. While the DLS shows an increasing number fluctuations affecting the quality of data, caused by short-lived long-distance interaction between particles – bridging flocculation. The presence of PHMB in the complex caused significant improvement in the antimicrobial effect recorded, while the Bare-AgNPs showed limited activity against bacteria. However, the improvement was due to the presence of the polymer, and the AgNPs were not activated as a result of stabilisation under the conditions tested.

Chapter 5. Formation of PHMB-AgNPs – interaction between silver nanoparticles and poly(hexamethylene biguanide) stabiliser

5.1. Introduction

The physical properties of the PHMB-AgNPs described in the chapters above are a result of the synthesis process. The size, shape, stability, and other variables defining the behaviour of the nanoparticles are a product of conditions during the synthesis process. Gaining insight into the formation of the particles is therefore important for better understanding how nanoparticle properties develop as well as providing tools for control.

A commonly found approach is to consider the nucleation of nanoparticles through the classical nucleation theory (CNT) [157, 158]. The nucleation occurs via homogeneous or heterogeneous processes at the same time. The former, due to the supercritical state, allows for the calculation of the critical radii – the first stable particle, nuclei. The latter as a nucleation at the interface between the solid state and the liquid or vapour. The addition of a reducing agent such as sodium borohydride initiates a fast reduction of ionic to atomic silver, thus causing supersaturation. The homogeneous nucleation is driven by the reduction of Gibbs free energy occurring as the bonding of monomers causes a decrease in the Gibbs bulk free energy ($|G_V|$) per unit volume. While the surface energy per unit area (γ) is increasing. Change in Gibbs free energy (ΔG) remain negative until a certain maximum radius is reached and the nucleation is no longer spontaneous, so the Eq. (5-1) becomes > 0.

$$\Delta G = -\frac{4}{3}\pi r^3 |G_V| + 4\pi^2\gamma \qquad \textit{Eq. 5-1}$$

Alongside the rapidly occurring homogenous nucleation, the heterogenous nucleation takes place at the interfaces, where the activation energy required is lowered. LaMer's theory advances the classical nucleation theory, by separating the two processes [157, 158]. The first stage of rapid nucleation is due to the supersaturation of monomers (homogeneous) leading to slow growth by adsorption to formed particles (heterogeneous). The process is often described

as a seed-growth process. It is important to note that the CNT and LaMer's mechanism were extended to metal nanoparticles rather than developed based on them. Unfortunately, often the data observed, i.e. for silver nanoparticles synthesised using sodium borohydride [159] does not always support this universal theory but instead suggests alternatives such as the Ostwald ripening and Digestive ripening. In which particles dissolve and reabsorb back on to the larger (for Ostwald) or smaller (for Digestive) particles with the process being driven by the reduction of their surface-to-volume ratio [158].

Another alternative explanation for silver nanoparticles formed without the addition of a stabiliser (Bare-AgNPs) was presented by Polte and his research team [157, 160-162]. These detailed studies using time-resolved SAXS to investigate the nucleation and growth process concluded that it occurred in four stages, that reduction and nucleation led to a final metastable state, and that coalescence of the particles occurred in short periods of time between the other stages. Following the initial reduction and nucleation, the mean particle size grew to about 2-3 nm, when the silver nanoparticles achieved colloidal stability. This was provided by the borohydride ions BH_4^-; however, at the same time a competing reaction takes place:

$$BH_4^- + 4H_2O \rightarrow B(OH)_4^- + 4H_2 \uparrow$$

As the ion was consumed to release the hydrogen, Wuithschick *et al*. [161] showed that the borohydride ion was fully used by the time the new colloidal stability was achieved. Furthermore, it was suggested that the decrease in colloidal stability was caused by the formation of silver oxide on the surface of the nanoparticles resulting from full consumption of the borohydride ion and that the abrupt surface modification led to coalescence. As a result, a degree of control over the synthesis reaction can be achieved by using a mixture of fresh sodium borohydride with one that has already been fully hydrolysed.

The literature available in relation to the nucleation and growth of silver nanoparticles is not conclusive. Often the presented data fit into the CNT, LaMer or one of the alternative

theories. The purpose of this study was to establish if characterisation data obtained at the intervals throughout the reaction can inform on the nucleation and growth of the AgNPs and if a degree of control can be exhibited over the reaction process.

5.2. Characterisation

Light spectroscopic methods such as dynamic light scattering (DLS) and visible light spectroscopy (UV-Vis) can be particularly useful due to their ease of use. The nanoparticles are produced in suspension; therefore, the sample preparation only requires concentration adjustment but remains in its native state. The sample remains intact following characterisation. Although both methods rely on light being scattered or absorbed, different processes are involved.

It was noted during the observations of the synthesis reaction that the solution in the beaker changes colour over time. The change observed was often dramatic, from light yellow to very dark burgundy. To track the colour of the reaction against time, a camera was set up to record the synthesis process. This method, developed for this research, is not sufficiently scientifically robust to provide conclusive information about the process under observation, but the recording was very helpful in tying the data from DLS and UV-Vis together. As neither of those methods were *in situ*, there was occasional delay between the time the samples were taken. The change in colour, tracked as Mean Gray Value, provided a valuable timeline and visual indication for the changes observed.

5.3. Methodology

5.3.1. Synthesis

Standard reaction (SR Samples)

The synthesis reaction methodology was described in Chapter 2 Methodology and Materials in section 2.1.1 Standard reaction, and is repeated here in abridged form for convenience. These samples are referred to as SR samples for the purpose of this Chapter.

At room temperature, an aqueous solution of PHMB (15 ml, various concentrations but between 20 and 200 µg/ml) was added to an aqueous solution of silver nitrate (25 ml, 1 mM) and left for two hours under vigorous stirring using a magnetic plate. A freshly prepared aqueous solution of sodium borohydride (5 ml, 0.8 mg/ml) was then added to the reaction. The reaction was left stirring for five hours and then kept for 24 hours in a dark cupboard before placing the suspension in the centrifuge filters (Amicon Ultra 15 filters) and spinning for 10 minutes at 6000 rpm. The silver nanoparticles were then pipetted out to a sample vial and stored in the cupboard at room temperature.

Kinetics reactions (KR Samples)

At room temperature, aqueous (fresh deionised water from a "Purite Select" purification system) solution of PHMB (Cosmocil® CQ 20%, Lonza – 20% aqueous solution) (15 ml, various concentrations) was added to an aqueous solution of silver nitrate (Sigma-Aldrich, >99%) (25 ml, 1 mM). Two identical reaction beakers were prepared; the first was stirred for about 50 minutes and the second for 2 hours before the addition of a freshly prepared aqueous solution of sodium borohydride (Merck-Millipore) (5 ml, 0.8 mg/ml) to the reaction. The reaction was left stirring for five hours. During this time, aliquots were extracted regularly by pipette for characterisation using DLS and UV-Vis. Samples were not centrifuged.

Sodium borohydride reactions (SB Samples)

At room temperature, aqueous (fresh deionised water from a "Purite Select" purification system) solution of PHMB (Comsocil® CQ 20%, Lonza – 20% aqueous solution) (15 ml, various concentrations) was added to an aqueous solution of silver nitrate (Sigma-Aldrich, >99%) (25 ml, 1 mM). Reaction beakers were stirred for 50 minutes before the addition of sodium borohydride (Merck-Millipore) (5 ml, 0.8 mg/ml) solution to the reaction. Five different $NaBH_4$ were used, as presented in Table 5-1. The old solution was prepared well in advance, with a small amount of $AgNO_3$ added to confirm that it was fully hydrolysed: if no visible change of colour took place, the solution was used for the reaction. The reaction solution

was left stirring for five hours. During this time, aliquots were extracted regularly by pipette for characterisation using DLS and UV-Vis.

Table 5-1 Ratio of the fresh to old NaBH4 used during the synthesis process.

Fresh $NaBH_4$	Old $NaBH_4$
25%	75%
50%	50%
65%	35%
75%	25%
100%	0%

5.3.2. Characterisation

DLS and Zeta potential

DLS and Zeta Potential measurements were carried out using a Malvern Zetasizer ZSP and analysed using the accompanying software v 7.13. For the KR and SB samples, a 1 ml aliquot was taken directly from the reaction beaker, analysed as is, and then discarded. Three measurements were taken with automatic settings for position and number of runs. For the SR samples, an aliquot of 40 µl of a sample was dissolved in 1 ml of DI water and six measurements were taken with automatic settings for position and the number of runs. The samples were analysed in PE single use cuvettes. Zeta potential was measured only using the SR samples using folded capillary cell with automated settings for the number of runs.

UV-Vis

For the SB and KR samples, a 1 ml aliquot was taken directly from the reaction beaker, mixed with 1 ml of DI water, analysed and then discarded. The SR samples were prepared by adding 2 µl of PHMB-AgNPs to 2 ml of deionized water and analysed using a SpectraMax M2 by Molecular Devices using SoftMax Pro 5 software and a 10 mm quartz cuvette. Due to the time required to complete the measurement, the wavelength was adjusted by 10 nm rather than the 1 nm used for SR samples.

Image analysis

The reaction was recorded using a Sony Z5 23-megapixel camera in HD mode (30 frames per second). The reaction beakers, frosted PE 80 ml containers, were placed on the magnetic stirrers in the fume cupboard with the light on in the cupboard to ensure consistent lighting (external lighting was time/motion controlled and would switch on/off at times). The recording was transferred to a computer and VLC software was used to create individual stills every one second for further image analysis using ImageJ software. A screen grab of each of the images was collected and analysed with measurement for Mean Grey Value (MGV) including standard deviation (omitted on the graphs for clarity). The same analysis area was used on each still.

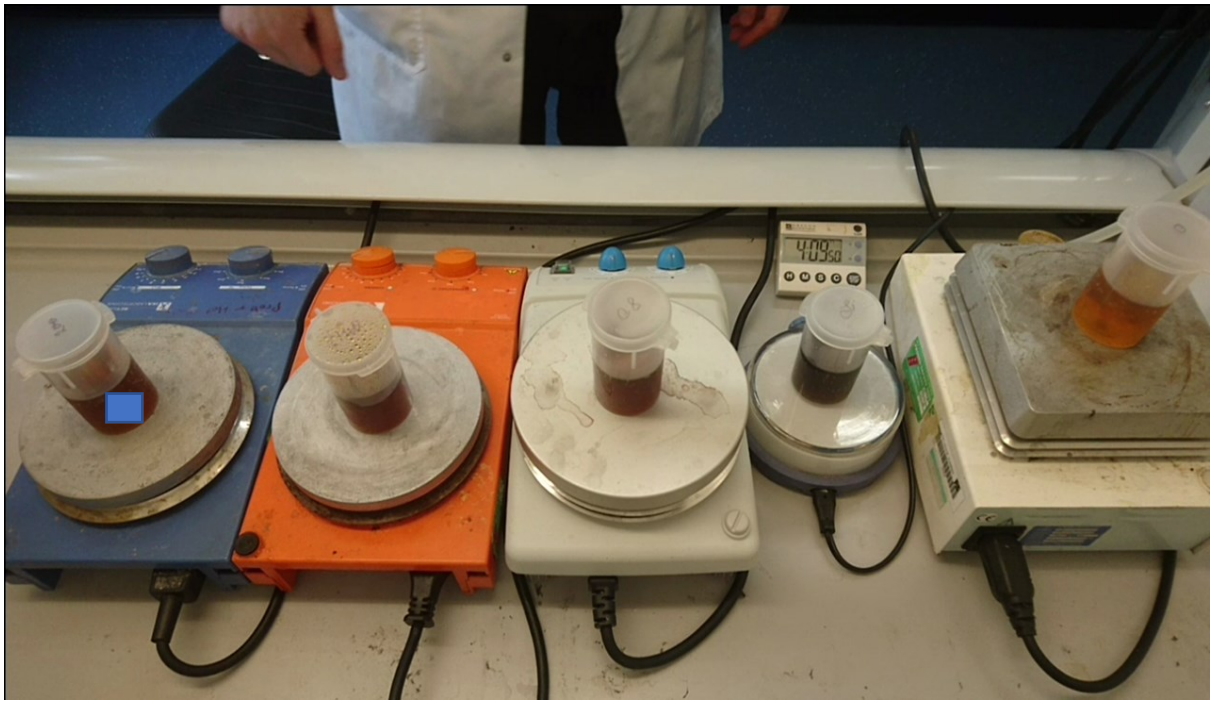

Figure 5-1. Example of a still taken from recording over the synthesis process. ImageJ was used to measure the Mean Grey Value of a square (400 x 400) pixel, rough size marked with a blue insert, the same area was measured over the length of the recording at 1s intervals.

5.4. Results and Discussion

In the previous chapters, samples obtained using standard reactions were extensively analysed and discussed. The results provided a benchmark against which results during the progression of the reaction can be reviewed and compared.

5.4.1. Progression of the reaction

To further study the reaction process, a series of kinetic reactions was carried out. The UV-Vis peaks obtained for the aliquots taken at the start of the reaction showed good similarity across a variety of PHMB concentrations, as presented in Figure 5-2. The significant difference in the spectra recorded with and without PHMB is that the polymer itself has an absorbance at around 236 nm [49] and so the spectra with PHMB drop at the start of measurement. In addition, for PHMB concentrations equal to or lower than 60 µg/ml, the peak is not visible, as the decline of the spectra continues. This caused difficulty in measuring the FWHM for the SB and KR samples, and in any case, making them incomparable with the FWHM obtained for the SR samples. The λ_{max} for those better-defined peaks was in roughly the same location of 390 nm, which was at odds with the SR samples, which exhibited a progressive increase in lambda maximum from 390 nm for Bare-AgNPs to 430 nm for 200 µg/ml PHMB-AgNPs.

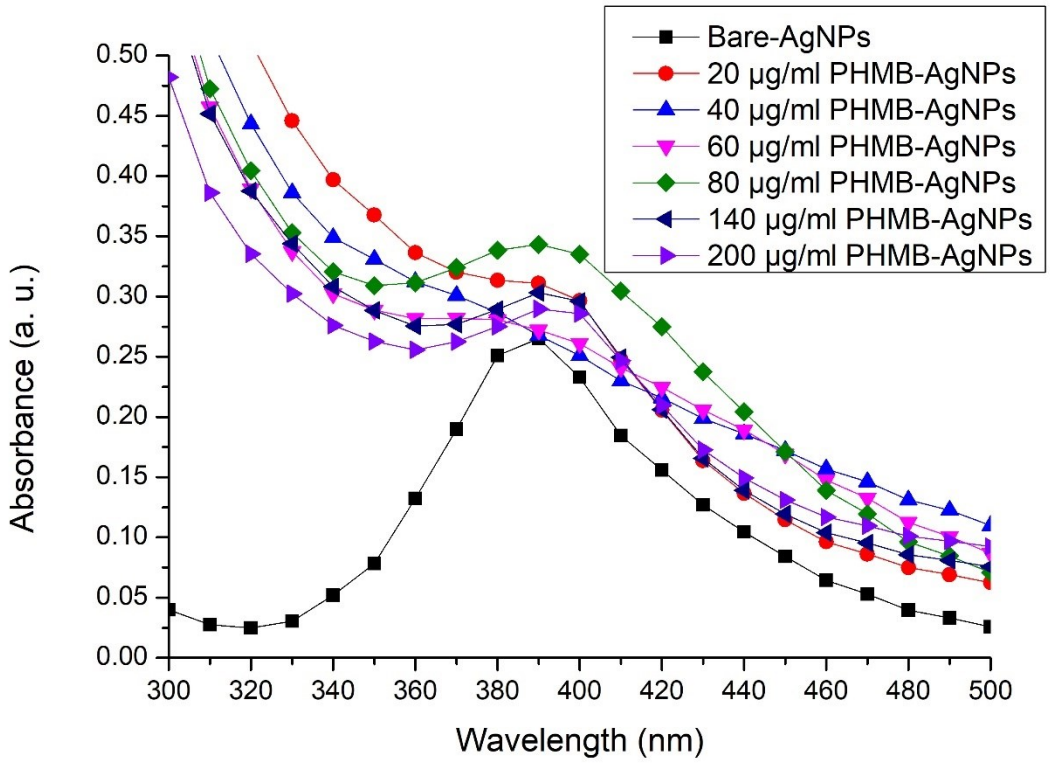

Figure 5-2 UV-Vis spectra obtained for the Bare and PHMB silver nanoparticles for the first measurement in the KR samples taken. The spectra were focused on the peak to assist with clarity.

To better understand how the UV-Vis data altered as a result of the addition of the PHMB to the AgNPs synthesis, tracking of the change in absorbance from 390 nm to 400 nm was introduced (Figure 5-3). In the early stages of the reaction, there was a shift in the position of the peak detected, λ_{max} no longer declined as rapidly as was observed for Bare-AgNPs; instead, for all PHMB concentrations tested, the change was either less negative, or was slightly positive. This very subtle change suggests that there was an interaction between the silver nanoparticles and the polymer stabilising them. It has been shown that the stabiliser causes a red shift for the λ_{max} [90]. However, the change did not increase with increasing stabiliser concentration, confirming that the shift was not related to changes in the refractive index of the solution, but that of the nanoparticles. The sharp increase in the peak difference was due to changes in colloidal stability and is discussed in more detail below.

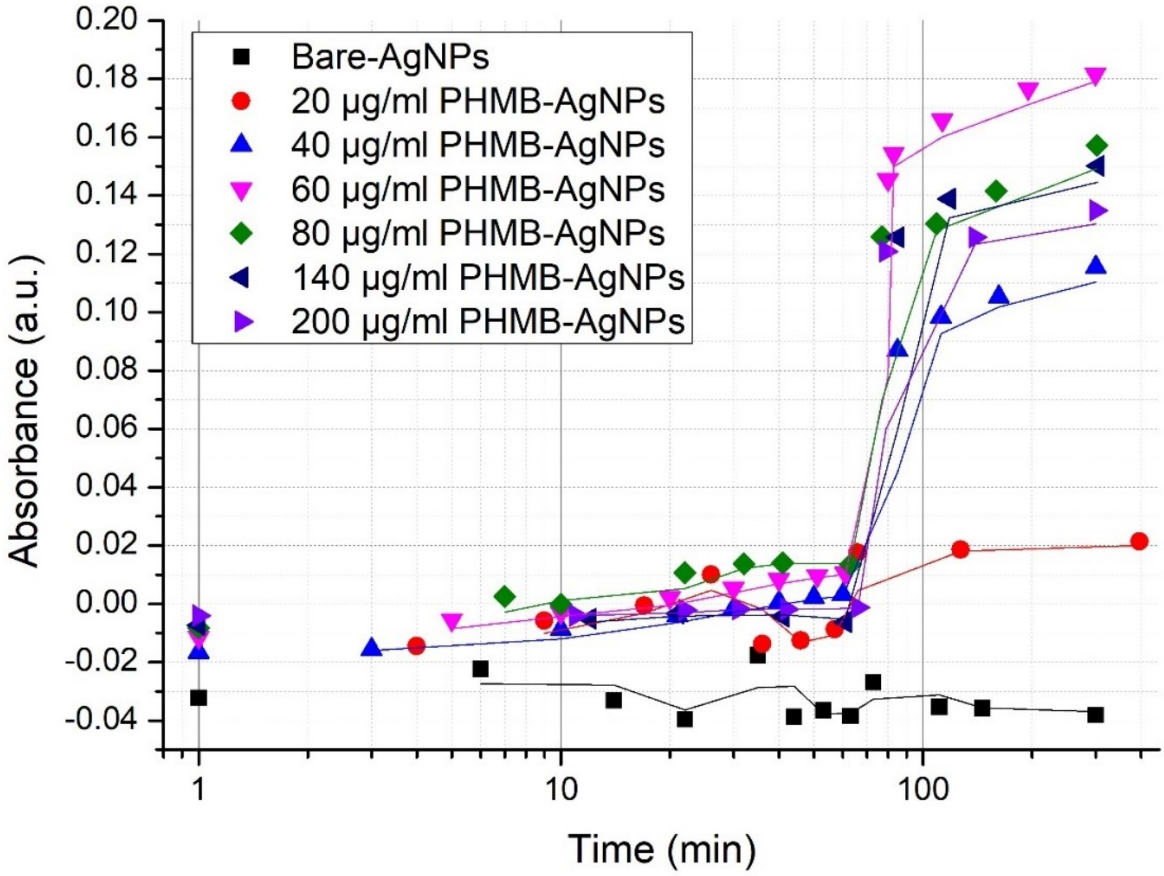

Figure 5-3 Tracking of the change in the peak from 390 to 400 nm showing the shift in the peak position for all of the PHMB-AgNPs. The line in the colour of the symbol used for concentration represents 2 point moving average.

At the same time, the results from DLS indicate that the hydrodynamic size of the nanoparticles has more or less doubled as a result of adding the stabiliser (Figure 5-4). Surprisingly, the doubling was not carried over to the next concentration tested, the 40 µg/ml PHMB-AgNPs.

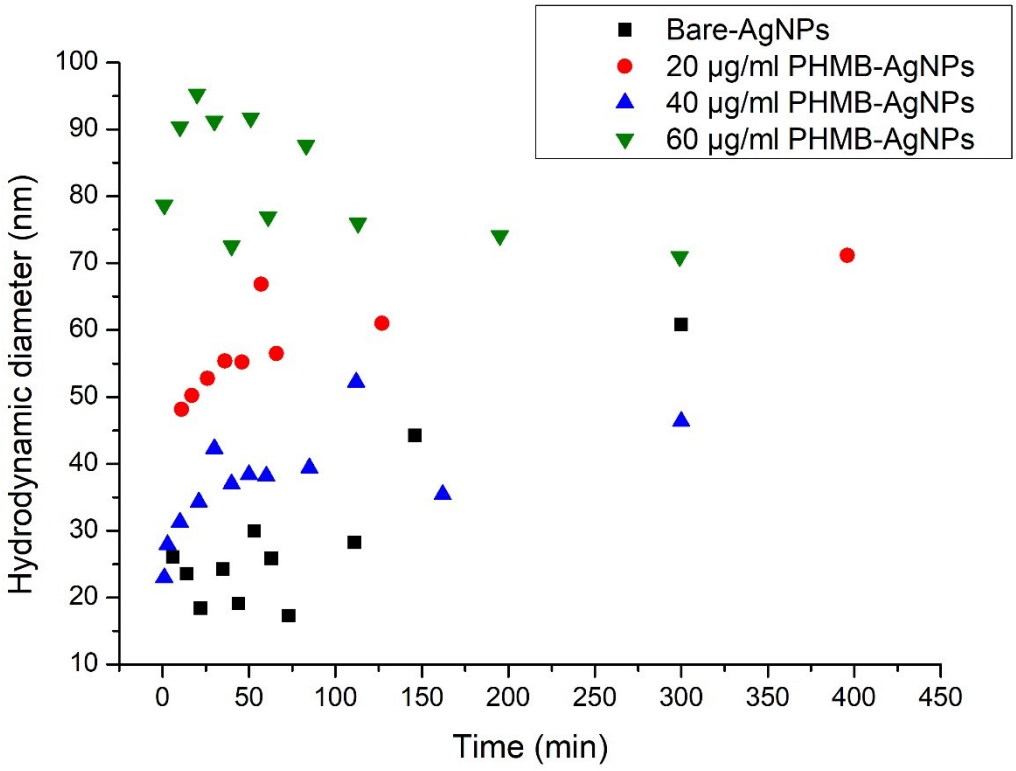

Figure 5-4 The size of the silver nanoparticles as measured by DLS over time of the reaction progression. For clarity, z-average data is used. The line in the colour of the sample symbol represents linear fit.

The Bare-AgNPs were used as a reference to investigate the changes when the stabiliser was introduced. It, therefore, required careful testing to be able to show the formation and the growth process. The video recordings taken for the reaction of the Bare-AgNPs KR samples show minor colour change at around 10 minutes, but in one of the reaction beakers only, and it was not confirmed with confidence. Interestingly, the colour change was observed for the SB samples (see Section 5.5). The minor colour change observed for Bare-AgNPs did not affect the UV-Vis spectra recorded, which all remain remarkably unchanged throughout the five hours of the experiment. The DLS sizing data taken at various points of the reaction did not show any trends in size increases/decreases, even if the peak tracking of the multimodal distributions was introduced (Figure 5-5). It is therefore difficult to support the thesis of staged growth presented by Polte *et al.* [157] using the available methodology.

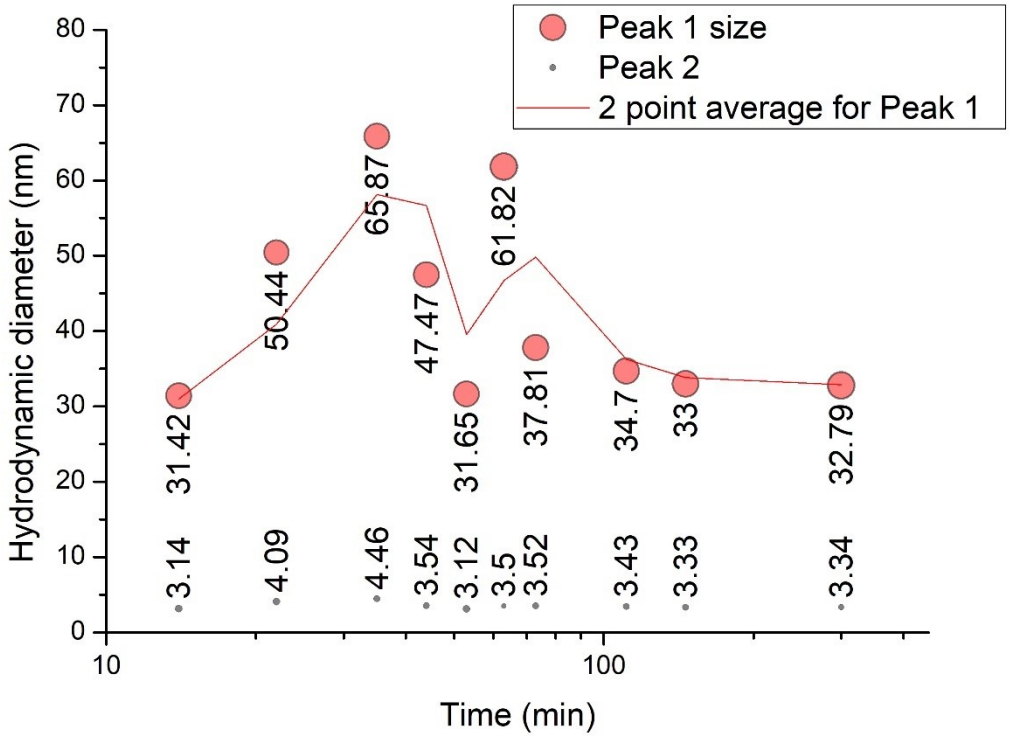

Figure 5-5 Tracking of nanoparticle size over the reaction time with differentiation between 2 sizes recorded using DLS. Bubble width represents the percentage of the size distribution. The standard deviation has been omitted for clarity but can be averaged to about 10 nm for peak 1 and between 1 and 2 nm for peak 2.

When PHMB was used as the stabiliser for the silver nanoparticles, a change in colour would occur at some point (Figure 5-6), but there is a high degree of variability between different experiment trials (see Section 5.5).

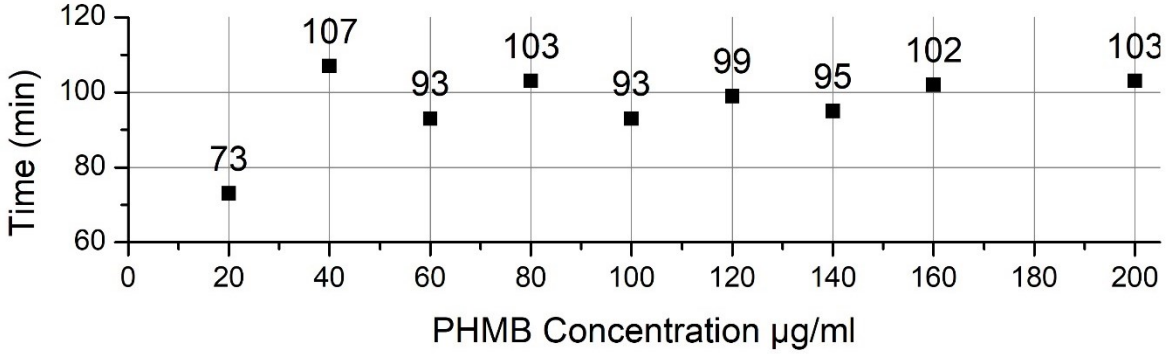

Figure 5-6 Time at which colour change of the reaction solution occurs, rounded to the nearest minute. Colour changes for Bare-AgNPs were not observed in the SR samples but were observed in the SB samples. (See Section 5.5). Time at which the colour changed varied considerable between experiments.

The colour change of the reaction for PHMB-AgNPs occurs at the same time as the changes in the UV-Vis spectra (Figure 5-7), absorbance increases, and the peak recorded broadens and shifts to a slightly higher λ_{max} position. The SPR theory indicates an increase in particle core size due to an increase in the FWHM. The red shift in the peak position, lambda max, should coincide with the increased thickness of the shell [90]. The colour change and the changes in the UV-Vis correspond to other AgNPs stabilised with Poly(vinylpyrrolidone) that also had delayed transition at times between 30 to 180 minutes [160].

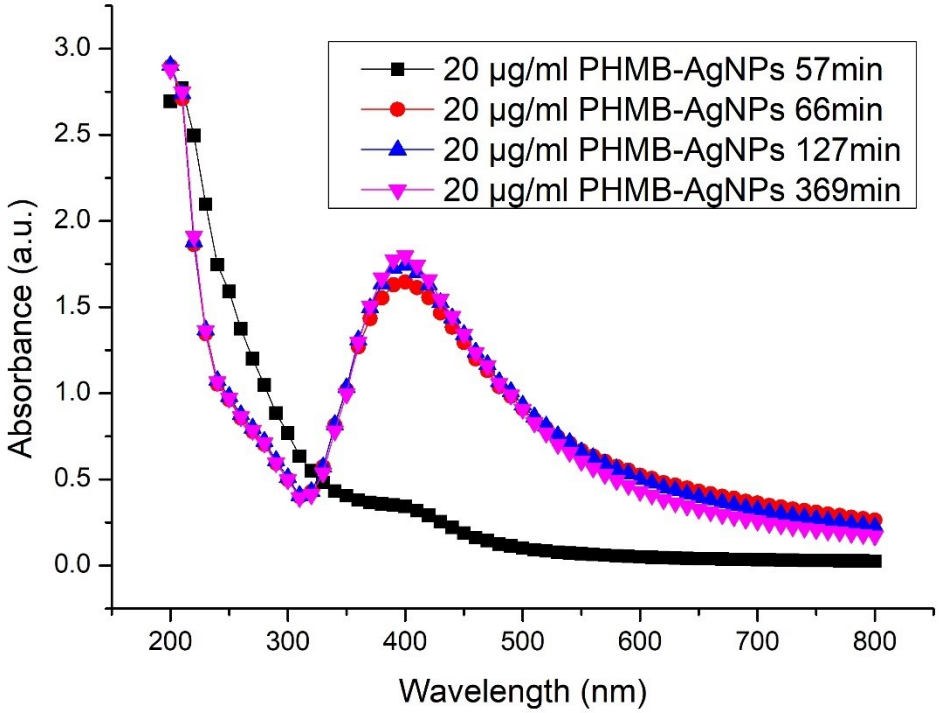

Figure 5-7 Change in the UV-Vis spectra following a change of the colour of the reaction solution indicating a potential change in the silver nanoparticles' size and/or coating

A close investigation of the DLS does not show any changes in the sample that could be associated with the increase in size. Even tracking individual peaks of the multimodal distribution (Figure 5-8) does not permit the conclusion that there is a change in size that could be associated with the second coalescence stage. The same is true of the DLS data for 40 and 60 µg/ml PHMB-AgNPs.

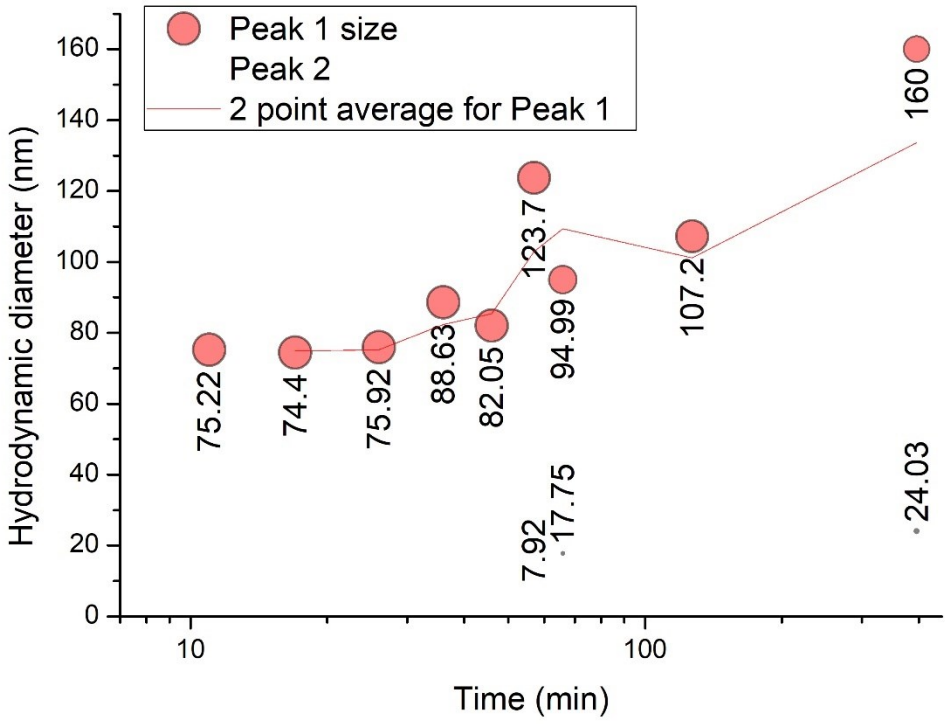

Figure 5-8 Tracking of the nanoparticle size over the reaction time with differentiation between 2 sizes recorded using DLS indicates that size does not change at the time when the colour of the reaction solution and the UV-Vis spectra change. Bubble width represents the percentage of the size distribution. The standard deviation has been omitted for clarity.

Alternatively, the changes observed in the colour of the reaction and the UV-Vis spectra may have been due to the modification of the refractive index of the polymeric shell. It may be posited that following hydrolysis of the borohydride ion, colloidal stability around the silver core transforms the PHMB into a different arrangement, affecting the refractive index in the process.

PHMB as a polyelectrolyte is able to assume a variety of conformations which are driven by van der Walls and Coulomb forces. Interestingly, silver nanoparticles can be considered as large counterions [103] and, therefore, as having an impact on the PHMB conformation. However, as AgNPs are neither mono- nor multivalent ions, the prediction of behaviour for PHMB was not possible. Understanding of the effect was further inhibited by the fact that the AgNPs were formed in stages, with periods of metastable state, meaning that

the charges experienced by the stabiliser may vary as the reaction progresses. The biguanide group exhibits hydrophobic properties, due to the slight positive charge on the carbons within the biguanide group [48].

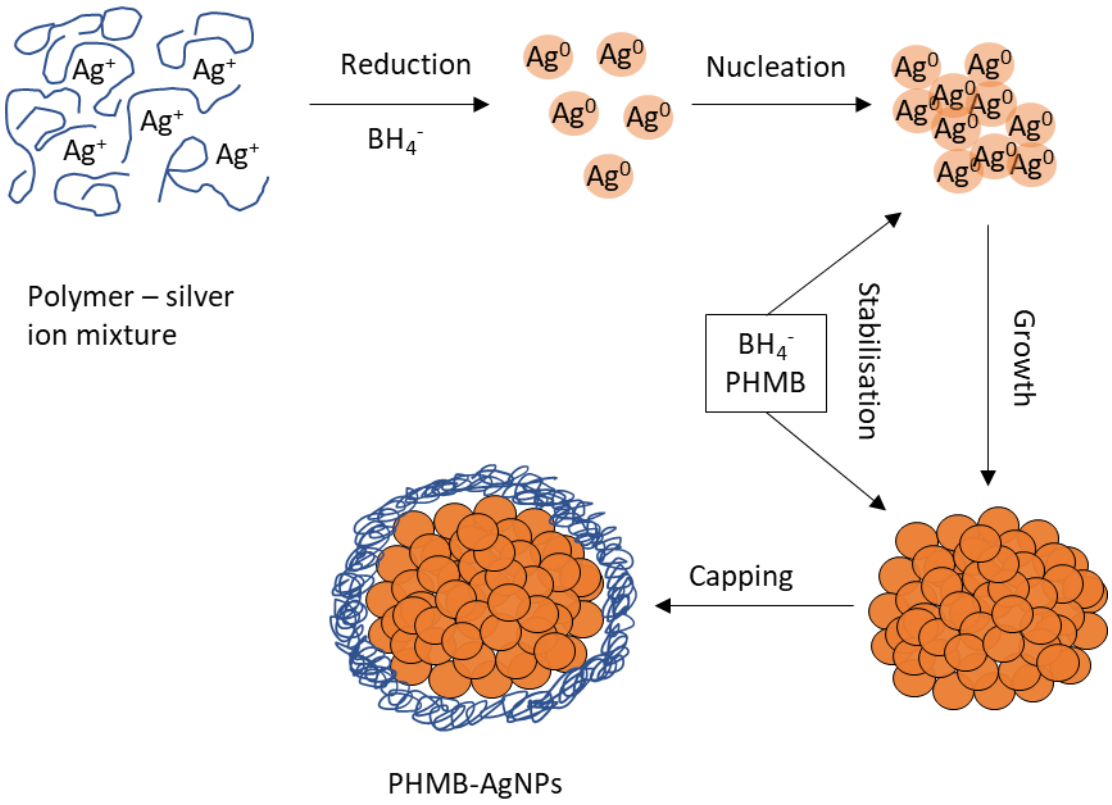

Figure 5-9 Schematic representation of the synthesis process, once the initial stage of nucleation is reached the silver nanoparticles are stabilised by the borohydride ion and the PHMB. As the hydrolysis of BH_4^- occurs change in the colloidal stability leads to the reorganisation of the polymer around the nanoparticle caping the growth.

There must be a saturation plateau when the polymer adsorbed to the surface repeals further adsorption. All silver ions were reduced to colloidal silver immediately with the addition of sodium borohydride. The interaction between the PHMB and AgNPs was therefore immediate, but the borohydride ion was present in the solution and was providing additional stabilisation to the silver core. As hydrolysis of the ion took place, the colloidal stability of the AgNPs was disrupted, leading to the reorganisation of the PHMB shell rather than coalescence (Figure 5-9).

PHMB has a number of tautomers in the unionised form which can be ionised +1 or +2 with pKa of around 13.5 for the +1 and 2.18–3.19 for the +2 form, hence the +1 being the prevalent form in these experiments. Based on the computational modelling, the most stable form of +1 charge delocalised over the biguanide group with the counterions introduced assuming a spherical globular assembly wrapped around itself [58]. It has been shown that the absorption of the PHMB into the cotton is much improved when the zeta potential of the cotton is reduced from -12 mV to -24 mV.[58]. AgNPs have a zeta potential of around -32 mV, which should significantly increase the electrostatic potential between the PHMB and AgNPs, making the adsorption stronger. With the increased concentration of PHMB, upon reaching the full adsorption potential of the AgNPs, multilayers were possibly formed through further oligomers interacting with the PHMB found on the surface of the AgNPs by means of stacking [58]. As these are dominated by weak hydrogen bonding, it seems more likely that the oligomers interact with the PHMB located on the nanoparticle found in the vicinity, aggregating the PHMB-AgNPs but insulating the silver cores from coming together. Oligomers of PHMB can interact with each other in a variety of ways, including side-to-side interaction existing in the bilayer conformations [58].

5.5. Control over the reaction

The change in colour during the reaction of the PHMB-AgNPs did not correspond to the changes in size measured by DLS, but the variation in the UV-Vis spectra was profound. It has been reported that for the Bare-AgNPs, the change in colloidal stability, which changes the size of the nanoparticle following the metastable stage and coalescence, is caused by hydrolysis of the borohydride ion [162]. Wuithschick *et al*. [161] showed that control over the synthesis process can be exerted by ageing the sodium borohydride by mixing fresh and old sodium borohydride solutions. Bare-AgNPs were synthesised using a selection of various mixtures of fresh to old $NaBH_4$ to establish whether the change in colour is manifested in the results

obtained using DLS or UV-Vis. The change in colour of the solution for Bare-AgNPs in 100% fresh $NaBH_4$ can be clearly noted with image analysis (Figure 5-10).

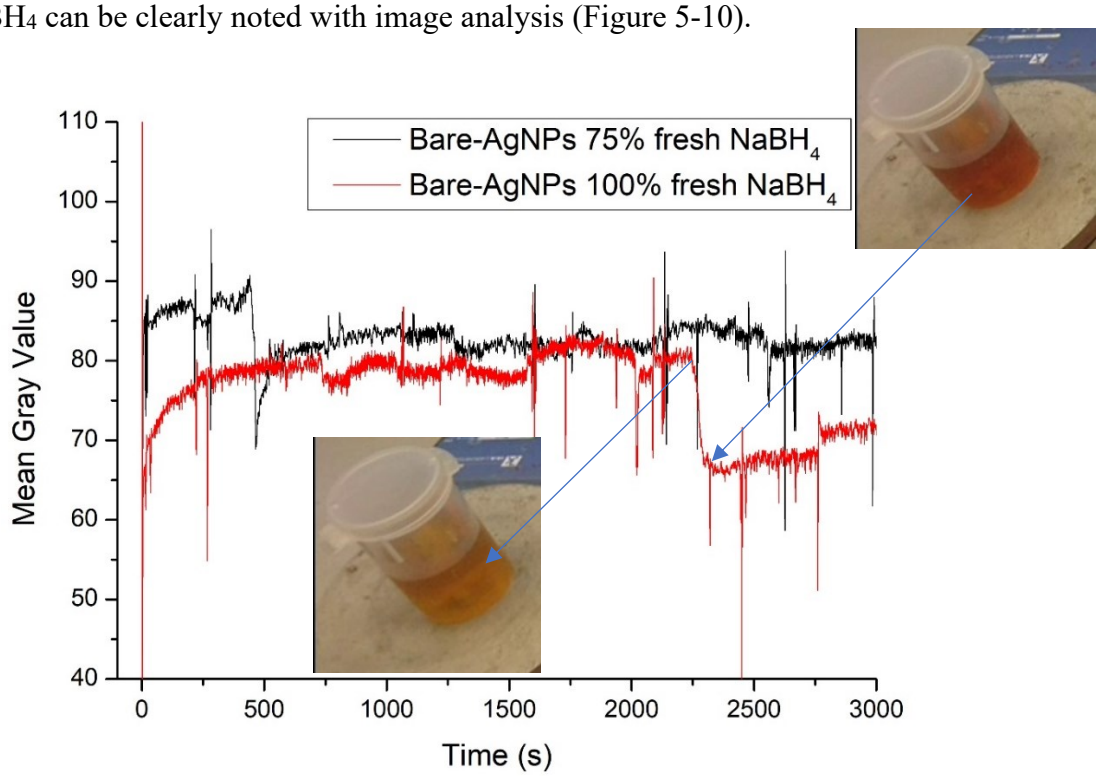

Figure 5-10 The image analysis of the colour of the reaction beaker showed a change in colour. The time of the change was correlated to the ratio of already hydrolysed and freshly prepared solution of $NaBH_4$. The picture inserts show a cropped image of the reaction beaker before and after the colour change. Similar changes were observed for PHMB-AgNPs.

However, the changes in colour observed were not mirrored in the changes to the UV-Vis spectra recorded or in the DLS results. As with the results obtained when using the KR samples, nanoparticle size varied with time but not in line with the expected results for the staged growth theory presented earlier. The introduction of the stabiliser changed the colloidal stability around the silver nanoparticle, but the borohydride ion was still responsible for the reduction of silver ions. In addition, the early stability of the PHMB-AgNPs was also provided by the borohydride ions, as was apparent when comparing the times at which the reaction changed colour with the ratio of fresh to old $NaBH_4$ (Figure 5-11). When using a different mixture of old and fresh $NaBH_4$, samples changed colour at different times subject to the ratio of $NaBH_4$ used. The time before the colour change decreased as the percentage of fresh $NaBH_4$ used was reduced. This shows that the silver nanoparticles were stabilised by the $NaBH_4$ and

PHMB at the same time over the first stage of the reaction and up to the point when hydrolysis of the $NaBH_4$ reached a point when other forces had to replace it. For Bare-AgNPs, this would be the reconfiguration of nanoparticles by coalescence and size change to find new stability. For PHMB-AgNPs, this was provided by the PHMB adopting a different configuration,

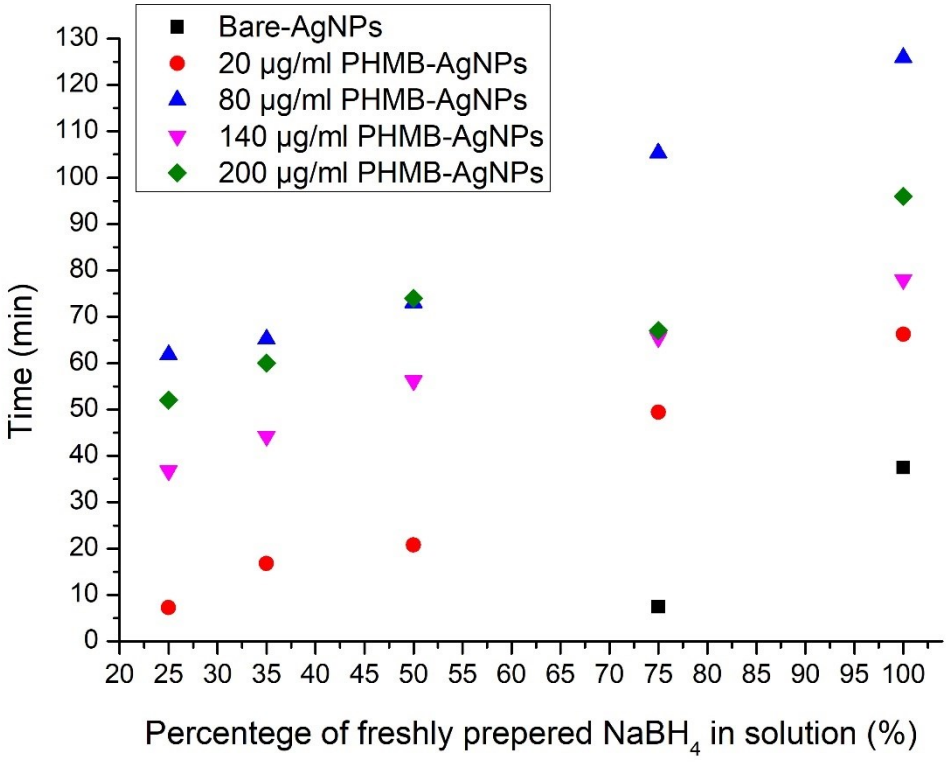

Figure 5-11 Time at which the reaction changed colour compared with the percentage of the freshly prepared sodium borohydride in the solution.

5.6. Conclusions

The properties of the silver nanoparticles are frequently determined by the reaction process. Least to say that the different synthesis methods allow for a wide range of shapes and sizes to be produced, changes introduced to the wet chemical reduction pathway used in this research had an impact on the formation of PHMB-AgNPs. Understanding the interactions between the polymer and silver nanoparticles as well the role the borohydride ion plays in the formation of the final product is a step towards exhibiting control over the reaction to produce nanoparticles with desired properties. In this chapter, it was shown that there is a change in the

colloidal stability of the nanoparticles during the synthesis process. This can be visually observed by a colour change of the solution, but the time of change depends on both concentration of the borohydride ion as well as that of PHMB. In the early stages of the reaction, both are taking part in stabilising silver nanoparticles but as the reaction progresses the hydrolysis of the borohydride ion reduces its concentration giving rise to a change in the colloidal stability. The literature suggests that for Bare-AgNPs it occurs with coalescence of the particles and corresponding increase in size, but this was not confirmed in this study. However, the presence of the PHMB and changes to the UV-Vis peaks indicates that the polymer becomes the main stabiliser. The change in the colloidal stability is dramatic, occurs within seconds and can be forced by varying ratios of borohydride to hydroxyborate ions.

Chapter 6. Stability of PHMB-AgNPs.

6.1. Introduction

The behaviour of the PHMB-AgNPs over time can provide important insights into the interactions that occur between various components of the system. It has already been established in previous chapters that the PHMB-AgNPs form a complex with particle-particle interactions over increasing polymer concentration. Investigating the stability of the silver nanoparticles offers an opportunity to observe the manifestations of those complex interactions over time by using data obtained from the characterisation of the final product over time to elucidate the process taking place during synthesis and storage. Although this approach is often criticised as flawed compared with *in-situ* characterisation, it offers an opportunity to use different methodologies to conduct characterisation, and a different level of detail, as the complexity of obtaining data from the ongoing reaction is removed. It, therefore, affords a complementary view of the results and conclusions obtained from the *in-situ* observations [165].

Understanding the behaviour of PHMB-AgNPs over time is equally important when considering potential biomedical applications. From the outset, this study focused on the antimicrobial properties of the system and the potential it presents as a topical active ingredient against biological infections. One of the prerequisites for such applications is understanding how the complex changes over time and the effect this has on the properties of the agent [166, 167]. Additionally, the PHMB-AgNPs would have to be applied using a delivery system, such as loading into hydrogels for contact lenses or wound dressings [168]. Changing storage conditions and the presence of additional factors would impact its stability over time, so this investigation would provide a benchmark for future developments.

To better understand the processes that take place in the PHMB-AgNPs system over time, two different data collection studies were designed and carried out. The first was to obtain repetitive data at very regular intervals on a short-term basis, and the second was to

recharacterise various samples synthesised over the course of the research to provide a less detailed but longer-term view of the changes. In the next sections, the data collection methodology is described, with results presented for the two approaches, short- and long-term. Two comparative analyses are carried out: first, the results from the time study and data obtained for 10 µg/ml PHMB-AgNPs are compared, and then the overlap between the short- and long-term studies is established to better understand how they align. A discussion follows on the importance of the results and how they fit into the wider understanding of the interactions taking place within the sample. Finally, concluding remarks are made in relation to the findings from this chapter.

6.2. Method

Synthesis of the samples was carried out using the same methodology as described in Chapter 2 - Methodology and Materials. Similarly, the same protocols are followed to characterise the samples using the techniques available. Data collection was carried out using two different approaches.

Short-term study

This study involved synthesising a single batch of AgNPs with a PHMB concentration ranging between 0 and 200 µg/ml. The synthesis was split into two batches of five samples synthesised within two weeks, and characterisation using DLS and UV-Vis was carried out on the fresh samples. Over the course of 18 weeks, the samples were re-analysed at regular intervals (2, 4, 6, 8, 11 and 18 weeks). The schedule of dates when measurements were taken is detailed in Appendix 6a. An attempt was made to use WetSTEM and STEM-in-SEM to obtain images at similar intervals, but this was not achieved due to equipment failure, though images were acquired during the last data collection at 18 weeks. Flow cytometer analysis was carried out using the same methodology as previously described, but due to external factors, investigations were limited to the following measurements. Fresh samples were assessed within 4 and 10 days from synthesis (for ease of reference, they are described as characterised within

10 days). A second analysis was carried out after 1 month (3 weeks for the sample of 40 µg/ml PHMB-AgNPs) from synthesis, and only for the concentrations of 0, 20, 40, 80, 140 and 200 µg/ml PHMB-AgNPs.

Long term study

The second approach involved re-analysis of samples collected over the course of the research. The high flux beamline available at Diamond Light Source offered an opportunity to characterise a large number of samples using Small Angle X-ray Scattering (SAXS). Samples were synthesised over a period of several months for the purpose of investigating various properties of PHMB-AgNPs. The batches prepared were analysed using DLS and UV-Vis shortly after synthesis and stored in a dark room. Once the samples had been characterised using SAXS, they were re-characterised using DLS and UV-Vis upon return, albeit with some delay due to the number of samples. For ease of reference, the batches of PHMB-AgNPs are referred to as presented in Table 6-1. However, when discussing an overlap between short- and long-term results a more detailed approach is taken with samples referenced to the nearest full week after synthesis. Appendix 6b presents details of the samples with relevant dates and times between dates.

Table 6-1 Naming conventions of the samples used for long-term study and analysis.

Sample name	Time reference for UV-Vis DLS	Time reference for SAXS
Oct19	2 months	X (fresh at the time
Jun19	6 months	4 months
Jan19	11 months	9 months
Nov18	13 months	11 months

6.3. Results – short-term

The sensitivity of the UV-Vis provided a high-resolution insight to determine if the changes could be observed in the samples measured. In reviewing the results obtained using the UV-Vis, it was noted that some of the peaks showed increasing peak width over time. There is a strong correlation between the FWHM (Full Width Half Maximum) increase and the concentration of the polymer used during synthesis. The change is particularly visible for 20 µg/ml PHMB-AgNPs, but other samples – 40, 60 and 80 µg/ml PHMB-AgNPs, also display a noticeable increase in peak width. However, further increasing the PHMB concentration had a diminishing effect on the observable changes to the FWHM (Figure 6-1). Detailed analysis of the 20 µg/ml PHMB-AgNPs showed that the single sharp peak observed for the fresh samples develops into a double peak observed over time (Figure 6-2). Such changes to the FWHM were not observed for any other sample in this part of the study.

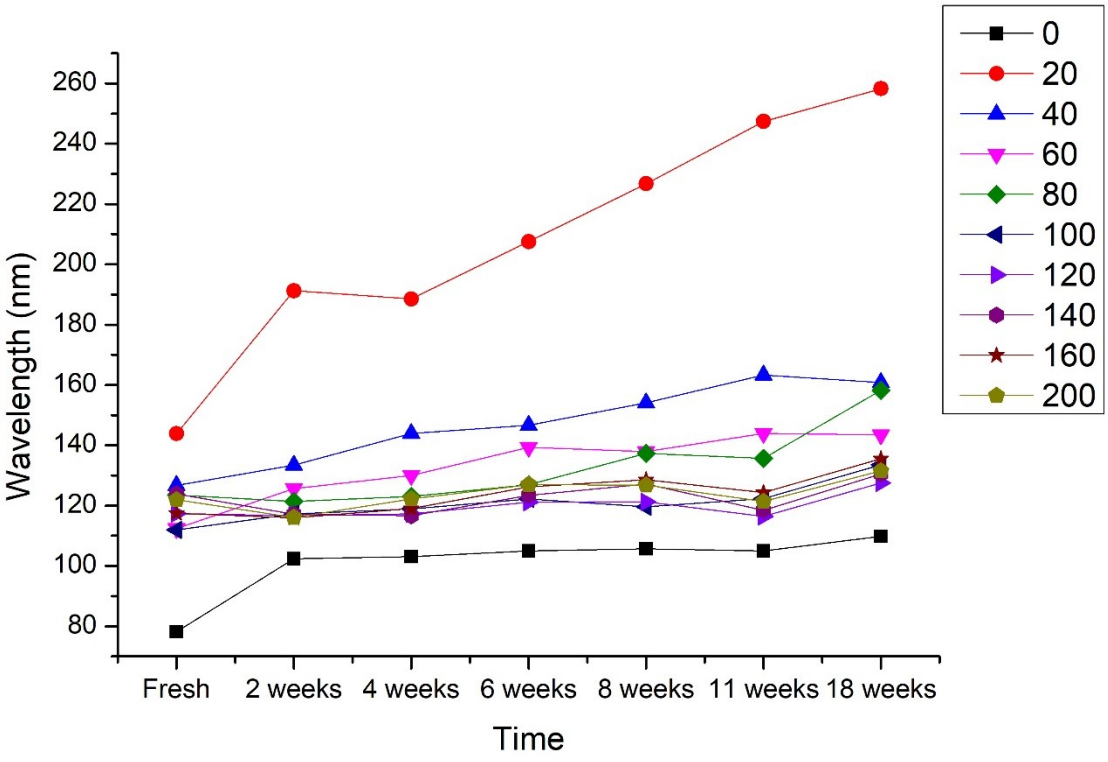

Figure 6-1 Change in the FWHM of the UV-Vis peaks for each sample of PHMB-AgNPs over time. The number next to the symbol used in the plot refers to the PHMB concentration used in the synthesis (µg/ml).

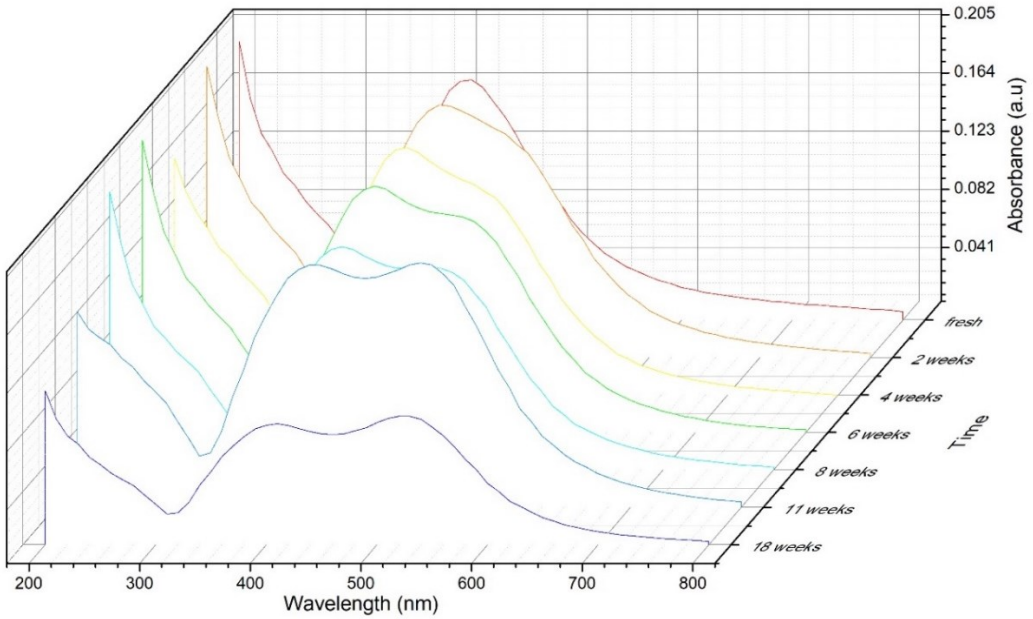

Figure 6-2 UV-Vis spectra for 20 µg/ml PHMB-AgNPs showing a change in the size and shape of the SPR peak over the course of 18 weeks. The width of the peaks is analysed in detail in Figure 6.1

The lambda maximum showed a slight increase in the peak position towards the higher wavelength. The initial difference between the lambda maximum becomes smaller with time (Figure 6-3).

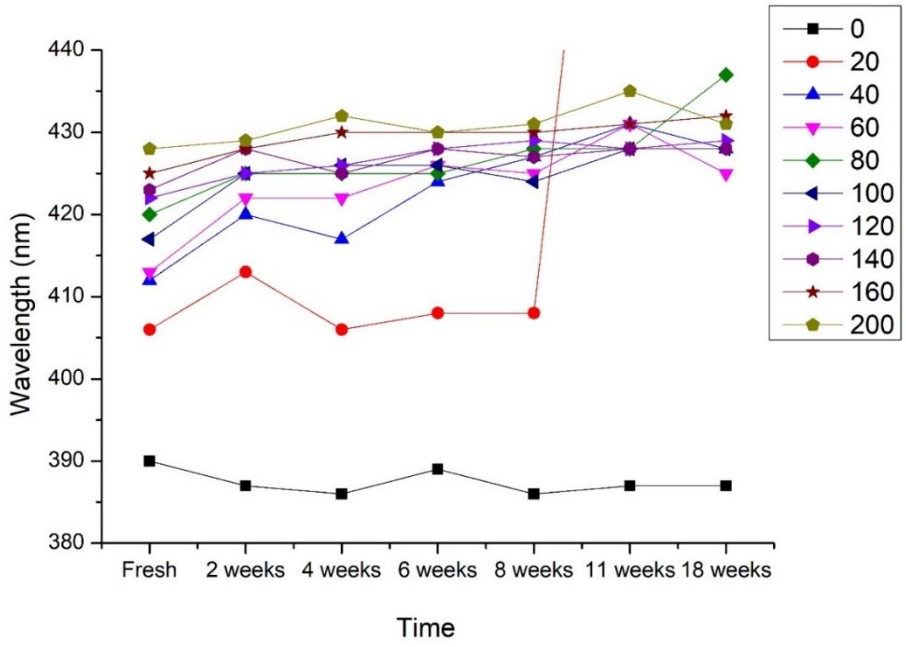

Figure 6-3 Change in the UV-Vis peak position as observed using lambda maximum. The 20 µg/ml PHMB-AgNPs after the 8th week was excluded from analysis, as the changes to the peak observed were not replicated in other concentrations and the sharp increase in the λ_{max} results from the second peak becoming dominant. The number next to the symbol used in the plot refers to the PHMB concentration used in the synthesis (µg/ml).

The maximum absorbance recorded using UV-Vis shows limited changes (Figure 6-4). Although a dip a reduction is noted for the 40, 60, 100, 120, 160 µg/ml PHMB-AgNPs in week 4, this is likely due to experimental error, as these concentrations were tested on the same day. Two striking features were noted. The first was the 80 µg/ml PHMB-AgNPs results, which show a degree of variability. The same issue is replicated within the other variables measured using UV-Vis. The second was a reduction in absorbance for the 20 µg/ml PHMB-AgNPs, noted in the measurement obtained at 18 weeks.

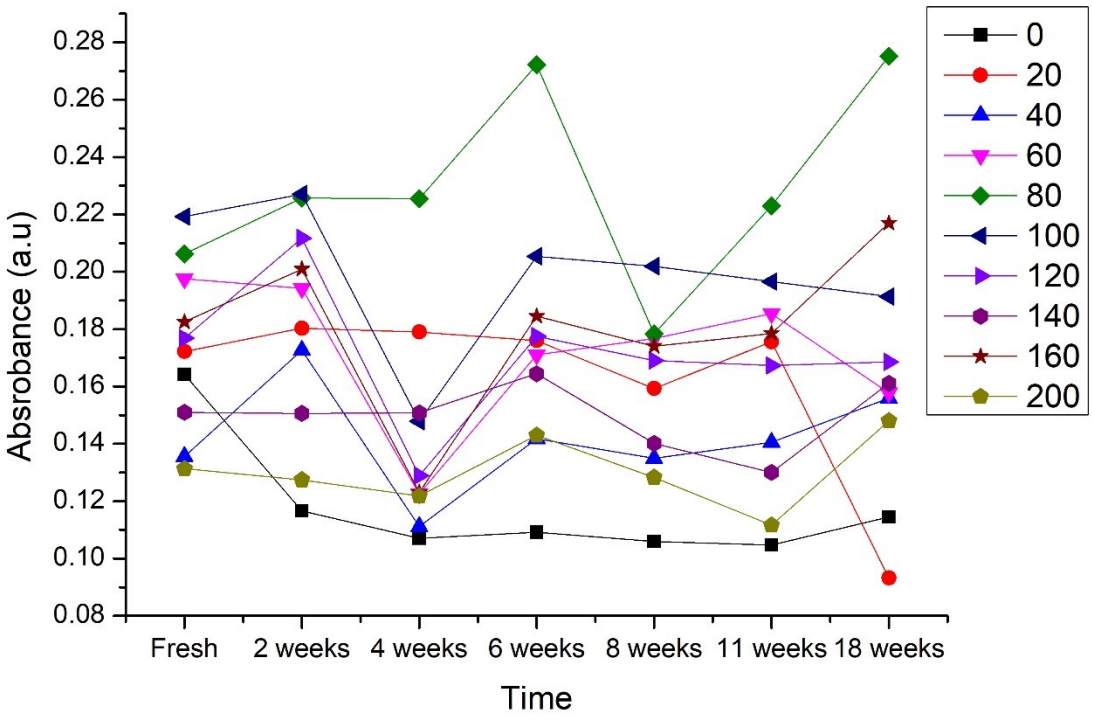

Figure 6-4 Changes to the maximum absorbance recorded using UV-Vis. It is important to note that the samples of 40,60, 100, 120 and 160 µg/ml PHMB-AgNPs were measured on the same day and these showed significant deviation in weeks 2 and 4. The number next to the symbol used in the plot refers to the PHMB concentration used in the synthesis (µg/ml).

As with previously discussed samples (Chapter 3, Section 3.2.3 - Dynamic light scattering (DLS) and zeta potential), the PHMB-AgNPs obtained in the Jul20 batch suffer from quality issues typical of DLS. There was a decrease in data reliability as the polymer concentration increased. However, the 'In Range' quality indicator did show some improvement over time. It lacked consistency, but of the 10 different PHMB concentrations synthesised, three met the quality criteria when fresh, and when the measurement was taken at 18 weeks, all except the 120 µg/ml PHMB-AgNPs sample improved to meet the criterion of at least 90% 'In Range' (Figure 6-5).

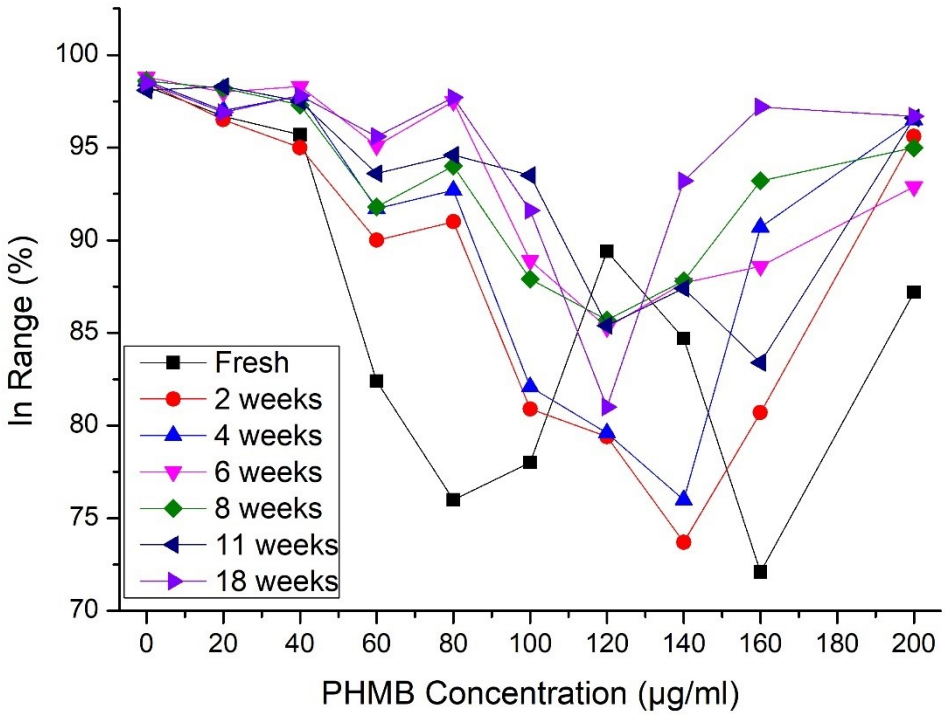

Figure 6-5 'In Range' results for the measurements obtained using DLS, showing improvement in this quality parameter over time. Bare-AgNPs are represented as 0 µg/ml PHMB concentration.

Reviewing the change of the z-average for the results that met quality criteria indicate limited changes in the samples over time. Some fluctuations in mean particle diameter were observed, and the particles formed in concentrations of 200 µg/ml PHMB display much larger particle diameter (Figure 6-6).

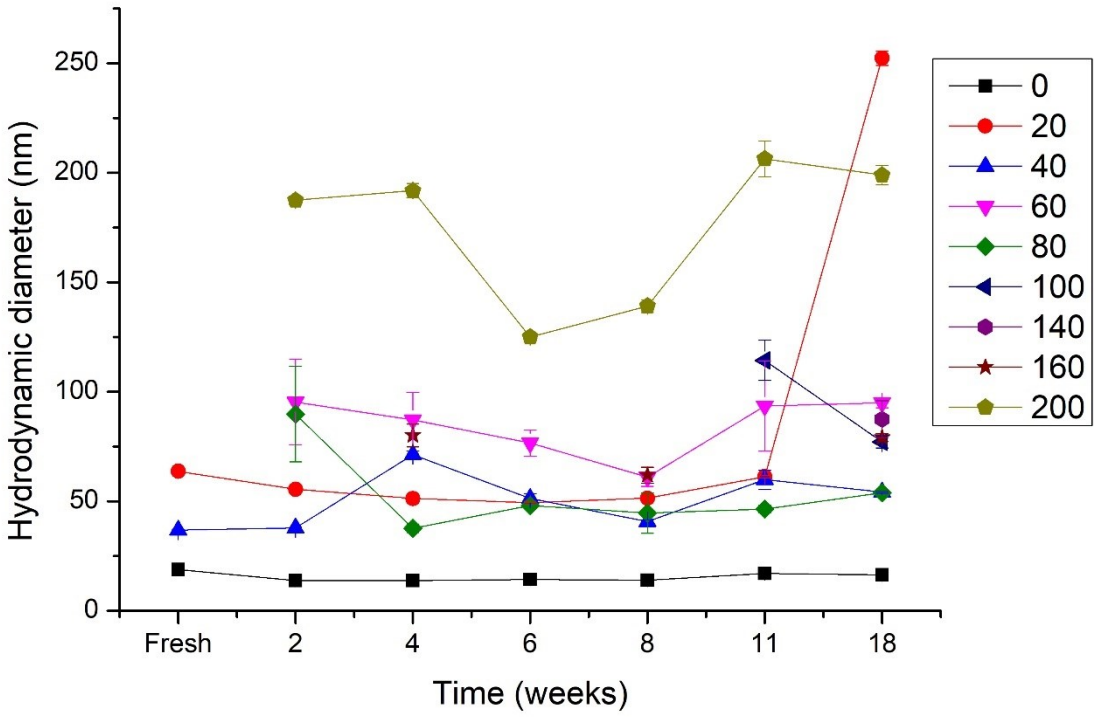

Figure 6-6 The z-average intensity distribution results of hydrodynamic diameter for the samples that met quality criteria of 'in range' over time. Some of the samples include multimodal distributions. The error bars show the standard deviation of measurement repeats. The number next to the symbol used in the plot refers to the PHMB concentration used in the synthesis (µg/ml).

Although, the z-average for multimodal samples is not a reliable means of size reporting as an average of two different populations can report a size not present with the sample at all the average can be used for observing trends. This limitation was particularly visible when a detailed investigation of the peaks in the intensity distribution was carried out for the 20 µg/ml PHMB-AgNPs. The z-average varied over the initial 11 weeks by around 15 nm, with a significant change in the final reading at 18 weeks (Figure 6-6 above). The multimodal distribution typically observed for 20 µg/ml PHMB-AgNPs of two nanoparticle populations of around 15 nm and 100 nm over time merges into one single population, which then shifts towards greater sizes for the reading taken at 18 weeks. (Figure 6-7).

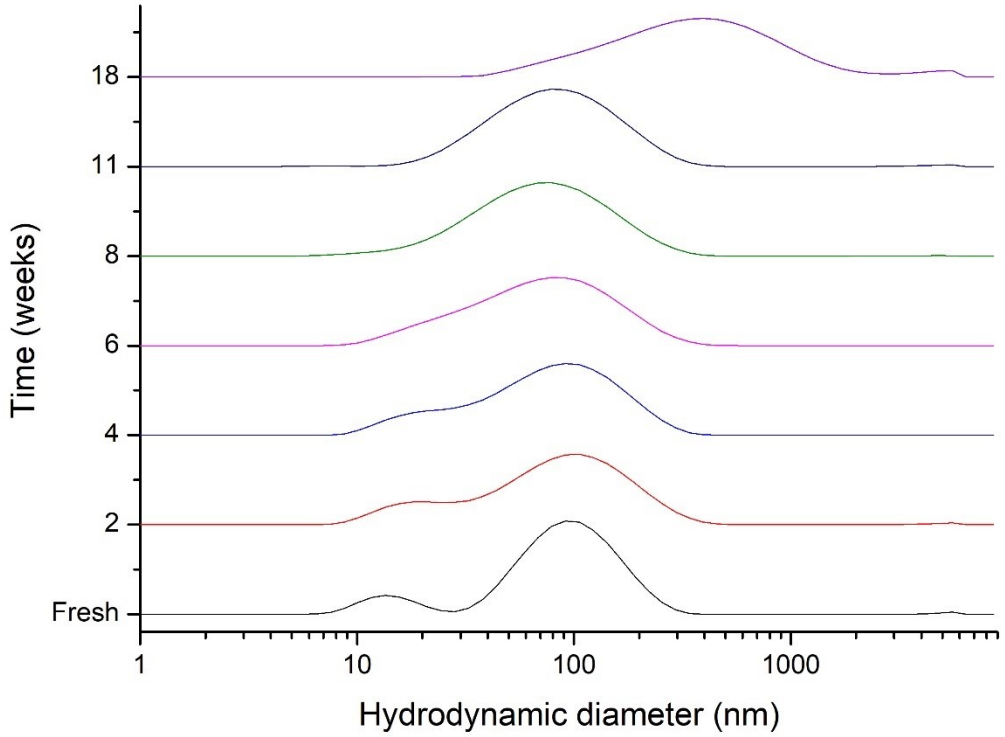

Figure 6-7 The intensity distribution DLS spectra for 20 µg/ml PHMB-AgNPs obtained over time showing a progressive change in particle size distribution from multimodal for fresh samples.

However, the same trends in size changes are not repeated in samples with different PHMB concentrations. Inspection of the particle distribution of the 40 µg/ml PHMB-AgNPs indicates the variability of results (Figure 6-8a), peak 1 and peak 2 do not merge and no other trend can be defined. The quality factor 'In Range' improved sufficiently after the first week's measurements to rely on the results obtained but further analysis of the individual peaks does not reveal any significant trends (Figure 6-8b).

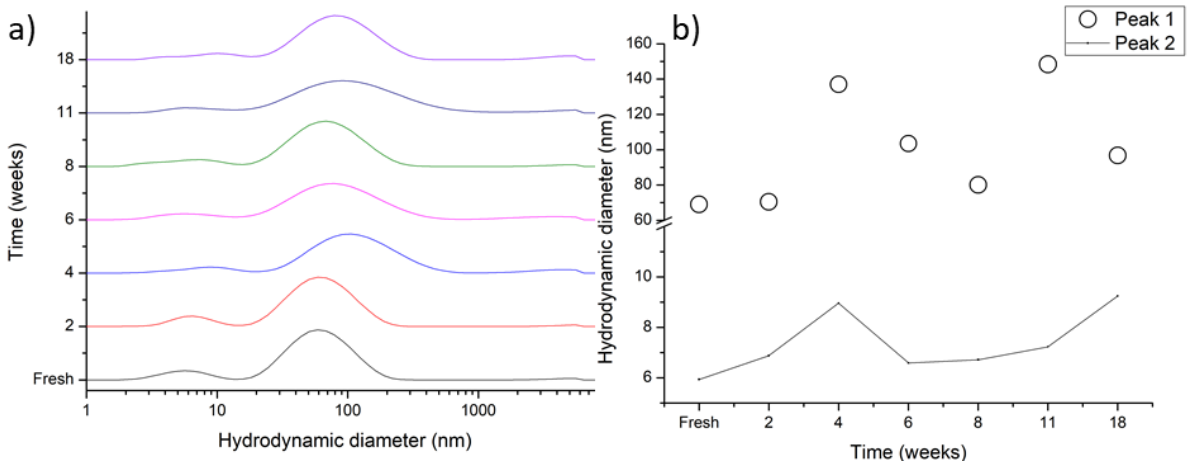

Figure 6-8 a) the intensity distributions DLS spectra for 40 µg/ml PHMB-AgNPs and the changes over time; to achieve better resolution of the populations, tracking of individual peaks in b) shows that no significant trends can be determined (size of the spots is proportional to the peak area).

A similar analysis was carried out for other PHMB-AgNPs samples formed, but results remained as uncertain as those for 40 µg/ml PHMB-AgNPs, inhibiting the definition of trends of how the samples change over time stored. The 'z-average' for the results obtained in this data collection fluctuates, but this was caused by shifting in the multimodal distribution rather than meaningful changes in the size of the nanoparticles. The increased size of the 200 µg/ml PHMB-AgNPs compared with other particles results from the missing minor population of the particle. The measurements for this sample indicated that a large population was dominating the intensity distribution (Figure 6-9).

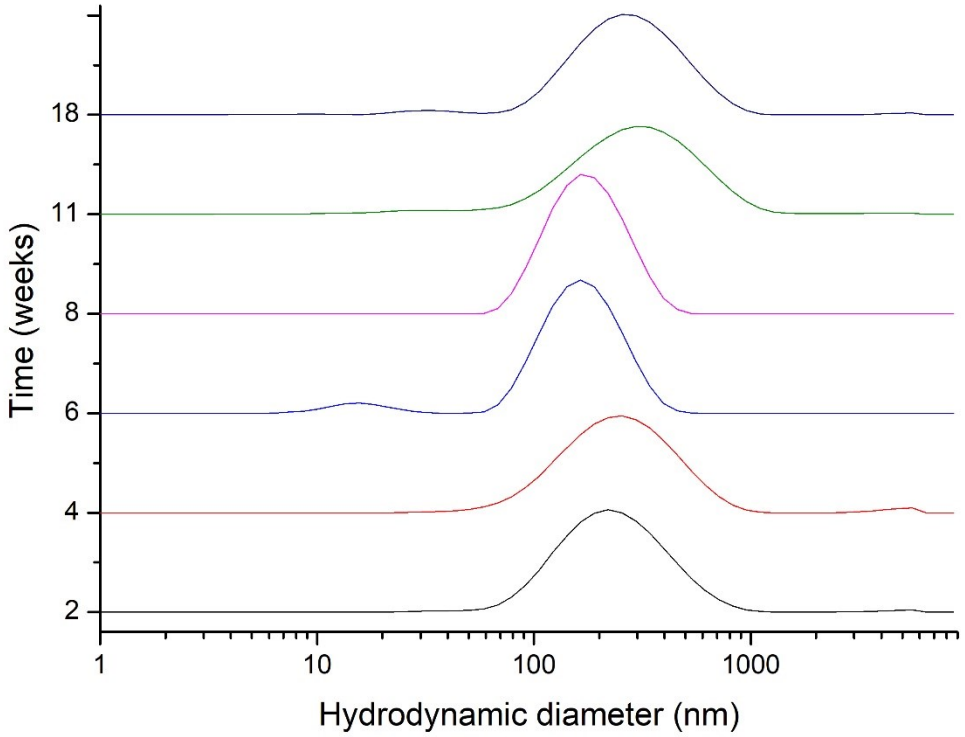

Figure 6-9 The intensity distribution DLS spectra for 200 µg/ml PHMB-AgNPs and the changes over time.

The results from flow cytometry (Figure 6-10) did not indicate that there was a change to the efficacy of the agent as a result of the time delay. The initial assessment had a limited number of repeats compared with that carried out after one month. Therefore, some discrepancy was expected, the results obtained for the fresh sample are within the standard deviation of the measurements made a month later. Analysis indicated that the 20 and 40 µg/ml PHMB-AgNPs are transition concentrations where a non-negligible number of bacteria remain healthy.

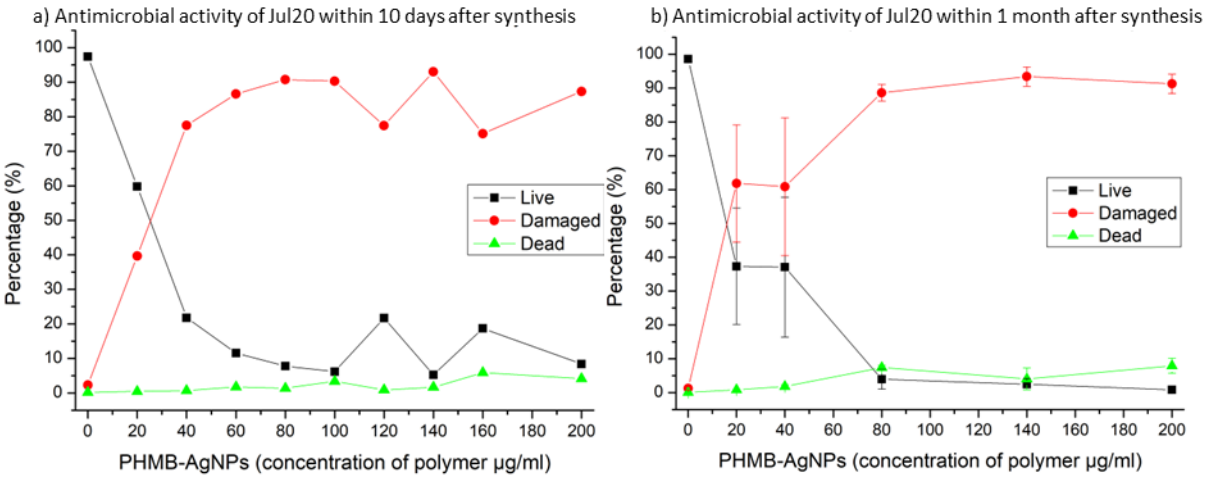

Figure 6-10 The results from the antimicrobial analysis obtained for a) fresh samples and b) the same samples after 1 month. There is no standard deviation in graph a) as the samples were measured only once compared to b) when samples were measured in triplicate.

Initial results obtained from WetSTEM suggested that there might be an increase in nanoparticle size over time, in particular in low PHMB concentrations (Figure 6-11). This was an expectation that corroborate with data obtained from UV-Vis and DLS.

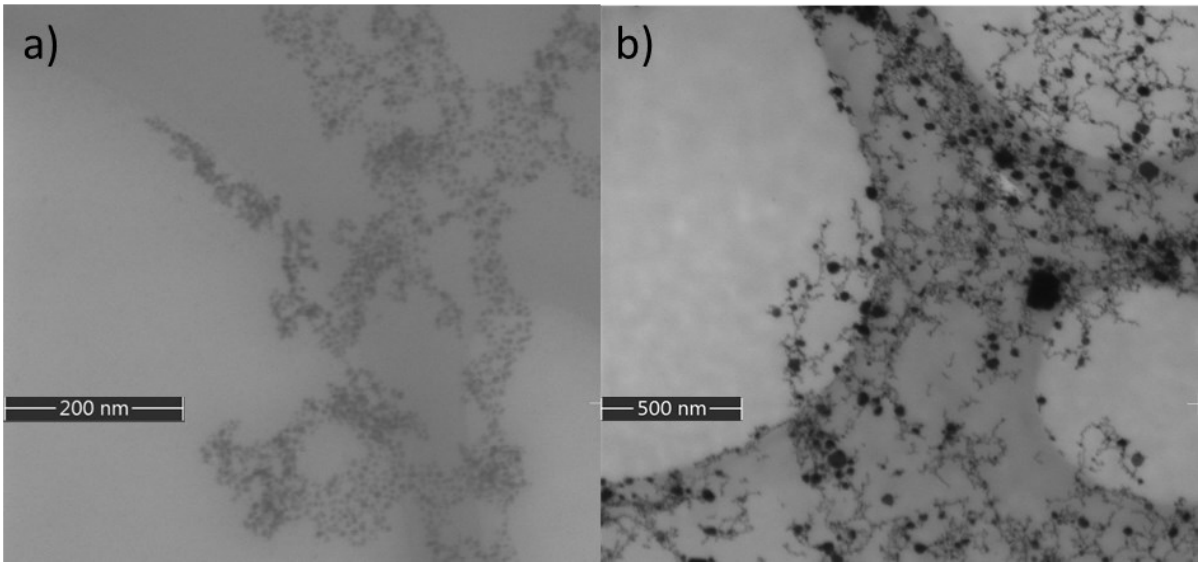

Figure 6-11 Images of the 20 µg/ml PHMB-AgNPs a) Fresh - Jan20 and b) Jul20 after 18 weeks.

However, a full analysis of the measurements taken contradicted this expectation (Figure 6-12). The results are remarkably similar to the aggregated and averaged results from various measurements. This finding reinforces the limitations of SEM, as when imaging the samples, it was understandable to be 'looking for' features, creating distorted assumptions.

When analysing such multimodal samples, such as the one under investigation here, applying automatic analysis of the images would ensure repeatability of the selection of a representative sample on the image.

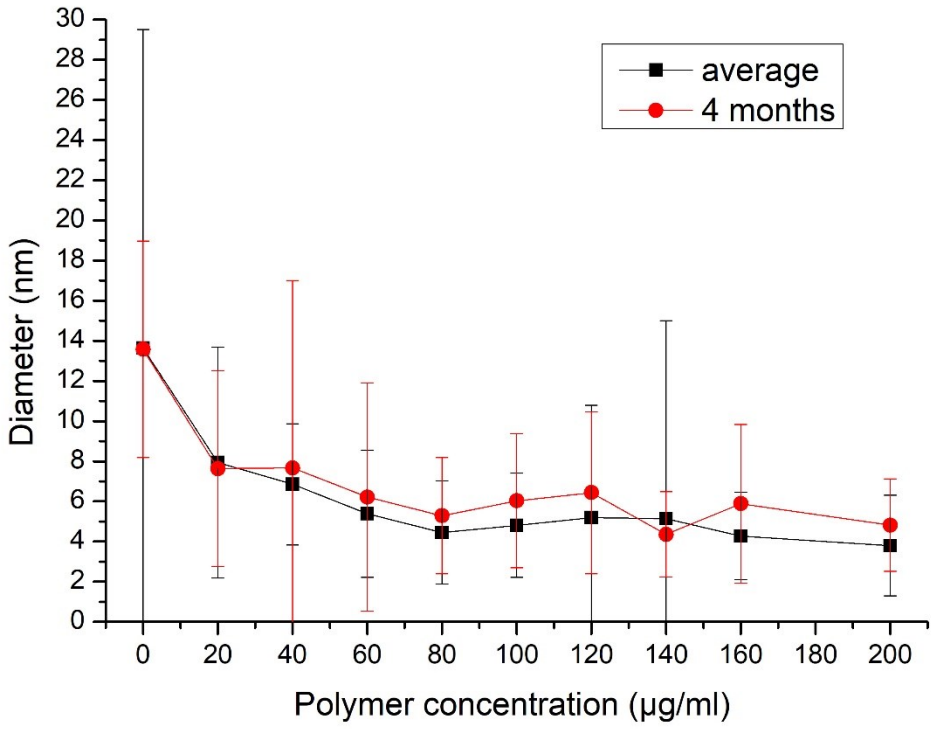

Figure 6-12 Analysis of the images obtained in STEM-in-SEM after 18 weeks (red full circles) compared to averaged results compiled using images in Appendix 4, representing between 61 and 450 measurements.

The EDX results did not indicate any deviation from the results previously observed and discussed in Chapter 3 and Chapter 4. The application of EDX in high-vacuum mode did show the presence of elemental silver, which was particularly visible in the areas with higher concentrations of nanoparticles.

6.3.1. Relationship with 10 µg/ml PHMB-AgNPs

In Section 4.2.2, the unusual case of 10 µg/ml PHMB-AgNPs was briefly discussed. The results obtained for the fresh samples showed double-peak UV-Vis spectra, while a single peak was recorded in the DLS intensity distribution with a z-average of 93.61 ± 0.53 nm. These

features bore a strong resemblance to the sample of 20 µg/ml PHMB-AgNPs after 11 weeks (Figure 6-13).

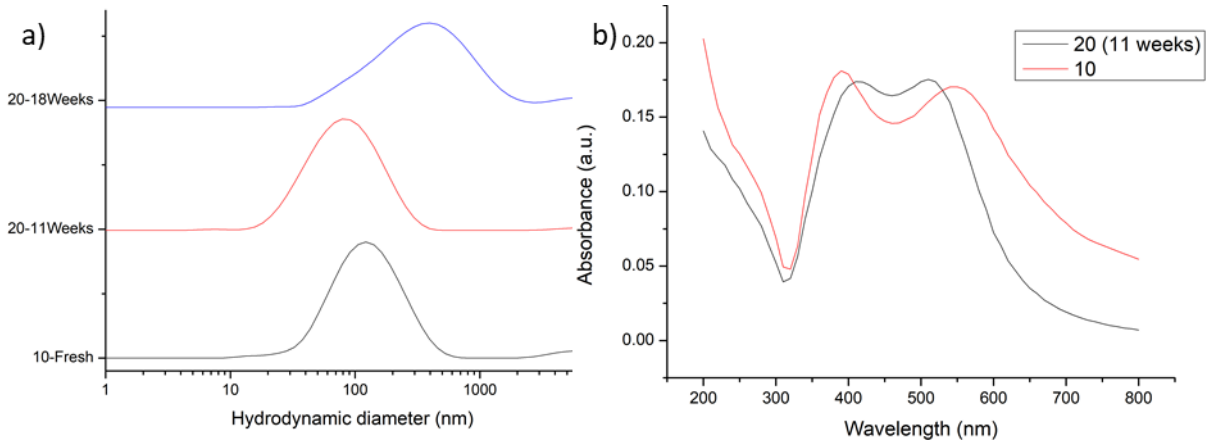

Figure 6-13 a) Intensity distribution DLS spectra for fresh 10 µg/ml PHMB-AgNPs (black) and 20 µg/ml PHMB-AgNPs at 11 weeks (red) and 18 weeks (blue) showing similarities in population distribution; b) UV-Vis spectra obtained for fresh 10 µg/ml PHMB-AgNPs (red) and 20 µg/ml PHMB-AgNPs at 11 weeks. The double peak observed for both samples indicates similarities in the changes that occur in those two samples.

Summary

The results from short-term data collection showed that the changes in the UV-Vis peaks correlated closely to the concentration of the polymer present in the sample. The development of the second peak for 20 µg/ml PHMB-AgNPs was an extreme example of this, but changes were reported up to and including polymer concentration of 80 µg/ml, which relates to both the FWHM and lambda maximum. The DLS results, in which quality also correlated to the polymer concentration and time in storage, showed changes in the sample of 20 µg/ml indicating a decrease in the less numerous smaller size population in favour of the more numerous larger in size population (Figure 6-7). No such changes were observed for any other samples. The important additional evidence obtained in this study was observed through the analysis of images obtained from STEM-in-SEM at 18 weeks. It showed remarkable similarity to the averages calculated from fresh samples, indicating that the silver nanoparticle core remains stable over the course of 4 months. The results from flow cytometry did not show significant changes in the antimicrobial efficacy of the PHMB-AgNPs agent.

The Bare-AgNPs synthesised as part of the Jul20 batch behaved in an unusual way compared with previously observations. It was typically observed that the Bare-AgNPs solution would lose colour over time to become transparent with visible dark particles as sediment. However, in this instance, no changes were observed over the time measured, and the DLS and UV-Vis results remained consistent. There was nothing done during the synthesis that this behaviour could be linked to but it points towards the general unpredictability in the behaviour of the nanoparticles and the need for introducing additional agents to control the properties.

6.4. Results – long term

The UV-Vis results obtained in the course of the long-term data collection showed trends in changes to the FWHM similar to those observed for data collected in the short-term study. The time between the characterisation of a fresh sample and the repeats caused the sample of 20 µg/ml PHMB-AgNPs to develop a double peak, making the FWHM much greater compared with all other readings. There is a noticeable increase in the FWHM for other low concentrations of PHMB (40, 60 µg/ml) that stand out from the readings obtained for higher PHMB concentrations. The 80 µg/ml PHMB-AgNPs display boundary features, for some readings, it was much greater than the original reading and for others, the increase was in between the low and high polymer concentrations (Figure 6-14). To minimise any error that might occur as a result of comparing samples synthesised in different batches, the change in the UV-Vis parameters was calculated as a percentage increase from the original reading. There is a degree of fluctuation in changes recorded between the batches, suggesting that there is certain variability between the batches. The peak for 40 µg/ml has a significantly wider peak and the lambda max shifts towards 450 nm, indicating the presence of the second population. There is also a noticeable increase for the 60 µg/ml PHMB-AgNPs, in particular for the sample measured at 11 and 13 months. The 80 µg/ml PHMB-AgNPs results were erratic and did not

conform to the changes observed for the concentrations lower than 80 µg/ml, but it did not show resilience to change observed for the concentrations above it.

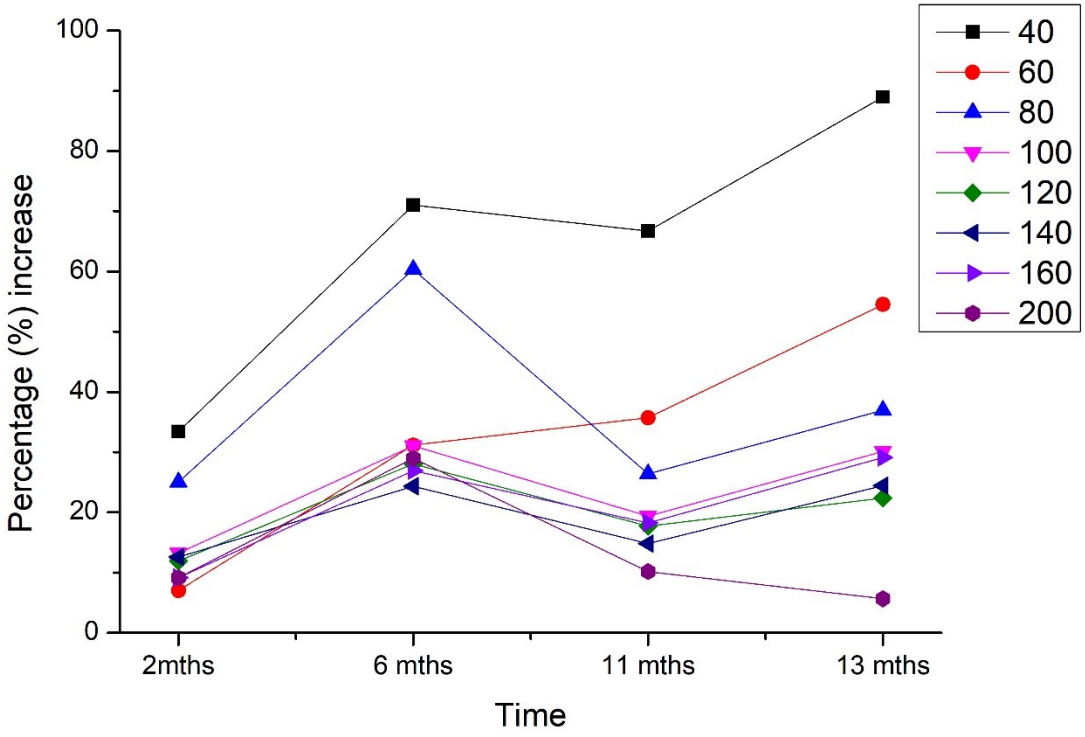

Figure 6-14 Percentage increase in the FWHM compared with the original measurement taken following synthesis. Each point in time reflects a different batch of PHMB-AgNPs samples (2mths – Oct19; 6mths – Jun19; 11mths – Jan19; 13mths – Nov18). The 20 µg/ml PHMB-AgNPs is excluded from the graph for clarity as the double peak causes a much greater FWHM increase. The number next to the symbol used in the plot refers to the PHMB concentration used in the synthesis (µg/ml).

The other variable tracked for the UV-Vis peaks, maximum absorbance, like the original reading, shows significant inconsistencies between readings. However, as with the variations in the FWHM, it shows similar differences within a particular batch that was synthesised together, indicating variability between the batches. The λ_{max} shifts no more than 4% from the original measurement, with the exception of the reading for 40 µg/ml PHMB-AgNPs, which shifted more than 12%. This difference could be accounted for by the development of the wider peak (Figure 6-15). The second peak developed in the 20 µg/ml PHMB-AgNPs has been excluded from the analysis.

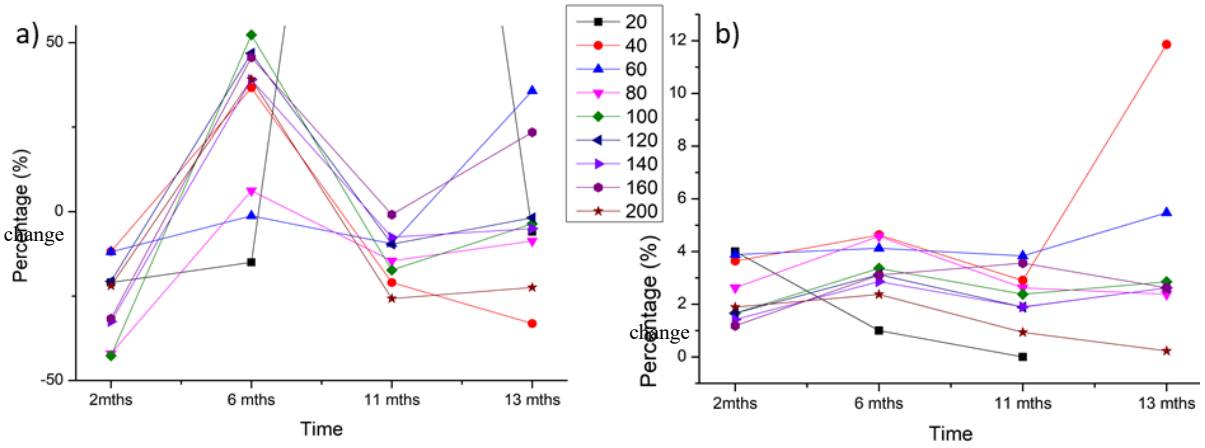

Figure 6-15 Percentage change in a) maximum absorbance showing inconsistent changes in the measurements taken, suggesting that any variation was likely to be a result of batch-to-batch deviation rather than time-related. Figure b) lambda maximum presents the minimal change in the peak position over time, with the exception of 40 µg/ml PHMB-AgNPs which increase might be associated with the slow development of the second peak in the UV-Vis causing the broadening. The number next to the symbol used in the plot refers to the PHMB concentration used in the synthesis (µg/ml).

The challenges of obtaining accurate and consistent results for the nanoparticle sizes using DLS have already been discussed. One of the key quality indicators for those measurements is the 'In Range' variable, which should be above 90% to have confidence in the readings obtained.

It has been observed that the quality of the DLS readings improved over time. This was visible with the samples from the batch Oct19: all samples with PHMB concentration lower than or equal to 120 µg/ml met the criteria after 2 months (Figure 6-16a). For older samples, all measurements except for one sample were of good quality (Figure 6-16b).

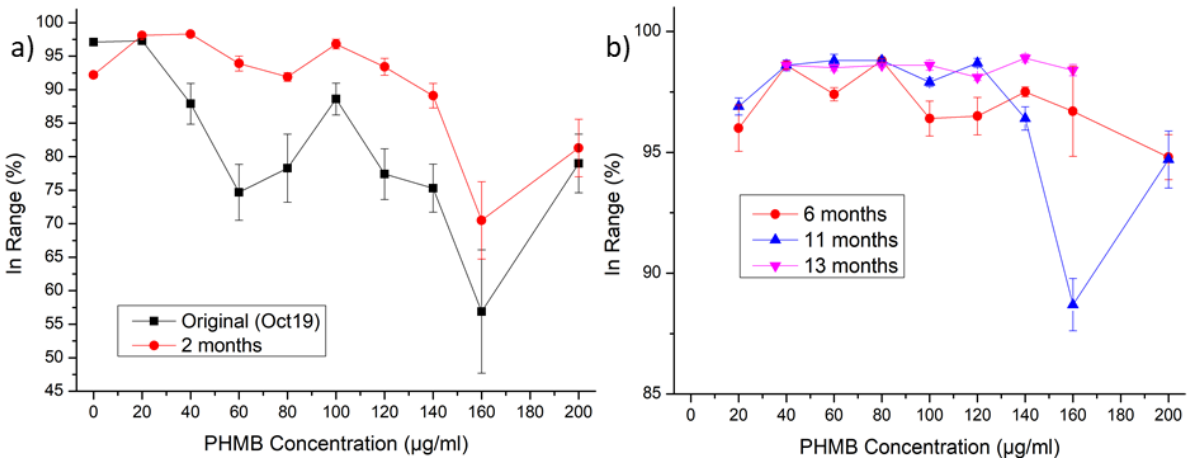

Figure 6-16 Changes to the 'In Range' parameter over time in a) fresh Oct19 batch (black squares) and the same sample after 2 months (red circles). b) 'In Range' for the rest of the batches showed similarly good data quality after months of storage. After 6 months, almost all of the measurements were above the 90% requirement.

The improvement in the quality measurements increases over time and although some outliers can be noted, the data quality becomes sufficient to rely on for the hydrodynamic diameter calculated by the equipment. Comparing the z-average result calculated for the results that met quality standards shows a degree of variability between the batches and sizes obtained (Figure 6-17). Unfortunately, data for the readings taken when fresh cannot be directly compared with those results due to poor quality. In addition, the cumulant fit error has been noted above the expected values, prescribing caution over the z-average. Provisional observations can be made about the size of PHMB-AgNPs formed in low concentrations of the polymer, i.e. the size increases with time. The size recorded for the 20 u/g PHMB-AgNPs after 11 months was recorded as 238.4 nm (omitted from Figure 6-17 for clarity). However, that trend is not replicated in any other concentrations.

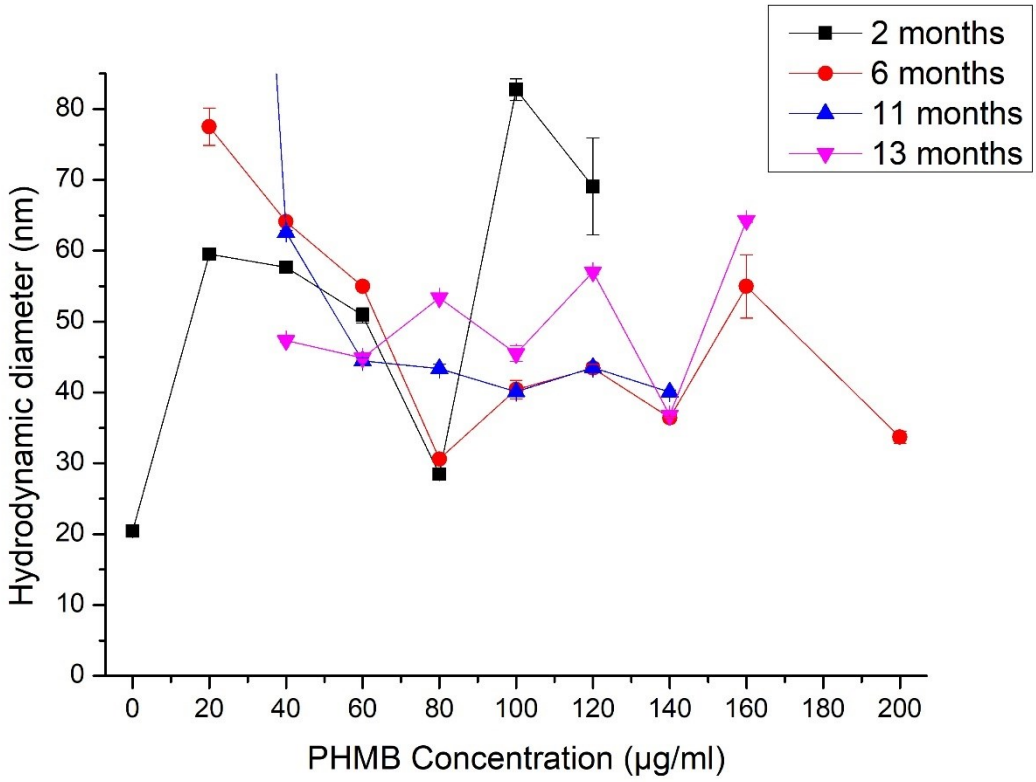

Figure 6-17 The z-average of the DLS for all the samples that meet quality criteria. The 20 µg/ml PHMB-AgNPs for the samples after 11 months measured as 238.4 nm was removed from the graph for clarity.

Using 'multimodal' analysis, the two peaks often present in the DLS measurements have been tracked to establish whether any trends can be noted at this more detailed level. Test analysis was carried out on the samples of 20 and 40 µg/ml PHMB-AgNPs, but no meaningful conclusions can be drawn based on the results obtained (Figure 6-18). The smaller population peak was only just present in the sample of 20 µg/ml PHMB-AgNPs and over time disappeared completely. The 40 µg/ml PHMB-AgNPs do not have a drastic increase in size over time, and the contribution from the minor population continues over time.

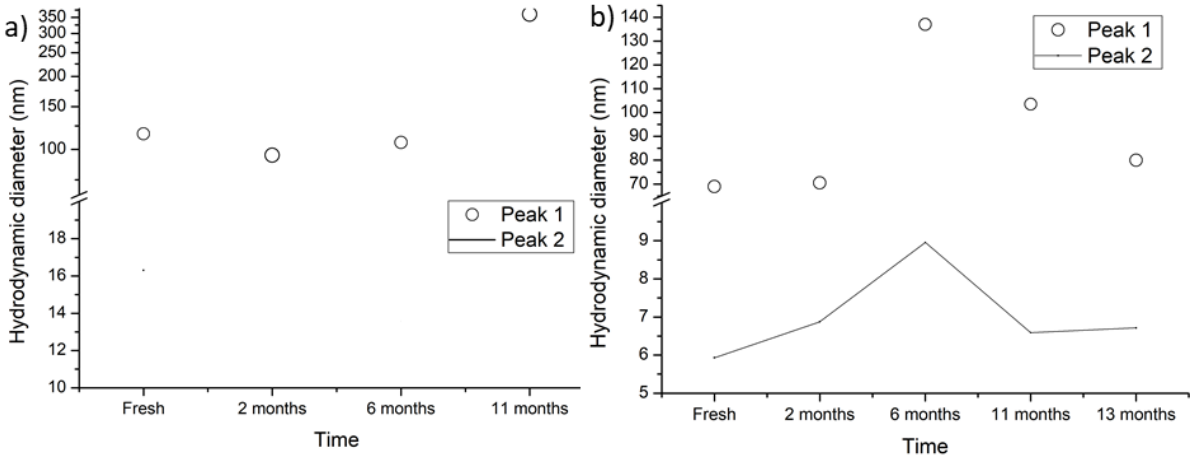

Figure 6-18 a) 20 µg/ml PHMB-AgNPs tracking of individual populations over time showed the disappearance of the smaller population initially recorded and an increase in size over time. The same is not observed in b) 40 µg/ml PHMB-AgNPs: the minor population remains throughout all of the measurements; the increase in z-average over time is not recorded (size of the spots proportional to the peak area).

The improvement in the reliability of the data obtained using DLS permitted reliance on the results. However, the calculated sizes did not agree with previous results from SAXS or SEM, therefore limiting their informative power. A further challenge was presented by the fact that it was not possible to rely on the fresh sample results, inhibiting comparative analysis to show relative change over time. No significant findings were made in relation to the changes in the peaks' percentage contribution to the overall distribution.

Fitting the SAXS data indicated that if there is any increase in the size of the particle over time, this increase is negligible since it lies within one standard deviation of the fresh nanoparticle size distribution (Figure 6-19). However, the reproducibility of results was not assessed using this methodology – only one fresh sample batch was analysed using this technique. Therefore, it was not possible to exclude the possibility that the minimal deviation in size was a result of variation from batch to batch rather than changes that may have occurred over time. The same trends were observed for all the measurements, and the data is very closely aligned.

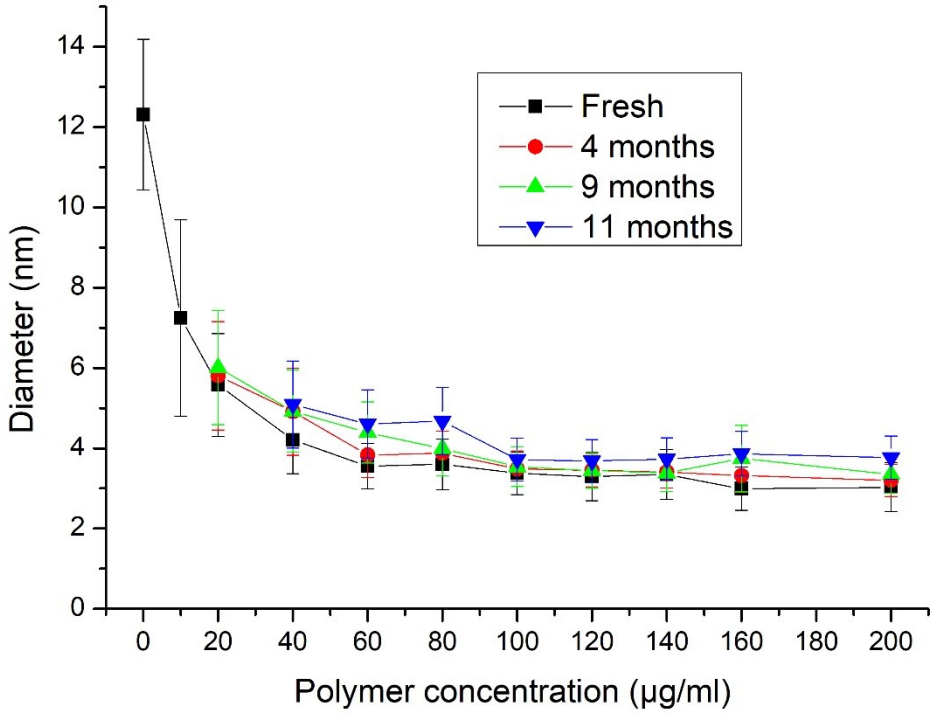

Figure 6-19 Mean size with standard deviation obtained as a result of scattering pattern analysis for samples synthesised as a part of batches Oct19 (black square), Jun19 (red circle), Jan19 (green triangle), Nov18 (blue reversed triangle).

6.4.1. Overlap between short- and long-term results

Establishing the relationship between the two sets of compiled data in this chapter was necessary to gain a better understanding of whether the changes over time reported in the short- and long-term studies overlap and if they are complementary. Both sets were characterised using UV-Vis and DLS, providing an opportunity to assess whether the same observations can be made at the same time interval.

The time difference between the measurements taken for the long-term change assessments for the sample of Oct19 has been calculated to be between 5 and 6 weeks (the exact calculation can be found in Appendix 6b). The short-term changes assessed using the batch of Jul20 samples were measured at a 6-week interval. The results obtained when the samples measured were fresh following synthesis showed a very good degree of reproducibility for the lambda max parameter (Figure 6-20a). The progressive increases of the λ_{max} with the

increasing concentration of the polymer can be observed for both batches of samples. The FWHM shows some variability, in particular in the lower concentrations of PHMB used in synthesis (Figure 6-20b). However, the same discrepancies were observed previously for other samples (See Chapter 4, section 4.2.1 – UV-Vis results).

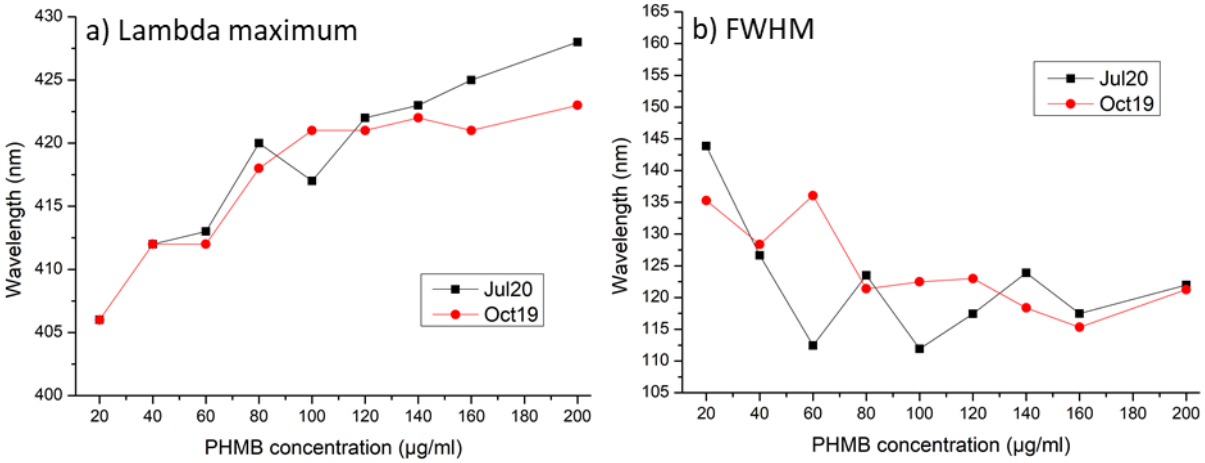

Figure 6-20 The key parameters of a) lambda maximum and b) FWHM obtained from UV-Vis spectra and compared between fresh samples of Oct19 and Jul20.

Samples were recharacterised after 6 weeks, and the UV-Vis spectra obtained were analysed for the λ_{max} and FWHM parameters (Figure 6-21). The peak position, lambda max, increased for all concentrations except 20 µg/ml PHMB-AgNPs to a level between 425 and 430 nm. The largest increase was observed for the lowest concentrations of PHMB, with the same found in the short-term study. The FWHM for both batches changed over time, although the width of the peak was not the same for the corresponding samples. The trends that emerged give a strong indication of similarities between the samples. An increase in the FWHM was observed for PHMB-AgNPs formed in low concentrations of polymer (20, 40, 60 µg/ml) and a minor change was noted for the samples formed in PHMB concentration over 100 µg/ml.

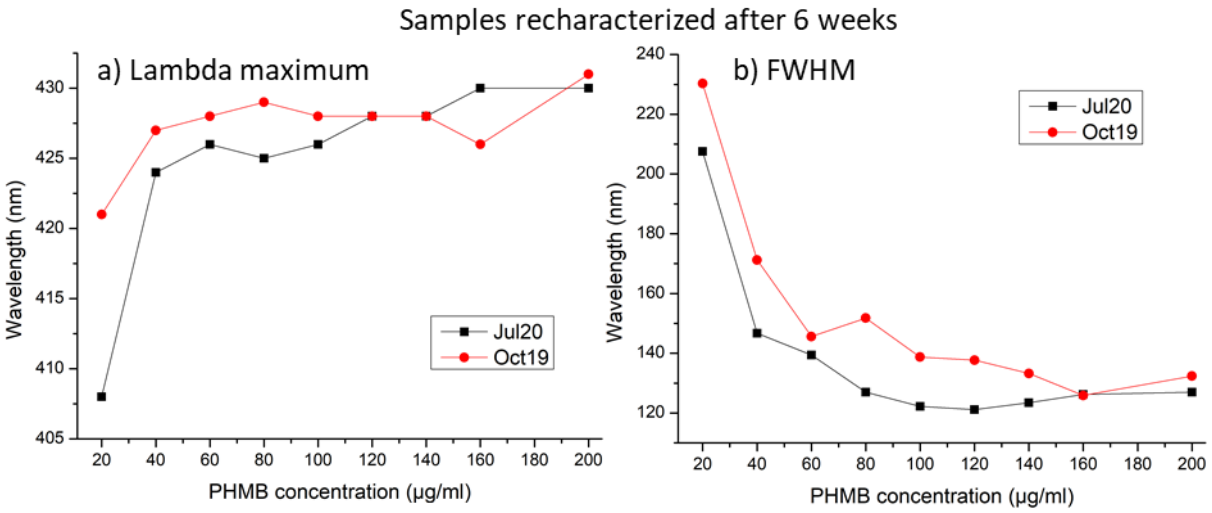

Figure 6-21 The key parameters a) lambda maximum and b) FWHM obtained from UV-Vis spectra and compared between recharacterised samples of Oct19 and samples of Jul20 at a corresponding time (6 weeks).

The most profound changes in the UV-Vis spectra observed in both batches were for the samples of 20 and 40 µg/ml PHMB-AgNPs. Direct comparisons of the plots obtained after 6 weeks of storage showed good similarity in the results (Figure 6-22). Close inspection of the 20 µg/ml PHMB-AgNPs displayed some differences, with a more pronounced double peak for the sample of Jul20, but this may also serve as an explanation for the difference in the lambda maximum recorded. The increased reading can be attributed to the prolonged peak observed for Oct20 compared with the sample of Jul19.

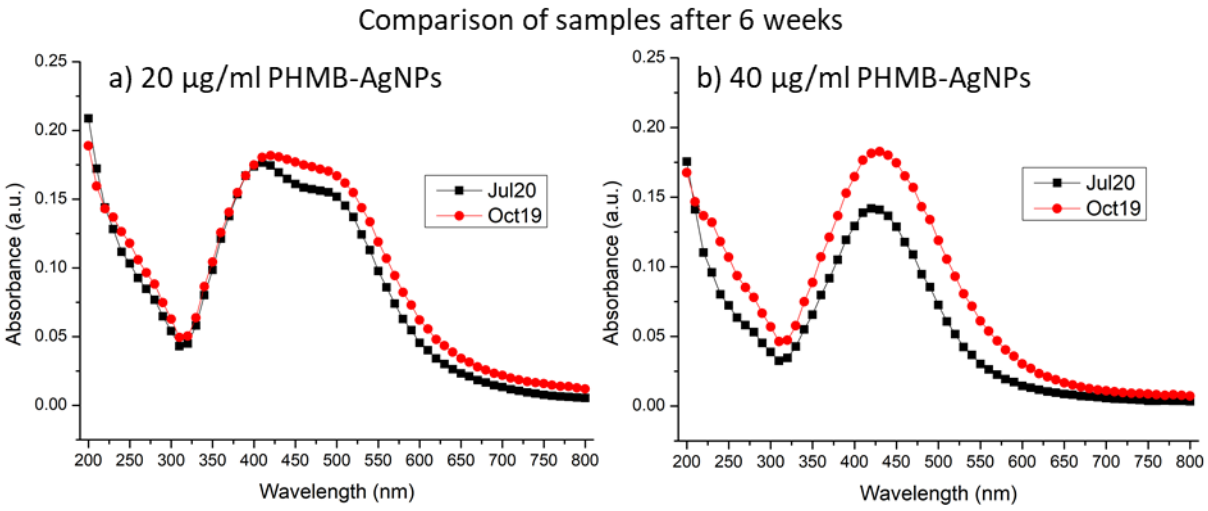

Figure 6-22 Compared UV-Vis spectra for the recharacterised samples of a) 20 µg/ml PHMB-AgNPs and b) 40 µg/ml PHMB-AgNPs obtained for Oct19 and Jul20 at the corresponding time (6 weeks) showing strong similarities between the present peaks.

The DLS results have been discussed already, and the data quality aspect in particular. A noticeable improvement in the reliability of the DLS measurements with time has been observed. The rate of quality increase differed between samples. For the batch Jul20, the initial measurements for Bare-AgNPs, 20 and 40 µg/ml PHMB-AgNPs were of suitable quality; two weeks later, 60, 80 and 200 µg/ml PHMB-AgNPs had also sufficiently improved. For the batch of Oct19, only Bare-AgNPs and 20 µg/ml PHMB-AgNPs initially met the quality standards, but when samples from two batches transverse the same time frame, results for 20, 40, 60 and 80 µg/ml PHMB-AgNPs can be relied on.

Comparing the DLS spectra obtained for 20 µg/ml PHMB-AgNPs from Oct19 and Jul20 (Figure 6-23) shows reasonable similarity between them. The minor peak in Oct19 is not as well pronounced as in Jul20, but a review of the individual peaks provides reassurance of the similarities. In addition, the area under the peaks has a close resemblance of 87.9% (Oct19) and 88.7% (Jul20).

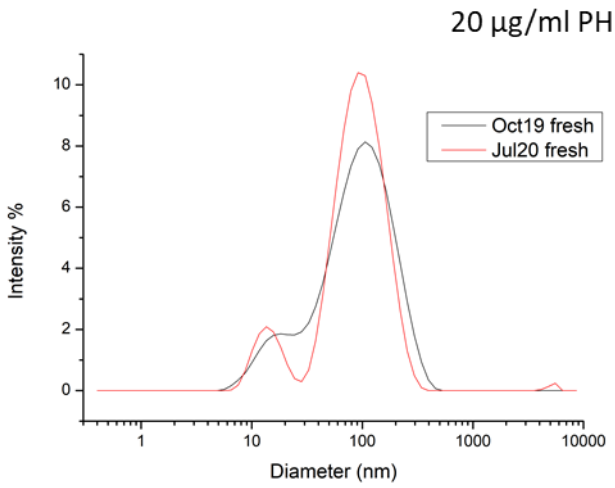

Sample	Peak 1 (nm)	Peak 2 (nm)	Z-ave. (nm)
Oct19	115.9 ± 70.12	16.31 ± 5.11	60.58
Jul20	106.5 ± 50.49	14.75 ± 4.51	63.72

Figure 6-23 Intensity distribution of hydrodynamic diameter of fresh 20 µg/ml PHMB-AgNPs obtained as part of Oct19 and Jul20 batches with key figures for peak position, width and z-average presented in the inserted table.

The changes over time to the two samples offering a suitable quality of data showed that the 20 µg/ml PHMB-AgNPs maintained very good similarity between batches (Figure 6-24a). The merging of the two peaks is complete and the positioning of the peaks from the two batches aligned. The results for other samples of 40 µg/ml and 80 µg/ml PHMB-AgNPs corresponded less strongly, but the spectra remain multimodal with similarly positioned population peaks (Figure 6-24b and c). The 60 µg/ml PHMB-AgNPs, however, showed significant discrepancies between the readings. The z-average for all samples (Figure 6-24e) indicated a fairly good correlation, providing some certainty in regard to the reproducibility of the Oct19 and Jul20 batches.

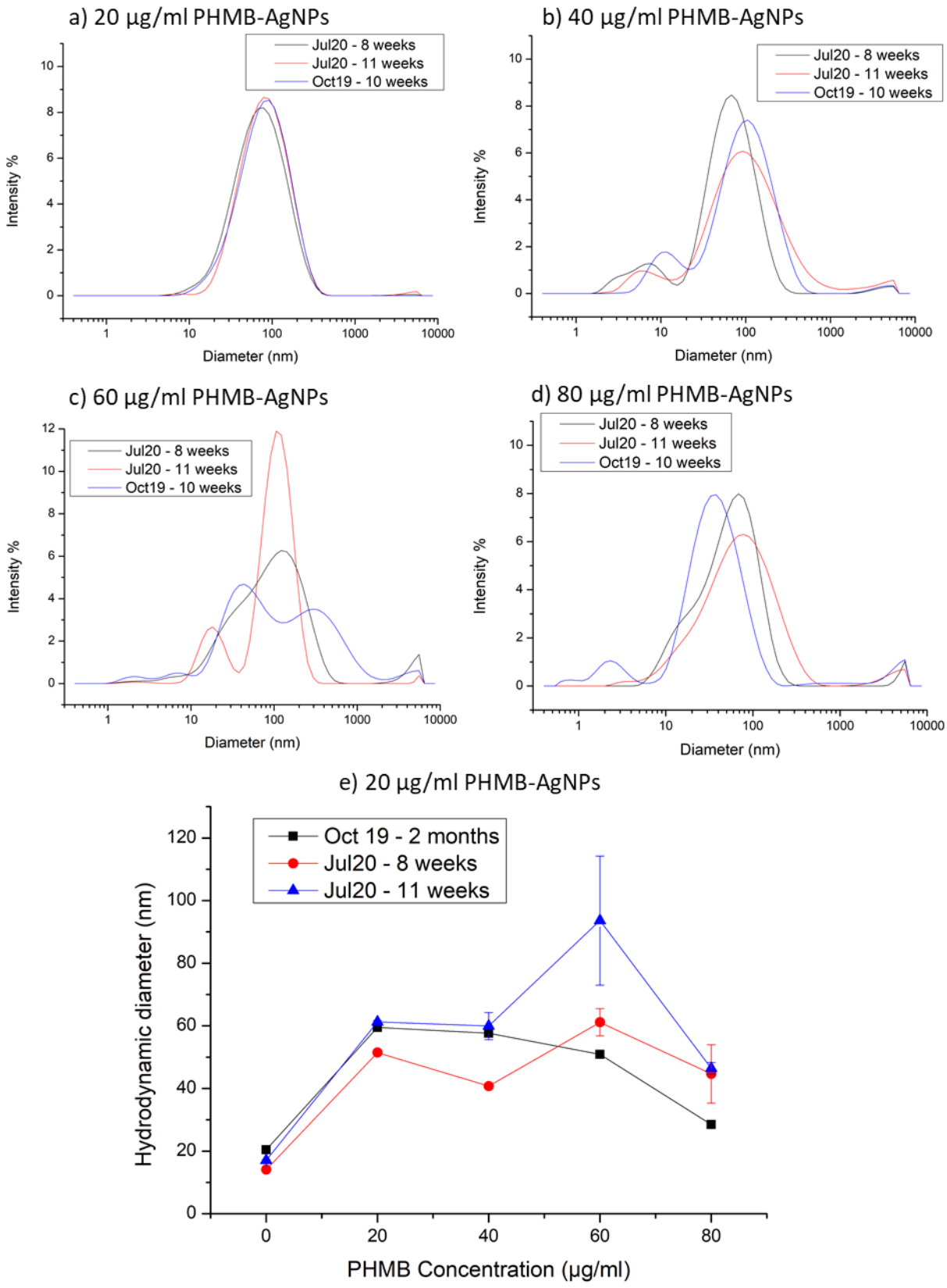

Figure 6-24 DLS spectra obtained for the PHMB-AgNPs samples that met quality criteria and compared between measurements taken for Oct19 and Jul20 at corresponding times for a) 20 µg/ml PHMB-AgNPs; b) 40 µg/ml PHMB-AgNPs, c) 60 µg/ml PHMB-AgNPs, d) 80 µg/ml PHMB-AgNPs; e) z-average for all samples that met quality criteria.

The reproducibility of the results has already been established (Chapter 3, section 3.2.3) providing confidence that regardless of some variability, the characterisation results from the various batches synthesised had sufficient similarity to trust in the synthesis process. Data collected from the recharacterization of the samples compared at the intercept, at the same period of time after synthesis, were well aligned for both UV-Vis and DLS, further reinforcing that confidence. As a result, it was possible to discuss both the short- and long-term studies together as a continuation of one another.

6.5. Stability

Changes in the FWHM, together with the increasing size of the 20 µg/ml PHMB-AgNPs noted over the weeks of measurement, paint a picture of increasing particle size over time. The ESEM images, when compared side-by-side support that theory. It would be easy to conclude that increasing the stabiliser concentration prevents the changes seen in the UV-Vis and data for 40 µg/ml PHMB-AgNPs. However, once the STEM-in-SEM images were analysed, the trends found closely resembled those observed for fresh nanoparticles: a consistent decrease in the size of the silver nanoparticles with increasing PHMB concentration, without any changes over time. Moreover, this observation was supported by the SAXS results from the long-term study to show that increase in average diameter, if any, was minimal.

Over time, the shift in the lambda maximum and increase in the FWHM observed using UV-Vis were closely related to the concentration of the polymer. Reducing it to 10 µg/ml immediately produced features observed after a few weeks for 20 µg/ml PHMB-AgNPs, and for those two samples, DLS intensity distribution strongly reinforced this view. Further increase in stabiliser concentration improved protection from the changes observed using UV-Vis. However, the results obtained from DLS became more variable and lacked clear patterns, making any significant findings using this methodology difficult. Relying on data obtained from SAXS and SEM that minimal changes to the diameter of the silver core occur over time,

a possible explanation for the observed changes in UV-Vis and DLS would be an aggregation/agglomeration. Amendola *et al.* [169] have shown that when using Discrete Dipole Approximation to model the theoretical SPR response of silver nanoparticles, aggregation of individual particles changed the excitation spectra to form double/triple peaks. The calculations consider that the silver nanoparticles were in direct contact with a possible gap to allow for a dielectric shell. There were a number of possibilities of how such interaction between particles can occur. If the PHMB were not providing full protective coverage over the nanoparticle, it would allow for partial flocculation of the particles. Alternatively, there might be a correlation between the polymer concentration and the interaction: bridging coagulation – coagulation resulting from interaction with the solvent, and depletion coagulation [170] – all might cause particle-particle interaction leading to UV-Vis double peak development. This would explain the changes in the UV-Vis spectra for 10 and 20 μg/ml PHMB-AgNPs and the size increase observed using DLS. However, the lack of a structural factor when modelling the SAXS patterns casts some uncertainty over this theory. The proximity of the electron-dense AgNPs core could be included in the model. Some first attempts at SAXS data analysis assumed clusters of nanoparticles akin to those found by James *at el.* [171], but the modelling using a double population was unsuccessful (Figure 6-25). Although it was possible to achieve good fitting of the parameters selected, the radius [A] for the structure factor had to be smaller than the size of the particles in contradiction to requirements. Therefore, the SAXS pattern modelling used did not include the low-Q region where such aggregates would typically be found. Observing such features was not possible using STEM-in-SEM, as the samples were dried for analysis. Clusters were observed using WetSTEM, but their shape and size were very irregular and did not produce well-defined peaks in DLS. It is also important to note that the changes in the UV-Vis peaks observed with the addition and increasing concentration of PHMB discussed in Chapter 3 were also not reflected in the corresponding measurements taken using DLS.

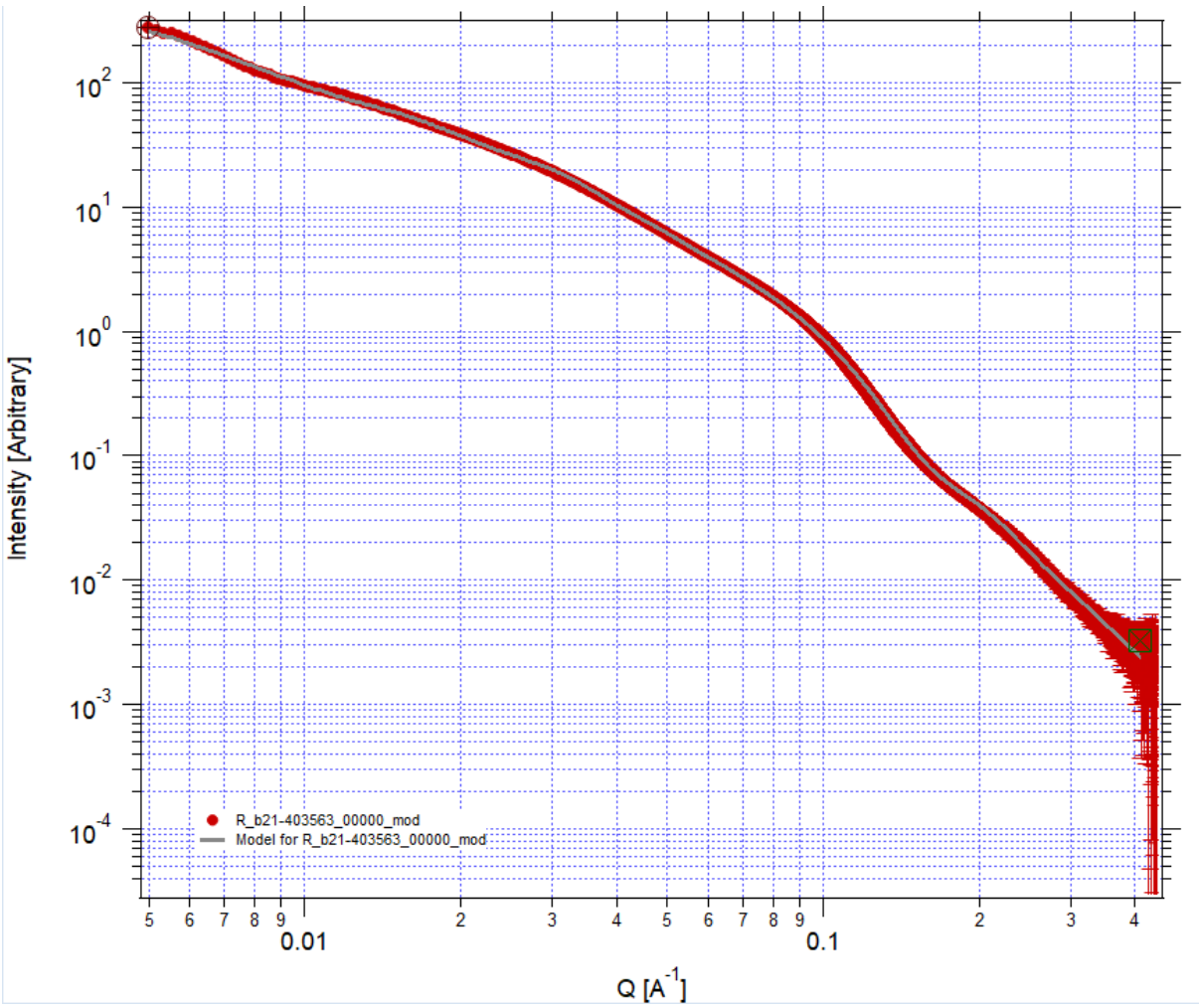

Figure 6-25 SAXS pattern fitted with double population model for 20 µg/ml PHMB-AgNPs (Oct19)

In Chapter 4, the reproducibility of the results was established as reliable. The AgNPs were produced with a low degree of variation between samples in different batches. Yet the results obtained from the long-term study indicate some variability between batches. In other words, the discrepancies observed from batch to batch increased over time when UV-Vis results were compared. The silver core as measured using SAXS and STEM-in-SEM remains unchanged, however. The complexity of the system made it difficult to fully characterise the system and to fully account for the behaviours observed.

It was noted in the results from short- and long-term studies that the 'In Range' parameter presented by DLS as a quality indicator improved over time. This improvement was correlated to the polymer concentration and time between synthesis and characterisation. The

higher the PHMB concentration and the shorter the delay, the lower the value and quality of the measurements. The reasons for low 'In Range' can be numerous, but most commonly include: large sedimenting particles, fluorescence, absorbance, or anything else that might cause either baseline definition problems or low intercept. The absorbance and fluorescence can be ruled out, as it has been shown that no changes occur to the silver core, which has a dominating effect on both. The improvement of the 'In Range' over time and correlation to the polymer suggest PHMB as the likely cause of reduced quality. The conjecture would be that increasing PHMB concentration causes increased polymer-polymer interaction, creating dynamic clusters of PHMB-AgNPs, which stabilise over time.

6.6. Conclusions

Investigation of how the stability of the PHMB-AgNPs changes over time was carried out to better understand the complex behaviour, taking into consideration the various levels of polymer concentrations present. It was also applied to gain more insight into the interactions between various components of the system by analysing their long-term effects.

It has been shown that the long-term stability of PHMB-AgNPs relates to the concentration of the polymer present in the synthesis. For PHMB-AgNPs synthesised in low concentrations of the polymer, especially 20 µg/ml but to a smaller extent in 40 and 60 µg/ml, observable changes to UV-Vis results were noted. There were no changes observed to the silver nanoparticles measured with SAXS and SEM. However, the hydrodynamic diameter increased significantly as reported by DLS. The PHMB-AgNPs were not sufficiently stabilised by the polymer and overtime formed aggregates. The same effect was produced in a fresh batch of 10 µg/ml PHMB-AgNPs. The silver nanoparticles samples over 100 µg/ml PHMB-AgNPs showed minimal changes but over time the short-lived long-distance interaction between particles – bridging flocculation, had settled reducing number fluctuations in the DLS measurements.

Chapter 7. Conclusions and Future Work

7.1. Final conclusions

The risk of antimicrobial resistance identified by scientists and recognised by policymakers resulted in increased awareness of this emerging threat to the human population. A multifaced approach has been proposed, one of the solutions offered to repurpose already known biocidal compounds. Poly(hexamethylene biguanide) and silver nanoparticles have been used as antibacterial agents for decades. Recently it has been reported that the PHMB can be used to stabilise silver nanoparticles giving the complex an increased, synergistic, antimicrobial activity. However, the literature review has shown that the interaction between the two compounds has not been explored to this date. Therefore, this research was designed to examine the formation of the PHMB-AgNPs complex, resulting physicochemical properties and long-term stability.

A range of PHMB-AgNPs characterisation methods was employed during this study and, although the availability of the techniques was an important factor when selecting them it was aimed to have a wide ranging approach to data collection. The electron microscopy and small angle X-ray scattering provided evidence on the electron dense silver nanoparticles; the dynamic light scattering and zeta potential provided insight into the polymer-particle and particle-particle interactions. While ultraviolet–visible spectroscopy served as a fast and efficient means of tracking the reproducibility of the reaction and linking different methods together. Finally, an initial screening for antimicrobial efficacy was carried out. Together those techniques provided a strong understanding of the formation, properties and long-term stability, however, it became important to acknowledge the limitation of the methods. In literature, frequent reliance on size distribution given by DLS needs to be challenged by investigating correlograms to ensure data quality is sufficient. Even when it is below expectations it can provide additional information on the PHMB-AgNPs and it is likely that other polycationic stabilisers will have similar features such as number fluctuations.

Formation of the complex took place immediately upon reduction of the Ag^+ to colloidal silver, the transparent mixture of silver nitrate and PHMB turned yellow upon the addition of the sodium borohydride. There was a change in zeta potential from negative to positive as a result of the PHMB presence imparting polymer-AgNPs complexation. A peak at around 390 appeared in the UV-Vis measurements, but the red shift in the peak as a result of polymer presence was not linear with increasing concentration of PHMB indicating that there was a limit to the amount of PHMB which was effectively able to interact with the silver nanoparticles, reaching maximum potential at around 40-80 µg/ml PHMB used in synthesis, subject to the characterisation method. The progression of the reaction was driven by the colloidal stability of the nanoparticles, enhanced by the borohydride ion and polymer. But the secondary change of solution colour implies the PHMB becoming the main stabiliser as the borohydride ion undergoes hydrolysis. The concentration of the polymer affected the time at which the final colour change occurred, peaking at 80 µg/ml PHMB-AgNPs. It was shown that some control over the reaction was achieved by manipulating a ratio of aged, fully hydrolysed, and freshly prepared sodium borohydride. Concentrations between 60 and 100 µg/ml PHMB-AgNPs appear to feature frequently for observed maxima, minima and modification to the rate of change. This thesis is also supported by the investigation of the infranatant for antimicrobial properties, which showed antimicrobial properties for those PHMB-AgNPs synthesised in higher polymer concentrations.

The mean size of the silver nanoparticles as characterised using SEM and SAXS, for Bare-AgNPs was recorded at around 12 nm, reducing to about 4 nm as PHMB concentration increased. The gradient of change became much smaller upon reaching a concentration of 80 µg/ml PHMB-AgNPs. The particles were observed to be spherical, though some agglomerates that resembled a fused beads structure were also noted for Bare-AgNPs. The results from microscopy also showed an increasing concentration of the polymer present in the sample with larger clusters present with increased thickness. Water is partially evaporated from the sample

when imagining in wet mode, the unabsorbed polymer present in the sample was causing depletion flocculation. In dry mode, drying artefacts were different between the higher and low/no polymer concentrations as the water was fully evaporated the polymer and PHMB-AgNPs formed clusters. The same effect was observed with results from DLS, they were unreliable for measurements of high concentration polymer presence. Importantly, those interactions reduced over time, with quality indicators improving, implying that colloidal stability was slow to achieve.

The stability of the PHMB-AgNPs varied between the samples and was correlated to the levels of polymer concentration. Samples synthesised in low (up to 40 μg/ml) polymer concentration were observed to display several changes, UV-Vis spectra recorded, displayed an agglomeration effect caused by flocculation. The results from SAXS and SEM did not show any change to the size of the silver core but the samples exhibited significant change in colour even when resuspended in water for analysis. As the change was irreversible this was caused by bridging flocculation or, a special case for polyelectrolytes, by electrostatic patch flocculation. PHMB-AgNPs synthesised in polymer concentration from 60 μg/ml were stable over the time tested (up to 13 months). It was concluded that sufficient polymer presence creates enough stabilisation to prevent agglomeration of the particles.

The antimicrobial polymer poly(hexamethylene biguanide) provides an effective stability to silver nanoparticle synthesised using sodium borohydride as a reducing agent in wet chemical reduction pathway. The polymer presence plays an important role in the formation and long-term stability and to prevent aggregation and flocculation of the particles a minimum concentration of PHMB must be added to the reaction. If insufficient bridging or electrostatic patch flocculation will take place, however, the excess unabsorbed polymer may cause depletion flocculation.

It was found using two different methodologies, zone of inhibition and flow cytometry, that there was a limited antimicrobial effect from Bare-AgNP, and that there was a substantial increase in activity when AgNPs were complexed with PHMB, as the polymer provided the observed antimicrobial effect. Although potentially discouraging, further investigations should be carried out on the long-term performance of the agent. There was some indication during this study that the small concentration of PHMB-AgNPs in samples used for UV-Vis testing lost colour within 2-4 weeks, suggesting that AgNPs might be dissolving over time. If this dissolution takes place by Ag oxidising to ionic silver, there is a scope to further measure whether long-term antimicrobial effects can be achieved with it. This would offer an opportunity for an agent that has an immediate antimicrobial effect provided by the polymer and a long-term effect from Ag dissolution: a complementary rather than synergistic relationship. This should be fully reviewed with insight from microbiologists to better understand the mode of action and how the particles interact with bacteria. The lack of antimicrobial effect from Bare-AgNPs under tested conditions should be tested to determine whether it extends into the inhibition of growth, and over time killing efficacy against already established cultures. A larger pool of bacteria strains should be considered, including antibiotic-resistant bacteria such as MRSA.

7.2. Future work

7.2.1. Introduction

The final section of this thesis is dedicated to potential applications of PHMB-AgNPs. Although further work is needed on the antimicrobial efficacy of the complex, it might be advantageous to conduct this work after deciding on the method of delivery of this active agent. Because the focus is placed on areas where this research might have immediate access for testing as a seedcorn project, the delivery media considered were hydrogels. It is therefore discussed how the loading of PHMB-AgNPs into this material could be conducted from the perspective of antimicrobial bandages. Two potential applications are considered, both of

which would be subject to the establishment of antimicrobial efficacy, as a topical antimicrobial broad-spectrum agent used in wound dressings or as a specialised focused agent against *Acanthamoeba keratitis* delivered as an ocular bandage.

7.2.2. Delivery Device – Hydrogels

Hydrogels are three-dimensional polymer networks with biocompatibility that place these materials at the forefront of drug delivery systems [172]. Hydrogels' properties vary based on the material selected for the formation, synthetic or natural, the overall polymerisation conditions, resulting configuration, appearance and others [36]. The unique structure of the hydrogels formed and the high hydrophilicity of the gel makes this material suitable for loading with antimicrobial agents [172].

There are several pathways for loading hydrogels with AgNPs [36]. These differ significantly but can be broadly grouped into four categories: diffusion – allowing the agent to soak up into the hydrogel; additive – adding the agent before the hydrogel is formed; coating – covering the hydrogel with the agent; and *in situ* formation – using the hydrogel matrix as a nanoreactor for the formation of AgNPs.

The method of loading is important because the interactions between the hydrogel and PHMB-AgNPs will have a significant impact on each other, marked by changes to the hydrogel's physical properties and the effectiveness of the agent [173]. Because of this interaction, the specific loading method is closely linked to the application.

7.2.3. PHMB-AgNPs loaded hydrogels

Wound dressings

The natural healing process that takes place within a wound occurs under specific circumstances, and certain conditions must be met for it to be successful [174]. The wound dressing should support this process, or at least not interfere with it. The unique properties of hydrogels such as gas permeability, fluid absorption, and others [172] make them particularly

suitable for this application. The variety of polymers (or blends) available offers an opportunity to control the conditions around the wound, support the regeneration of the skin layers, prevent water loss and create a barrier against infections from outside [174].

Nanoparticle-loaded hydrogels investigated as wound dressings are frequently prepared by loading the hydrogels with a precursor, i.e. silver nitrate, and reduced *in situ* [175] or in one-pot reactions designed to produce hydrogels and nanoparticles at the same time [176]. However, the aim of this section is to consider the applications of already synthesised PHMB-AgNPs. Synthesising silver nanoparticles *in situ* would require detailed studies to investigate how the presence of the polymers impacts formation and how the interaction between substrates affects colloidal stability. This is because the synthetic matrix might take control over the formation of AgNPs, preventing the formation of PHMB-AgNPs. The loading of already synthesised AgNPs has also been explored by adding them to the polymer solution before the mixture is treated with ultraviolet light [177, 178] or gamma irradiation [11] to create nanocomposites. However, an alternative hybrid approach is also available, with the coating or loading of AgNPs carried out on another material that forms a part of the wound dressing. It is based on the technology of coating various textiles (cotton [179], silk [180]) with nanoparticles, which has already been used in the product development of materials used in hospitals and sportswear. Such an approach is particularly strong, as it opens up the possibility to introduce new materials such as coated nanofibers [181] into the wound dressings, akin to those described by Tian *et al.* [182]. It has been shown that coating of the nanofibers with stabilised AgNPs can be achieved by immersion of nanofibers in the AgNPs solution. A similar approach was also taken with AgNPs stabilised by chitosan, which like PHMB is a polyelectrolyte [183].

Developing PHMB-AgNPs carriers in the form of a mat, which then can be sandwiched between layers of hydrogel to provide control over agent release to the site, and may be favoured from the synthesis perspective. Such a two-component system allows for careful

design of the properties required and is not without precedent. The Acticoat™ marketed by Smith & Nephew operates on the basis of polyethylene nets coated with silver nanoparticles with an absorbing polyester matrix sandwiched between the nets. AgNPs-loaded mats are located on the outside of the dressing, promoting the dissociation of silver into the wound, which improves the antibacterial effect but also increases cytotoxicity [184]. The loading of the mat with the PHMB-AgNPs can be done in two ways, by electrospinning material with the agent within it, most likely to produce a slow release of the antimicrobial agent, or by solvent casting, letting the mat soak in the agent, which may offer a short burst of antimicrobial effect. The anecdotal evidence suggests that direct electrospinning with 88% poly(vinyl alcohol) in water could be possible to form nanofibre mats. However, it is unknown how PHMB-AgNPs would impact the electrospinning process or how the interaction between PHMB, AgNPs and PVA be affected by the conditions. Aliko *et al.* [185] blended antimicrobial agents with the polymer and electrospun it to produce mats, and the same might be possible with PHMB-AgNPs. With the alternative, to solvent cast the PHMB-AgNPs on to the PVA mat, the release of the agent could be faster and much more radical. However, if the approach were taken to use the mat as a support sandwiched between hydrogel, such layers could slow the release of the agent into the wound.

Contact lenses

There are a number of factors that incline the cornea to develop infections, including chemical body trauma, foreign body trauma, allergic reactions, and others. One organism causing several corneal infections potentially leading to blindness is a free–living amoeba, *Acanthamoeba.* The treatment following infections is lengthy and requires significant effort. Although various therapies are available, the agents used, such as diamidine, are not only toxic to corneal cells, but also cause severe eye inflammation and do not guarantee success [186]. More recently, an approach exploring a more effective drug cocktail combining biguanides (i.e. PHMB), diamidine and Neomycin has been successfully tested [187]. It has also been found

that silver can have a positive impact on the treatment of *Acanthamoeba*. AgNPs improved the biostatic efficacy of nystatin and amphotericin B [188], agents used in treatment. In addition, silver reduced adherence and promoted the internalisation of trophozoites, forms of *Acanthamoeba* [189], therefore serving an auxiliary role in therapy. Although the PHMB-AgNPs as a complex were not tested against this organism, the individual components, in particular, PHMB, are used in its treatment.

Typically, medication is delivered to the eye using drops, but it is estimated that their bioavailability is as low as 5% due to various physiological and anatomical barriers such as lacrimal drainage [190]. Those barriers can be mitigated by the use of contact lenses as a delivery medium, a specialised form of a wound dressing which is applied to an eye – an ocular bandage. There is a wide choice of polymers used to manufacture contact lenses, which can be broadly categorised as rigid and soft. The former category, mainly represented by poly(methyl methacrylate) (PMMA), is reporting a steady decline in use due to various issues such as low permeability, discomfort or blepharoptosis [191]. Soft contact lenses have much greater biological compatibility and provide enhanced comfort when wearing [192]. These are typically made with various hydrophilic monomers such as (hydroxyethyl)methacrylate (HEMA), but various other compounds can be used. In addition, silicon hydrogel contact lenses are made with silicon-containing materials such as (trimethyl-siloxy)-g-methacryloxy-propysilane (TRIS) that allow greater control over the physical properties of the lenses.

Loading contact lenses with AgNPs is similar to the methods described for wound dressings. Kharaghani *et al.* [193] soaked poly(vinyl alcohol) (PVA) hydrogel and the commercially available Nelfilcon A contact lens – principal component modified PVA – in a silver precursor. Following *in situ* reduction, nanoparticles sized between 50 and 60 nm were obtained, evenly distributed across the discs and covalently bonded to the PVA. A similar approach in loading AgNPs, with *in situ* reduction of silver nitrate in silicone hydrogel, was

presented by Helaly *et al.* [194]. However, other pathways, more suitable for using pre-synthesised PHMB-AgNPs have also been explored for contact lenses. Bazzaz *et al.* [195] synthesised soft contact lenses, with AgNPs from a commercial supplier added to the reaction mix. A variation of this pathway was also exploited by Mourad *et al.* [134]: AgNPs were synthesised in a polymerisation mixture before hydrogel formation took place to produce AgNPs-loaded silicone hydrogel. In addition, it has been shown that simple soaking of commercially available contact lenses (Etafilcon A – HEMA with methacrylic acid) [196], or HEMA-based hydrogels (with various functional monomers) [197] resulted in measurable loading of the material with AgNPs. The final alternative in PHMB-AgNPs loading would be to develop liposomes carrying the active agent and surface-immobilising them on the contact lens [198]. However, liposome immobilisation is a multistep process that could pose a formidable challenge to test and adapt to include silver nanoparticles. On the other hand, the release of the active agent takes place as a result of eyelid friction, and this approach could offer the greatest control over the delivery rate and stability of the final product. Alternatively, polymer-lipid nanoparticles such as Astosomes [199] may more within a reach to be utilised for this purpose.

In each case described above, the material loaded with AgNPs exhibited a strong antimicrobial response against a range of bacteria and acceptable cytotoxicity. In addition, Willcox *et al.* [196] also found a positive killing effect on *Acanthamoeba Castellani*. However, it is important to recognise that some of the studies are investigating colonisation and growth prevention, which are not the same as eradicating already established infections. The overall concentration of the nanoparticles used for the preparation of loaded hydrogels varies, and the toxicity towards pathogens and mammalian cells has to be assessed on a case-by-case basis to account for the properties of the delivery device [200]. For treatment purposes, to achieve a suitable response against already established infections, in particular, those caused by resistant strains of bacteria or (e.g.) *Acanthamoeba*, the concentration of the agent might have to be

elevated at the risk of cytotoxicity. One other drawback which cannot be omitted is the possible yellow discolouration that might affect vision and potentially lens wear comfort.

7.2.4. Challenges

The use of hydrogels loaded with PHMB-AgNPs for any treatment requires pre-screening cytotoxicity studies. Neither PHMB nor silver nanoparticles are without side effects, though silver has been studied much more extensively. The toxicity toward mammalian cells and the corresponding argyria is a well-known and documented phenomenon. Silver is capable of crossing the blood-brain and blood-testes barriers [201], and can potentially damage various bodily organs [202], including the eyes [203]. The effect is highly dependent on the levels of silver that the mammalian cells are exposed to, and therefore on the concentration of AgNPs and Ag^{+} ions as the nanoparticles dissolve [204]. However, Nesporova *et al.* [205] found that the toxicity of silver-loaded wound dressings depends on the construction of the dressing and the type of silver present, not just the ion concentration. As a result, in contrast to the potential dangers of loading with AgNPs, it is possible to produce effective and safe products [206]. The area of silver cytotoxicity has been substantially researched providing a strong background for any application-specific investigation.

One final consideration must be given to the development of resistance to silver. Although the antimicrobial response has not been fully understood, and the consensus is that the multimodal mode of action of silver on the bacteria limits the development of resistance, some instances of acquired resistance have been reported [207]. Adding an additional antimicrobial agent, PHMB, might further reduce any such developments, but it cannot be ruled out and should be monitored.

7.2.5. Summary

The PHMB-AgNPs synthesised in this research study have shown antimicrobial properties that warrant further investigation into the possible applications of this agent. For

topical treatments in wound and eye infections, it would require a bespoke delivery system, with hydrogels a likely candidate. Where the transparency of the hydrogel is unimportant, e.g. wound dressings, the most promising means of loading the PHMB-AgNPs is the coating or electrospinning mats to be sandwiched between the appropriate hydrogels. For contact lenses, the challenge of imbedding the agent is much greater, but the potential specialised application against *Acanthamoeba Keratitis* might warrant investment to improve treatment against this severe sight-threatening infection. In any case, any future development requires detailed cytotoxicity studies and the monitoring of antimicrobial resistance towards the PHMB-AgNPs complexes.

References

1. Bengtsson-Palme, J., E. Kristiansson, and D.G.J. Larsson, *Environmental factors influencing the development and spread of antibiotic resistance.* Fems Microbiology Reviews, 2018. **42**(1): p. 68-80.
2. Prestinaci, F., P. Pezzotti, and A. Pantosti, *Antimicrobial resistance: a global multifaceted phenomenon.* Pathogens and Global Health, 2015. **109**(7): p. 309-318.
3. ECDC/EMEA, *The bacterial challenge: time to react* 2009, European Centre for Disease Prevention and Control/European MedicinesAgency (ECDC/EMEA) Joint Technical Report: Stockholm,.
4. O'Neil, J., *Tackling Drug-Resistant Infections Globally: final report and recomendations. Review on Antimicrobial Resistance*. 2016, Wellcome Trust and HM Government.
5. European Comission, *A European One Health Action Plan against Antimicrobial Resistance (AMR)*. 2017.
6. Wagner, F.E., et al., *Before striking gold in gold-ruby glass.* Nature, 2000. **407**(6805): p. 691-692.
7. Gubala, V., et al., *Engineered nanomaterials and human health: Part 1. Preparation, functionalization and characterization (IUPAC Technical Report).* Pure and Applied Chemistry, 2018. **90**(8): p. 1283-1324.
8. Tran, Q.H., V.Q. Nguyen, and A.T. Le, *Silver nanoparticles: synthesis, properties, toxicology, applications and perspectives.* Advances in Natural Sciences-Nanoscience and Nanotechnology, 2013. **4**(3).
9. Rodrigues, T.S., et al., *Synthesis of Colloidal Metal Nanocrystals: A Comprehensive Review on the Reductants.* Chemistry-a European Journal, 2018. **24**(64): p. 16944-16963.
10. Kang, H., et al., *Stabilization of Silver and Gold Nanoparticles: Preservation and Improvement of Plasmonic Functionalities.* Chemical Reviews, 2019. **119**(1): p. 664-699.
11. Boonkaew, B., et al., *Development and Characterization of a Novel, Antimicrobial, Sterile Hydrogel Dressing for Burn Wounds: Single-Step Production with Gamma*

Irradiation Creates Silver Nanoparticles and Radical Polymerization. Journal of Pharmaceutical Sciences, 2014. **103**(10): p. 3244-3253.
12. Alarcon, E.I., et al., *Coloured cornea replacements with anti-infective properties: expanding the safe use of silver nanoparticles in regenerative medicine.* Nanoscale, 2016. **8**(12): p. 6484-6489.
13. Abou El-Nour, K.M.M., et al., *Synthesis and applications of silver nanoparticles.* Arabian Journal of Chemistry, 2010. **3**(3): p. 135-140.
14. Haider, A. and I.K. Kang, *Preparation of Silver Nanoparticles and Their Industrial and Biomedical Applications: A Comprehensive Review.* Advances in Materials Science and Engineering, 2015.
15. Guzman, M., J. Dille, and S. Godet, *Synthesis and antibacterial activity of silver nanoparticles against gram-positive and gram-negative bacteria.* Nanomedicine-Nanotechnology Biology and Medicine, 2012. **8**(1): p. 37-45.
16. Roy, A., et al., *Green synthesis of silver nanoparticles: biomolecule-nanoparticle organizations targeting antimicrobial activity.* Rsc Advances, 2019. **9**(5): p. 2673-2702.
17. Dong, X., et al., *Shape Control of Silver Nanoparticles by Stepwise Citrate Reduction.* The Journal of Physical Chemistry C, 2009. **113**(16): p. 6573-6576.
18. Soliman, M.G., et al., *Phase Transfer and Polymer Coating Methods toward Improving the Stability of Metallic Nanoparticles for Biological Applications.* Chemistry of Materials, 2015. **27**(3): p. 990-997.
19. Tadros, T.F., *Basic Principles of Interface Science and Colloid Stability*. 2017, Berlin/Boston, GERMANY: Walter de Gruyter GmbH.
20. Li, X., J.J. Lenhart, and H.W. Walker, *Aggregation Kinetics and Dissolution of Coated Silver Nanoparticles.* Langmuir, 2012. **28**(2): p. 1095-1104.
21. Hasegawa, S., et al., *New Magic Au24 Cluster Stabilized by PVP: Selective Formation, Atomic Structure, and Oxidation Catalysis.* JACS Au, 2021. **1**(5): p. 660-668.
22. Luty-Blocho, M., *THE INFLUENCE OF STERIC STABILIZATION ON PROCESS OF Au, Pt NANOPARTICLES FORMATION.* Archives of Metallurgy and Materials, 2019. **64**(1): p. 55-63.
23. Wang, C., et al., *Preparation, Characterization and Application of Polysaccharide-Based Metallic Nanoparticles: A Review.* Polymers, 2017. **9**(12).
24. Kora, A.J. and L. Rastogi, *Green synthesis of palladium nanoparticles using gum ghatti (Anogeissus latifolia) and its application as an antioxidant and catalyst.* Arabian Journal of Chemistry, 2018. **11**(7): p. 1097-1106.
25. Martinez-Gutierrez, F., et al., *Synthesis, characterization, and evaluation of antimicrobial and cytotoxic effect of silver and titanium nanoparticles.* Nanomedicine-Nanotechnology Biology and Medicine, 2010. **6**(5): p. 681-688.
26. Ramazanov, M.A. and F.V. Hajiyeva, *Copper and copper oxide nanoparticles in polypropylene matrix: synthesis, characterization, and dielectric properties.* Composite Interfaces, 2020. **27**(11): p. 1047-1060.
27. Zheltonozhskaya, T.B., et al., *The process of nickel nanoparticle formation in hydrophilic polymer/inorganic matrices.* Molecular Crystals and Liquid Crystals, 2021. **716**(1): p. 13-28.
28. Wang, H.C., et al., *Synthesis and surface modification of cobalt nanoparticles and electromagnetic property of Co/PPy nanocomposites.* Rare Metals, 2015. **34**(4): p. 223-228.
29. Tadros, T., *General Principles of Colloid Stability and the Role of Surface Forces*, in *Colloid Stability*, T.F. Tadros, Editor. 2011. p. 1-22.

30. Zhang, W., et al., *Attachment Efficiency of Nanoparticle Aggregation in Aqueous Dispersions: Modeling and Experimental Validation.* Environmental Science & Technology, 2012. **46**(13): p. 7054-7062.
31. Bhattacharjee, S., *DLS and zeta potential - What they are and what they are not?* Journal of Controlled Release, 2016. **235**: p. 337-351.
32. El Badawy, A.M., et al., *Impact of Environmental Conditions (pH, Ionic Strength, and Electrolyte Type) on the Surface Charge and Aggregation of Silver Nanoparticles Suspensions.* Environmental Science & Technology, 2010. **44**(4): p. 1260-1266.
33. Prathna, T.C., N. Chandrasekaran, and A. Mukherjee, *Studies on aggregation behaviour of silver nanoparticles in aqueous matrices: Effect of surface functionalization and matrix composition.* Colloids and Surfaces a-Physicochemical and Engineering Aspects, 2011. **390**(1-3): p. 216-224.
34. Klasen, H.J., *Historical review of the use of silver in the treatment of burns. I. Early uses.* Burns, 2000. **26**(2): p. 117-130.
35. Klasen, H.J., *A historical review of the use of silver in the treatment of burns. II. Renewed interest for silver.* Burns, 2000. **26**(2): p. 131-138.
36. Mekkawy, A.I., et al., *Silver Nanoparticles-loaded Hydrogels, A Potential Treatment for Resistant Bacterial Infection and Wound Healing: A Review.* British Journal of Pharmaceutical Research, 2016. **14**(2).
37. Le Ouay, B. and F. Stellacci, *Antibacterial activity of silver nanoparticles: A surface science insight.* Nano Today, 2015. **10**(3): p. 339-354.
38. Pelgrift, R.Y. and A.J. Friedman, *Nanotechnology as a therapeutic tool to combat microbial resistance.* Advanced Drug Delivery Reviews, 2013. **65**(13-14): p. 1803-1815.
39. Taglietti, A., et al., *Antibacterial Activity of Glutathione-Coated Silver Nanoparticles against Gram Positive and Gram Negative Bacteria.* Langmuir, 2012. **28**(21): p. 8140-8148.
40. Guo, L.Y., et al., *Polymer/nanosilver composite coatings for antibacterial applications.* Colloids and Surfaces a-Physicochemical and Engineering Aspects, 2013. **439**: p. 69-83.
41. Lara, H.H., et al., *Bactericidal effect of silver nanoparticles against multidrug-resistant bacteria.* World Journal of Microbiology & Biotechnology, 2010. **26**(4): p. 615-621.
42. Martínez-Gutierrez, F., et al., *Antibacterial activity, inflammatory response, coagulation and cytotoxicity effects of silver nanoparticles.* Nanomedicine: Nanotechnology, Biology and Medicine, 2012. **8**(3): p. 328-336.
43. Grosse, S., L. Evje, and T. Syversen, *Silver nanoparticle-induced cytotoxicity in rat brain endothelial cell culture.* Toxicology in Vitro, 2013. **27**(1): p. 305-313.
44. Rose, F.L. and G. Swain, *Polymeric Diguanides*, Patent, Editor. 13 January 1954: Great Britain.
45. Rose, F.L. and G. Swain, *850. Bisdiguanides having antibacterial activity.* Journal of the Chemical Society (Resumed), 1956(0): p. 4422-4425.
46. East, G.C., J.E. McIntyre, and J. Shao, *Polybiguanides: Synthesis and characterization of polybiguanides containing hexamethylene groups.* Polymer, 1997. **38**(15): p. 3973-3984.
47. Jiang, Z.W., et al., *Structural Characterization and Bacteriostatic and Cytotoxicity to 3T3 Cells Study of Oligobiguanidine (Polyhexamethylene Biguanidine Hydrochloride) and its 3-Glycidoxypropyltrimethoxysilane Derivatives.* Journal of Macromolecular Science Part a-Pure and Applied Chemistry, 2012. **49**(11): p. 952-962.

48. Zaki, A.M., A. Troisi, and P. Carbone, *Unexpected Like-Charge Self-Assembly of a Biguanide-Based Antimicrobial Polyelectrolyte.* Journal of Physical Chemistry Letters, 2016. **7**(19): p. 3730-3735.
49. de Paula, G.F., G.I. Netto, and L.H.C. Mattoso, *Physical and Chemical Characterization of Poly(hexamethylene biguanide) Hydrochloride.* Polymers, 2011. **3**(2): p. 928-941.
50. *Poly (hexamethylenebiguanide) hydrochloride; SDS No. 14 [Online]; Lonza (Arch Chemicals Ltd): Amboise Cedex - FRANCE, 27.02.2013, https://www.allswimltd.com/msds/Baquacil%20PHMB.pdf (accessed 4 April 2021).*
51. European Commission, *Opinion on polyaminopropyl biguanide (PHMB) - submission III*, S.C.O.C. Safety, Editor. 2017.
52. Nandi, S.D., *Spectrophotometric (UV) investigation on biguanide and substituted biguanides.* Tetrahedron, 1972. **28**(3): p. 845-&.
53. Masadome, T., et al., *Determination of Polyhexamethylene Biguanide Hydrochloride Using Photometric Colloidal Titration with Crystal Violet as a Color Indicator.* Analytical Sciences, 2011. **27**(8): p. 817-821.
54. Abad-Villar, E.M., et al., *Determination of chlorhexidine digluconate and polyhexamethylene biguanide in eye drops by capillary electrophoresis with contactless conductivity detection.* Analytica Chimica Acta, 2006. **561**(1-2): p. 133-137.
55. Rowhani, T. and A.F. Lagalante, *A colorimetric assay for the determination of polyhexamethylene biguanide in pool and spa water using nickel-nioxime.* Talanta, 2007. **71**(2): p. 964-970.
56. Arora, A., A. Ali, and M.T. Zzaman, *Simple and sensitive method for determination of polyhexanide in multipurpose solution.* Electronic Journal of Biomedicine, 2009. **2**: p. 30-37.
57. Shriver, D.F. and P.W. Atkins, *Shriver & Atkins' inorganic chemistry*. 5th ed. 2010: Oxford University Press.
58. Blackburn, R.S., et al., *Sorption of poly(hexamethylenebiguanide) on cellulose: Mechanism of binding and molecular recognition.* Langmuir, 2006. **22**(13): p. 5636-5644.
59. Daeschlein, G., et al., *Feasibility and clinical applicability of polihexanide for treatment of second-degree burn wounds.* Skin Pharmacology and Physiology, 2007. **20**(6): p. 292-296.
60. Hansmann, F., et al., *Polyhexamethylbiguanid (PHMB) as preoperative antiseptic for cateract surgery.* Ophthalmologe, 2004. **101**(4): p. 377-383.
61. Kaehn, K., *Polihexanide: A Safe and Highly Effective Biocide.* Skin Pharmacology and Physiology, 2010. **23**: p. 7-16.
62. Gerli, S., D. Rossetti, and G.C. Di Renzo, *A new approach for the treatment of bacterial vaginosis: Use of polyhexamethylene biguanide. A prospective, randomized study.* European Review for Medical and Pharmacological Sciences, 2003. **7**(5): p. 127-130.
63. Minnich, K.E., et al., *The effect of a wound care solution containing polyhexanide and betaine on bacterial counts: Results of an in vitro study.* Ostomy Wound Management, 2012. **58**(10): p. 32-36.
64. Mulder, G.D., J.P. Cavorsi, and D.K. Lee, *Polyhexamethylene biguanide (PHMB): An addendum to current topical antimicrobials.* Wounds-a Compendium of Clinical Research and Practice, 2007. **19**(7): p. 173-182.
65. Kawabata, A. and J.A. Taylor, *The effect of reactive dyes upon the uptake and antibacterial efficacy of poly(hexamethylene biguanide) on cotton. Part 3: Reduction in the antibacterial efficacy of poly(hexamethylene biguanide) on cotton, dyed with*

bis(monochlorotriazinyl) reactive dyes. Carbohydrate Polymers, 2007. **67**(3): p. 375-389.
66. Rosin, M., et al., *Effect of a polyhexamethylene biguanide mouthrinse on bacterial counts and plaque.* Journal of Clinical Periodontology, 2001. **28**(12): p. 1121-1126.
67. Alkharashi, M., et al., *Medical interventions for acanthamoeba keratitis.* Cochrane Database of Systematic Reviews, 2015(2): p. 26.
68. Wessels, S. and H. Ingmer, *Modes of action of three disinfectant active substances: A review.* Regulatory Toxicology and Pharmacology, 2013. **67**(3): p. 456-467.
69. Gilbert, P. and L.E. Moore, *Cationic antiseptics: diversity of action under a common epithet.* Journal of Applied Microbiology, 2005. **99**(4): p. 703-715.
70. Ikeda, T., et al., *Interaction of a polymeric biguanide biocide with phospholipid-membranse.* Biochimica Et Biophysica Acta, 1984. **769**(1): p. 57-66.
71. Chindera, K., et al., *The antimicrobial polymer PHMB enters cells and selectively condenses bacterial chromosomes.* Scientific Reports, 2016. **6**.
72. O'Malley, L.P., A.N. Collins, and G.F. White, *Biodegradability of end-groups of the biocide polyhexamethylene biguanide (PHMB) assessed using model compounds.* Journal of Industrial Microbiology & Biotechnology, 2006. **33**(8): p. 677-684.
73. Mueller, G. and A. Kramer, *Biocompatibility index of antiseptic agents by parallel assessment of antimicrobial activity and cellular cytotoxicity.* Journal of Antimicrobial Chemotherapy, 2008. **61**(6): p. 1281-1287.
74. Koburger, T., et al., *Standardized comparison of antiseptic efficacy of triclosan, PVP-iodine, octenidine dihydrochloride, polyhexanide and chlorhexidine digluconate.* Journal of Antimicrobial Chemotherapy, 2010. **65**(8): p. 1712-1719.
75. Krebs, F.C., et al., *Polybiguanides, particularly polyethylene hexamethylene biguanide, have activity against human immunodeficiency virus type 1.* Biomedicine & Pharmacotherapy, 2005. **59**(8): p. 438-445.
76. Valluri, S., et al., *In vitro and in vivo effects of polyhexamethylene biguanide against herpes simplex virus infection.* Cornea, 1997. **16**(5): p. 556-559.
77. Messick, C.R., et al., *In-vitro activity of polyhexamethylene biguanide (PHMB) against fungal isolates associated with infective keratitis.* Journal of Antimicrobial Chemotherapy, 1999. **44**(2): p. 297-298.
78. Chen, F., et al., *Biguanide Iridium(III) Complexes with Potent Antimicrobial Activity.* Journal of Medicinal Chemistry, 2018. **61**(16): p. 7330-7344.
79. Hubberstey, P. and U. Suksangpanya, *Hydrogen-bonded supramolecular chain and sheet formation by coordinated guanidine derivatives.* Supramolecular Assembly Via Hydrogen Bonds Ii, 2004. **111**: p. 33-+.
80. Lebel, O., T. Maris, and J.D. Wuest, *Hydrogen-bonded networks in crystals built from bis(biguanides) and their salts.* Canadian Journal of Chemistry-Revue Canadienne De Chimie, 2006. **84**(10): p. 1426-1433.
81. Yi, J.L., et al., *Effect of polyhexamethylene biguanide functionalized silver nanoparticles on the growth of Staphylococcus aureus.* Fems Microbiology Letters, 2019. **366**(4): p. 10.
82. Ashraf, S., et al., *Polyhexamethylene biguanide functionalized cationic silver nanoparticles for enhanced antimicrobial activity.* Nanoscale Research Letters, 2012. **7**.
83. Gusev, A.A., et al., *Versatile synthesis of PHMB-stabilized silver nanoparticles and their significant stimulating effect on fodder beet (Beta vulgaris L.).* Materials Science & Engineering C-Materials for Biological Applications, 2016. **62**: p. 152-159.
84. Krutyakov, Y.A., et al., *Synthesis of positively charged hybrid PHMB-stabilized silver nanoparticles: the search for a new type of active substances used in plant protection products.* Materials Research Express, 2017. **4**(7).

85. Williams, D.H. and I. Fleming, *Spectroscopic methods in organic chemistry*. fourth ed. 1995, London: McGraw-Hill Book Company.
86. Tranter, G.E., *UV-Visible Absorption and Fluorescence Spectrometers*, in *Encyclopedia of Spectroscopy and Spectrometry*, J.C. Lindon, Editor. 1999, Elsevier: Oxford. p. 2383-2389.
87. Salamon, Z. and G. Tollin, *Surface Plasmon Resonance, Theory*, in *Encyclopedia of Spectroscopy and Spectrometry*, J.C. Lindon, Editor. 1999, Elsevier: Oxford. p. 2311-2319.
88. Bohren, C.F., *How can a particle absorb more than the light incident on it.* American Journal of Physics, 1983. **51**(4): p. 323-327.
89. Herrera, L.J.M., et al., *Sizing and Eddy currents in magnetic core nanoparticles: an optical extinction approach.* Physical Chemistry Chemical Physics, 2017. **19**(4): p. 3076-3083.
90. Roldan, M.V., et al., *Optical properties and extinction spectroscopy to characterize the synthesis of amine capped silver nanoparticles.* Materials Chemistry and Physics, 2008. **112**(3): p. 984-990.
91. Santillan, J.M.J., L.B. Scaffardi, and D.C. Schinca, *Quantitative optical extinction-based parametric method for sizing a single core-shell Ag-Ag2O nanoparticle.* Journal of Physics D-Applied Physics, 2011. **44**(10).
92. Scaffardi, L.B., et al., *Sizing gold nanoparticles by optical extinction spectroscopy.* Nanotechnology, 2005. **16**(1): p. 158-163.
93. Scaffardi, L.B. and J.O. Tocho, *Size dependence of refractive index of gold nanoparticles.* Nanotechnology, 2006. **17**(5): p. 1309-1315.
94. Schinca, D.C. and L.B. Scaffardi, *Core and shell sizing of small silver-coated nanospheres by optical extinction spectroscopy.* Nanotechnology, 2008. **19**(49).
95. Tomaszewska, E., et al., *Detection Limits of DLS and UV-Vis Spectroscopy in Characterization of Polydisperse Nanoparticles Colloids.* Journal of Nanomaterials, 2013.
96. Schnablegger, H. and Y. Singh, *The SAXS guide: getting acquainted with the principles*. 4th ed. 2017, Austria: Anton Paar GmbH.
97. Ingham, B., *X-ray scattering characterisation of nanoparticles.* Crystallography Reviews, 2015. **21**(4): p. 229-303.
98. Narayanan, T. and O. Konovalov, *Synchrotron Scattering Methods for Nanomaterials and Soft Matter Research.* Materials, 2020. **13**(3): p. 52.
99. Beaucage, G. and D.W. Schaefer, *Structural studies of complex systems using small-angle scattering: a unified Guinier/power-law approach.* Journal of Non-Crystalline Solids, 1994. **172-174**: p. 797-805.
100. Pauw, B.R., C. Kastner, and A.F. Thunemann, *Nanoparticle size distribution quantification: results of a small-angle X-ray scattering inter-laboratory comparison.* Journal of Applied Crystallography, 2017. **50**: p. 1280-1288.
101. Sun, Y.G. and Y. Ren, *In Situ Synchrotron X-Ray Techniques for Real-Time Probing of Colloidal Nanoparticle Synthesis.* Particle & Particle Systems Characterization, 2013. **30**(5): p. 399-419.
102. Garcia, P., et al., *Combining Small-Angle X-ray Scattering and X-ray Powder Diffraction to Investigate Size, Shape and Crystallinity of Silver, Gold and Alloyed Silver-Gold Nanoparticles.* Brazilian Journal of Physics, 2019. **49**(2): p. 183-190.
103. Skoglund, S., et al., *A novel explanation for the enhanced colloidal stability of silver nanoparticles in the presence of an oppositely charged surfactant.* Physical Chemistry Chemical Physics, 2017. **19**(41): p. 28037-28043.
104. Yeh, Y. and H.Z. Cummins, *Localized fluid flow measurements with an He–Ne laser spectrometer.* Applied Physics Letters, 1964. **4**(10): p. 176-178.

105. Pecora, R., *Doppler Shifts in Light Scattering from Pure Liquids and Polymer Solutions.* The Journal of Chemical Physics, 1964. **40**(6): p. 1604-1614.
106. Brar, S.K. and M. Verma, *Measurement of nanoparticles by light-scattering techniques.* Trac-Trends in Analytical Chemistry, 2011. **30**(1): p. 4-17.
107. Sutherland, W., *LXXV. A dynamical theory of diffusion for non-electrolytes and the molecular mass of albumin.* The London, Edinburgh, and Dublin Philosophical Magazine and Journal of Science, 1905. **9**(54): p. 781-785.
108. von Smoluchowski, M., *Zur kinetischen Theorie der Brownschen Molekularbewegung und der Suspensionen.* Annalen der Physik, 1906. **326**(14): p. 756-780.
109. Einstein, A., *Investigations on the Theory of the Brownian Movement*, ed. R. Furth. 1956: Dover Publications, Inc.
110. Koppel, D.E., *Analysis of macromolecular polydispersity in intensity correlation spectroscopy - method of cummulants.* Journal of Chemical Physics, 1972. **57**(11): p. 4814-&.
111. Provencher, S.W., *A constrained regularization method for inverting data represented by linear algebraic or integal-equations.* Computer Physics Communications, 1982. **27**(3): p. 213-227.
112. Dobrovolskaia, M.A., et al., *Protein corona composition does not accurately predict hematocompatibility of colloidal gold nanoparticles.* Nanomedicine: Nanotechnology, Biology and Medicine, 2014. **10**(7): p. 1453-1463.
113. Lorber, B., et al., *Protein analysis by dynamic light scattering: Methods and techniques for students.* Biochemistry and Molecular Biology Education, 2012. **40**(6): p. 372-382.
114. Kaszuba, M., et al., *High-concentration zeta potential measurements using light-scattering techniques.* Philosophical Transactions of the Royal Society a-Mathematical Physical and Engineering Sciences, 2010. **368**(1927): p. 4439-4451.
115. Ruiz-Cabello, F.J.M., et al., *Electric double-layer potentials and surface regulation properties measured by colloidal-probe atomic force microscopy.* Physical Review E, 2014. **90**(1).
116. Robins, M. and A. Fillery-Travis, *Colloidal dispersions*. Journal of Chemical Technology & Biotechnology, ed. E. by. Vol. 54. 1989, Cambridge, UK: Cambridge University Press. 201-202.
117. Henry, D.C. and A. Lapworth, *The cataphoresis of suspended particles. Part I. The equation of cataphoresis.* Proceedings of the Royal Society of London. Series A, Containing Papers of a Mathematical and Physical Character, 1931. **133**(821): p. 106-129.
118. Doane, T.L., et al., *Nanoparticle zeta-Potentials.* Accounts of Chemical Research, 2012. **45**(3): p. 317-326.
119. Suresh, A.K., et al., *Cytotoxicity Induced by Engineered Silver Nanocrystallites Is Dependent on Surface Coatings and Cell Types.* Langmuir, 2012. **28**(5): p. 2727-2735.
120. Parks, G.A., *The Isoelectric Points of Solid Oxides, Solid Hydroxides, and Aqueous Hydroxo Complex Systems.* Chemical Reviews, 1965. **65**(2): p. 177-198.
121. Sadowski, Z., et al., *Synthesis of silver nanoparticles using microorganisms.* Materials Science-Poland, 2008. **26**(2).
122. Sylvestre, J.P., et al., *Surface chemistry of gold nanoparticles produced by laser ablation in aqueous media.* Journal of Physical Chemistry B, 2004. **108**(43): p. 16864-16869.
123. Siskova, K., et al., *Ion-specific effects on laser ablation of silver in aqueous electrolyte solutions.* Journal of Physical Chemistry C, 2008. **112**(12): p. 4435-4443.

124. Stokes, D.J., *Principles and Practice of Variable Pressure/Environmental Scanning Electron Microscopy (VP - ESEM)*. 2008, UK: John Wiley & Sons, Ltd.
125. Bogner, A., et al., *Wet STEM: A new development in environmental SEM for imaging nano-objects included in a liquid phase.* Ultramicroscopy, 2005. **104**(3-4): p. 290-301.
126. Patel, B., R. Pearson, and M. Watanabe, *Bright Field and Dark Field STEM-IN-SEM Imaging of Polymer Systems.* Journal of Applied Polymer Science, 2014. **131**(19): p. 8.
127. Brydson, R., et al., *Microscopy of nanoparticulate dispersions.* Journal of Microscopy, 2015. **260**(3): p. 238-247.
128. Van Tendeloo, G., et al., *Advanced Electron Microscopy for Advanced Materials.* Advanced Materials, 2012. **24**(42): p. 5655-5675.
129. Roomans, G.M. and A. Dragomir, *X-Ray Microanalysis in the Scanning Electron Microscope*, in *Electron Microscopy*, J. Kuo, Editor. 2010, Humana Press. p. 507-528.
130. Goodhew, P.J., J. Humphreys, and R. Beanland, *Electron Microscopy and Analysis*. 2000: Taylor & Francis Group.
131. Godfriend, R.M. and D. Anca, *X-Ray Microanalysis in the Scanning Electron Microscope*, in *Electron Microscopy*, J. Kuo, Editor. 2010, Humana Press. p. 507-528.
132. Newbury, D.E. and N.W.M. Ritchie, *Performing elemental microanalysis with high accuracy and high precision by scanning electron microscopy/silicon drift detector energy-dispersive X-ray spectrometry (SEM/SDD-EDS).* Journal of Materials Science, 2015. **50**(2): p. 493-518.
133. Dhand, V., et al., *Green synthesis of silver nanoparticles using Coffea arabica seed extract and its antibacterial activity.* Materials Science & Engineering C-Materials for Biological Applications, 2016. **58**: p. 36-43.
134. Mourad, R., et al., *Antimicrobial and physicomechanical natures of silver nanoparticles incorporated into silicone-hydrogel films.* Contact Lens & Anterior Eye, 2019. **42**(3): p. 325-333.
135. Ristig, S., et al., *Nanostructure of wet-chemically prepared, polymer-stabilized silver-gold nanoalloys (6 nm) over the entire composition range.* Journal of Materials Chemistry B, 2015. **3**(23): p. 4654-4662.
136. Korshed, P., et al., *Effect of Storage Conditions on the Long-Term Stability of Bactericidal Effects for Laser Generated Silver Nanoparticles.* Nanomaterials, 2018. **8**(4): p. 12.
137. Balouiri, M., M. Sadiki, and S.K. Ibnsouda, *Methods for in vitro evaluating antimicrobial activity: A review.* Journal of Pharmaceutical Analysis, 2016. **6**(2): p. 71-79.
138. Matuschek, E., D.F.J. Brown, and G. Kahlmeter, *Development of the EUCAST disk diffusion antimicrobial susceptibility testing method and its implementation in routine microbiology laboratories.* Clinical Microbiology and Infection, 2014. **20**(4): p. O255-O266.
139. CLSI, *Performance Standards for Antimicrobial Disk Susceptibility Test*. 2018, CLSI Standard M02. 13th ed. Clinical and Laboratory Standards Institute: Wayne, PA.
140. CLSI, *Performance Standards for Antimicrobial Susceptibility Test*. 2021, CLSI Supplement M100. 31st ed. Clinical and Laboratory Standards Institute.
141. Chen, Q.C., et al., *Preparation, Antibacterial, and Antioxidant Activities of Silver/Chitosan Composites.* Journal of Carbohydrate Chemistry, 2014. **33**(6): p. 298-312.

142. CLSI, *Methods for Determining Bactericidal Activity of Antimicrobial Agent, Approved Guideline* 1999: 950 West Valley Road, Suite 2500, Wayne, Pennsylvania 19087, USA, .
143. Borazjani, R.N., et al., *Flow cytometry for determination of the efficacy of contact lens disinfecting solutions against Acanthamoeba spp.* Applied and Environmental Microbiology, 2000. **66**(3): p. 1057-1061.
144. Ilavsky, J. and P.R. Jemian, *Irena: tool suite for modeling and analysis of small-angle scattering.* Journal of Applied Crystallography, 2009. **42**(2): p. 347-353.
145. *Sample dispersion and refractive index guide*. 2007, England: Malvern Instruments Ltd.
146. Teulon, J.M., et al., *On the Operational Aspects of Measuring Nanoparticle Sizes.* Nanomaterials, 2019. **9**(1): p. 29.
147. Lorenzo-Morales, J., N.A. Khan, and J. Walochnik, *An update on Acanthamoeba keratitis: diagnosis, pathogenesis and treatment.* Parasite, 2015. **22**: p. 20.
148. Paramelle, D., et al., *A rapid method to estimate the concentration of citrate capped silver nanoparticles from UV-visible light spectra.* Analyst, 2014. **139**(19): p. 4855-4861.
149. Amirjani, A., F. Firouzi, and D.F. Haghshenas, *Predicting the Size of Silver Nanoparticles from Their Optical Properties.* Plasmonics, 2020. **15**(4): p. 1077-1082.
150. Sheehy, K., et al., *Antimicrobial properties of nano-silver: a cautionary approach to ionic interference.* J Colloid Interface Sci, 2015. **443**: p. 56-64.
151. Boonkaew, B., et al., *Antimicrobial efficacy of a novel silver hydrogel dressing compared to two common silver burn wound dressings: Acticoat((TM)) and PolyMem Silver (R).* Burns, 2014. **40**(1): p. 89-96.
152. Bhui, D.K., et al., *Synthesis and UV-vis spectroscopic study of silver nanoparticles in aqueous SDS solution.* Journal of Molecular Liquids, 2009. **145**(1): p. 33-37.
153. Khlebtsov, N.G., L.A. Trachuk, and A.G. Mel'nikov, *The effect of the size, shape, and structure of metal nanoparticles on the dependence of their optical properties on the refractive index of a disperse medium.* Optics and Spectroscopy, 2005. **98**(1): p. 77-83.
154. Fernandez-Castane, A., et al., *Flow cytometry as a rapid analytical tool to determine physiological responses to changing O-2 and iron concentration by Magnetospirillum gryphiswaldense strain MSR-1.* Scientific Reports, 2017. **7**.
155. Zheng, K.Y., et al., *Antimicrobial silver nanomaterials.* Coordination Chemistry Reviews, 2018. **357**: p. 1-17.
156. Lucas, A.D., E.A. Gordon, and M.E. Stratmeyer, *Analysis of polyhexamethylene biguanide in multipurpose contact lens solutions.* Talanta, 2009. **80**(2): p. 1016-1019.
157. Polte, J., *Fundamental growth principles of colloidal metal nanoparticles - a new perspective.* Crystengcomm, 2015. **17**(36): p. 6809-6830.
158. Thanh, N.T.K., N. Maclean, and S. Mahiddine, *Mechanisms of Nucleation and Growth of Nanoparticles in Solution.* Chemical Reviews, 2014. **114**(15): p. 7610-7630.
159. Yan, S., et al., *Time-Resolved Small-Angle X-ray Scattering Study on the Growth Behavior of Silver Nanoparticles.* Journal of Physical Chemistry C, 2014. **118**(21): p. 11454-11463.
160. Polte, J., et al., *Formation Mechanism of Colloidal Silver Nanoparticles: Analogies and Differences to the Growth of Gold Nanoparticles.* Acs Nano, 2012. **6**(7): p. 5791-5802.
161. Wuithschick, M., et al., *Size-Controlled Synthesis of Colloidal Silver Nanoparticles Based on Mechanistic Understanding.* Chemistry of Materials, 2013. **25**(23): p. 4679-4689.

162. Wuithschick, M., et al., *Illustrating the formation of metal nanoparticles with a growth concept based on colloidal stability.* Physical Chemistry Chemical Physics, 2015. **17**(30): p. 19895-19900.
163. Ranoszek-Soliwoda, K., et al., *The role of tannic acid and sodium citrate in the synthesis of silver nanoparticles.* Journal of Nanoparticle Research, 2017. **19**(8): p. 15.
164. Agnihotri, S. and S. Mukherji, *Size-controlled silver nanoparticles synthesized over the range 5-100 nm using the same protocol and their antibacterial efficacy.* Rsc Advances, 2014. **4**(8): p. 3974-3983.
165. Laborda, F., et al., *Detection, characterization and quantification of inorganic engineered nanomaterials: A review of techniques and methodological approaches for the analysis of complex samples.* Analytica Chimica Acta, 2016. **904**: p. 10-32.
166. Fernando, I., T.T. Qian, and Y. Zhou, *Long term impact of surfactants & polymers on the colloidal stability, aggregation and dissolution of silver nanoparticles.* Environmental Research, 2019. **179**: p. 9.
167. Pinto, V.V., et al., *Long time effect on the stability of silver nanoparticles in aqueous medium: Effect of the synthesis and storage conditions.* Colloids and Surfaces a-Physicochemical and Engineering Aspects, 2010. **364**(1-3): p. 19-25.
168. Zambelli, A.M., et al., *Diffusion of Antimicrobials Across Silicone Hydrogel Contact Lenses.* Eye & Contact Lens-Science and Clinical Practice, 2015. **41**(5): p. 277-280.
169. Amendola, V., O.M. Bakr, and F. Stellacci, *A Study of the Surface Plasmon Resonance of Silver Nanoparticles by the Discrete Dipole Approximation Method: Effect of Shape, Size, Structure, and Assembly.* Plasmonics, 2010. **5**(1): p. 85-97.
170. Kamiya, H., et al., *Chapter 3 - Characteristics and behavior of nanoparticles and its dispersion systems*, in *Nanoparticle Technology Handbook*, M. Hosokawa, et al., Editors. 2008, Elsevier: Amsterdam. p. 113-176.
171. James, A.M., et al., *Dispersible microporous diblock copolymer nanoparticles via polymerisation-induced self-assembly.* Polymer Chemistry, 2019. **10**(28): p. 3879-3886.
172. Yang, K.R., et al., *Antimicrobial hydrogels: promising materials for medical application.* International Journal of Nanomedicine, 2018. **13**: p. 2217-2263.
173. Thoniyot, P., et al., *Nanoparticle-Hydrogel Composites: Concept, Design, and Applications of These Promising, Multi-Functional Materials.* Advance Science, 2015. **2**.
174. Kalantari, K., et al., *Wound dressings functionalized with silver nanoparticles: promises and pitfalls.* Nanoscale, 2020. **12**(4): p. 2268-2291.
175. Mohan, Y.M., et al., *Hydrogel networks as nanoreactors: A novel approach to silver nanoparticles for antibacterial applications.* Polymer, 2007. **48**(1): p. 158-164.
176. Jiao, T.F., et al., *Reduced Graphene Oxide-Based Silver Nanoparticle-Containing Composite Hydrogel as Highly Efficient Dye Catalysts for Wastewater Treatment.* Scientific Reports, 2015. **5**: p. 12.
177. Levi-Polyachenko, N., et al., *Chitosan wound dressing with hexagonal silver nanoparticles for hyperthermia and enhanced delivery of small molecules.* Colloids and Surfaces B-Biointerfaces, 2016. **142**: p. 315-324.
178. Lee, W.F. and K.T. Tsao, *Effect of silver nanoparticles content on the various properties of nanocomposite hydrogels by in situ polymerization.* Journal of Materials Science, 2010. **45**(1): p. 89-97.
179. Granados, A., R. Pleixats, and A. Vallribera, *Recent Advances on Antimicrobial and Anti-Inflammatory Cotton Fabrics Containing Nanostructures.* Molecules, 2021. **26**(10): p. 22.
180. Marin, C.B., et al., *Silk Polymers and Nanoparticles: A Powerful Combination for the Design of Versatile Biomaterials.* Frontiers in Chemistry, 2020. **8**: p. 22.

181. Rath, G., et al., *Collagen nanofiber containing silver nanoparticles for improved wound-healing applications.* Journal of Drug Targeting, 2016. **24**(6): p. 520-529.
182. Tian, J., et al., *Topical delivery of silver nanoparticles promotes wound healing.* Chemmedchem, 2007. **2**(1): p. 129-136.
183. Mokhena, T.C. and A.S. Luyt, *Electrospun alginate nanofibres impregnated with silver nanoparticles: Preparation, morphology and antibacterial properties.* Carbohydrate Polymers, 2017. **165**: p. 304-312.
184. Burd, A., et al., *A comparative study of the cytotoxicity of silver-based dressings in monolayer cell, tissue explant, and animal models.* Wound Repair and Regeneration, 2007. **15**(1): p. 94-104.
185. Aliko, K., et al., *Poly(butylene succinate) fibrous dressings containing natural antimicrobial agents.* Journal of Industrial Textiles, 2021: p. 1528083720987209.
186. Papa, V., et al., *Acanthamoeba keratitis therapy: time to cure and visual outcome analysis for different antiamoebic therapies in 227 cases.* British Journal of Ophthalmology, 2020. **104**(4): p. 575-581.
187. Somani, S.N., Y. Ronquillo, and M. Moshirfar, *Acanthamoeba Keratitis*. Updated 2021 Jan 21, StatPearls Publishing: Treasure Island (FL).
188. Anwar, A., et al., *Silver nanoparticle conjugation affects antiacanthamoebic activities of amphotericin B, nystatin, and fluconazole.* Parasitology Research, 2018. **117**(1): p. 265-271.
189. Ullah, I., et al., *Comparative study on the antileishmanial activities of chemically and biologically synthesized silver nanoparticles (AgNPs).* 3 Biotech, 2018. **8**: p. 8.
190. Raviola, G., *The structural basis of the blood-ocular barriers.* Experimental Eye Research, 1977. **25**: p. 27-63.
191. Xu, J.W., et al., *A comprehensive review on contact lens for ophthalmic drug delivery.* Journal of Controlled Release, 2018. **281**: p. 97-118.
192. Tighe, B.J., *A Decade of Silicone Hydrogel Development: Surface Properties, Mechanical Properties, and Ocular Compatibility.* Eye & Contact Lens, 2013. **39**(1): p. 4-12.
193. Kharaghani, D., et al., *Development of antibacterial contact lenses containing metallic nanoparticles.* Polymer Testing, 2019. **79**: p. 8.
194. Helaly, F.M., et al., *Synthesis and characterization of nanosilver-silicone hydrogel composites for inhibition of bacteria growth.* Contact Lens & Anterior Eye, 2017. **40**(1): p. 59-66.
195. Bazzaz, B.S.F., et al., *Preparation, characterization and antimicrobial study of a hydrogel (soft contact lens) material impregnated with silver nanoparticles.* Contact Lens & Anterior Eye, 2014. **37**(3): p. 149-152.
196. Willcox, M.D.P., et al., *Ability of silver-impregnated contact lenses to control microbial growth and colonisation.* Journal of Optometry, 2010. **3**(3): p. 143-148.
197. Rad, M.S., et al., *Antibacterial Activity of Silver Nanoparticle-Loaded Soft Contact Lens Materials: The Effect of Monomer Composition.* Current Eye Research, 2016. **41**(10): p. 1286-1293.
198. Danion, A., et al., *Fabrication and characterization of contact lenses bearing surface-immobilized layers of intact liposomes.* Journal of Biomedical Materials Research Part A, 2007. **82A**(1): p. 41-51.
199. Punyamoonwongsa, P. and B.J. Tighe. *A Smart Hydrogel-Based System for Controlled Drug*. 2005.
200. Ayala-Núñez, N.V., et al., *Silver Nanoparticles Toxicity and Bactericidal Effect Against Methicillin-Resistant Staphylococcus aureus: Nanoscale Does Matter.* NanoBiotechnology, 2009. **5**(1): p. 2-9.

201. Borm, P.J.A. and W. Kreyling, *Toxicological hazards of inhaled nanoparticles - Potential implications for drug delivery.* Journal of Nanoscience and Nanotechnology, 2004. **4**(5): p. 521-531.
202. Yang, Y., et al., *Toxicity assessment of nanoparticles in various systems and organs.* Nanotechnology Reviews, 2017. **6**(3): p. 279-289.
203. Soderstjerna, E., et al., *Silver and Gold Nanoparticles Exposure to In Vitro Cultured Retina - Studies on Nanoparticle Internalization, Apoptosis, Oxidative Stress, Glial- and Microglial Activity.* Plos One, 2014. **9**(8): p. 16.
204. Konop, M., et al., *Certain Aspects of Silver and Silver Nanoparticles in Wound Care: A Minireview.* Journal of Nanomaterials, 2016.
205. Nesporova, K., et al., *Effects of wound dressings containing silver on skin and immune cells.* Scientific Reports, 2020. **10**(1): p. 14.
206. Kokura, S., et al., *Silver nanoparticles as a safe preservative for use in cosmetics.* Nanomedicine-Nanotechnology Biology and Medicine, 2010. **6**(4): p. 570-574.
207. Ellis, D.H., et al., *Silver nanoparticle antibacterial efficacy and resistance development in key bacterial species.* Biomedical Physics & Engineering Express, 2019. **5**(1): p. 13.

Appendices

Appendix 1 – Table with all relevant parameters for modelling of small angle X-ray scattering obtained.

#	Sample name	Diamond ref	Batch	Age at scan	Population size (radi [A])		st dev [A]	B	P	Aspect Ratio	Rg cut off	Bckg
1	Bare-AgNPs	b21-403562.nxs	Oct19	Fresh	61.53		9.39	1.19E-02	0.2295	2.37	169	0.0000
2	10 PHMB-AgNPs	b21-403573.nxs	Oct19	Fresh	36.24		12.22	9.84E-07	2.0914	1.00	50	0.0025
3	20 PHMB-AgNPs	b21-403563.nxs	Oct19	Fresh	27.89		6.39	0.000113814	1.1376	1.00	50	0.0024
4	40 PHMB-AgNPs	b21-403564.nxs	Oct19	Fresh	21.02		4.18	0.000152159	0.9963	1.67	50	0.0025
5	60 PHMB-AgNPs	b21-403574.nxs	Oct19	Fresh	17.64		2.69	1.32E-05	1.2168	1.70	33	0.0000
6	80 PHMB-AgNPs	b21-403566.nxs	Oct19	Fresh	17.99		3.13	1.41E-05	1.3079	1.45	33	0.0000
7	100 PHMB-AgNPs	b21-403567.nxs	Oct19	Fresh	16.89		2.65	8.18E-07	1.8338	1.83	33	0.0002
8	120 PHMB-AgNPs	b21-403568.nxs	Oct19	Fresh	16.47		3.00	3.62E-06	1.4467	1.59	33	0.0000
9	140 PHMB-AgNPs	b21-403569.nxs	Oct19	Fresh	16.73		3.09	2.47E-05	1.0192	1.46	33	0.0000
10	160 PHMB-AgNPs	b21-403570.nxs	Oct19	Fresh	14.97		2.71	6.37E-05	0.4978	1.73	33	0.0009
11	200 PHMB-AgNPs	b21-403571.nxs	Oct19	Fresh	15.15		3.05	5.20E-05	0.6605	1.68	33	0.0007
12	20 PHMB-AgNPs	b21-403582.nxs	Jun19	4 months	29.04		6.74	4.58E-05	1.3479	1.00	50	0.0036
13	40 PHMB-AgNPs	b21-403583.nxs	Jun19	4 months	24.55		5.39	0.000263355	0.8977	1.00	50	0.0000
14	60 PHMB-AgNPs	b21-403584.nxs	Jun19	4 months	19.16		2.80	2.91E-06	1.7025	1.90	33	0.0000
15	80 PHMB-AgNPs	b21-403585.nxs	Jun19	4 months	19.37		2.80	6.82E-07	2.3906	0.00	33	0.0012
16	100 PHMB-AgNPs	b21-403586.nxs	Jun19	4 months	17.45		2.21	2.82E-06	1.8879	2.24	33	0.0018
17	120 PHMB-AgNPs	b21-403587.nxs	Jun19	4 months	17.26		2.08	1.83E-06	1.9527	2.08	33	0.0027
18	140 PHMB-AgNPs	b21-403588.nxs	Jun19	4 months	17.03		1.95	4.54E-08	2.9373	2.74	33	0.0016
19	160 PHMB-AgNPs	b21-403589.nxs	Jun19	4 months	16.60		2.06	2.58E-06	1.8447	1.88	33	0.0014

20	200 PHMB-AgNPs	b21-403590.nxs	Jun19	4 months	16.00		1.98	9.33E-07	2.0289	2.21	33	0.0023
21	20 PHMB-AgNPs	b21-403612.nxs	Jan19	9 months	30.05		7.10	8.41E-05	1.2168	1.00	50	0.0050
22	40 PHMB-AgNPs	b21-403613.nxs	Jan19	9 months	24.62		5.09	0.00181219	0.0018	1.00	50	0.0026
23	60 PHMB-AgNPs	b21-403614.nxs	Jan19	9 months	21.96		3.80	1.14E-05	0.0000	1.00	33	0.0048
24	80 PHMB-AgNPs	b21-403615.nxs	Jan19	9 months	19.96		3.40	1.96E-05	1.5215	1.30	33	0.0039
25	100 PHMB-AgNPs	b21-403616.nxs	Jan19	9 months	17.70		2.47	2.44E-06	1.9416	2.22	33	0.0027
26	120 PHMB-AgNPs	b21-403617.nxs	Jan19	9 months	17.23		2.22	1.64E-06	2.0213	2.15	33	0.0000
27	140 PHMB-AgNPs	b21-403618.nxs	Jan19	9 months	16.91		2.27	3.45E-06	1.6652	2.27	33	0.0003
28	160 PHMB-AgNPs	b21-403619.nxs	Jan19	9 months	18.72		4.13	3.88E-06	1.8391	1.06	33	0.0035
29	200 PHMB-AgNPs	b21-403620.nxs	Jan19	9 months	16.73		2.35	1.60E-05	1.2770	2.05	33	0.0041
30	40 PHMB-AgNPs	b21-403621.nxs	Nov18	11 months	25.46		5.41	0.000723176	0.0007	1.00	50	0.0046
31	60 PHMB-AgNPs	b21-403622.nxs	Nov18	11 months	23.03		4.24	4.29E-06	1.8226	1.00	33	0.0036
32	80 PHMB-AgNPs	b21-403623.nxs	Nov18	11 months	23.40		4.18	1.62E-06	2.0646	1.00	33	0.0004
33	100 PHMB-AgNPs	b21-403624.nxs	Nov18	11 months	18.60		2.66	3.68E-06	1.8950	1.75	33	0.0028
34	120 PHMB-AgNPs	b21-403625.nxs	Nov18	11 months	18.41		2.66	1.09E-06	2.1459	1.92	33	0.0034
35	140 PHMB-AgNPs	b21-403626.nxs	Nov18	11 months	18.67		2.65	1.67E-06	2.0622	1.74	33	0.0025
36	160 PHMB-AgNPs	b21-403627.nxs	Nov18	11 months	19.32		2.77	5.62E-07	2.4390	1.86	33	0.0018
37	200 PHMB-AgNPs	b21-403629.nxs	Nov18	11 months	18.83		2.71	6.10E-06	1.5894	1.60	33	0.0006

Appendix 1b – Examples of model fitting into the scattering data obtained from Small Angle X-ray Scattering with the parameters are defined in Appendix 1

Bare-AgNPs (Oct19)

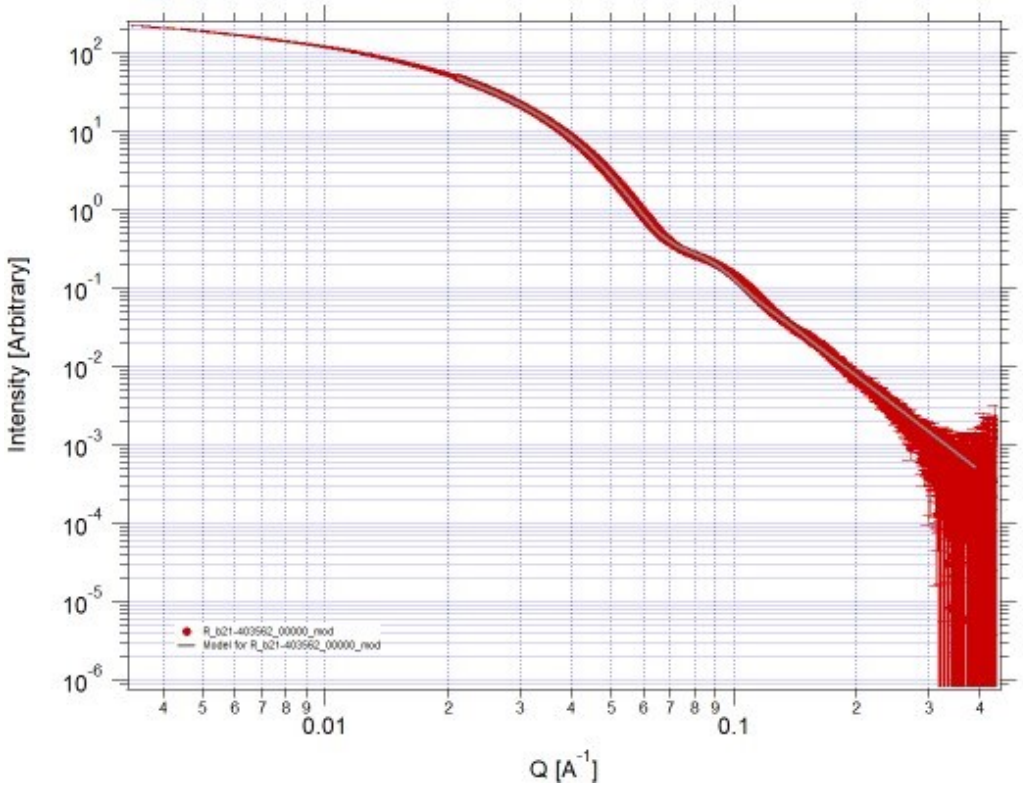

10 µg/ml PHMB-AgNPs (Oct19)

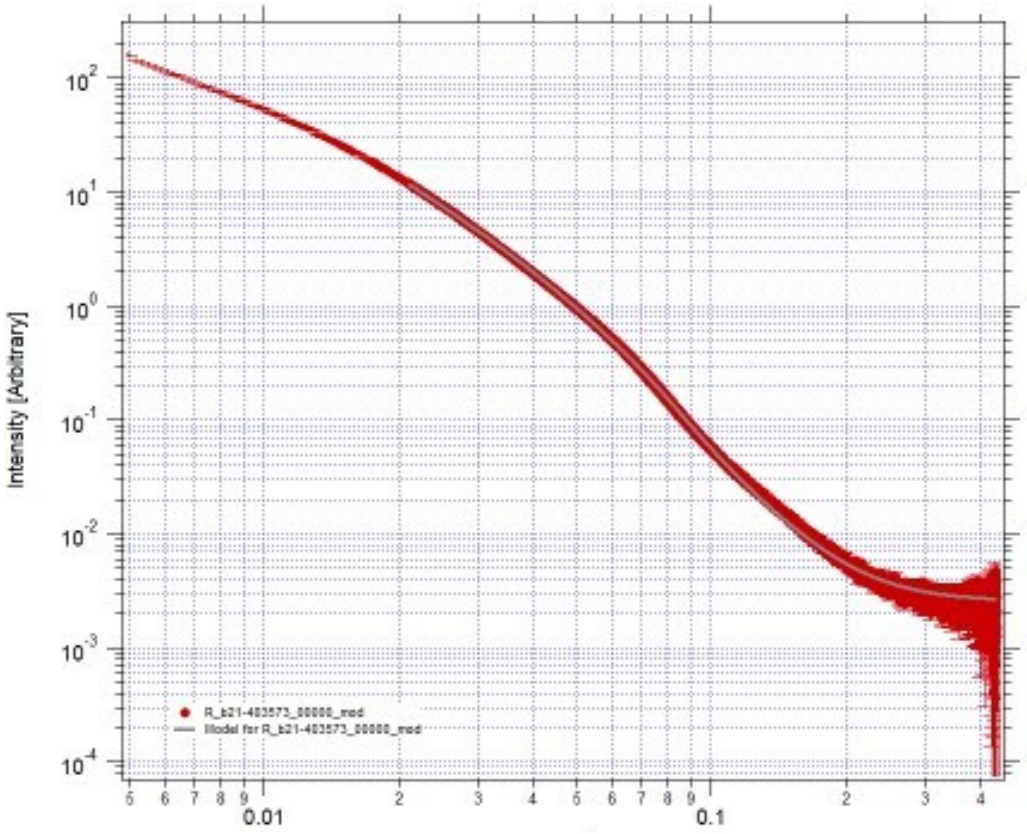

20 µg/ml PHMB-AgNPs (Oct19)

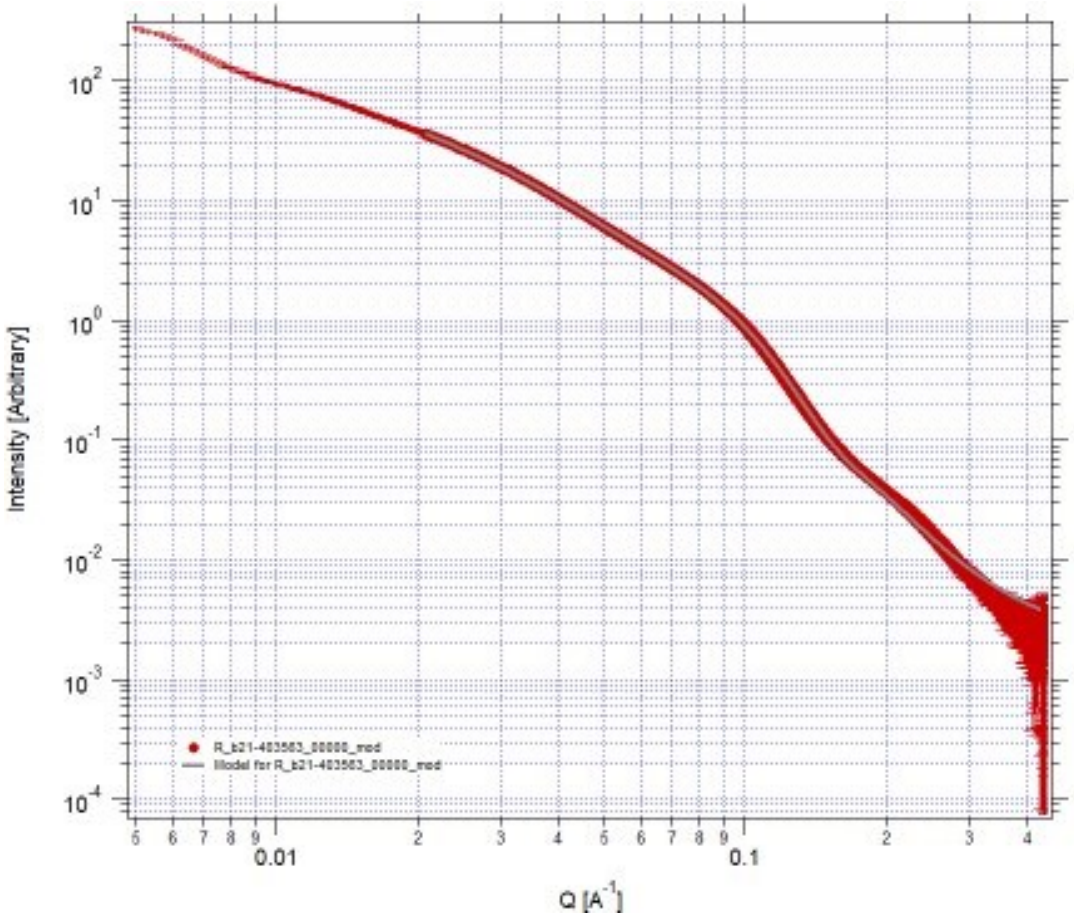

60 µg/ml PHMB-AgNPs (Oct19)

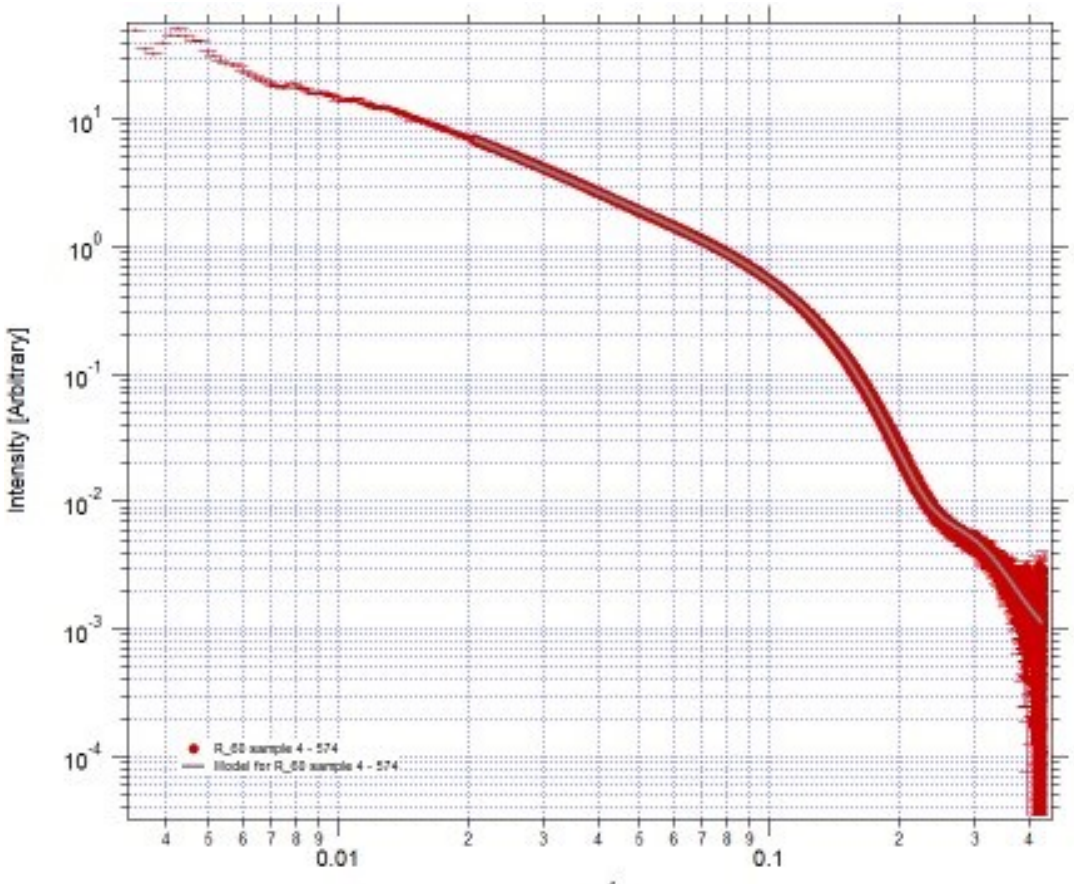

80 µg/ml PHMB-AgNPs (Oct19)

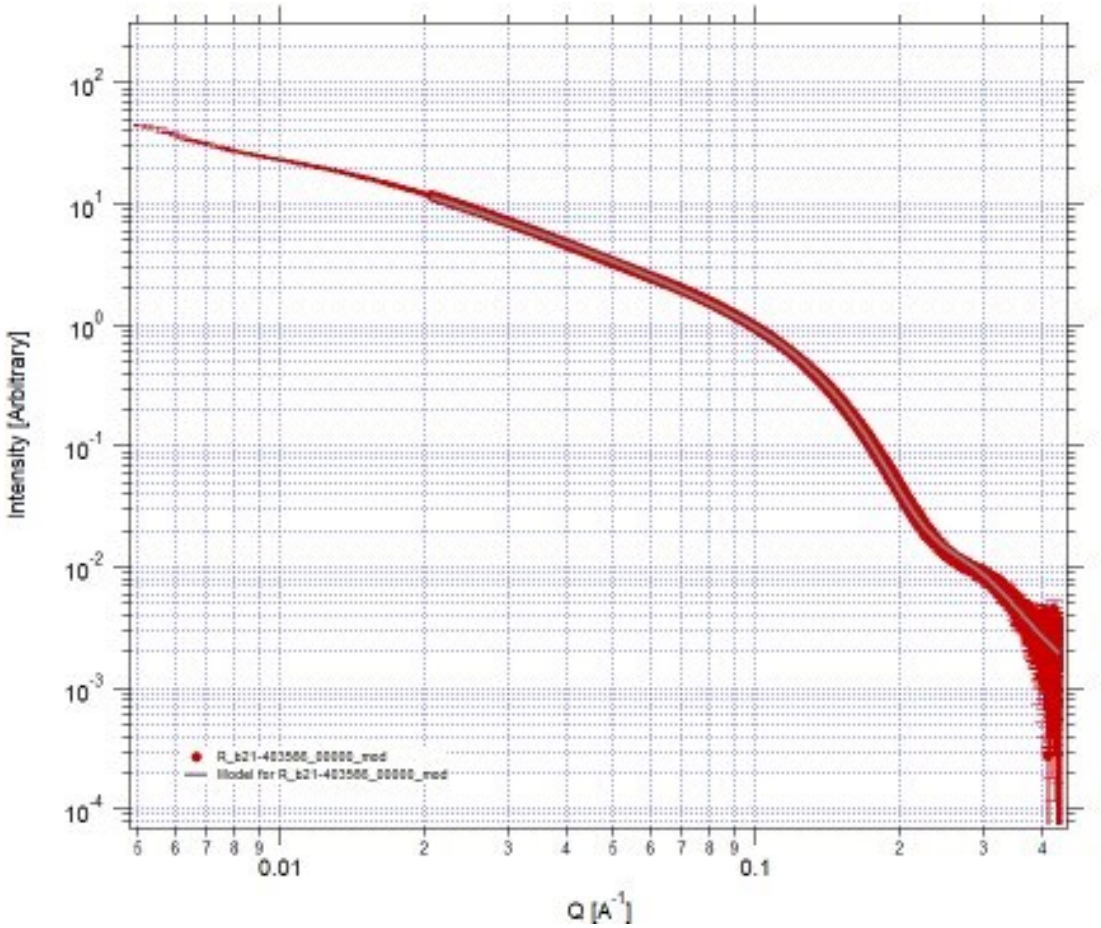

100 µg/ml PHMB-AgNPs (Oct19)

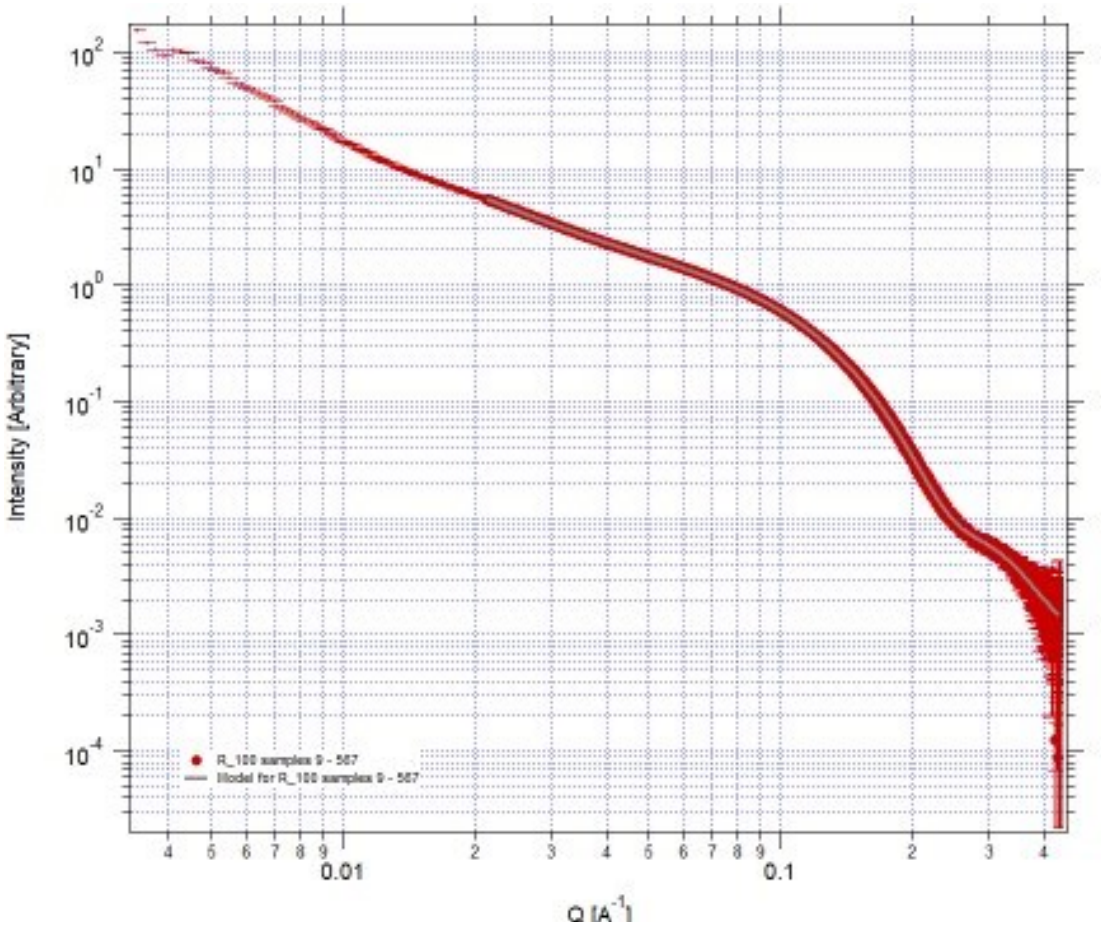

160 µg/ml PHMB-AgNPs (Oct19)

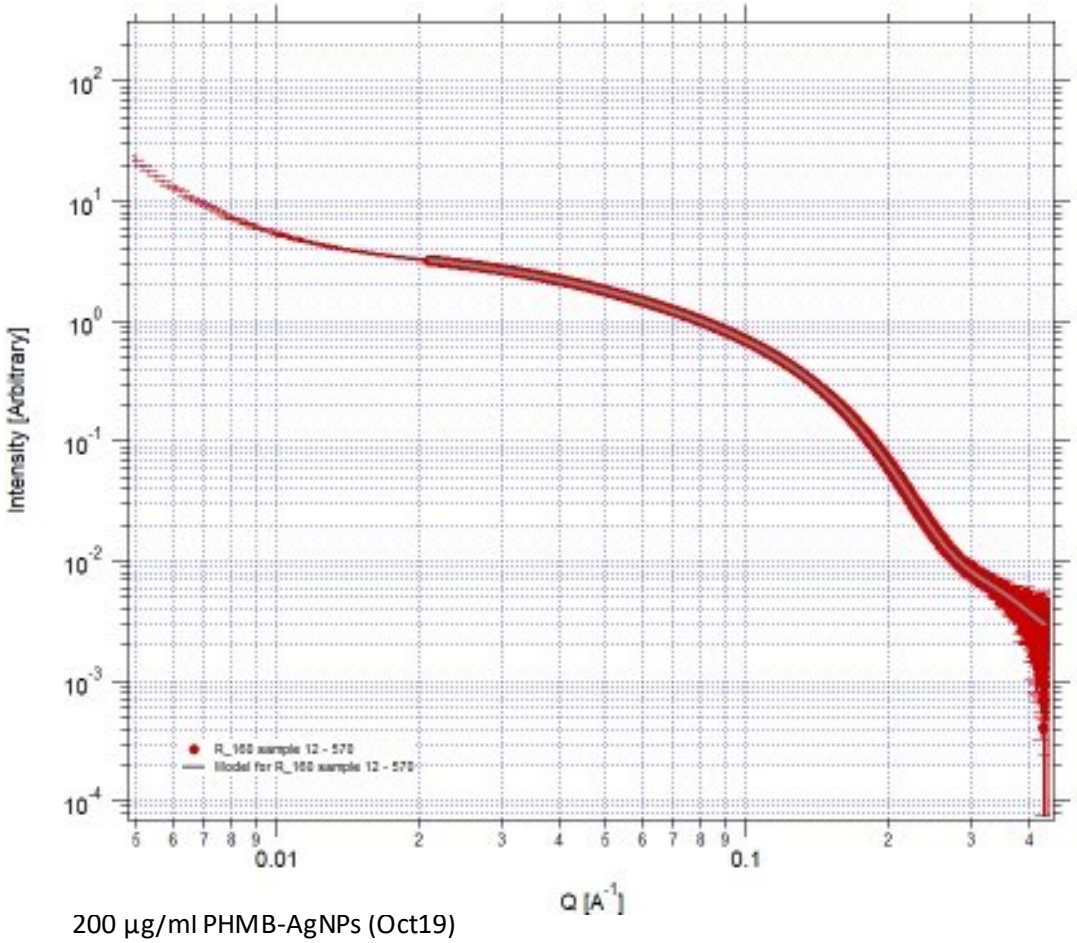

200 µg/ml PHMB-AgNPs (Oct19)

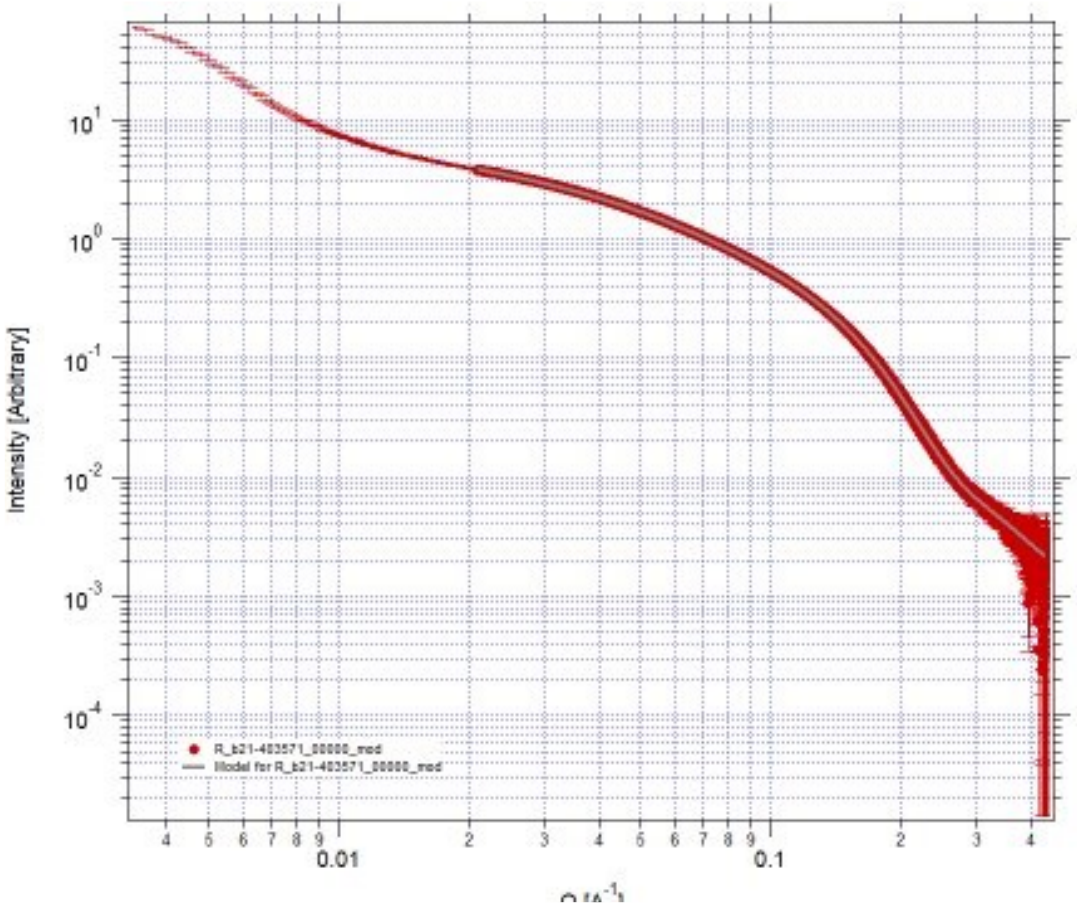

Appendix 1c – Two population modelling for 20 and 80 µg/ml PHMB-AgNPs.

Results saved on 16 Apr 2020 12:34:06

Single data set used:

FolderName_set1 = root:SAS:ImportedData:'b21-403563_00000':

IntensityDataName_set1 = R_b21-403563_00000_mod

QvecDataName_set1 = Q_b21-403563_00000_mod

ErrorDataName_set1 = S_b21-403563_00000_mod

UserDataSetName_set1 = R_b21-403563_00000_mod

DataScalingFactor_set1 = 1

ErrorScalingFactor_set1 = 1

Qmin_set1 = 0.0049807

Qmax_set1 = 0.40902

Background_set1 = 0

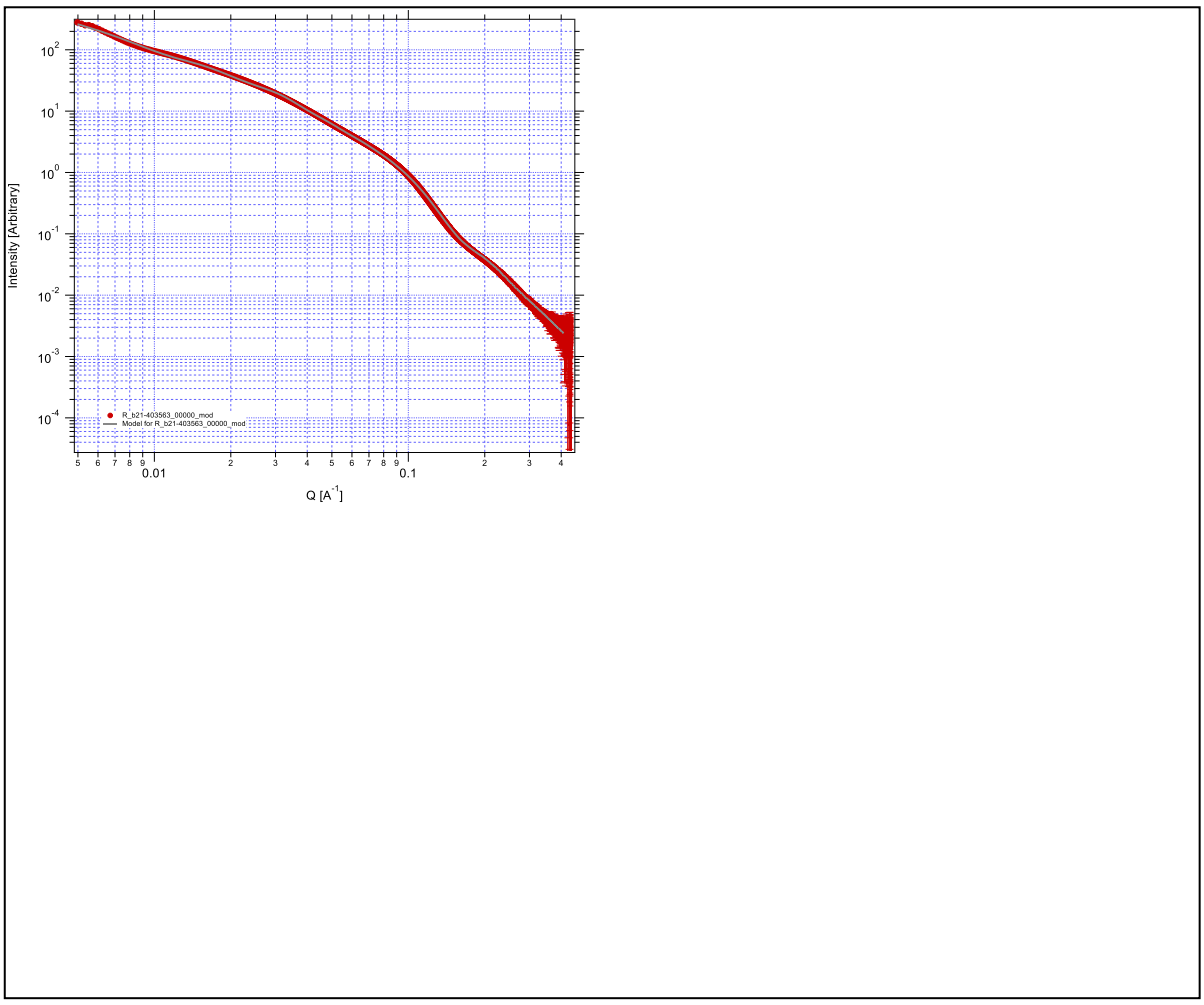

LSQF2 main data window

Model data for 3 population(s) used to obtain above results

Summary results for population 1

This population was Size Distribution

Scale	=	9.1765e-05
Mean	=	27.597
Mode	=	27.597
Median	=	27.597
FWHM	=	11.319
Distribution Type	=	Gauss
GaussMean	=	27.597
GaussWidth	=	4.8039
Contrast	=	4643
FormFactor	=	Spheroid
Aspect Ratio (FormFactor_Param1)	=	1
StructureFactor	=	Dilute system

Summary results for population 2

This population was Size Distribution

Scale	=	0.00011723
Mean	=	50.414
Mode	=	44.28
Median	=	48.497
FWHM	=	81.57
Distribution Type	=	Gauss
GaussMean	=	44.28
GaussWidth	=	34.634
Contrast	=	4643
FormFactor	=	Spheroid
Aspect Ratio (FormFactor_Param1)	=	1
StructureFactor	=	HardSpheres
Radius (StructureParam1)	=	189.02
Volume fraction (StructureParam2)	=	0.1145

Summary results for population 3

This population was Unified level

Contrast	=	100
Unified level Rg	=	10000
Unified level G	=	1e+05
Unified level B	=	0.067081
Unified level P	=	0.72817
Unified level RGCo	=	200
Unified level K	=	1

Structure factor description and parameters

StructureFactor	=	Dilute system

Appendix 1d – Two population modelling for 80 µg/ml PHMB-AgNPs.

Results saved on 10 Feb 2020 16:40:01

Single data set used:

FolderName_set1		***=root:SAS:ImportedData:'b21-403566_00000':***
IntensityDataName_set1	=	R_b21-403566_00000_mod
QvecDataName_set1	=	Q_b21-403566_00000_mod
ErrorDataName_set1	=	S_b21-403566_00000_mod
UserDataSetName_set1	=	R_b21-403566_00000_mod
DataScalingFactor_set1	=	1
ErrorScalingFactor_set1	=	1
Qmin_set1	=	0.0049807
Qmax_set1	=	0.42433
Background_set1	=	0

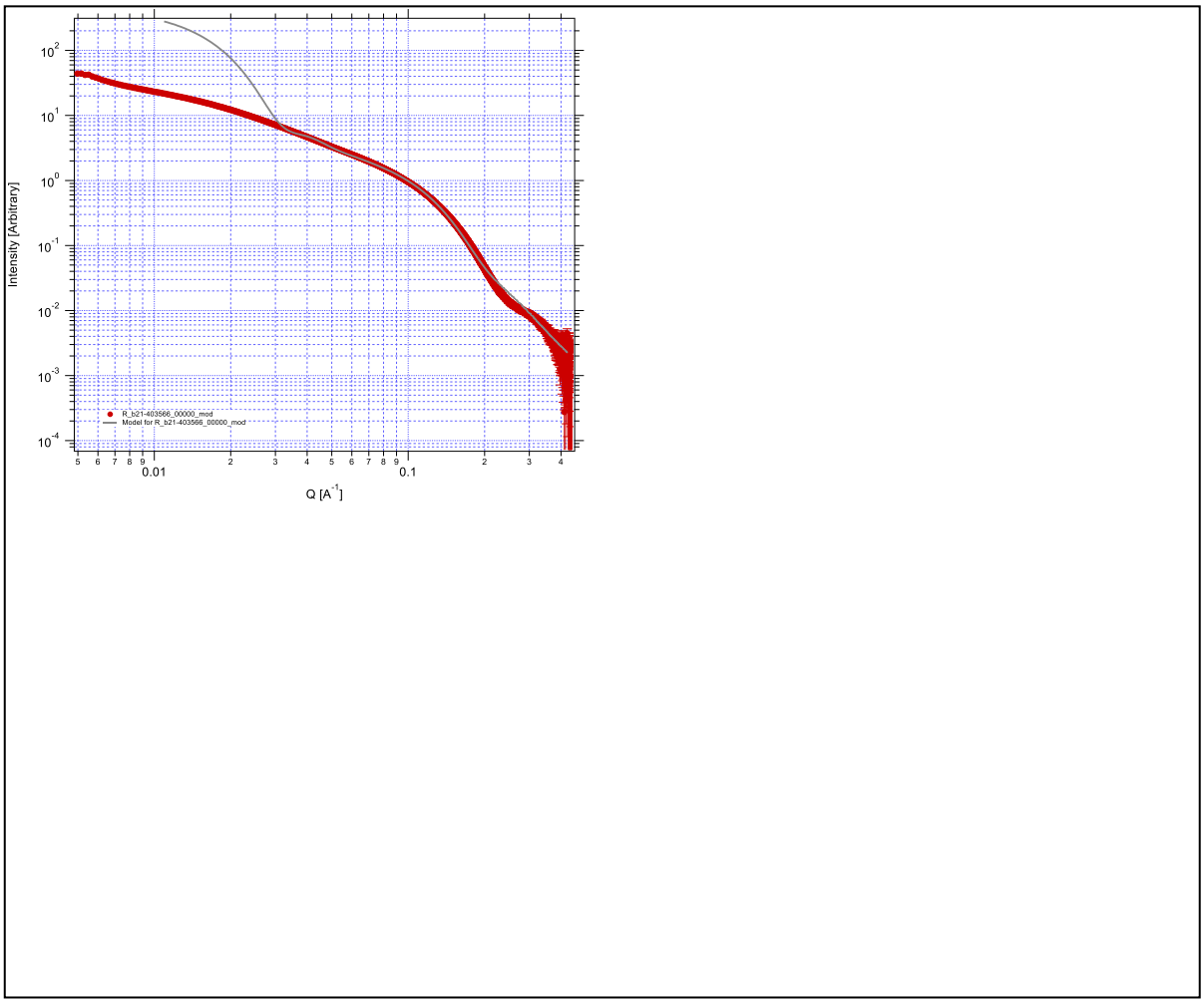

LSQF2 main data window

Model data for 3 population(s) used to obtain above results

Summary results for population 1

This population was Size Distribution

Scale	=	0.00014588
Mean	=	20.728
Mode	=	20.728
Median	=	20.728

FWHM	=	11.046
Distribution Type	=	Gauss
GaussMean	=	20.728
GaussWidth	=	4.6882
Contrast	=	4643
FormFactor	=	Spheroid
Aspect Ratio (FormFactor_Param1)	=	1
StructureFactor	=	Dilute system

Summary results for population 2

This population was Size Distribution

Scale	=	8.8545e-05
Mean	=	135.6
Mode	=	135.6
Median	=	135.6
FWHM	=	54.693
Distribution Type	=	Gauss
GaussMean	=	135.6
GaussWidth	=	23.212
Contrast	=	4643
FormFactor	=	Spheroid
Aspect Ratio (FormFactor_Param1)	=	1
StructureFactor	=	Dilute system

Summary results for population 3

This population was Unified level

Contrast	=	100
Unified level Rg	=	10000
Unified level G	=	1e+05
Unified level B	=	9.9252e-05
Unified level P	=	0.27805
Unified level RGCo	=	300
Unified level K	=	1

Structure factor description and parameters

StructureFactor	=	Dilute system

Appendix 2 – Table of all measurements taken with DLS when investigating impact of the concentration on the results obtained

Record	Sample Name	Measurement Date and Time	Z-Ave	PdI	Derived Count Rate	Atten-ator	Measur-ement Position	Mean Count Rate	In Range	Cumulants Fit Error	Multimodal Fit Error	Measured Intercept
			d.nm		kcps		mm	kcps				
25	20 µg/ml PHMB-AgNPs un 1	18/01/2019 15:08	64.94	0.427	822720.6	4	0.85	494.1	95.7	0.00955	0.00123	0.613
26	20 µg/ml PHMB-AgNPs un 2	18/01/2019 15:10	68.38	0.403	823526.9	4	0.85	494.6	96	0.0115	0.00101	0.616
27	20 µg/ml PHMB-AgNPs un 3	18/01/2019 15:12	78.35	0.331	837888.6	4	0.85	503.2	96.5	0.017	0.00111	0.62
28	20 µg/ml PHMB-AgNPs 1:1 1	18/01/2019 15:28	48.77	0.678	316371.3	5	1.05	448.2	98	0.00261	4.35E-04	0.629
47	20 µg/ml PHMB-AgNPs 1:1 1	18/01/2019 17:09	47.04	0.557	92614.7	6	1.25	334.9	93.9	0.00304	0.00127	0.637
48	20 µg/ml PHMB-AgNPs 1:1 2	18/01/2019 17:11	64.18	0.283	86886.4	6	1.25	314.2	89.7	0.0161	0.00189	0.658
49	20 µg/ml PHMB-AgNPs 1:1 3	18/01/2019 17:13	46.14	0.615	89564.8	6	1.25	323.9	95.2	0.00255	0.00101	0.639
50	20 µg/ml PHMB-AgNPs 1:2 1	18/01/2019 17:21	51.01	0.481	154692	5	1.25	219.1	94.8	0.00503	0.00177	0.659
51	20 µg/ml PHMB-AgNPs 1:2 2	18/01/2019 17:23	69.41	0.257	148955	5	1.25	211	89.6	0.0192	0.00212	0.677
52	20 µg/ml PHMB-AgNPs 1:2 3	18/01/2019 17:25	60.83	0.272	147577.9	5	1.25	209.1	94.4	0.0153	0.00218	0.659
53	20 µg/ml PHMB-AgNPs 1:3 1	18/01/2019 17:32	62.66	0.326	434942.8	4	1.05	261.2	90.9	0.0128	0.00185	0.664
54	20 µg/ml PHMB-AgNPs 1:3 2	18/01/2019 17:34	51.34	0.48	419607.7	4	1.05	252	94.9	0.00503	0.00117	0.655

Record	Sample Name	Measurement Date and Time	Z-Ave	PdI	Derived Count Rate	Atten-ator	Measur-ement Position	Mean Count Rate	In Range	Cumulants Fit Error	Multimodal Fit Error	Measured Intercept
55	20 µg/ml PHMB-AgNPs 1:3 3	18/01/2019 17:37	47.86	0.658	422724	4	1.05	253.9	89.9	0.00271	6.90E-04	0.66
56	20 µg/ml PHMB-AgNPs 1:4 1	18/01/2019 17:44	57.88	0.551	633721.3	4	0.85	380.6	95.4	0.00497	9.13E-04	0.644
57	20 µg/ml PHMB-AgNPs 1:4 2	18/01/2019 17:46	55.76	0.613	643166.4	4	0.85	386.3	95.8	0.00401	5.63E-04	0.637
58	20 µg/ml PHMB-AgNPs 1:4 3	18/01/2019 17:48	55.89	0.615	647245.8	4	0.85	388.7	96.2	0.00384	9.16E-04	0.642
59	20 µg/ml PHMB-AgNPs 1:6 1	18/01/2019 17:54	57.2	0.345	245995.9	5	1.25	348.5	93.3	0.00965	0.00201	0.647
60	20 µg/ml PHMB-AgNPs 1:6 2	18/01/2019 17:56	59.5	0.269	247979.9	5	1.25	351.3	92.6	0.0148	0.00242	0.64
61	20 µg/ml PHMB-AgNPs 1:6 3	18/01/2019 17:59	83.52	0.257	261245.5	5	1.25	370.1	83.9	0.0299	0.0026	0.689
62	20 µg/ml PHMB-AgNPs 1:6 1	22/01/2019 10:15	64.89	0.555	655491.2	4	0.85	393.7	94	0.00655	6.33E-04	0.653
63	20 µg/ml PHMB-AgNPs 1:6 2	22/01/2019 10:18	61.5	0.586	657411.1	4	0.85	394.8	96	0.00524	7.44E-04	0.645
64	20 µg/ml PHMB-AgNPs 1:6 3	22/01/2019 10:20	61.66	0.515	654878.1	4	0.85	393.3	98.4	0.00622	6.64E-04	0.637
65	20 µg/ml PHMB-AgNPs 1:8 1	22/01/2019 10:26	55.22	0.3	282412.6	5	1.25	400.1	92.8	0.0121	0.00203	0.639
66	20 µg/ml PHMB-AgNPs 1:8 2	22/01/2019 10:28	53.08	0.335	290913.1	5	1.25	412.1	93.7	0.0101	0.0021	0.64
67	20 µg/ml PHMB-AgNPs 1:8 3	22/01/2019 10:30	51.2	0.364	285529.2	5	1.25	404.5	93.8	0.00888	0.00201	0.635
68	20 µg/ml PHMB-AgNPs 1:10 1	22/01/2019 10:37	93.83	0.276	426944.9	4	1.05	256.4	89.8	0.0253	0.00341	0.684

Record	Sample Name	Measurement Date and Time	Z-Ave	PdI	Derived Count Rate	Atten-ator	Measur-ement Position	Mean Count Rate	In Range	Cumulants Fit Error	Multimodal Fit Error	Measured Intercept
69	20 µg/ml PHMB-AgNPs 1:10 2	22/01/2019 10:39	60.12	0.585	417284.7	4	1.05	250.6	94.4	0.00554	0.00151	0.663
70	20 µg/ml PHMB-AgNPs 1:10 3	22/01/2019 10:42	61.95	0.542	419120.4	4	1.05	251.7	94.7	0.0066	9.09E-04	0.663
71	20 µg/ml PHMB-AgNPs 1:12 1	22/01/2019 10:52	98.31	0.611	1376026	3	0.85	168.6	95.8	0.00458	0.00104	0.32
72	20 µg/ml PHMB-AgNPs 1:12 2	22/01/2019 10:54	111.1	0.396	1426723	3	0.85	174.8	97.8	0.00839	0.00127	0.309
73	20 µg/ml PHMB-AgNPs 1:12 3	22/01/2019 10:57	93.93	0.653	1442648	3	0.85	176.8	97.7	0.00334	7.21E-04	0.299
74	20 µg/ml PHMB-AgNPs 1:14 1	22/01/2019 11:05	313.7	0.372	14482.7	7	4.65	182.7	86.2	0.0801	0.0315	0.792
75	20 µg/ml PHMB-AgNPs 1:14 2	22/01/2019 11:08	75.55	0.129	14245.7	7	4.65	179.7	92.4	0.0624	0.00484	0.667
76	20 µg/ml PHMB-AgNPs 1:14 3	22/01/2019 11:10	59.15	0.194	13888.4	7	4.65	175.2	91.9	0.0257	0.00321	0.661
77	20 µg/ml PHMB-AgNPs 1:16 1	22/01/2019 11:18	60.68	0.753	317898.8	5	0.85	450.3	97.4	0.00287	9.51E-04	0.613
78	20 µg/ml PHMB-AgNPs 1:16 2	22/01/2019 11:20	67.79	0.491	315622.6	5	0.85	447.1	97.3	0.00746	5.83E-04	0.612
79	20 µg/ml PHMB-AgNPs 1:16 3	22/01/2019 11:22	59.61	0.735	315181.3	5	0.85	446.5	97.3	0.00286	5.60E-04	0.611
80	20 µg/ml PHMB-AgNPs 1:18 1	22/01/2019 11:38	115	0.188	22721	7	4.65	286.6	91.9	0.0563	0.0103	0.674
81	20 µg/ml PHMB-AgNPs 1:18 2	22/01/2019 11:40	133.4	0.172	22703.5	7	4.65	286.4	88	0.0693	0.0111	0.681
82	20 µg/ml PHMB-AgNPs 1:18 3	22/01/2019 11:42	48.22	0.456	22695.7	7	4.65	286.3	95	0.0049	0.00224	0.639

Record	Sample Name	Measurement Date and Time	Z-Ave	PdI	Derived Count Rate	Atten-ator	Measur-ement Position	Mean Count Rate	In Range	Cumulants Fit Error	Multimodal Fit Error	Measured Intercept
83	20 µg/ml PHMB-AgNPs 1:20 1	22/01/2019 12:25	50.12	0.429	215666.6	5	1.05	305.5	93.1	0.00596	0.00173	0.643
84	20 µg/ml PHMB-AgNPs 1:20 2	22/01/2019 12:27	48.46	0.444	213176.8	5	1.05	302	94.5	0.00494	0.00107	0.641
85	20 µg/ml PHMB-AgNPs 1:20 3	22/01/2019 12:29	45.73	0.482	209666	5	1.05	297	97.5	0.00386	7.84E-04	0.633
86	20 µg/ml PHMB-AgNPs 1:25 1	22/01/2019 12:39	47.94	0.508	178890.1	5	1.05	253.4	96	0.00377	0.00133	0.648
87	20 µg/ml PHMB-AgNPs 1:25 2	22/01/2019 12:41	50.39	0.424	180939.1	5	1.05	256.3	94.4	0.00586	0.00102	0.646
88	20 µg/ml PHMB-AgNPs 1:25 3	22/01/2019 12:43	49.84	0.49	179554.3	5	1.05	254.4	95.9	0.00508	0.00111	0.659
89	20 µg/ml PHMB-AgNPs 1:40 1	22/01/2019 12:50	120.4	0.196	43844.8	6	4.65	158.5	94.3	0.0596	0.0124	0.702
90	20 µg/ml PHMB-AgNPs 1:40 2	22/01/2019 12:53	119.8	0.157	44634.4	6	4.65	161.4	92.7	0.0735	0.0106	0.69
91	20 µg/ml PHMB-AgNPs 1:40 3	22/01/2019 12:55	63.61	0.159	44809.9	6	4.65	162	93.7	0.0259	0.00443	0.669
92	20 µg/ml PHMB-AgNPs 1:50 1	22/01/2019 13:04	329.4	0.389	46673.2	6	4.65	168.8	88.7	0.0842	0.0368	0.797
93	20 µg/ml PHMB-AgNPs 1:50 2	22/01/2019 13:06	87.45	0.147	46435.8	6	4.65	167.9	89.3	0.06	0.00516	0.69
94	20 µg/ml PHMB-AgNPs 1:50 3	22/01/2019 13:09	64.13	0.162	47578.4	6	4.65	172	90.9	0.0285	0.0034	0.673
95	20 µg/ml PHMB-AgNPs 1:75 1	22/01/2019 13:16	95.82	0.158	41254.7	6	4.65	149.2	96.3	0.0553	0.00723	0.688
96	20 µg/ml PHMB-AgNPs 1:75 2	22/01/2019 13:18	68.59	0.17	41715	6	4.65	150.8	93	0.0293	0.005	0.681

Record	Sample Name	Measurement Date and Time	Z-Ave	PdI	Derived Count Rate	Atten-ator	Measur-ement Position	Mean Count Rate	In Range	Cumulants Fit Error	Multimodal Fit Error	Measured Intercept
97	20 µg/ml PHMB-AgNPs 1:75 3	22/01/2019 13:21	45.25	0.487	40904.4	6	4.65	147.9	94.5	0.00412	0.00198	0.659
98	20 µg/ml PHMB-AgNPs 1:100 1	22/01/2019 13:28	46.18	0.489	54327.7	6	1.25	196.4	93.9	0.00391	0.00156	0.65
99	20 µg/ml PHMB-AgNPs 1:100 2	22/01/2019 13:30	53.26	0.3	54605.7	6	1.25	197.4	91.9	0.0127	0.00221	0.66
100	20 µg/ml PHMB-AgNPs 1:100 3	22/01/2019 13:33	45.25	0.474	54135	6	1.25	195.7	93.1	0.004	0.00127	0.649
101	20 µg/ml PHMB-AgNPs 1:150 1	22/01/2019 13:41	74	0.124	26595.3	7	4.65	335.5	93.6	0.0519	0.00577	0.651
102	20 µg/ml PHMB-AgNPs 1:150 2	22/01/2019 13:43	47.56	0.409	26400.1	7	4.65	333	94.6	0.00597	0.00273	0.64
103	20 µg/ml PHMB-AgNPs 1:150 3	22/01/2019 13:45	61.21	0.153	26652.9	7	4.65	336.2	93	0.0253	0.00453	0.646
104	20 µg/ml PHMB-AgNPs 1:200 1	22/01/2019 13:51	79.98	0.133	21920.1	7	4.65	276.5	95.7	0.0497	0.00676	0.66
105	20 µg/ml PHMB-AgNPs 1:200 2	22/01/2019 13:53	70.12	0.121	21993.6	7	4.65	277.4	93.5	0.0687	0.00525	0.659
106	20 µg/ml PHMB-AgNPs 1:200 3	22/01/2019 13:55	58.81	0.151	21954.1	7	4.65	276.9	92.8	0.0284	0.00388	0.65
Mean 25-28,47-106			74.28	0.387	293071.5	5	2.23	289	93.7	0.0204	0.00371	0.641
Std Dev			49.27	0.176	341906	1	1.71	100.7	2.89	0.023	0.00615	0.081

Appendix 3 – Table with factors and results when assessing statistical significance of time, volume and concentration of PHMB-AgNPs against *E. Coli* using design of experiment.

Run	Factor 1 - Volume (µl)	Factor 2 - time (min)	Factor 3 - Concentration (µg/ml)	Response 1 - Q1 - Live	Response 2 - Q2 - Damaged	Response 3 - Q3 - Dead
1	2.00	40.08	200	3.2	95.8	1
2	10.00	36.00	20	7.6	91.9	0.5
3	10.00	60.00	140	1	98.8	0.2
4	6.00	12.00	20	17.7	81.8	0.5
5	3.74	49.44	140	0.2	98.9	0.9
6	9.60	19.81	80	0.6	99	0.4
7	8.76	57.36	200	2.9	96.8	0.4
8	3.80	22.56	0	96.7	3.2	0.1
9	8.20	23.04	140	0.9	98.3	0.8
10	3.80	22.56	0	97.2	2.7	0.1
11	9.84	47.52	80	0.9	97.7	1.4
12	9.89	27.84	200	12.7	87.3	0
13	8.20	49.44	0	94.6	4.9	0.4
14	2.00	60.00	0	98.4	1.2	0.4
15	10.00	12.00	20	7.9	91.3	0.8
16	2.00	35.76	20	12.2	87.1	0.6
17	5.12	12.72	80	0.2	99.4	0.4
18	4.52	59.28	200	1	98	0.9
19	3.74	49.44	140	0.4	98.2	1.4
20	2.53	54.07	80	0.8	97.2	1.9
21	8.20	23.04	140	0.4	98.9	0.7
22	10.00	12.00	0	99.5	0.4	0
23	9.89	27.84	200	4.2	94	1.8
24	8.20	49.44	0	96.2	3.4	0.4
25	2.80	16.32	200	0.3	99.7	0.1
26	2.00	12.00	140	0.3	99	0.7
27	6.00	60.00	20	10.4	87.5	2.1
28	2.00	29.28	80	4.6	92.8	2.6

Appendix 4 – Summary table for all measurements taken on STEM-in-SEM images to calculate statistical values.

	N total	Mean	Standard Deviation	Sum	Minimum	Median	Maximum
Bare	338	13.6367	15.86685	4609.204	2.935	10.9315	176.602
20	451	7.9422	5.75538	3581.931	1.526	5.99	40.49
40	61	6.85146	3.01362	417.939	3.313	5.871	16.042
60	150	5.39308	3.17062	808.962	0.698	4.6765	21.105
80	450	4.45147	2.56678	2003.161	1.383	3.8885	28.212
100	150	4.80723	2.59295	721.084	1.115	4.132	16.722
120	150	5.20058	5.59285	780.087	1.247	4.085	41.638
140	452	5.14009	9.86821	2323.319	1.56	3.965	205.551
160	150	4.2797	2.16763	641.955	0.616	3.9055	12.409
200	300	3.79838	2.5034	1139.515	1.548	3.309	33.405

Appendix 5a – All autoidentified elements

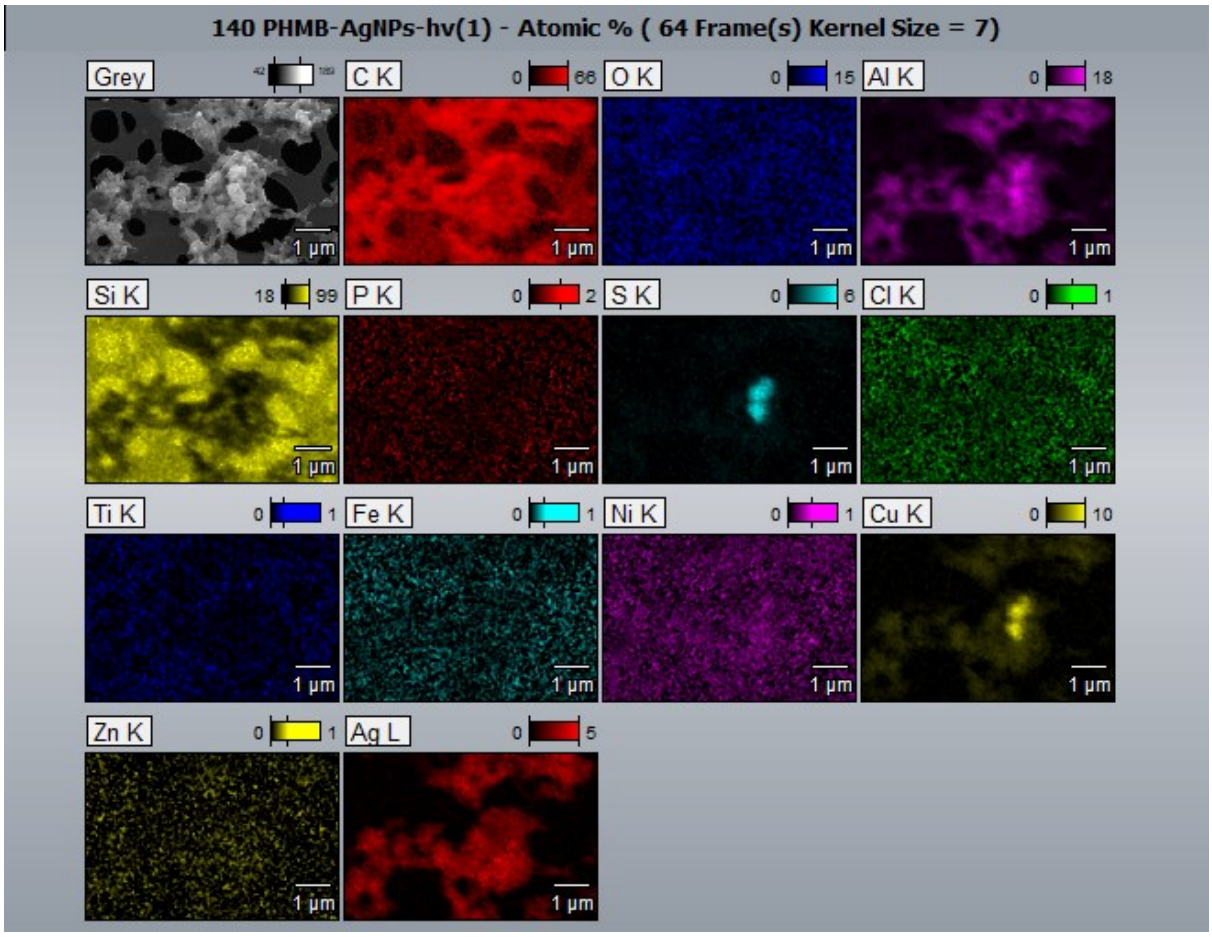

Appendix 5b - All autoidentified elements

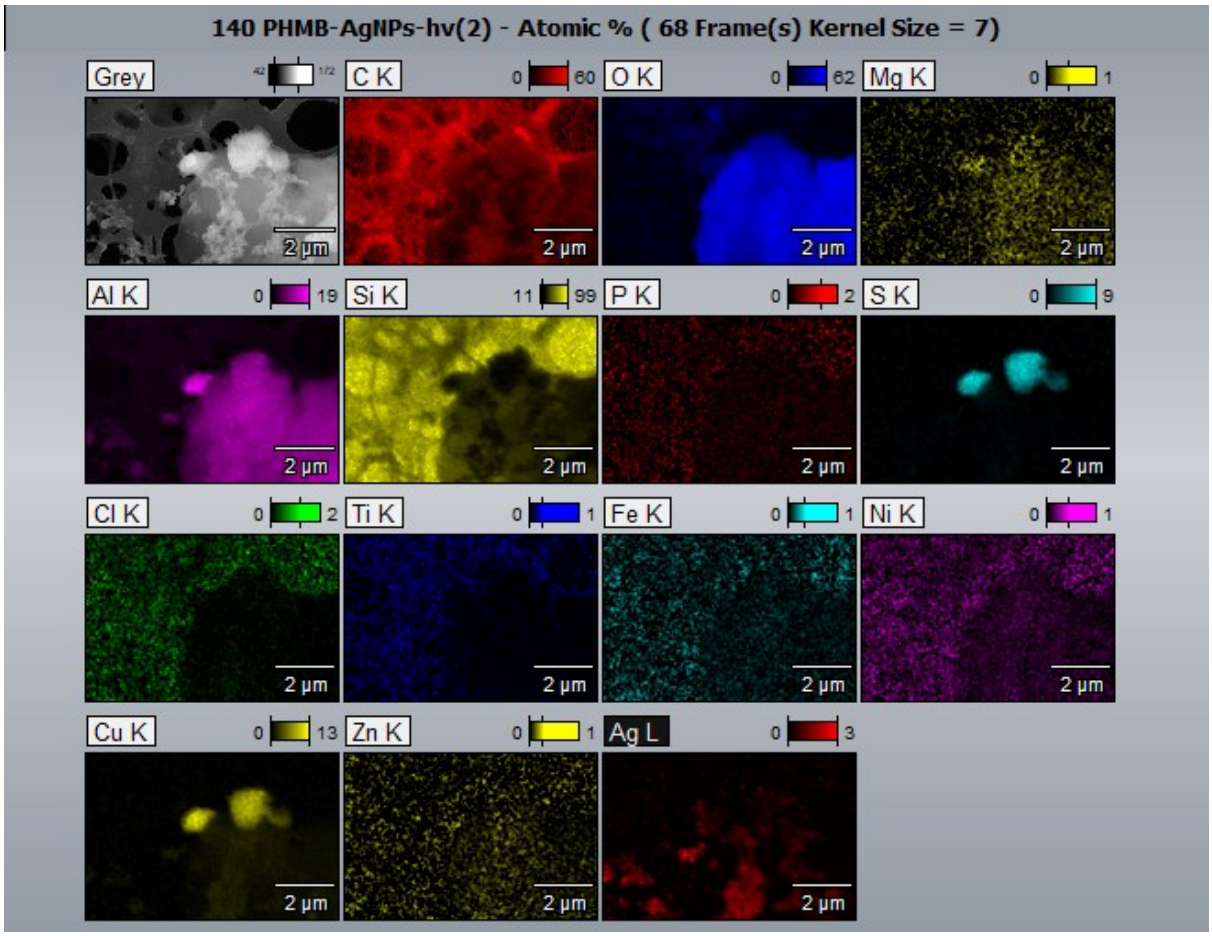

Appendix 6a – Time of measurements taken for the short-term study

Sample name	Synthesis/ centrifuge date	UV vis and DLS measurements taken on	Flow cytometer first and second measur.	Imagining using SEM
Jun20				
Bare-AgNPs	29/06/2020 30/06/2020	30/06/2020 14/07/2020 28/07/2020 11/08/2020 24/08/2020 15/09/2020 03/11/2020	10/07/2020 31/07/2020	5,6,9/11/2020
20 µg/ml PHMB-AgNPs	29/06/2020 30/06/2020		10/07/2020 31/07/2020	5,6,9/11/2020
80 µg/ml PHMB-AgNPs	29/06/2020 30/06/2020		10/07/2020 31/07/2020	5,6,9/11/2020
140 µg/ml PHMB-AgNPs	29/06/2020 30/06/2020		10/07/2020 31/07/2020	5,6,9/11/2020
200 µg/ml PHMB-AgNPs	29/06/2020 30/06/2020		10/07/2020 31/07/2020	5,6,9/11/2020
40 µg/ml PHMB-AgNPs	6/07/2020 7/07/2020	07/07/2020 21/07/2020 04/08/2020 18/08/2020 03/09/2020 29/09/2020 10/11/2020	10/07/2020 07/08/2020	12,13,16/11/2020
60 µg/ml PHMB-AgNPs	6/07/2020 7/07/2020		10/07/2020 N/A	12,13,16/11/2020
100 µg/ml PHMB-AgNPs	6/07/2020 7/07/2020		10/07/2020 N/A	12,13,16/11/2020
120 µg/ml PHMB-AgNPs	6/07/2020 7/07/2020		10/07/2020 N/A	12,13,16/11/2020
160 µg/ml PHMB-AgNPs	6/07/2020 7/07/2020		10/07/2020 N/A	12,13,16/11/2020

Appendix 6b - Time of measurements taken for the long-term study

Sample name	Centrifuge date (synthesis prev. day)	1st measurement /DLS/UV-Vis	2nd measurement /DLS	Time between measurements DLS		2nd measurement /UV-Vis	Time between measurements UV-Vis		Time between centrifuge /SAXS	SAXS time reference
Oct19			22/12/2020	days	weeks		days	weeks		
Bare-AgNPs	18/10/2019	18/10/2019	27/11/2019	40	5.71	22/11/2019	35	5.00	2 days	Fresh
10 µg/ml PHMB-AgNPs						22/11/2019				Fresh
20 µg/ml PHMB-AgNPs	09/10/2019	09/10/2019	16/12/2019	68	9.71	22/11/2019	44	6.29	11 days	Fresh
40 µg/ml PHMB-AgNPs	09/10/2019	09/10/2019	16/12/2019	68	9.71	22/11/2019	44	6.29	11 days	Fresh
60 µg/ml PHMB-AgNPs	15/10/2019	15/10/2019	16/12/2019	62	8.86	22/11/2019	38	5.43	5 days	Fresh
80 µg/ml PHMB-AgNPs	09/10/2019	09/10/2019	16/12/2019	68	9.71	22/11/2019	44	6.29	11 days	Fresh
100 µg/ml PHMB-AgNPs	15/10/2019	15/10/2019	16/12/2019	62	8.86	22/11/2019	38	5.43	5 days	Fresh
120 µg/ml PHMB-AgNPs	15/10/2019	15/10/2019	16/12/2019	62	8.86	22/11/2019	38	5.43	5 days	Fresh
140 µg/ml PHMB-AgNPs	17/10/2019	17/10/2019	17/12/2019	61	8.71	22/11/2019	36	5.14	11 days	Fresh
160 µg/ml PHMB-AgNPs	15/10/2019	15/10/2019	17/12/2019	63	9.00	22/11/2019	38	5.43	5 days	Fresh
200 µg/ml PHMB-AgNPs	11/10/2019	11/10/2019	17/12/2019	67	9.57	22/11/2019	42	6.00	11 days	Fresh

Sample name	Centrifuge date (synthesis prev. day)	1st measurement /DLS/UV-Vis	2nd measurement /DLS	Time between measurements DLS		2nd measurement /UV-Vis	Time between measurements UV-Vis		Time between synthesis/ SAXS	SAXS time reference
Jun19				days	Months		days	Months		
Bare-AgNPs	06/06/2019	06/06/2019	20/12/2019	197	6.48	16/12/2019	193	6.35	4.47 mths	6 months
20 µg/ml PHMB-AgNPs	06/06/2019	06/06/2019	20/12/2019	197	6.48	16/12/2019	193	6.35	4.47 mths	6 months
40 µg/ml PHMB-AgNPs	07/06/2019	07/06/2019	20/12/2019	196	6.45	16/12/2019	192	6.32	4.44 mths	6 months
60 µg/ml PHMB-AgNPs	07/06/2019	07/06/2019	20/12/2019	196	6.45	16/12/2019	192	6.32	4.44 mths	6 months
80 µg/ml PHMB-AgNPs	06/06/2019	06/06/2019	20/12/2019	197	6.48	16/12/2019	193	6.35	4.47 mths	6 months
100 µg/ml PHMB-AgNPs	07/06/2019	07/06/2019	20/12/2019	196	6.45	16/12/2019	192	6.32	4.44 mths	6 months
120 µg/ml PHMB-AgNPs	07/06/2019	07/06/2019	20/12/2019	196	6.45	16/12/2019	192	6.32	4.44 mths	6 months

140 µg/ml PHMB-AgNPs	06/06/2019	06/06/2019	20/12/2019	197	6.48	16/12/2019	193	6.35	4.47 mths	6 months
160 µg/ml PHMB-AgNPs	07/06/2019	07/06/2019	20/12/2019	196	6.45	16/12/2019	192	6.32	4.44 mths	6 months
200 µg/ml PHMB-AgNPs	06/06/2019	06/06/2019	20/12/2019	197	6.48	16/12/2019	193	6.35	4.47 mths	6 months

Sample name	Centrifuge date (synthesis prev. day)	1st measurement /DLS/UV-Vis	2nd measurement /DLS	Time between measurements DLS		2nd measurement /UV-Vis	Time between measurements UV-Vis		Time between synthesis/ SAXS	SAXS time reference
Jan19				days	Months		days	Months		
Bare-AgNPs		20/02/2019								
20 µg/ml PHMB-AgNPs		20/02/2019	20/12/2019	303	9.97	17/12/2019	300	9.87		9 months
40 µg/ml PHMB-AgNPs		20/02/2019	20/12/2019	303	9.97	17/12/2019	300	9.87		9 months
60 µg/ml PHMB-AgNPs		20/02/2019	20/12/2019	303	9.97	17/12/2019	300	9.87		9 months
80 µg/ml PHMB-AgNPs		20/02/2019	20/12/2019	303	9.97	17/12/2019	300	9.87		9 months
100 µg/ml PHMB-AgNPs		20/02/2019	20/12/2019	303	9.97	17/12/2019	300	9.87		9 months
120 µg/ml PHMB-AgNPs		20/02/2019	20/12/2019	303	9.97	17/12/2019	300	9.87		9 months
140 µg/ml PHMB-AgNPs		20/02/2019	20/12/2019	303	9.97	17/12/2019	300	9.87		9 months
160 µg/ml PHMB-AgNPs		20/02/2019	20/12/2019	303	9.97	17/12/2019	300	9.87		9 months
200 µg/ml PHMB-AgNPs		20/02/2019	20/12/2019	303	9.97	17/12/2019	300	9.87		9 months

Sample name	Centrifuge date (synthesis prev. day)	1st measurement /UV-Vis	2nd measurement /DLS	2nd measurement /UV-Vis	Time between measurements UV-Vis		Time between synthesis/ SAXS	SAXS time reference
Nov18					days	Months		
Bare-AgNPs								
20 µg/ml PHMB-AgNPs	16/11/2018	16/11/2018	20/12/2019	19/12/2019	398	13.09	11.12 mths	11 months
40 µg/ml PHMB-AgNPs	22/11/2018	22/11/2018	20/12/2019	19/12/2019	392	12.89	10.92 mths	11 months
60 µg/ml PHMB-AgNPs	22/11/2018	22/11/2018	20/12/2019	19/12/2019	392	12.89	10.92 mths	11 months
80 µg/ml PHMB-AgNPs	16/11/2018	16/11/2018	20/12/2019	19/12/2019	398	13.09	11.12 mths	11 months

100 µg/ml PHMB-AgNPs	27/11/2018	27/11/2018	20/12/2019	19/12/2019	387	12.73	10.76 mths	11 months
120 µg/ml PHMB-AgNPs	27/11/2018	27/11/2018	20/12/2019	19/12/2019	387	12.73	10.76 mths	11 months
140 µg/ml PHMB-AgNPs	22/11/2018	22/11/2018	20/12/2019	19/12/2019	392	12.89	10.92 mths	11 months
160 µg/ml PHMB-AgNPs	16/11/2018	16/11/2018	20/12/2019	19/12/2019	398	13.09	11.12 mths	11 months
180 µg/ml PHMB-AgNPs	22/11/2018	22/11/2018	20/12/2019	19/12/2019	392	12.89	10.92 mths	11 months
200 µg/ml PHMB-AgNPs	16/11/2018	16/11/2018	20/12/2019	19/12/2019	398	13.09	11.12 mths	11 months